

UNIVERSITY OF ZAGREB

FACULTY OF SCIENCE

*Marko Kraji*

***Electron states in ultra thin silver films  
on (100) vanadium surface***

*Doctoral thesis*

submitted to the Department of Physics,  
Faculty of Science, University of Zagreb  
for the academic degree of  
Doctor of Natural Sciences (Physics)

Zagreb, 2003

SVEUČILIŠTE U ZAGREBU

PRIRODOSLOVNO-MATEMATIČKI FAKULTET  
POSLIJEDIPLOMSKI STUDIJ PRIRODNIH ZNANOSTI  
FIZIKA

*Marko Kraj*

***Elektronska stanja u ultra tankim slojevima srebra  
na (100) površini vanadija***

*Doktorska teza*

predložena Fizičkom odsjeku  
Prirodoslovno-matematičkog fakulteta Sveučilišta u Zagrebu  
radi stjecanja akademskog stupnja  
doktora prirodnih znanosti (fizika)

Zagreb, 2003

## BASIC DOCUMENTATION CARD

UNIVERSITY OF ZAGREB  
FACULTY OF SCIENCE  
DEPARTMENT OF PHYSICS

DOCTORAL THESIS

*ELECTRON STATES IN ULTRA THIN SILVER FILMS ON (100) VANADIUM SURFACE*

MARKO KRALJ  
INSTITUTE OF PHYSICS, ZAGREB

IN THIS THESIS THE RESULTS OF HIGH-RESOLUTION ANGLE-RESOLVED ULTRAVIOLET PHOTOELECTRON SPECTROSCOPY (HRARUPS) AND SCANNING TUNNELLING MICROSCOPY (STM) INVESTIGATIONS OF THE VALENCE BAND ELECTRONIC STRUCTURE OF ULTRA THIN SILVER LAYERS ON A VANADIUM (100) SUBSTRATE ARE PRESENTED. THE S-P AND D-SYMMETRY QUANTUM WELL STATES HAVE BEEN CHARACTERISED IN GREAT DETAIL. FOR 1-8 MONOLAYERS (ML) Ag S-P STATES WE FOUND THE EFFECTS OF HYBRIDISATION WITH THE SUBSTRATE AND THE ENHANCEMENT AND VARIATION OF THE HOLE-PHONON COUPLING STRENGTH WITH FILM THICKNESS. THE D-BAND STATES WERE FOUND TO BE PERFECTLY CONFINED WITHIN THE FILM PRESENTING AN IDEAL EXAMPLE OF A TWO-DIMENSIONAL SYSTEM. THE SURFACE FERMI CONTOUR WAS DETERMINED FOR 1-5 ML Ag FROM STM MEASUREMENTS AND CORRELATED TO THE ELECTRONIC STRUCTURE OF THE SYSTEM.

(154 PAGES, 110 FIGURES, 197 REFERENCES, ORIGINAL IN ENGLISH)

KEYWORDS: ANGLE RESOLVED PHOTOEMISSION; METALLIC FILMS; QUANTUM WELL STATES; SCANNING TUNNELLING MICROSCOPY; SILVER; VANADIUM

SUPERVISOR: DR. PETAR PERVAN

REVIEWERS: PROF. DR. AMIR HAMZIĆ, PROF. DR. MARIJAN ŠUNJIĆ, DR. PETAR PERVAN,  
PROF. DR. KLAUS WANDEL, PROF. DR. DAVID PHIL WOODRUFF

THESIS ACCEPTED:

## TEMELJNA DOKUMENTACIJSKA KARTICA

SVEUČILIŠTE U ZAGREBU  
PRIRODOSLOVNO-MATEMATIČKI FAKULTET  
FIZIČKI ODSJEK

DOKTORSKA TEZA

*ELEKTRONSKA STANJA U ULTRA TANKIM SLOJEVIMA SREBRA NA (100) POVRŠINI VANADIJA*

MARKO KRALJ  
INSTITUT ZA FIZIKU, ZAGREB

U OVOJ DISERTACIJI PRIKAZANI SU REZULTATI ISTRAŽIVANJA VALENTNE ELEKTRONSKE STRUKTURE ULTRA TANKIH SLOJEVA SREBRA NA VANADIJEVOJ (100) POVRŠINI METODAMA KUTNO RAZLUČIVE FOTOLEKTRONSKE SPEKTROSKOPIJE VISOKE ENERGETSKE I KUTNE RAZLUČIVOSTI (HRARUPS) I SKENIRAJUĆE-TUNELIRAJUĆE MIKROSKOPIJE (STM). STANJA KVANTNIH JAMA (QWS) S-P I D-SIMETRIJE DETALJNO SU KARAKTERIZIRANA. ZA S-P STANJA U SREBRNOM SLOJU DEBLJINE 1-8 ATOMSKIH SLOJEVA (ML) PRONAŠLI SMO EFEKTE HIBRIDIZACIJE SA PODLOGOM, TE POJAČANJE I VARIJACIJU ELEKTRON-FONON VEZANJA OVISNO O DEBLJINI FILMA. ZA D-STANJA NALAZIMO DA SU SAVRŠENO KVANTIZIRANA UNUTAR SREBRNOG SLOJA ŠTO IH ČINI IDEALNIM PRIMJEROM DVODIMENZIONALNOG ELEKTRONSKOG SISTEMA. POVRŠINSKA FERMIJEVA PLOHA ODREĐENA JE ZA 1-5 ML SREBRA NA TEMELJU STM MJERENJA I KORELIRANA JE S ELEKTRONSKOM STRUKTUROM SISTEMA.

(154 STRANICA, 110 SLIKA, 197 LITERATURNIH NAVODA, JEZIK IZVORNIKA: ENGLESKI)

KLJUČNE RIJEČI: KUTNO-RAZLUČIVA FOTOLEKTRONSKA SPEKTROSKOPIJA; METALNI SLOJEVI; SKENIRAJUĆA-TUNELIRAJUĆA MIKROSKOPIJA; SREBRO; STANJA KVANTNIH JAMA; VANADIJ

MENTOR: DR. PETAR PERVAN  
OCJENJIVAČI: PROF. DR. AMIR HAMZIĆ, PROF. DR. MARIJAN ŠUNJIĆ, DR. PETAR PERVAN,  
PROF. DR. KLAUS WANDEL, PROF. DR. DAVID PHIL WOODRUFF

RAD PRIHVAĆEN:

## ACKNOWLEDGEMENTS

THE WORK PRESENTED HERE HAS BEEN CARRIED OUT AT THE INSTITUTE OF PHYSICS IN ZAGREB BUT ALSO INCLUDED SYNCHROTRON MEASUREMENTS AT THE NATIONAL SYNCHROTRON LIGHT SOURCE (BROOKHAVEN) AND ELETTRA (TRIESTE) AND STM MEASUREMENTS AT THE INSTITUTE FOR PHYSICAL AND THEORETICAL CHEMISTRY IN BONN.

I WISH TO THANK **DR. PETAR PERVAN** FOR HIS MENTORSHIP, ADVICES AND UNLIMITED SUPPORT DURING ALL THESE YEARS. I EXPRESS MY GRATITUDE TO **DR. MILORAD MILUN** FOR NUMEROUS ADVICES AND AN ENTHUSIASTIC LEADERSHIP OF A VERY SUCCESSFUL PROJECT THAT ENABLED THE REALIZATION OF THIS THESIS. I MET **DR. TONICA VALLA** WHILE HE WAS STILL AT THE INSTITUTE OF PHYSICS. I THANK HIM FOR THE KNOWLEDGE HE SHARED WITH ME DURING THESE DAYS, BUT ALSO FOR A CONTINUOUS HELP AFTER HE MOVED TO BROOKHAVEN. MANY THANKS TO A COLLEAGUE AND FRIEND **DR. ANTONIO ŠIBER** WITH WHOM I HAD ENDLESS DISCUSSIONS, SOME OF WHICH RESULTED IN A WELL DEFINED SCIENTIFIC IDEAS THAT ARE PRESENTED IN THIS WORK. I ALSO WISH TO THANK ALL THE PEOPLE WORKING AT THE INSTITUTE OF PHYSICS FOR PROVIDING A FRUITFUL WORKING ENVIRONMENT AND IN PARTICULAR OUR LAB TECHNICIAN **MILAN VUKELIĆ**.

I ACKNOWLEDGE **PROF. DR. KLAUS WANDEL**T FOR ENCOURAGING ME TO ADOPT NEW KNOWLEDGE AND SKILLS RELATED TO THE STM TECHNIQUE. I WISH TO THANK HIM FOR THE INTERESTING DISCUSSIONS AND HIS INFINITE HOSPITALITY THAT MADE MY RESEARCH IN BONN PARTICULARLY STIMULATING. I ALSO THANK **DR. JÖRG SCHNEIDER** AND **DR. AXEL ROSENHANN**, FORMER MEMBERS OF THE UHV-STM LAB FROM BONN THAT HELPED ME A LOT REGARDING ALL THE PROBLEMS THAT OCCURRED WITH THE STM IN ZAGREB.

I THANK **PROF. DR. PHIL WOODRUFF** WHOSE COLLABORATION WITH OUR GROUP RESULTED IN A PART OF THE SYNCHROTRON MEASUREMENTS PRESENTED HERE. MANY THANKS TO **PROF. DR. PETER JOHNSON** FOR PROVIDING A PLEASANT AND STIMULATING ENVIRONMENT DURING THE MEASUREMENTS AT NSLS AND ALSO FOR HIS SUPPORT SINCE THEN. ALSO, I WISH TO THANK **DR. RADOVAN BRAKO** FROM THE RUDER BOŠKOVIĆ INSTITUTE IN ZAGREB FOR PRODUCTIVE DISCUSSIONS CONCERNING PARTS OF THE WORK PRESENTED IN THIS THESIS.

AND FINALLY, DURING ALL THESE YEARS THE SUPPORT FROM **ANA**, FAMILY AND FRIENDS HAS BEEN INVALUABLE FOR ME.

THE *PDF* FILE OF THIS THESIS IS  
ALSO AVIALABLE FOR DOWNLOAD AT:

[HTTP://BOBI.IFS.HR/~MKRALJ/PHD/DOWNLOAD.HTM](http://BOBI.IFS.HR/~MKRALJ/PHD/DOWNLOAD.HTM)

# Table of contents

<b>1. Introduction</b>	<b>1</b>
<b>2. Experimental methods</b>	<b>5</b>
2.1. Scanning tunnelling microscopy	5
2.1.1. Introduction	5
2.1.2. The tunnelling process	6
2.1.3. The tunnelling current	7
2.1.4. Constant-current imaging	7
2.1.5. Scanning tunnelling spectroscopy	8
2.1.6. STM and localised electronic states	8
2.1.7. Fourier transform STM	9
2.1.8. FTSTM principles	10
2.1.9. FTSTM analysis	11
2.2. Valence states photoelectron spectroscopy	12
2.2.1. Introduction	12
2.2.2. The photocurrent	13
2.2.3. Photoemission from 3-D and 2-D states	15
2.2.4. High resolution ARPES	16
2.2.5. Two-dimensional ARPES detector	18
2.2.6. Extracting quasiparticle parameters from HRARPES spectra	19
<b>3. Apparatus</b>	<b>23</b>
<b>4. Quantum well states</b>	<b>27</b>
4.1. Ultra thin film states	28
4.1.1. Introduction	28
4.1.2. Multiple reflection model	33
4.2. Electronic structure of ultra thin silver films	37
<b>5. The substrate</b>	<b>45</b>
5.1. Introduction	45
5.1.1. Clean V(100) surface	45
5.1.2. The 5×1 reconstructed V(100) surface	46
5.2. Preparation and characterisation of the surface	48
5.2.1. Preparation procedure	48
5.2.2. Intrinsic chemical composition of the (5×1) reconstructed surface	49
5.2.3. Atomically resolved STM characterisation	50
5.3. Discussion	51

<b>6. Ag/V(100) measurements</b>	<b>53</b>
6.1. Structural characterisation	53
6.1.1. Preparation of silver layers	53
6.1.2. Photoemission characterisation	55
6.1.3. LEED measurements	56
6.1.4. STM characterisation	57
6.2. HRARUPS measurements	62
6.2.1. s-p QW states: angle resolved measurements	62
6.2.2. s-p QWS lineshape analysis	67
6.2.3. s-p QWS temperature dependence	68
6.2.4. Electron-phonon coupling analysis	75
6.2.5. d-band QW states	77
6.3. Ag/V(100) electronic structure probed by STM	81
6.3.1. Characterisation of standing wave patterns	81
6.3.2. Fourier transform analysis	83
<b>7. Ag/V(100) discussion</b>	<b>89</b>
7.1. Formation of an ordered silver film	89
7.1.1. Removal of the (5×1) vanadium reconstruction	89
7.1.2. Tetragonal silver	91
7.2. s-p derived QW states	93
7.2.1. Dispersions and effective masses	93
7.2.2. Temperature induced static effects	95
7.2.3. Temperature induced dynamic effects	99
7.2.4. Temperature induced effects - discussion	101
7.2.5. Temperature induced effects beyond the simple model	104
7.2.6. Film-vacuum vs. film-substrate interface influence	106
7.3. d-derived QW states	107
7.3.1. Phase accumulation analysis for the d-band QWS	107
7.3.2. Reflectivity of the vanadium-silver interface	109
7.3.3. Silver monolayer	111
7.4. STM and the electronic structure	113
7.4.1. Surface waves and surface electronic structure	113
<b>8. Summary and conclusions</b>	<b>117</b>
<b>9. Sažetak (prema poglavljima)</b>	<b>121</b>
9.1. Uvod	121
9.2. Eksperimentalne metode	123
9.2.1. Skenirajuća-tunelirajuća mikroskopija	123
9.2.2. Fotoelektronska spektroskopija	124
9.3. Uređaji	125
9.4. Stanja kvantnih jama	126
9.4.1. Stanja u ultra tankim slojevima	126

## TABLE OF CONTENTS

9.4.2. Literaturni pregled	127
9.5. Podloga	127
9.5.1. (5×1) rekonstruirana V(100) površina	127
9.5.2. Priprema i karakterizacija površine	128
9.5.3. STM karakterizacija	128
9.5.4. Diskusija	129
9.6. Ag/V(100): rezultati	129
9.6.1. Strukturna karakterizacija	129
9.6.2. HRARUPS mjerenja	130
9.6.3. STM kao proba elektronske strukture	135
9.7. Ag/V(100): diskusija	136
9.7.1. Uređeni srebrni sloj	136
9.7.2. s-p stanja kvantne jame	137
9.7.3 d-stanja kvantne jame	138
9.7.4. STM i elektronska struktura	139
9.8. Zaključak	140
<b>10. References</b>	<b>145</b>



## 1. Introduction

It is well known that the materials of reduced dimensionality can exhibit substantially different properties (electronic, magnetic, transport, ...) with respect to the bulk. Ultimately, when the dimensions are reduced down to the nanometer, i.e. atomic scale, a so-called quantum size effect (QSE) starts to play an important role in determining the system characteristics. Consequently, new materials with novel properties can be designed. Possible benefits of nanometer sized structures are nowadays integrated within the growing fields of nanoscience and nanotechnology. A manifestation of QSE is found in ultra thin films (UTF). Namely, the characteristics of UTF are related to the existence of discrete electronic states, so-called quantum well states (QWS). The QWS energy and spatial extension perpendicular to the surface depend on the film thickness. These states can be used to tailor the properties of the system. With that respect, one of the examples that is already commercialised is based on thin metallic multilayered structures that display a phenomenon of a giant magnetoresistance and which are used as sensors for advanced magnetic disk drives [1].

The discretization of electronic states in UTF can be, in principle, understood in terms of a very simple quantum particle in a one-dimensional box picture, where most of the parameters of the film electronic structure are determined by its thickness and by the potential barriers that localise the electrons within the film: at the film-vacuum and at the film-substrate interface. It is particularly interesting that for the proper combination of metals the potential barrier at the film-substrate interface can be formed due to the different symmetries of energy bands in the substrate and the overlayer film. It appears that this kind of hybridisation gaps are very effective in the localisation of electrons in the films grown on substrate surfaces. However, the QWS may to some extent hybridise with substrate states. Another aspect related to the observation of discrete electronic states is the film-substrate matching, i.e. the film growth. A uniform growth with atomically discrete thickness is essential for the possibility to study QWS with today's accuracy.

Ultra thin films of noble metals on transition metal substrates have been extensively studied. The discretization of electronic bands as a function of a film thickness has been established for s-p and d-symmetry. Mainly, the s-p QWS have been investigated, while d-QWS have been much less characterised. Up to now, the bulk of the research has been focused on the QWS ground state properties. The photoemission was used to measure the binding energy of QW peaks that were usually interpreted applying a simple phase accumulation model. Other methods as Fabry-Perot were used to estimate a degree of QWS confinement. The discretization of states in UTF provides an elegant way to map the dispersion of particular bulk bands. Also, the measurements of the photoemission cross section as a function of photon energy showed that the mechanism of photoemission from

different QW systems may be quite different in the sense that there can be a different level of importance of periodic potential (within the film) and the potentials at the film-vacuum and the film-substrate interface. These issues can be found in recent review papers [2,3,4].

In this thesis we focus on the investigation of ultra thin silver films supported by the vanadium (100) substrate. To some extent this system has been already investigated [5]. Its electronic properties were studied mainly in terms of ground state properties. The goal of this thesis was to further investigate structural and valence electronic properties of this interesting QW system. Specifically, we have studied silver films up to 8 atomic layers thick (monolayers (ML)). Previous studies indicate that the variety of different aspects that influence the properties of the film are significantly differing for ultra thin films ( $< 10$  ML) compared to thicker films (10-100 ML). To elucidate the electronic properties of the system we use angle-resolved ultraviolet photoelectron spectroscopy (ARUPS) and scanning tunnelling microscopy (STM). ARUPS is traditionally widely used to explore the bulk and the surface electronic structure. For two-dimensional systems, like surface states or QW states, it has a unique capability to directly probe the photohole spectral function [6,7,8], where such measurements can be used to determine quasiparticle properties, i.e. interactions in the system. On the other hand, STM as a more recent technique has proved as a very efficient tool to investigate not only the atomic structure, but also the electronic structure at the surface. The advantages, disadvantages and comparison of both techniques are, at length, discussed in the paper of Matzdorf [9].

For s-p QW states we have measured their dispersions and explored the effects of the hybridisation with the substrate (effective masses, avoided crossing, ...). Further we have studied the dynamical properties of s-p QW states. From the photoemission temperature dependence we explored the binding energy, effective masses and lifetime changes. We isolated and determined the strength of the electron-phonon interaction in the system. For d-QW states we followed the development of quantized states with film thickness and investigated the degree of confinement of d-electrons within the silver film. We used STM to probe the electronic structure of Ag/V(100) at the surface, or more specifically to measure the surface Fermi contour for different film thicknesses.

The layout of this thesis is as follows;

In the first part (chapters 2-4) we introduce the experimental techniques, briefly describe apparatuses and give an introduction on QW states.

In chapter 2 (*Experimental methods*) we describe basic physical processes that govern ARUPS and STM. Also, some particular aspects (Fourier-transform STM (FTSTM) and high resolution ARUPS (HRARUPS)) are utilised. These are closely related to the physical information that we extract from measurements.

## 1. INTRODUCTION

In chapter 3 (*Apparatus*) five separate experimental systems that were used to acquire the presented results and some technical details are described.

In chapter 4 (*Quantum well states*) ultra thin film states are defined and described. The so called multiple reflection model that is used for the description of surface and QW states is introduced. At the end of this chapter we give a relevant literature overview regarding the work on QW states, and especially ultra thin silver QWS.

In the second part of the thesis (chapters 5-7) all experimental results are presented and discussed.

In chapter 5 (*The substrate*) the reconstructed V(100)-(5×1) surface preparation procedure is described. The substrate is characterised by means of high-resolution Auger electron spectroscopy (HRAES), low energy electron diffraction (LEED) and STM techniques.

In the most extensive chapter 6 (*Ag/V(100) measurements*) first the structural and the growth properties of ultra thin silver films grown on a well defined V(100)-(5×1) substrate are studied. Accompanying STM analysis, the results of Auger electron spectroscopy (AES), ARUPS and LEED characterisations are presented. A well defined procedure for obtaining ordered silver monolayers is established. Next, high resolution ARUPS (ARUPS) measurements are presented. The s-p QW states dispersions are measured and the s-p effective masses around the Brillouin zone center are determined. Further, the photohole spectral functions are characterised and the hole-electron, the hole-impurity and the hole-phonon contributions are evaluated at constant temperature. The measurements of the photoemission spectra temperature dependence for 1-8 ML Ag enable reliable determination of the hole-phonon coupling parameter. Regarding the d-band region, in HRARUPS measurements we have followed the development of QW states in ultra thin films up to 5 ML Ag. For 1 ML Ag/V(100) we have identified all QW peaks. We have measured the width of QW well peaks and also identified a peak splitting for 1 and 2 ML Ag. Chapter 6 is completed with STM measurements that were used to investigate the surface Fermi contour of the system for 1-5 ML Ag. Constant current STM imaging is used to map the crucial points in the k-space in the region of Fermi level.

In chapter 7 (*Ag/V(100) discussion*) the experimental results from chapter 6 are discussed. We propose the mechanism that explains the formation of ordered and uniform silver layers on a vanadium surface, which is accompanied with the removal of vanadium reconstruction. Measured dispersions of the s-p QW states are discussed and deviations from the parabolic dispersions as well as the effective mass enhancement are ascribed to the hybridisation effects with the substrate states. The hole-phonon interaction in the system is modelled and a good qualitative and quantitative agreement between the simple model and measured data is found. The importance of the film-vacuum and the film-substrate interface is discussed here in great detail. Regarding the d-band region the leading d-QW peak widths are analysed. We propose that there is a perfect reflection at the film-substrate interface, i.e. an ideal two-dimensional confinement. The energy and thickness dependence of the d-QW

## 1. INTRODUCTION

states have been accurately reproduced by the phase accumulation analysis. The TB calculations properly described the observed peak splitting and showed that there is a strong interaction with the substrate for 1 ML film. The by the STM measured surface Fermi contour is discussed and correlated to the photoemission data. We proposed that the surface Fermi contour is determined by the substrate state that has hybridised with silver s-p QW states.

Summary and conclusions (chapter 8) are presented in the third part of the thesis. This part also contains a summary in Croatian (chapter 9).

## **2. Experimental methods**

In this chapter the main experimental techniques used to obtain the information presented in this thesis are discussed. The techniques are the scanning tunnelling microscopy (STM) and the photoelectron spectroscopy (PES). The basic physical processes that govern the photoemission and the STM are briefly described. Additionally, some particular aspects that are closely related to the physical information that is extracted from the measurements in this work are discussed. For the characterisation purposes in this thesis we have also used Auger electron spectroscopy and low energy electron diffraction. For details about those techniques we refer the reader to Ref. [10].

### ***2.1. Scanning tunnelling microscopy***

#### ***2.1.1. Introduction***

Scanning tunnelling microscopy is the surface science technique that gives information of the atomic structure at surfaces. Even close-packed noble metal surfaces are imaged with atomic resolution in STM at large tip-sample distances exhibiting high corrugation amplitudes. Apart from the high spatial sensitivity of the STM its ability to probe the local electronic structure of the surface makes the STM a very powerful tool for electronic structure investigations. This is particularly pronounced in its spectroscopic mode which is called scanning tunnelling spectroscopy (STS).

While the number of experiments and studied systems evolved exponentially, the theory is lagging behind, making the understanding of STM images sometimes arbitrary. The first theoretical approach to the STM imaging is based on the perturbation theory [11]. A major problem in this case is that perturbation treatment neglects the tip-sample interaction and scattering of the injected electron by the localised tip potential and the potential in the sample or in the tip. Refinement of the theory with the inclusion of dynamical screening, i.e. interaction with charge fluctuation may lead to the asymmetry in the barrier and also in the tunnelling currents and conductivities. Dynamical screening also causes the modifications of the tunnelling barrier which is lowered near the tip apex and which leads to focusing of the tunnelling current and increased lateral resolution of STM [12,13,14]. For a further overview of the STM we refer the reader to recent review papers of Besenbacher [15], Briggs and Fisher [16] and Drakova [17]. The first one offers an experimental overview, the second one addresses the theory of STM on clean and adsorbate covered semiconductor surfaces, and the third one the theory of STM of the metal surfaces.

### 2.1.2. The tunnelling process

The physical phenomenon at the origin of STM is the tunnelling of electrons through a vacuum barrier. A tip, i.e. a sharpened metallic wire is brought close to the conducting surface of the sample. If this close distance is of the range of few Ångströms electrons will tunnel between the electrodes. A voltage,  $V_{\text{Bias}}$ , is applied between the two electrodes and gives rise to a tunnelling current, the sign of which depends on the sign of voltage. Conventionally, the bias voltage is defined as a sample voltage with respect to the referent tip potential (virtual ground). Positive bias voltages correspond to the tunnelling into unoccupied states of the sample, while negative bias corresponds to the tunnelling from occupied states of the sample into empty states of the tip. A schematic of the tunnelling process is given in Fig. 2.1.

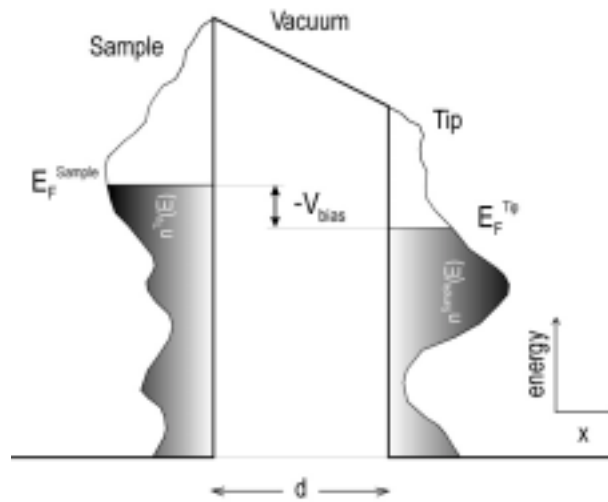


Fig. 2.1. A schematic of the tunnelling process: the corresponding one-dimensional potential energy diagram.

The intensity of the tunnelling current,  $I$ , should decrease when the distance ( $d$ ) between the electrodes increases. In analogy with the one-dimensional tunnel effect between two identical planar electrodes, one can make an estimate of the tunnelling current and its variation. Supposing that the  $V_{\text{Bias}}$  is much smaller than the potential height,  $V-E$ , one gets:

$$I \propto V_{\text{Bias}} \cdot e^{-2 \cdot \kappa \cdot d} \quad (2.1)$$

The wave vector  $\kappa$  governs the exponential decrease of the wave function in the vacuum and it is given by:

$$\kappa = \frac{\sqrt{2 \cdot m \cdot (V - E)}}{\hbar} \quad (2.2)$$

For typical values ( $V-E \cong 5$  eV,  $d \cong 5$  Å,  $2\kappa \cdot d \cong 11.4$ ) the tunnelling current will decrease by an order of a magnitude when  $d$  is increased by 1 Å. In this simple model, the obtained sensitivity explains the excellent vertical resolution of the STM (picometer or better).

However, the key characteristic of the STM is that it is essentially a three-dimensional technique sensitive to the local structure (geometric and electronic) of the surface.

### 2.1.3. The tunnelling current

A simple first order perturbation approach that takes into account the atomic and the electronic structure of both electrodes has been introduced by Tersoff and Hamann (TH theory) [11]. The expression for the tunnelling current is:

$$I \propto \sum_v |\psi_v(\vec{r}_0)|^2 \cdot \delta(E_v - E_F) \quad (2.3)$$

where  $E_F$  is the tip Fermi level, and  $E_v$  the energy of the surface wave function  $\psi_v$ .  $r_0$  denotes the position of the centre of the tip. The given expression is valid under the assumption that the tip is infinitely sharp which would make the corresponding wave functions that are describing the tip delta functions. Under those circumstances one directly measures the surface local density of states (LDOS) at the Fermi level,  $\rho_{\text{Surface}}(\mathbf{r}, E_F)$ . In reality the tunnelling tip is not infinitely sharp and a more appropriate approximation gives:

$$I \propto \sum_{\mu, v} |M_{\mu, v}|^2 \cdot \delta(E_v - E_F) \cdot \delta(E_\mu - E_F) \quad (2.4)$$

where the tunnelling matrix element,  $M_{\mu, v}$ , occurs. In this case the tunnelling current is weighted not only by the surface density of states but as well by the tip density of states. It describes the tunnelling rate between the unperturbed wave functions of the tip ( $\psi_\mu$ ) and the surface ( $\psi_v$ ) in the system:

$$M_{\mu, v} \equiv \langle \psi_\mu | U_T | \psi_v \rangle = \frac{\hbar}{2 \cdot m} \cdot \int_{\Sigma} dS \cdot (\psi_\mu^* \cdot \vec{\nabla} \psi_v - \psi_v^* \cdot \vec{\nabla} \psi_\mu) \quad (2.5)$$

where  $U_T$  is the effective potential at the system interface, and where the integration is evaluated over any surface that includes the whole barrier region. The matrix element depends roughly exponentially on the barrier width,  $d$ . Also it depends on the electron momentum parallel to the surface,  $\mathbf{p}_\parallel$ . The electrons of the total energy  $E$  with small parallel momentum tunnel with higher probability than electrons of the same total energy and large  $\mathbf{p}_\parallel$ .

### 2.1.4. Constant-current imaging

In constant-current imaging the tunnelling current is compared to a preset current value  $I_0$ . The difference signal,  $I - I_0$ , is a feed-back to the voltage applied to the z-piezo: the tip-sample distance is adjusted to minimise the difference signal. With the voltage applied to the z-piezo that keeps the current constant, a so-called topography  $z(x, y) |_{I, V}$ , is recorded:

$$z(x, y) |_{I, V} = d(x, y) |_{I, V} + t(x, y) \quad (2.6)$$

Here  $t(x,y)$  characterises the topography of the surface – a virtual plane corresponding to the positions of the surface atom nuclei. The term topography is misleading in the sense that, except for some very special cases,  $z(x,y)|_{I,V}$  is not directly an image of the positions of the atomic nuclei, but rather a surface of constant local density of states of the sample. It contains not only information on the topography but also on the electronic structure. For that reason one always has to be careful in interpreting constant current images in terms of surface topography.

### 2.1.5. Scanning tunnelling spectroscopy

In the scanning tunnelling spectroscopy (STS) one measures I-V curves, or equivalently  $dI/dV$ -V curves at fixed location and fixed tip-sample distance. Under the assumption that in the bias voltage range of interest the tip density of states is much less structured than the surface density of states ( $\rho_{\text{Surface}}$ ) one derives:

$$\frac{dI}{dV}(V, x, y) \propto \rho_{\text{Surface}}(V, x, y) \quad (2.7)$$

The assumption is justified whenever there are sharp features in the sample density of states. For instance, this is definitely true for single adatoms or molecules with strong resonances. Combined with the high spatial resolution of STM  $dI/dV$  spectra may provide valuable information about the local electronic structure of the sample.

In the presence of LDOS oscillations (see Fig. 2.2) the STM becomes sensitive to the wave vector, i.e. LDOS oscillations open up an access to the surface state band structure. To measure the dispersion of a surface state a single linescan perpendicular to the LDOS pattern suffices, where a conductance map  $dI/dV(E)|_x$  should be taken along the linescan [18]. If one succeeds in keeping the tip height position constant, the only contribution to spatial variations in  $dI/dV(E)|_x$  comes from the surface density of states.

### 2.1.6. STM and localised electronic states

A drastic example on how the term topography for the STM is misleading is found when localised electronic states are present at the surface. Localised states may contribute significantly to the surface LDOS. These primarily include intrinsic surface states and surface resonances, which are extensively investigated. As an example, Fig. 2.2a shows the scattering and the decay pattern of copper surface states electrons on the Cu(111) surface imaged with STM [19].

In fact, since 1993 and fascinating interference patterns imaged in quantum corrals (Fig. 2.2b) [20], many authors have discussed possible contributions of quasiparticle interactions, in general, and electron-phonon interactions, in particular, to the damping of

## 2. EXPERIMENTAL METHODS

measured interference patterns and spectroscopic linewidths [20,21,22,23,24,25]. However it took some time until the first quantitative evaluation of the surface state lifetime was achieved with STM by Li et al. [26,27]. The influence of surface defects to the electron lifetime can be controlled in STM measurements and it does not surprise that STS experiments have corrected the lifetimes of surface states measured by means of ARPES. This additionally helped to understand the screening process in the systems of reduced dimensionality [28]. Indirectly, imaging of the standing waves in the limit of small concentration of surface scatterers enabled, for instance, the study of the long range interactions between adatoms [29]. Not only for adatoms, but also for subsurface defects or impurities the scattering of surface state led to measurable effects in STM and STS [30,31,32].

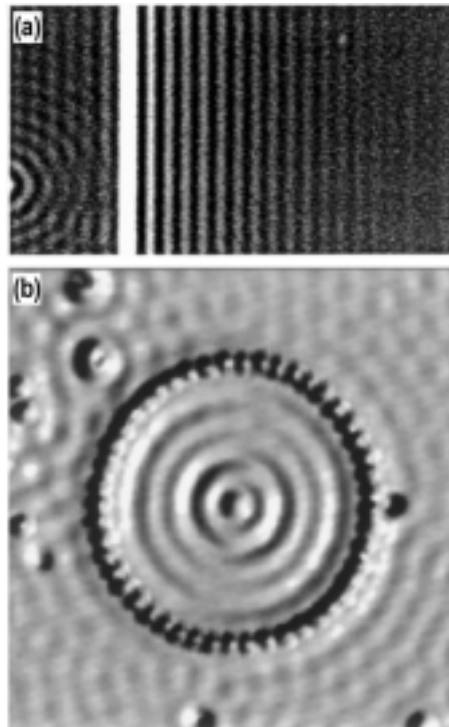


Fig. 2.2. (a)  $dI/dV$  image at a straight Cu(111) step edge (taken from Ref. [19]). The step edge itself is imaged as a white stripe and the upper terrace is on the right hand side. To the very left a surface impurity is visible. LDOS oscillations at the step edge and impurity atom are both clearly visible. (b) STM image of a “quantum corral” made out of 48 Fe atoms on the Cu(111) surface (Ref. [20]).

### 2.1.7. Fourier transform STM

Recently a new prospect was recognised in low-temperature low-bias constant current STM images exhibiting standing wave features. In Fourier transforms of such images a wealth of information is supplied. A method based on a Fourier transform analysis is generally named Fourier transform – scanning tunnelling microscopy (FTSTM). For systems with surface states that cross the Fermi level a method has been developed by Besenbacher and co-workers where the full quantitative potential was first recognised when it was used to

directly determine the surface Fermi contour [33,34]. A sort of an overview paper dealing with achievements of Fermi contour FTSTM is given in Ref. [35]. In Fig. 2.3 an example of the Cu(110) surface is given [36]. The constant current STM image is shown in Fig. 2.3a, while the Fourier transform exhibiting an anisotropic Fermi contour is shown in Fig. 2.3b.

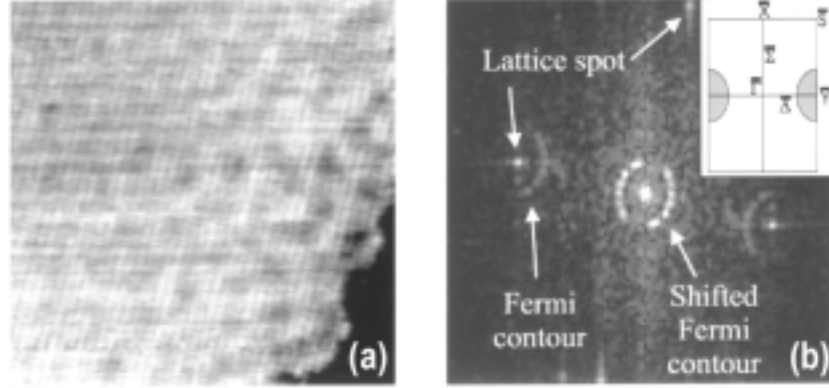


Fig. 2.3. (a) Low-bias low-temperature constant current STM image of the Cu(110) surface. (b) Fourier transform of (a). In the inset a surface Brillouin zone of Cu(110) is sketched. Image is taken from Ref. [36].

### 2.1.8. FTSTM principles

Here we briefly outline the basic concept that governs the standing wave phenomenon observed by STM. The waves imaged on the surface are fingerprints of the scattering of the electrons from defects. They are assigned by the electron gas to minimise the influence of imperfection potentials. This purely quantum mechanical phenomenon leads to an electron wave function in the form of a standing wave. The screening phenomenon is known in the bulk as Friedel oscillations [37,38].

Let us consider simplified two-dimensional situation. In a free electron gas, the wave functions are plane waves –  $e^{i\mathbf{k}\cdot\mathbf{r}}$ ,  $\mathbf{r} = x\mathbf{i} + y\mathbf{j}$ . We set an infinite potential wall that extends in the  $y$  direction. The in plane part of the wave function takes a form:

$$\psi_{\vec{k}}(x,y) = C \cdot e^{ik_y \cdot y} \cdot \sin(k_x \cdot x) \quad (2.8)$$

where  $C$  is a normalisation constant. The local density of states is defined as:

$$\text{LDOS}(\vec{r}, E) = \sum_{\vec{k}} |\psi_{\vec{k}}(\vec{r})|^2 \cdot \delta(E - E_{\vec{k}}) \quad (2.9)$$

At a given energy  $E$ , all states having a wave vector  $\mathbf{k}_E$  contribute to the sum, where  $\mathbf{k}_E$  is dictated by the dispersion relation  $E(\mathbf{k})$ . Putting the wave function (2.8) into the expression (2.9) gives:

$$\text{LDOS}(\vec{r}, E) \propto \int_0^\pi \sin^2(\vec{k}_E \cdot \mathbf{x} \cdot \sin \theta) \cdot d\theta \propto 1 - J_0(2 \cdot \vec{k}_E \cdot \mathbf{x}) \quad (2.10)$$

where  $J_0$  is a Bessel function that behaves as a decaying sine wave. The standing wave in the LDOS extends from the step with a wave vector  $q = 2 \cdot k_E$ . The factor of two enters because the LDOS is related to the norm square of the wave function. Thus, LDOS oscillations can be considered as energy-resolved Friedel oscillations. The total charge density is related to the LDOS by:

$$\rho(\vec{r}) = -e \cdot \int \text{LDOS}(\vec{r}, E) \cdot f(E, T) \cdot dE \quad (2.11)$$

where  $f(E, T)$  is the Fermi-Dirac distribution.

Only electrons with an energy up to  $E_F$  contribute to the charge density. All  $k$ -vectors from 0 to  $k_F$  contribute to the Friedel oscillation (because of the energy integration), whereas essentially only  $q = 2 \cdot k_F$  contributes to the standing wave in  $\text{LDOS}(E_F)$ , since the low-bias STM image is proportional to the  $\text{LDOS}(E_F)$ . The occurrence of surface waves in STM has to do with the electronic states at the surface close to the Fermi level.

### 2.1.9. FTSTM analysis

The data analysis and calibration procedure, that is also used in this thesis, is illustrated in an example of Be(0001) (Fig. 2.4) [34]. In this case a relatively short wavelength of the Friedel surface waves causes that the circular Fermi contour of the surface state extends throughout much of the reciprocal unit cell. The FTSTM image also reveals spots corresponding to the reciprocal lattice of the Be(0001) atomic array. Such situation is particularly suitable, since it allows an internal calibration to a quantitative measurement of the surface wave vector. It is calibrated with respect to the  $\mathbf{G}$  vectors of the reciprocal lattice. With such kind of calibration, at least along the high symmetry directions, the possible experimentally induced distortion (thermal drift, etc.) can be bypassed.

We should mention that the momentum resolution in the Fourier transformed images is related to the real-space size of the analysed image. For the discrete FT the resolution is  $\Delta k = 2 \cdot \pi / (\text{image size})$ . If an electronic state that exhibits the standing wave feature has a rather fast dispersion, then poor  $\Delta k$  resolution would destroy the quality, i.e. sharpness of the standing wave features. Other aspects influencing the quality of surface waves and, consequently, the surface Fermi contour obtained in FTSTM are the finite temperature and bias voltage. At finite temperatures the broadening of the Fermi-Dirac distribution leads to the broadening of the energy window that contributes to the tunnelling current ( $\Delta E \cong 3k_B T$ ) and due to the dispersion of the electronic state this leads to the broadening of the distribution of  $k$  vectors contributing to the standing wave pattern. In a similar way high bias voltages result in electrons from a broad energy and, thus, momentum window contributing to the STM image.

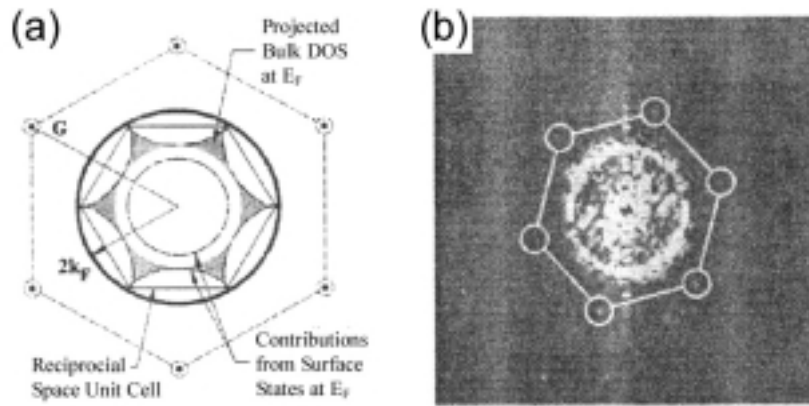


Fig. 2.4. (a) The 2D Brillouin zone of Be(0001). (b) An FTSTM image of Be(0001) at 150 K. The hexagonal array of spots corresponds to the reciprocal lattice (indicated with  $\mathbf{G}$  vectors in (a)) and the circular feature corresponds to the Fermi surface contributions. Image is taken from Ref. [34].

## 2.2. Valence states photoelectron spectroscopy

### 2.2.1. Introduction

In this type of experiment an electron, initially in an eigenstate of energy  $E_i$  belonging to the occupied part of the valence band, is excited into an eigenstate above the vacuum level by the absorption of a photon of energy  $h\nu$ . In order to eject the electron from the crystal, the photon energy should at least be higher than the work function,  $\phi$ , of the material. The simple Einstein's relation, through the conservation of energy, determines the kinetic energy of the escaping electron:

$$E_{\text{kin}} = E_i + h\nu - \phi \quad (2.12)$$

Due to the scattering, only electrons from a very small depth escape unscattered into the vacuum, which results in the well-known surface sensitivity of photoemission. When the photoelectrons are collected in all directions the energy distribution spectrum of the photoemitted elastic electrons is a function of initial and final densities of states with, possibly, large modulations due to the optical transition probabilities. The real power of the technique lies in the angular, i.e. the momentum sensitivity. The so called angle-resolved photoelectron spectroscopy, ARPES, nowadays is one of the most powerful and most important tools for studying the electronic structure of solids [7,8,39].

Using variable photon energies the three-dimensional valence band structure of the bulk bands can be measured directly. Typically, energy distribution curves (EDC) are measured as a function of the photon energy and the electron emission angle. In a kinematical analysis using energy and momentum conservation laws the energy of the wave

vector relation  $E(\mathbf{k})$  is determined. In such band structure measurements only energetic peak positions are analysed, while the shape and the intensity of the photoemission peak is generally not interpreted at all. Peak intensities strongly depend on the polarisation of light, sample temperature, and quality of the surface. Moreover, the shape of the photoemission peak contains a valuable information about the quasiparticle nature of the excited photohole.

### 2.2.2. The photocurrent

The rate of the excitation of electrons from the initial states  $i$  with the wave function  $\psi_i$  to the final states  $f$  with the wave function  $\psi_f$  is governed by the transition probability,  $w$ , which can be calculated by Fermi's Golden Rule (first order perturbation):

$$w \propto \frac{2\pi}{\hbar} \cdot \left| \langle \psi_f | \vec{r} | \psi_i \rangle \right|^2 \cdot \delta(E_f - E_i - \hbar \cdot \omega) \quad (2.13)$$

where the delta function represents the conservation of energy and the rest is the square of the transition matrix element. In the simplest case one can consider the system within the one-electron approximation for the initial- and final-state. This allows the separation of the initial and the final state wave functions of the system as a product of the orbital of interest and the wave function of the remaining electrons. The transition matrix element in that form reads:

$$\langle \psi_f | \vec{r} | \psi_i \rangle = \langle \phi_{f,E_{\text{kin}}} | \vec{r} | \phi_{i,k} \rangle \cdot \langle \psi_{f,R}^{\bar{k}}(N-1) | \psi_{i,R}^{\bar{k}}(N-1) \rangle \quad (2.14)$$

The matrix element is thus the product consisting of a one-electron matrix element and a  $(N-1)$ -electron overlap integral. After the ejection of the electron, the final state part with  $N-1$  electrons will differ from the corresponding initial state part with  $N-1$  electrons. By the readjustment within  $N-1$  charges the system will try to minimise the energy. There will be many possible final states and we have to sum over all possible states:

$$c_s = \langle \psi_{f,s}^{\bar{k}}(N-1) | \vec{r} | \psi_{i,R}^{\bar{k}}(N-1) \rangle \quad (2.15)$$

$$\langle \Psi_f | \vec{r} | \Psi_i \rangle = \langle \phi_{f,E_{\text{kin}}} | \vec{r} | \phi_{i,\bar{k}} \rangle \sum_s c_s$$

For strongly correlated systems many coefficients  $c_s$  are nonzero.

To evaluate the photocurrent,  $I$ , that is measured in the photoemission experiment one has to make a summation of all transition probabilities, i.e. over all possible final and initial states. In the formalism developed in solid state physics photocurrent takes the form [40]:

## 2. EXPERIMENTAL METHODS

$$I \propto \sum_{f,i,k} \left| \langle \phi_{f,E_{kin}} | \vec{r} | \phi_{i,\vec{k}} \rangle \right|^2 A(\vec{k}, E) \quad (2.16)$$

$$A(\vec{k}, E) = \sum_s |c_s|^2 \cdot \delta(E_F - E_s(N-1) - E_0(N) - \hbar\omega)$$

The  $A(\mathbf{k}, E)$  is the so-called spectral function for the wave number  $\mathbf{k}$  and energy  $E$ . Thus, in the experiment one measures the spectral function of the system. The spectral function and the Green's function are related:

$$A(\vec{k}, E) = \frac{1}{\pi} \text{Im} |G(\vec{k}, E)| \quad (2.17)$$

$A(\mathbf{k}, E)$  describes the probability of removing (or adding) an electron with the energy  $E$  and the wave vector  $\mathbf{k}$  from (to) the interacting  $N$ -electron system. For a noninteracting system with the one-electron energy  $E_{\mathbf{k}}^0$  one finds:

$$G_0(\vec{k}, E) = \frac{1}{E - E_{\vec{k}}^0 - i\varepsilon} \quad (2.18)$$

Here  $\varepsilon$  is being very small, and:

$$A_0(\vec{k}, E) = \delta(E - E_{\vec{k}}^0) \quad (2.19)$$

In this case the spectral function is a delta function located at  $E = E_{\mathbf{k}}^0$ . In an interacting electron system the electron energy is renormalized by the so-called self energy, a complex value,  $\Sigma(\mathbf{k}, E) = \text{Re}\{\Sigma(\mathbf{k}, E)\} + i \cdot \text{Im}\{\Sigma(\mathbf{k}, E)\}$ . The Green's function and the spectral function are now:

$$G(\vec{k}, E) = \frac{1}{E - E_{\vec{k}}^0 - \Sigma(\vec{k}, E)} \quad (2.20)$$

$$A(\vec{k}, E) = \frac{1}{\pi} \cdot \frac{\text{Im}\{\Sigma(\vec{k}, E)\}}{\left[ E - E_{\vec{k}}^0 - \text{Re}\{\Sigma(\vec{k}, E)\} \right]^2 + \left[ \text{Im}\{\Sigma(\vec{k}, E)\} \right]^2}$$

If all the interactions in the system are small ( $\text{Im}\{\Sigma(\mathbf{k}, E)\}$  small) the situation will be similar to the noninteracting system – in this case a slightly modified electron is called a quasiparticle and its mass is renormalized (Fig. 2.5). The real part of the self energy describes the screening, shifting the energy from the Hartree value, and the imaginary part describes the decay or inelastic scattering process [39]. In a Fermi liquid [41], electrons are considered as quasiparticles – the electrons dressed by virtual excitations that move with them coherently.

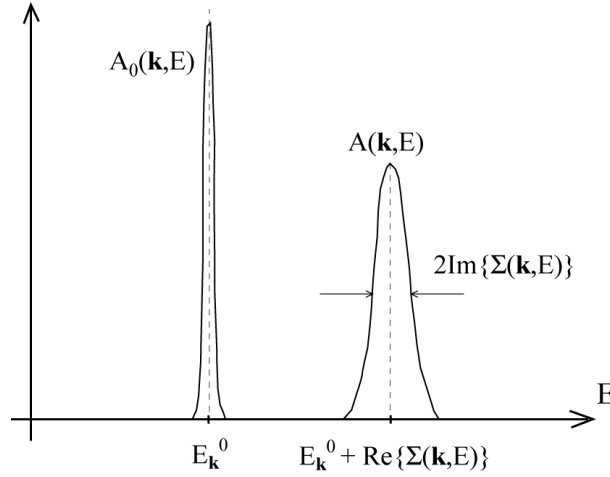


Fig. 2.5. Spectral function of the noninteracting and the interacting electron.

### 2.2.3. Photoemission from 3-D and 2-D states

In the photoemission process two quasiparticle states are involved – the excited electron and the hole (also called photohole) state. The conservation of energy implies that the sum of their energies with respect to the ground state energy is equal to the photon energy used for the excitation. The interaction of both particles can usually be neglected. The hole, as a quasiparticle in the sea of other electrons, can be described approximately in the one-electron picture. Its energy is equal to the binding energy of a single electron in the corresponding state plus the real part of the self energy  $\text{Re}\{\Sigma\}$  including the correlation effects. The inverse of the imaginary part of  $\Sigma$  is proportional to the lifetime of the hole state and basically results in a Lorentzian line shape with a full width at half maximum of  $\Gamma = 2 \cdot \text{Im}\{\Sigma\}$ . The quasiparticle of the excited electron has a finite lifetime as well, and affects the measured linewidth indirectly. In the experiment one can distinguish between scattered and unscattered photoelectrons. Photoelectrons that have been scattered considerably out of their original state by other electrons, phonons, or defects (impurities) change their energy and/or emission direction and can be identified in the energy and angle-resolved detection – they are typically treated in the data analysis as a background. Only unscattered photoelectrons are considered in the analysis of direct transitions. For the three-dimensional bulk states, in general, electron bands show dispersion with  $k_{\perp}$  (Fig. 2.6a). This results in an additional line “broadening”. The measured linewidth  $\Gamma$  includes a nontrivial linear combination of lifetime broadening of the hole and the photoelectron [9], that can be written in the form:

$$\Gamma_{\text{exp}} = \left( \Gamma_{\text{hole}} + \frac{v_{\text{hole}}}{v_{\text{electron}}} \cdot \Gamma_{\text{electron}} \right) \cdot \left( \left| 1 - \frac{v_{\text{hole}}}{v_{\text{electron}}} \right| \right)^{-1} \quad (2.21)$$

## 2. EXPERIMENTAL METHODS

Here  $v_{\text{hole}}$  and  $v_{\text{electron}}$  are the corresponding band velocities. From that point of view there are two cases where the hole lifetime is reflected directly in the measured photoemission linewidth,  $\Gamma_{\text{exp}}$ : either the initial state does not depend on the electron wave vector component perpendicular to the surface (as is the case for two-dimensional states that have no dispersion with  $k_{\perp}$ ), or the transition occurs at symmetry points of the 3D bulk bands, where the band velocity is zero. Consequently, the linewidth measured with ARPES in those cases directly reflects the hole lifetime without any broadening contribution which would include the final state lifetime (Fig. 2.6b). Crystal surfaces are a perfect playground for studying quasi two-dimensional electron systems. Suitable states are surface states, adsorbate states and, as in this thesis, quantum well states in ultra thin metallic films.

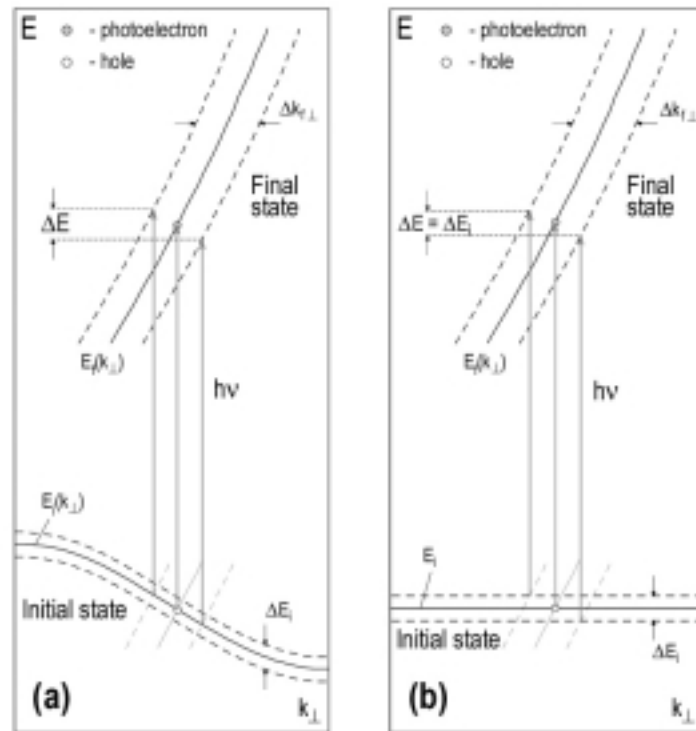


Fig. 2.6. Contribution to the measured linewidth  $\Delta E$  by initial and final state lifetime broadening. Solid lines are initial and final state band dispersions while dashed lines indicate the lifetime broadening. (a) photoemission from 3-D, and (b) photoemission from 2-D system.

### 2.2.4. High resolution ARPES

As already pointed out, the angle-resolved photoemission accesses the lifetimes of electronic states via the energetic broadening of photoemission peaks. Only recently, from the middle of 1990's, high energy and angular resolution ARPES (HRARPES) analysers enabled the experimental study of long living states close to the Fermi level by overcoming the effects of instrumental Gaussian broadening of photoemission lines [8]. In fact, this improvements enabled the studies of strongly correlated phenomena characterised by the meV energy scale [42], like superconductivity, charge density waves, et cetera. Nowadays HRARPES stands for

## 2. EXPERIMENTAL METHODS

the analysers of an energy resolution ( $\Delta E$ ) better than 10 meV and an angular resolution ( $\Delta\theta$ ) better than  $\pm 0.5^\circ$ . The limit is pushed even more – analysers of  $\Delta E \cong 1$  meV and  $\Delta\theta \cong \pm 0.1^\circ$  are starting to operate. This will enable to investigate long living and fast dispersing states that were not accessible in the experiments so far. Fig. 2.7 illustrates the difference in the line shape of the photoemission spectrum collected from the same surface, but with different analysers (a, Ref. [43]) or the same analyser but different angular resolution (b and c, Ref. [8]).

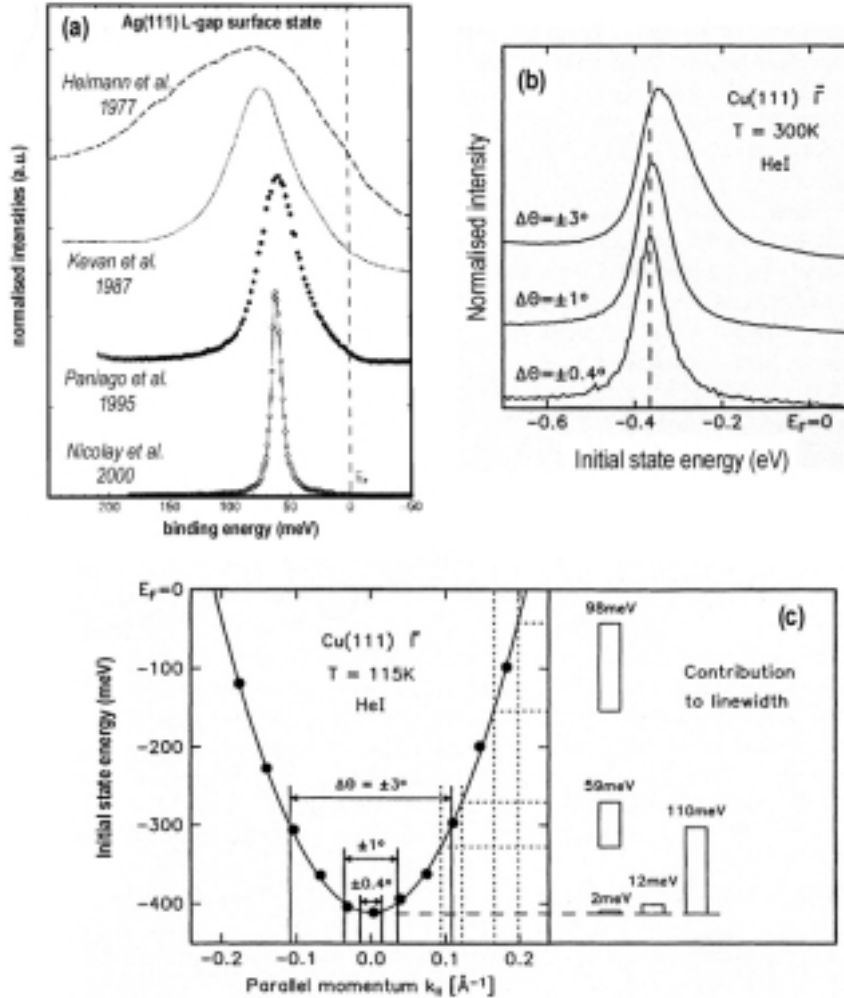


Fig. 2.7. (a) Technological development in PES since the first observation of the Ag(111) surface state in photoemission spectra [43]. (b) Photoemission spectra of the Cu(111) surface state measured with different angular resolutions. The vertical dashed line indicates the initial state energy measured with best resolution [8]. (c)  $E(k_{||})$  dispersion of a Schockley surface state on Cu(111). Contributions to the line width of the photoemission peak measured at different angular resolutions in normal emission are schematically indicated on the right [8].

### 2.2.5. Two-dimensional ARPES detector

Since 1993 when a commercial version of the Gammadata's Scienta SES 200 hemispherical analyser with multichannel 2-D detector appeared, the new era in the ultra high electron spectroscopy began [44]. Most of the high resolution data in this thesis were obtained with this type of analyser. A short description of the basic steps of data analysis follows. For illustration in Fig. 2.8 an example of a typical photoemission spectrum collected in a single scan is shown. The spectrum was collected with the SES 100 analyser that is recently in operational use in our laboratory in Zagreb and that is, by performance, very similar to the SES 200 analyser. There are three basic information contained in such spectra:

- energy (x-axis),
- angle, i.e. wave vector (y-axis), and
- photoemission intensity (z-axis; black – no counts, white – maximum number of counts).

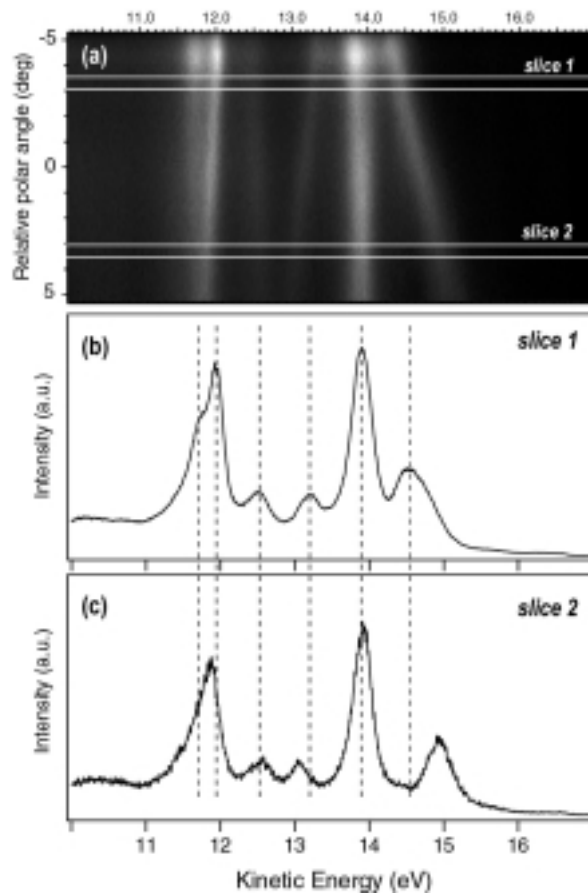


Fig. 2.8. (a) An example of the 2-D grey-scale photoemission intensity spectrum obtained with the SES 100 analyser in a single scan. The sample is 1 ML of Ag on a Cu(100) surface,  $T = 200$  K,  $h\nu = 21.2$  eV. The sample was rotated  $19^\circ$  from the normal emission position. (b) and (c) – EDC spectra obtained by a slice cut in the SES 100 spectrum shown in (a) around the analyser angles of  $-3.25^\circ$  and  $+3.25^\circ$ , respectively. The vertical dashed lines are drawn through peak positions of slice 1 for easier observation of relative peak shifts compared to slice 2.

## 2. EXPERIMENTAL METHODS

These spectra should be angularly calibrated to the experimental geometry to obtain the actual polar angle scale and eventually a proper  $k_{\parallel}$  [7]. By taking an angular slice cut around a fixed angle one obtains conventional energy distribution curve (EDC) spectrum. The reasonable slice width should be at least or higher than the angular resolution (typically  $0.2^\circ$ ). In Fig. 2.8b and c slice cuts of  $0.5^\circ$  width around analyser angle of  $-3.25^\circ$  and  $3.25^\circ$  in Fig. 2.8a are shown, respectively.

### 2.2.6. Extracting quasiparticle parameters from HRARPES spectra

Important aspect in the HRARPES data analysis is a proper extraction of peak parameters from the recorded photoemission peaks. Since ARPES, in principle, measures the quasiparticle spectral function (see Eq. (2.16)), momentum resolved self energies are directly accessible in the experiment. Fig 2.9 illustrates the example where the photohole self-energy is extracted from HRARPES measurement of the Mo(110) surface state [45].

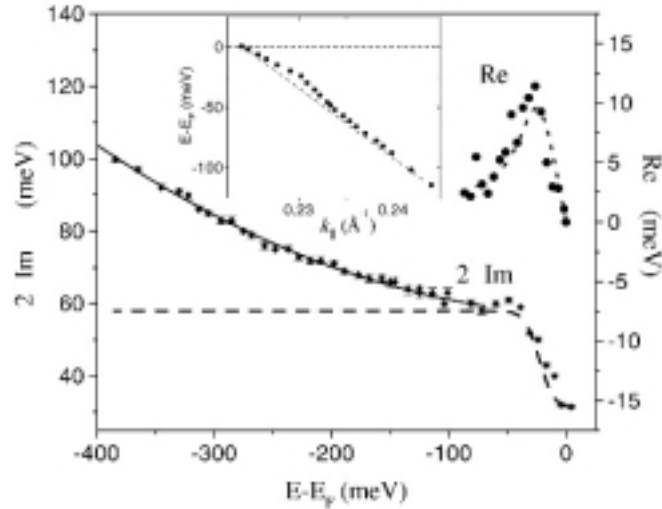


Fig. 2.9. [45] The Mo(110) surface state photo-hole self-energy as a function of binding energy at 70 K. The real part is obtained from the dispersion and the imaginary part from the width of the quasiparticle peak.

The quasiparticle interactions included in the photoemission information from two-dimensional electronic states are:

- the hole-electron (h-e)
- the hole-phonon (h-p)
- the hole-impurity (h-i)

Each contributes to the reduction of the inverse width (quasiparticle lifetime) of the photoemission peak. Implying the justified Mathiessen type superposition one can write:

$$\frac{1}{\tau} = \frac{1}{\tau_{h-e}} + \frac{1}{\tau_{h-p}} + \frac{1}{\tau_{h-i}} \quad (2.22)$$

## 2. EXPERIMENTAL METHODS

or equivalently:

$$\Gamma = \Gamma_{h-e} + \Gamma_{h-p} + \Gamma_{h-i} \quad (2.23)$$

For a given temperature we assume the Fermi-liquid behaviour of the imaginary part of the spectral function (see Fig. 2.5). It can be written in the form [46]:

$$2 \cdot \text{Im}[\Sigma(E)] = \Gamma_0 + 2 \cdot \beta \cdot E^2 \quad (2.24)$$

where the hole-electron contribution is contained in the  $2 \cdot \beta \cdot E^2$  part. The energy is referred to the Fermi level as the origin ( $E_F = 0$ ). The hole-electron coupling parameter  $\beta$  describes the strength of the h-e interaction. The hole-phonon and the hole-impurity parts are contained in the energy-independent  $\Gamma_0$  part. Depending on the value of  $\beta$ , the shape of the photoemission peak may vary between the symmetric Lorentzian ( $2 \cdot \beta \cdot E^2$  small) and completely asymmetric ( $2 \cdot \beta \cdot E^2$  significant). Furthermore, depending on the portion of the  $\Gamma_0$  part compared to the  $2 \cdot \beta \cdot E^2$  part, the Fermi liquid fitting procedure may or may not be sensitive to the choice of the  $\beta$  parameter (for instance if  $2 \cdot \beta \cdot E^2 \ll \Gamma_0$ ).

The hole-phonon coupling strength is extracted from the temperature dependent measurements. The important assumption is that the residual part of  $\Gamma_0$  does not depend on the temperature, i.e. that the hole-impurity interaction is constant with respect to the temperature. On the basis of the Debye model, the h-p contribution to the quasiparticle lifetime is [47]:

$$\frac{\hbar}{\tau_{h-p}} = 2\pi\hbar \cdot \int_0^{\omega_D} d\omega \left( \lambda \cdot \left( \frac{\omega}{\omega_D} \right)^2 \cdot \{1 - f(E - \hbar\omega, T) + 2b(\hbar\omega, T) + f(E + \hbar\omega, T)\} \right) \quad (2.25)$$

where  $f$  is the Fermi-Dirac and  $b$  the Bose-Einstein distribution function and  $\omega_D$  is the Debye frequency. Already for  $k_B T \geq 0.5\hbar \cdot \omega_D$  the inverse lifetime increases linearly with temperature and from the slope one can read the h-p coupling strength,  $\lambda$ :

$$\frac{\hbar}{\tau_{h-p}} = 2\pi \cdot \lambda \cdot k_B \cdot T \quad (2.26)$$

And finally, since the photoemission averages the information over the certain surface area ( $\sim 1 \text{ mm}^2$ ) the measured quasiparticle lifetime will always be influenced by the presence of impurities (steps, defects, adsorbates, ...). After one has determined the h-p coupling parameter the h-p contribution can be extracted down to  $T = 0 \text{ K}$ , and what is left in  $\Gamma_0$  is the hole-impurity contribution to the quasiparticle lifetime. Fig. 2.10 shows the measured and calculated temperature dependence of surface states widths of the Cu(111) and Ag(111) surface [48].

## 2. EXPERIMENTAL METHODS

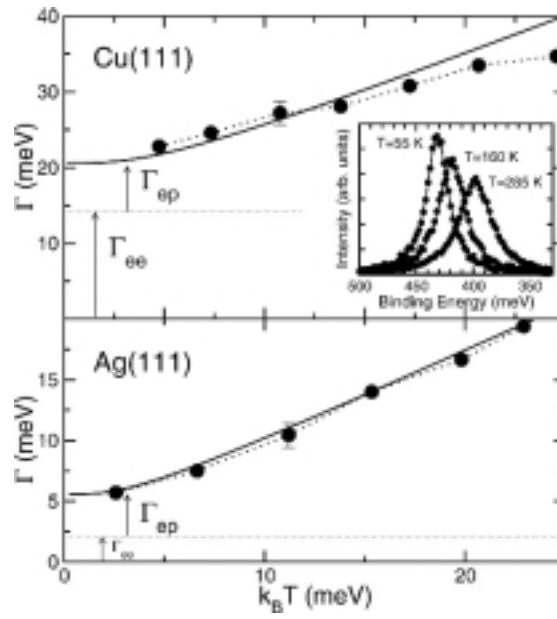


Fig. 2.10. The calculated and measured lifetime broadening for the Cu(111) and Ag(111) surface states at the band minimum as a function of temperature [48].



### 3. Apparatus

The experimental results presented in this thesis were obtained in five separate experimental ultra high vacuum (UHV) systems. Two of them include synchrotron facilities. The used experimental techniques were: high resolution angle resolving photoemission, scanning tunnelling microscopy, Auger electron spectroscopy and low energy electron diffraction.

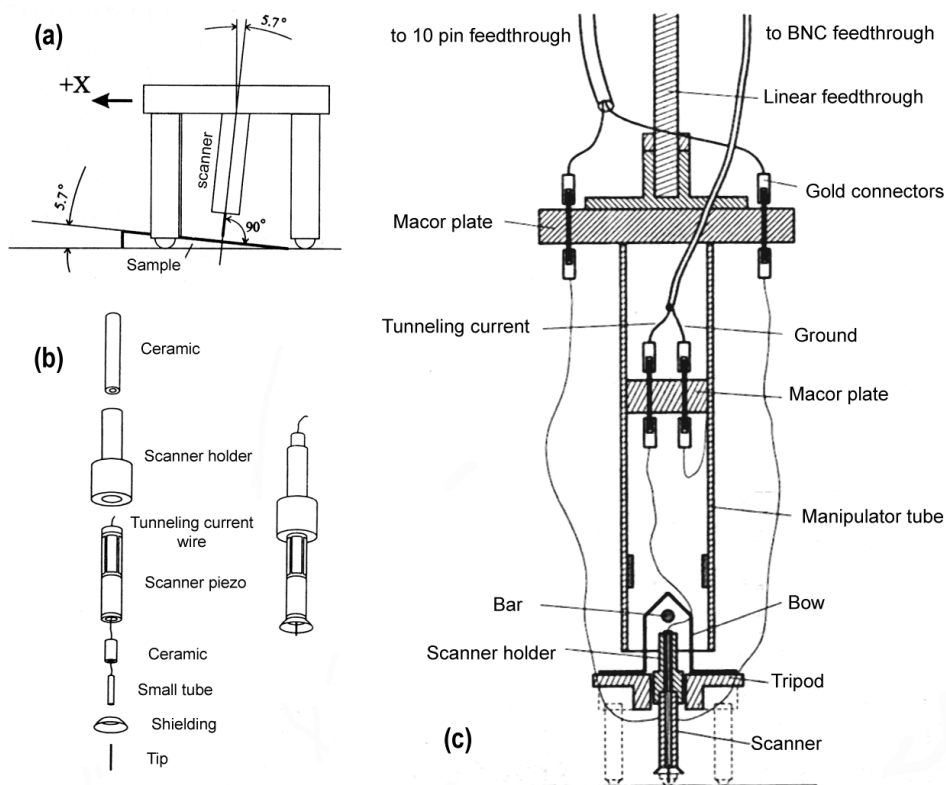


Fig. 3.1. Schematic overview of a home build STM [49] we have used in the experiment. (a) "Beetle" in coarse approach modus. (b) Mounting of the scanner. (c) Cross section of the tunnelling unit.

The first UHV set-up (Zagreb) enables use of all techniques. The room temperature STM apparatus is a home build STM [49] (Fig. 3.1). The electron energy analyser was a Scienta SES 100 analyser with the acceptance angle of  $\pm 0.2^\circ$  and the energy resolution of 5 meV that simultaneously records a large energy and angular window of  $\approx 12^\circ$  (see Fig. 3.2). As a photon source a high intensity helium discharge lamp with polariser was used (SPECS). With respect to the used technique in Zagreb, i.e. used sample holder, during the preparation the sample could be cooled down to LN<sub>2</sub> temperature and heated up to 1800 K.

### 3. APPARATUS

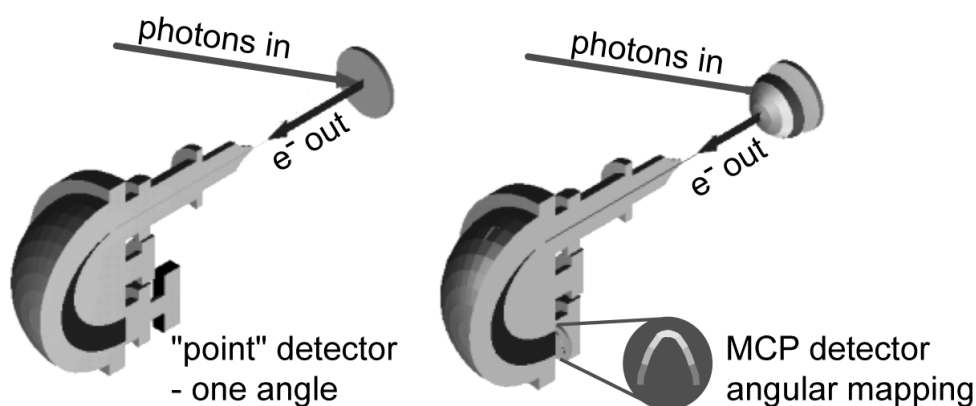


Fig. 3.2. Comparison of two different generations of hemispherical electron analysers. Major improvements regard electron focusing and detection where in newest versions a 2D multichannel plate and CCD camera serve as a detection system .

The UHV set-up in Bonn consists of STM, AES and Kelvin probe techniques.

At the National Synchrotron Light Source in Brookhaven we used the undulator beamline U13UB [50] which provides photon energies in the range between 16 and 23 eV. The electron energy analyser was a Scienta SES 200 with similar characteristics as the previously described SES 100 analyser. The combined instrumental energy resolution could be set to a value in the range 8-25 meV, small enough to make no significant contribution to the measured photoemission peak width from the QW states. This chamber is also equipped with an He discharge lamp and LEED. Construction of the manipulator and sample holder was such that during the measurements the sample temperature could be varied and controlled in the range of 30-2500 K.

At the synchrotron ELETTRA experiments were performed at the 3.2 R VUV photoemission beamline [51]) in a much wider photoemission energy range (18-100 eV). The energy resolution of the angle-resolving VSW-50 analyser was 30 meV and the angular resolution was  $\pm 0.5^\circ$ . In order to control the orientation, the structure and the quality of the surface ordering the LEED technique was used.

In Ljubljana experiments were performed on a VG Microlab 310F system. The system is designed to perform SEM, HRAES and XPS analysis. Auger measurements were performed here at a beam energy of 10 keV. This system was specifically used to characterise the substrate.

### 3. APPARATUS

In each case the base pressure was in the low  $10^{-10}$  mbar region, or lower. In all experiments the same vanadium (100) single crystal of 99.99% nominal purity and a maximum misalignment of  $0.5^\circ$  from the (100) plane was used. The diameter of the crystal is 6 mm and the thickness is 2 mm. The substrate was prepared by well known sputtering – annealing cycles [52]. For the ion bombardment of the surface  $\text{Ar}^+$  was used. Typical sputtering currents of 2-4  $\mu\text{A}$  at 1 keV beam energy were applied. The sample was heated either directly, through resistive Ta wires, or indirectly using electron bombardment. Because of the specific materials used on the STM sample holder, the annealing temperature in that case was limited to 1200 K.

For the STM experiments that followed longer annealing periods the drift reached quite high values up to  $\approx 1$  nm/s. Cooling of the sample holder with liquid nitrogen was applied in order to lower the temperature gradient after annealing. For the Fourier transform STM analysis 8 nm was the typical size of the analysed images which sets up the limit in the momentum resolution to  $\cong 0.08 \text{ \AA}^{-1}$  ( $\Delta k = 2\cdot\pi/(\text{image size})$ ). However, the actual resolution also depends on the quality of the image, the sample temperature and the bias voltage used. Thus we estimate the resolution to be  $\cong 0.15 \text{ \AA}^{-1}$  in our measurements.

Chemical composition of the surface during the characterisation and preparation procedure was checked by AES. A detailed chemical mapping of the well ordered V(100)-(5 $\times$ 1) substrate was performed in the laboratory in Ljubljana. The quality of surface ordering was assessed by the sharpness of LEED patterns, and statistically by the average size of terraces and the number of defects in STM images. When available, LEED was also used to calibrate the normal emission position for ARUPS and to check the orientation of the high symmetry crystal axes compared to the direction of sample or analyser rotations.

The silver films were deposited onto the substrate by the resistive heating of a tungsten basket that contained a silver droplet. Silver thickness and deposition rates were calibrated using Auger silver to vanadium intensity ratios. In Brookhaven and in Trieste a quartz microbalance was additionally used. Information about the coverage is also contained in the photoemission spectra since they are characterised by distinct quantum well peaks in both the s-p and the d-band. Our studies included uniform silver thickness in the range 1-8 ML.



## 4. Quantum well states

In principle, the electronic structure is related to the atomic structure and vice versa. For instance, the electronic structure at the crystal surface is altered compared to the bulk environment. Breaking of the crystal three-dimensional periodicity introduces strong modifications into the electronic states in the vicinity of the surface. In the presence of the surface, the wave functions of the valence electrons have two possible forms:

- Extended wave functions, corresponding to electrons which move towards the surface and are reflected back into the bulk, decaying exponentially into the vacuum.
- Localised wave functions, i.e. wave functions which decrease exponentially on both sides (bulk and vacuum) of the surface but propagate along the surface plane. In such two-dimensional surface states the electrons are trapped in the vicinity of the surface.

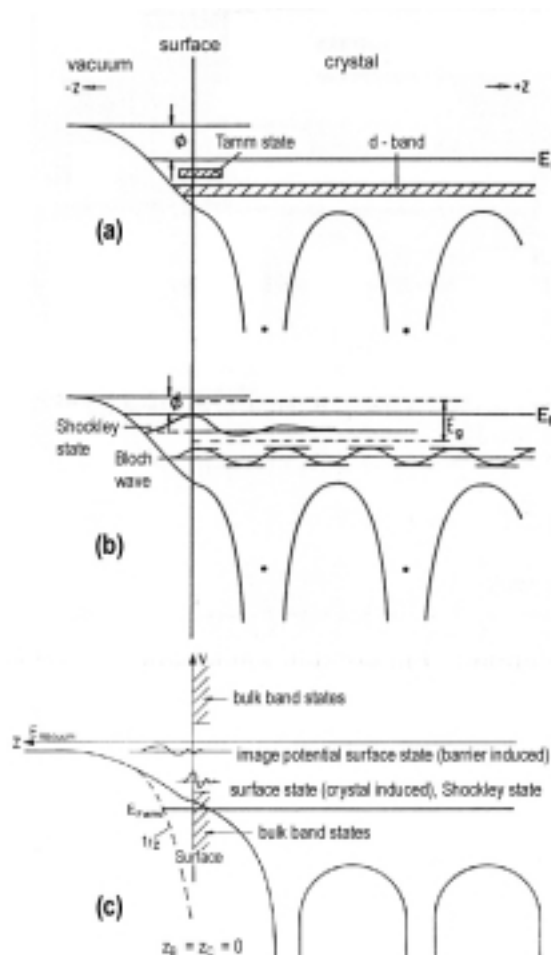


Fig. 4.1. [7] (a) A Tamm state is a split off from a band (d-band here) of the crystal by the change of the potential at the surface. (b) A Shockley state is created in a band gap of the bulk band structure due to the termination of the crystal by a surface. (c) Distinction between the crystal (Shockley states) or barrier induced (image states) surface states.

Such characterisation may serve as a quite general definition of the bulk and the surface state, respectively. More serious considerations of the surface lead to the distinction about the possible types of surface states. One can distinguish surface states of s-p (Shockley states [53], resonances [54], image states [55]), or of more localised d- or f-origin (Tamm states [56]). Fig. 4.1 schematically illustrates this distinction.

For various ultra thin films on various substrates, similarly to surfaces, the existence of localised states is also possible. These states are usually called quantum well states (QWS). The possible existence and the character of these states is governed not only by the film and its surface (film-vacuum interface) but also by the substrate, i.e. the interface towards the substrate (film-substrate interface). For a detailed introduction about the metal-on-metal quantum well states we refer the reader to recent review papers dealing with this issue [2-4]. In this chapter first we define quantum well states and give some illustrative examples. Further we introduce the so-called multiple reflection model (MRM) that is used for the description of surface and QW states. Finally, related to concepts and investigations in this thesis we address the relevant published work on QW and surface states.

## 4.1. Ultra thin film states

### 4.1.1. Introduction

In the bulk, valence electrons propagate in an infinitely periodic potential forming quasi-continuous electronic states, i.e. electronic bands. Suppose that we can make very thin crystals that are thick only few atomic layers ( $\sim$  nm). This would lead to the formation of discrete localised states. Electrons are trapped by the vacuum barriers on each side of the very thin crystal. Applying the particle in the box concept (the one-dimensional Schrödinger equation) one finds that for nanometer thick crystals the electron states are separated typically in the range of electronvolts. Fig. 4.2 illustrates the solutions of the one-dimensional Schrödinger equation for several different symmetric one-dimensional potentials. The equation reads:

$$\frac{\hbar^2}{2m} \cdot \frac{d^2\psi(z)}{dz^2} + [E - V(z)] \cdot \psi(z) = 0 \quad (4.1)$$

In practice, however, the formation of a self standing ultra thin crystal is not possible. Thin and ultra thin films can only be formed on a bulky substrates. This complicates the situation from several different aspects. A degree of interaction of electron in the overlayer film with the substrate will influence a level of confinement. Rare gas layers physisorbed on solid surfaces are a good example where this interaction is so small that the overlayer film can be regarded as almost free standing. Some examples are found in Refs. [57,58,59,60, 61,62]. But, even in such simple cases investigations reveal that the interaction of a rare gas film with a substrate can not be entirely neglected [63].

#### 4. QUANTUM WELL STATES

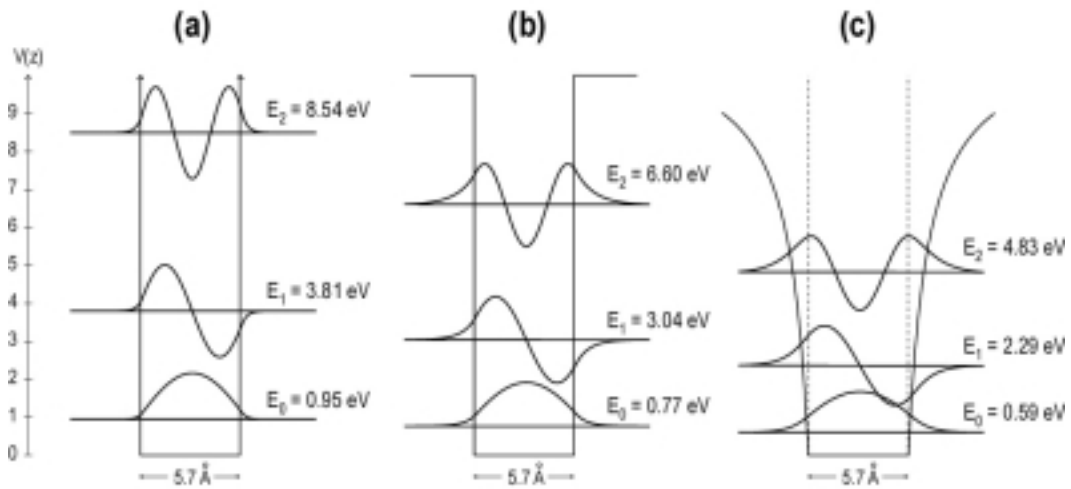


Fig. 4.2. Schematic representation of one-dimensional potentials and their solutions that model the quantization perpendicular to the surfaces of a self standing layer. In each case the well width is 5.7 Å. For (a) and (b) the surface is modelled with step like potentials, while in the case of (c) the image-like barrier represents the surface. Potential well heights are: (a) 50 eV (simulates infinitely high barrier), (b) 10 eV, (c) 10 eV.

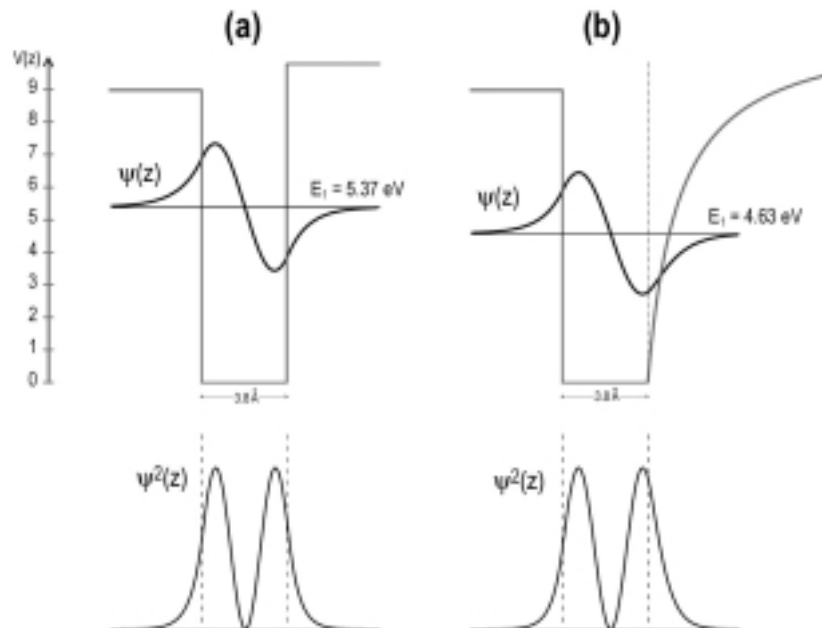


Fig. 4.3. The one-dimensional non symmetric well simulating the substrate supported quantum well – wave functions and their densities: (a) quadratic well, (b) image potential well.

#### 4. QUANTUM WELL STATES

Generally, the substrate influences the potential barrier at the film-substrate interface. Instead of symmetrical potential barriers, in the presence of a substrate the potential symmetry is lost (Fig.4.3). For the description of the film-substrate interface related potential the geometric parameters (position of the interface in z-direction) will not suffice. The energy dependence is also important.

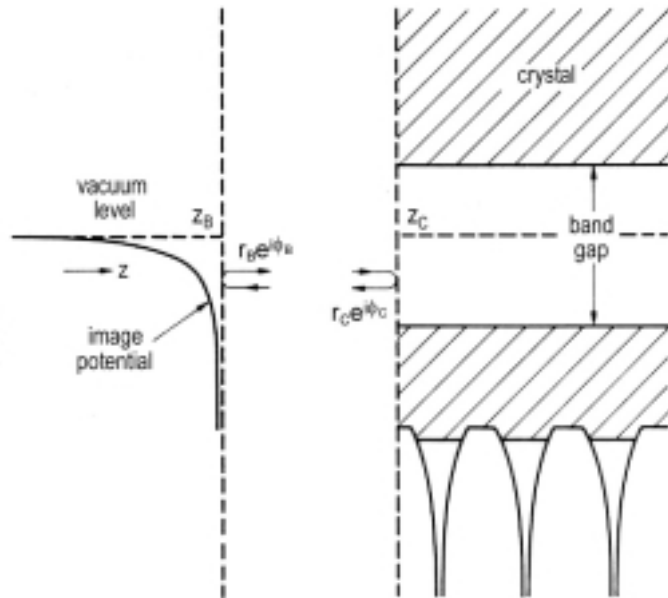


Fig. 4.4. [64] Schematic one-dimensional view that describes co-ordinate and energy dependence of the  $V(z,E)$  potential that leads to the formation of quantum well states in ultra thin films. The film thickness is determined by  $z_B - z_C$ . Note that in the limit  $z_B - z_C = 0$  the surface states are also described within this picture.

The potential,  $V(z,E)$ , at the interface in detail depends on the electronic structure of both the substrate and the film. The barrier is formed if an energy band gap exists in the substrate with respect to the film electronic states (see Fig. 4.4). However, it has been shown that symmetry or hybridisation band gaps are as efficient as energy band gaps in confinement of electrons in the overlayer films. An example is the Ag/V(100) system. In Fig. 4.5 we compare the calculated band structure of the bcc vanadium and the fcc silver along the  $\Gamma$ - $\Delta$ -H and the  $\Gamma$ - $\Delta$ -X direction, respectively [65]. One should note two shaded regions representing hybridisation gaps for the states of  $\Delta_1$  and  $\Delta_2$  symmetry (s-p and d-electrons in silver films). The upper gap extends in the region  $\cong 2$  eV above and below the Fermi level. Namely, in this energy region no electronic states of  $\Delta_1$  symmetry are allowed. Therefore, electrons in the overlayer silver film with  $\Delta_1$  symmetry will be scattered back at the vanadium-silver interface if their energy is in the range 0-2 eV below the Fermi level. In a similar way the (100) surface of vanadium is also suitable for studying QW states of d-symmetry (see lower gap in Fig. 4.5). The relative position of the silver d-bands with respect to these in vanadium is such that the Ag 4d band falls into the d-symmetry band gap of the vanadium substrate – in the centre of the Brillouin zone of the (100) vanadium surface the d-symmetry band gap opens at around

#### 4. QUANTUM WELL STATES

3.0 eV binding energy which is well above the top of the Ag 4d band at 3.7 eV, making the relative shift of d-bands in vanadium and silver as big as 0.7 eV.

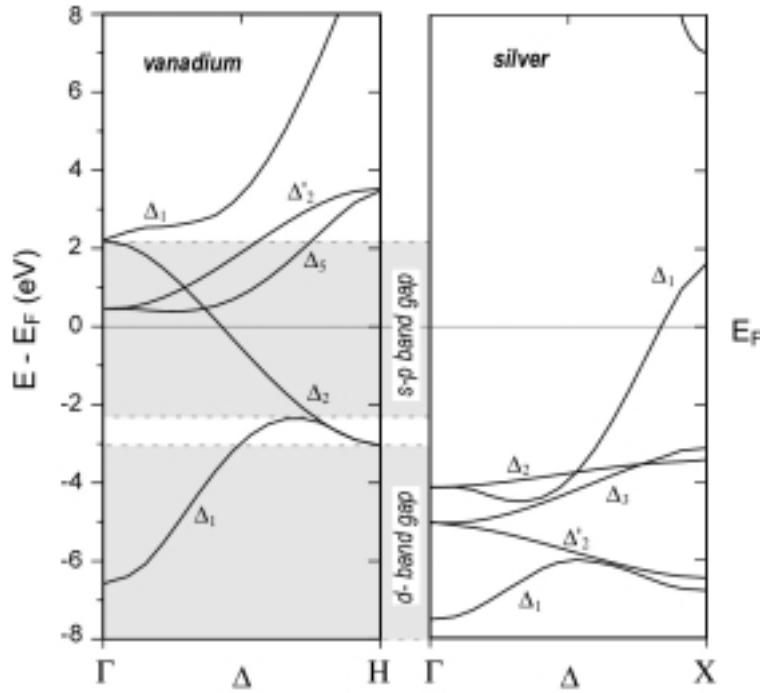


Fig. 4.5. Calculated energy bands of bcc vanadium and fcc silver along  $\Gamma$ - $\Delta$ -H and  $\Gamma$ - $\Delta$ -X high symmetry directions of the bulk Brillouin zone, respectively [65]. Note the existence of two shaded band gap regions for the electrons of  $\Delta_1$  and  $\Delta_2$  symmetry. For details see text.

Even for systems with metals whose electronic structure does not differ significantly, i.e. where the hybridisation gaps are much narrower than in the previously described example, the quantum well states have been detected in photoemission experiments. For example, this is the case of Ag/Au(111) [66].

In the case that no band gap (energy or hybridisation) exists the electrons in the overlayer film will be partially reflected at the interface and they will form so-called quantum well resonances (QWR). These states are usually formed near the band gap edges, i.e. in the regions where no actual band gap exist. Such states are found, for example, in Ag/Au/Ag(111) [67] or Cu/Co(100) [68].

For the formation of QW states the film growth and its epitaxy are important as well. The way how the film grows is, among other things, determined by the atomic radii and matching to the substrate and by the energy balance in the system (surface free energies of the substrate and the film and the interface free energy are the key parameters). In the ultra thin film limit (one or several atomic layers) the problem of growth is crucial for the existence of a smooth film-substrate interface, an ordered uniform layer and, eventually, quantum wells.

#### 4. QUANTUM WELL STATES

The mismatch between lattice parameters of the substrate and the film affects the overlayer growth, whereas quantum well states require interfaces smoother than the electron wavelength. The mismatch gives rise to an incommensurate or reconstructed interface. An electron incident normal on the interface may scatter to many different directions. In such situations the matching of the wave functions at the interface becomes x-y dependent and rather complicated. Eventually, for rough interfaces quantum well peaks may appear to evolve continuously as a function of coverage. The examples are Ag/Ni(111) [69] and Ag/Cu(111) [70,71].

On the other hand, quantum well states in atomically uniform films are a function of a discrete layer thickness and their binding energy is fixed. Probably, the best example of such system is silver on a Fe(100) whisker [3,72], where it is possible to grow up to  $\approx 100$  layers of atomically uniform thickness. This fact is corroborated by the photoemission experiment. In Fig. 4.6. an example is illustrated, where the spectra of 38, 38.5 and 39 ML thick silver films in the s-p quantum well region are shown. The spectra demonstrate the atomic uniformity of films of integer monolayer coverages.

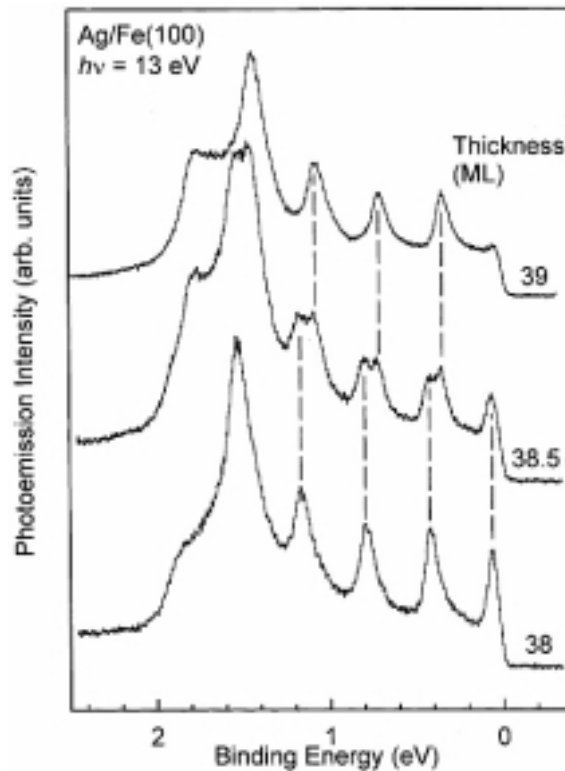


Fig. 4.6. [3] Normal emission photoemission spectra for 38, 38.5 and 39 ML thick Ag film on Fe (100) whisker. The quantum well peak positions are indicated by dashed lines. The 38.5 ML spectrum exhibits two sets of quantum well peaks indicating the simultaneous presence of areas covered by 38 and 39 ML of Ag.

### 4.1.2. Multiple reflection model

A particularly elegant way to describe a surface has been introduced by Echenique and Pendry [73,74]. This method was successfully applied in a description of many surface states and later also QW states [54,55,75,76,77,78,79,80]. The method is known as a multiple reflection model (MRM), or alternatively as a phase accumulation model (PAM). The electrons are described as being repeatedly reflected between the image potential barrier, at  $z_B$ , which prevents them from escaping into the vacuum, and the crystal, at  $z_C$  (via a band gap). For surface states the surface plane ( $z_B$ , a reference surface plane) and the crystal plane ( $z_C$ ) are the same, whereas for the ultra thin film  $z_B - z_C$  has a physical meaning and represents the film thickness (see Fig. 4.4). Let us denote electron reflectances at barriers at  $z_C$  and  $z_B$  by  $r_C \cdot \exp(i \cdot \phi_C)$  and  $r_B \cdot \exp(i \cdot \phi_B)$ , respectively. Here  $r_B$  and  $r_C$  are the real parts of the reflection coefficients and  $\phi_B$  and  $\phi_C$  are the phase changes occurring upon reflection. The wave function's phase is also changed when it propagates between the barriers by  $2 \cdot \kappa \cdot (z_B - z_C)$ , where  $\kappa$  is the perpendicular wave vector. The total amplitude is given by the summation of an infinite number of reflections and reads:

$$\frac{1}{1 - r_B \cdot r_C \cdot e^{i \cdot (\phi_B + 2 \cdot \kappa \cdot (z_B - z_C) + \phi_C)}} \quad (4.2)$$

Confined states at certain energy will correspond to the poles in the total amplitude. This brings us to the Bohr-Sommerfeld quantization rule:

$$r_B \cdot r_C = 1 \quad \phi_B + 2 \cdot \kappa \cdot (z_B - z_C) + \phi_C = 2 \cdot \pi \cdot n \quad (4.3)$$

where  $n$  has to be an integer. For the substantial film thickness in the phase condition the  $2\kappa \cdot \Delta z$  part prevails. In the opposite limit, zero thickness reduces the phase condition to  $\phi_B + \phi_C = 2 \cdot \pi \cdot n$ . In principle, for a certain surface we can deduce  $\phi_B$  and  $\phi_C$  if we have at least two states available, or  $\phi_B + \phi_C$  with just one state (image state, for instance). The condition is satisfied for some values of wave vector  $\kappa$ . Related to this wave vector (perpendicular to the surface) we may introduce the perpendicular kinetic energy of the state,  $\varepsilon$ :

$$\varepsilon = \frac{\hbar^2 \kappa^2}{2m} = E - \frac{\hbar^2 k_{\parallel}^2}{2m} \quad (4.4)$$

where  $E$  is the electron energy measured from the bottom of the inner potential well.

For a crystal phase shift,  $\phi_C$ , one has to find and match wavefunctions that decay into the vacuum as well as into the bulk. To achieve this one has to introduce a periodic crystal potential – within the crystal a simple potential of a form  $V(z) = 2V_G \cdot \cos([2\pi/a] \cdot z)$  is assumed. In the nearly free electron model (NFE) [38,81] a weak periodic potential is applied ( $V_G$  is small). In the simplest form the termination of the crystal at the surface can be modelled by a step potential (see Fig. 4.7).

#### 4. QUANTUM WELL STATES

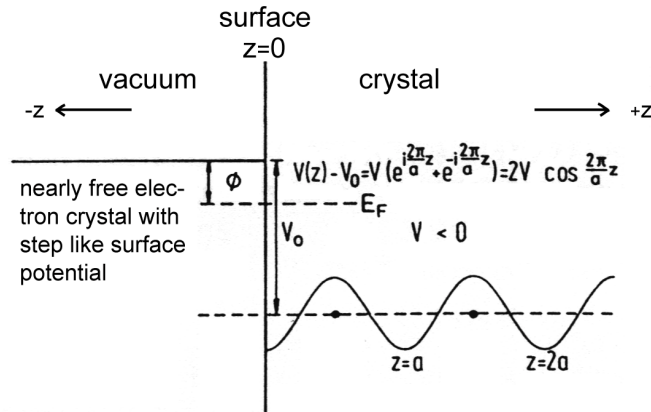


Fig. 4.7. [7] Representation of the surface of a crystal: step potential as a crystal termination and nearly free electron solid with a potential  $V(z) = V_0 + 2V \cdot \cos([2\pi/a] \cdot z)$ ,  $V < 0$ .

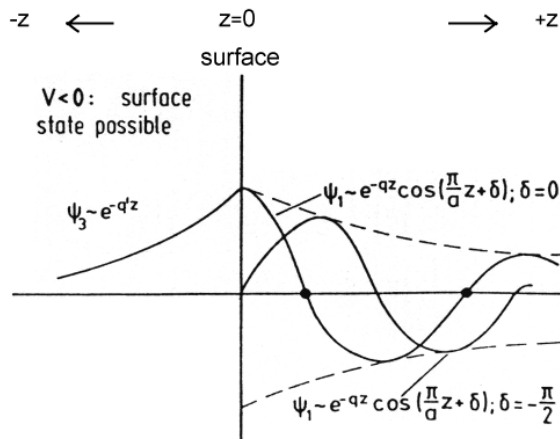


Fig 4.8. [7] The solution of the Schrödinger equation within the band gap for the potential drawn in Fig. 4.7.

Introduction of a periodic potential has a strong physical meaning. The band structure of a crystal can often be described by the nearly free electron model. On a qualitative level the model describes almost all phenomena related to the behaviour of electrons in metals. A striking feature that emerges with the NFE model is modification of the free electron bands by opening of the energy gap at the Brillouin zone boundaries at  $k_{BZ} = \pm\pi/a, \pm 2\pi/a, \dots$ , in which no extended electronic states can exist. The free electron parabolic dispersion is split into two bands (a so-called two-band model). Dealing with the Schrödinger equation near the Brillouin zone boundary one can try to find the solutions within the energy gap. For that purpose one has to use a complex wave vector, i.e.,  $k_z = p \pm iq$ . After some calculation, substitutions (introduction of a phase parameter  $\delta$ ;  $\delta = 0$  at the bottom edge of the band gap and  $\delta = \pi/2$  at the top edge of the band gap) and taking into account physically allowed solutions one gets that, for the choice  $V_G < 0$ , the existence of surface states is possible and the surface state wave function has a form (see Fig. 4.8):

#### 4. QUANTUM WELL STATES

$$\begin{array}{ll}
 \text{Inside the crystal} & - \quad \psi = A \cdot e^{-qz} \cdot \cos\left(\frac{\pi}{a} \cdot z + \delta\right) \quad z > 0 \\
 \text{Outside the crystal} & - \quad \psi = B \cdot e^{-q'z} \quad z < 0
 \end{array} \quad (4.5)$$

Matching the wave function slopes inside and outside the crystal gives the relation  $q' = -q - p \cdot \tan(\delta)$ . If the wave function is evaluated at  $z = z_C$  (note that in Fig 4.7 and 4.8 the choice is  $z_C = 0$ ), after some calculation one can get the expression:

$$\kappa \cdot \tan\left(\frac{\phi_C}{2}\right) = p \cdot \tan(p \cdot z_C + \delta) - q \quad (4.6)$$

where the crystal phase shift,  $\phi_C$ , associated with the phase change upon the reflection at the crystal surface has appeared in the equation. To a good approximation that is valid for the free-electron like or even more complicated systems, one can take  $\phi_C = 2 \cdot \delta$  [73]. This means that  $\phi_C$  must change by  $\pi$  from the bottom to the top of the band gap. A purely approximate and empirical formula has been derived for the crystal phase shift:

$$\phi_C = 2 \cdot \arcsin\left(\sqrt{\frac{E - E_L}{E_U - E_L}}\right) \quad (4.7)$$

where  $E_L$  and  $E_U$  are the energies of the lower and upper positions of the band gap ( $E_U - E_L = 2V_G$ ). Fig. 4.9 illustrates the  $\phi_C$  phase change within the band gap region.

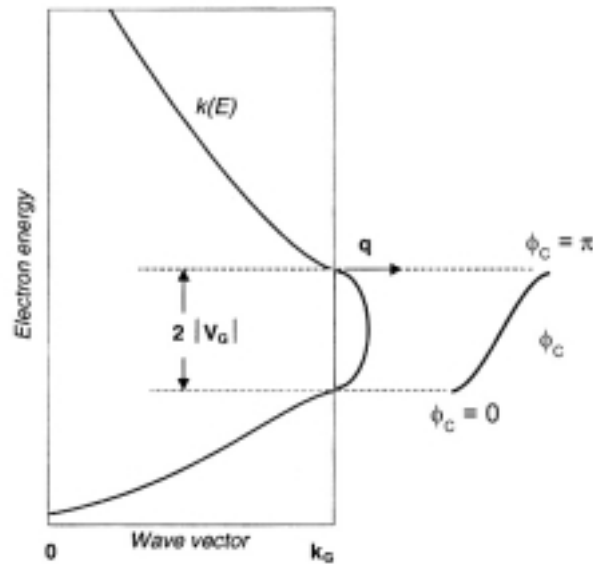


Fig. 4.9. [4] Schematic model of a free electron band gap (left) and the associated phase change (right) as a function of the energy within the gap.

For the potential that is defined as in Fig. 4.7 ( $z_C = 0$ , atomic positions at  $z = a/2, 3a/2, 5a/2$ , etc.) let us consider the situation when  $V_G$  is negative. The lowest order solution at the bottom of the gap will be proportional to the sine function (the p-type wave function), whereas the solution at the top of the gap will be proportional to the cosine function (the s-type wave

#### 4. QUANTUM WELL STATES

function). In atomic systems the p-level is usually found above the s-level. Thus, the resulting gap for  $V_G < 0$  is sometimes called a Shockley-inverted band gap [7].

The phase shift  $\phi_B$  (reflection at the surface barrier) may be derived by matching the wave function and its derivative at the boundary  $z_B$ . Analytical expressions are obtainable only for some simple approximations of the surface barrier. For the finite step barrier:

$$\tan \frac{\phi_B}{2} = -\sqrt{\frac{E_V - \varepsilon}{\varepsilon}} \quad (4.8)$$

For the image barrier ( $\sim 1/z$ ), using the WKB approximation, one gets:

$$\frac{\phi_B}{\pi} = \sqrt{\frac{3.4\text{eV}}{E_V - \varepsilon}} - 1 \quad (4.9)$$

where  $E_V$  is the energy of the vacuum level that can be deduced from the work function of the surface. Note that for the image potential barrier  $\phi_B$  diverges, when approaching the vacuum level. This means that the phase condition can be satisfied infinitely many times (Rydberg-like solutions).

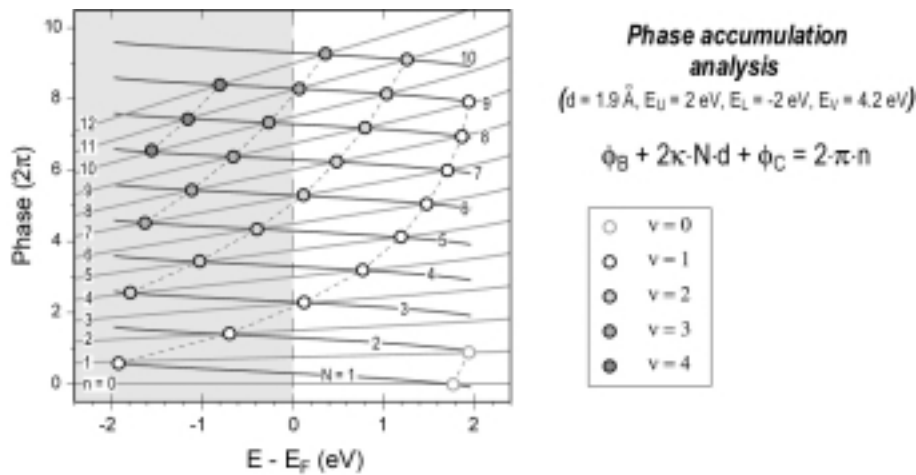


Fig. 4.10. Graphical solution of the phase equation. The parameters include the layer thickness of 1.9 Å,  $E_U = 2$  eV (upper position of the band gap),  $E_L = -2$  eV (lower position of the band gap),  $E_V = 4.2$  eV (vacuum level). The solutions are found in the intersection of full lines and are denoted with circles. The shaded region includes the energies below the Fermi level, thus is accessible by the photoemission experiment.

The suitable way to solve the phase equation (4.3) is to do it graphically. Fig. 4.10 illustrates how to obtain the solutions for the particular set of chosen parameters. The solutions are found in the intersections of full lines (grey and black) which are together constituting Eq. (4.3). The shaded region denotes the area which is accessible in the photoemission experiment (filled states). The families of states with the same quantum number  $v = N - n$  are noted with differently shaded circles and connected with dashed lines.

#### 4.2. Electronic structure of ultra thin silver films

The quantization effect in thin films was first observed in 1970 in the low energy electron experiment on thin gold film [82]. Thin film quantization effects were probed by different experimental techniques: electron tunnelling through thin metallic films [83,84,85] reflectivity and transmission of normally incident electrons [86,87,88,89], electrical conductivity and resistivity [90,91,92,93,94], helium atom scattering [95], Hall effect [96], workfunction [97], etc. Photoemission was used to study layered systems like: Mn/Cu(100) [98], Fe/Au(100) [99], Rh/Ag(100) [100], Cr/Fe(100) [101] and the particularly interesting and perhaps most thoroughly studied QW system Cu/Co(100) [102]. Since STM and STS have a unique ability to locally probe the electronic structure of surfaces, one would expect that these techniques are frequently used to study ultra thin film states. In contrast, there are very few STM or STS studies of quantum well properties in ultra thin metallic systems [103,104,105]. In the low temperature study of Na/Cu(111) [104] STS measurements of the electronic structure are correlated to the structural phases observed on the surface. For Na islands on graphite a combined low temperature STM-ARPES study characterised the geometry and the electronic structure of the system [105].

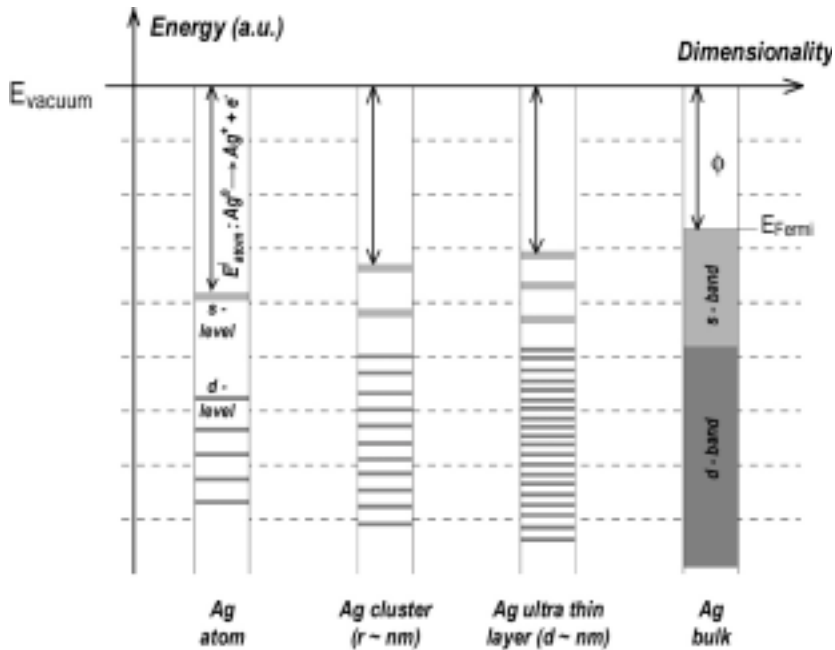


Fig. 4.11. [109] Illustrative overview: evolution from one-dimensional silver (single atom) towards three-dimensional silver (bulk). Clusters and ultra thin layers are in an intermediate region.

#### 4. QUANTUM WELL STATES

Fig. 4.11 illustratively suggests how the dimensionality of silver affects its electronic structure. Silver has been investigated in a cluster-like form and some of these investigations were focused on quantum-size effects. Recent work of Becker et al. [106], for example, illustrates how a well ordered ultra thin oxide film may serve as a template for the self-organised nanostructured silver cluster growth. The quantum size effect has been, for instance, observed in a size-selected Ag cluster electron energy loss spectroscopy (EELS) study on MgO(100) films [107], or in an STS study of silver nanoclusters on a graphite surface [108,109]. One may also find numerous investigations of silver ultra thin films deposited on various substrates. In this overview we focus on the properties of silver ultra thin films deposited on metallic substrates.

In 1983 Loly and Pendry [110] in a theoretical paper pointed out that photoemission from thin films should result in a set of sharp photoemission peaks, where the peak positions and widths should allow a precise determination of the bulk band structure and the photohole lifetime. At about the same time one of the first detailed ARUPS studies of a silver monolayer deposited on a Cu(100) substrate was reported by Tobin et al. [111]. Due to the relative shift of the copper and silver bulk bands, the electrons in the silver 4d-band were confined in the overlayer film showing a two-dimensional behaviour. These states were later recognised as quantum well states.

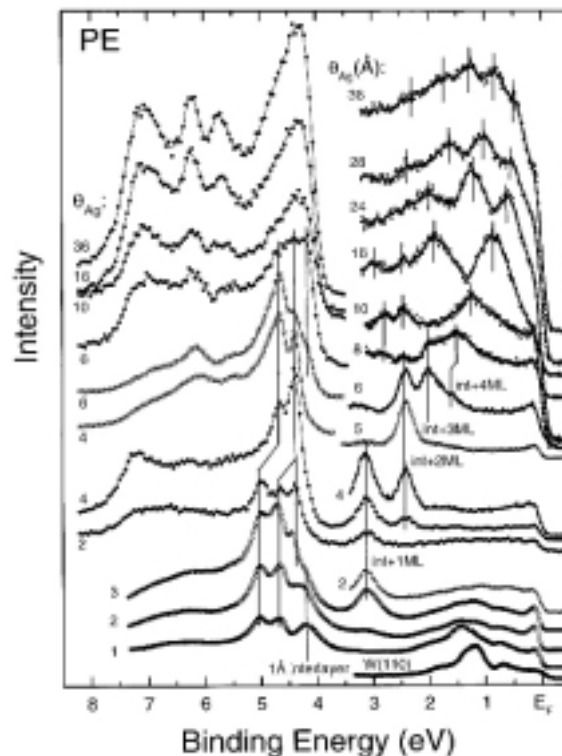


Fig. 4.12. Normal emission photoemission spectra for Ag/W(110) obtained for different Ag thicknesses [115].

#### 4. QUANTUM WELL STATES

With respect to the origin, i.e. the symmetry of the electrons forming QW states, we deal with the s-p or the d-derived QW states in ultra thin films. Examples exhibiting s-p QW states observed in the photoemission experiments on silver films are: Ag/Au(111) [66], Ag/Ni(111) [69], Ag/Cu(111) [70,71], Ag/V(100) [5,112], Ag/Fe(100) [77,113], Ag on Fe(100) whisker [72], Ag/W(110) [114,115], Ag/Ta(110) [116]. In Fig. 4.12 an example is given where photoemission spectra that characterise the s-p and the d-band region of Ag/W(110) are shown [115].

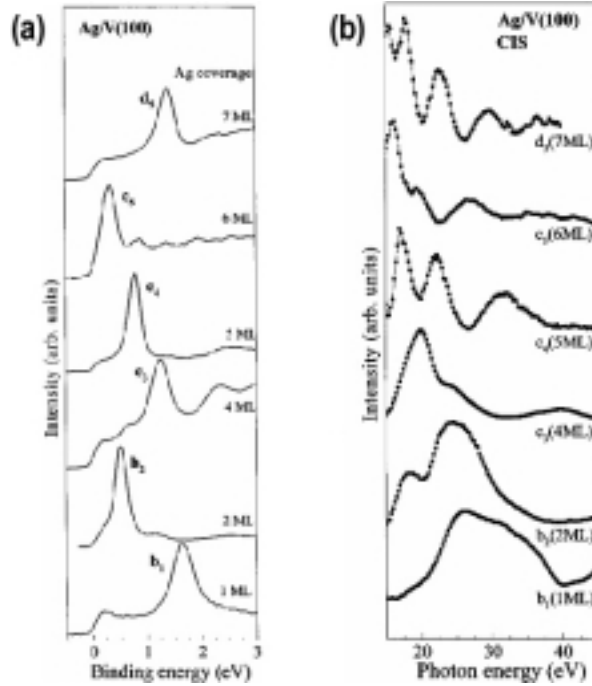
In contrast to the rough interface found for Ag on Ni(111) [69] and Cu(111) [70], the lattices of Ag and Au are almost perfectly matched forming a smooth, commensurate interface [66]. For Ag/Au(111) a surface state is formed (the L-gap surface state usually found on (111) noble metal surfaces) located above the top of the Ag(111) s-p band which does not depend on the film thickness, and true QW states which are formed within a region 0.8 eV wide due to the mismatch between the top of the Au(111) and the Ag(111) s-p band.

For Ag/Fe(100) the spin polarisation of quantum wells has been studied using spin-polarised detection [77]. In this system the hybridisation of s-p QW states with lower lying 3d band was found, which is important for the understanding of spin polarisation in noble-metal – magnetic-metal multilayered structures [2]. Multiple reflection analysis for s-p quantum wells and resonances was, in general, successfully used to describe the QW peak positions and to model reflectivities at interfaces.

As already mentioned Ag on Fe(100) can be considered as a perfect example of atomically uniform silver. However, photoemission investigations indicate that the silver-iron interface is not fully confining [72]. This seems to be the element related to the problems in the formation of well defined confined states in the limit of ultra thin thicknesses (several atomic layers). Measurements of s-p QW states allowed a highly accurate silver bulk s-p band structure determination [117]. The temperature stability of silver films was investigated in this system and related to the binding energy of s-p QW states [118]. The relation between the s-p QW states and the stability of the silver film was in the same way studied for Ag/Ta(110) [116].

The ground state properties of s-p QW states for Ag/V(100) have been already characterised [112]. For these states also the dependence of ARUPS intensities on the incident photon energy was investigated [119,120,121] and it was found that the photoemission intensity shows a strong oscillatory character. In Fig. 4.13a the photoemission spectra of 1-7 ML Ag/V(100) of the s-p quantum well region are shown. Fig. 4.13b shows the experimentally measured ARUPS intensity oscillations (constant-initial spectra, CIS) [119]. This investigation provided valuable information which enables optimised high-resolution synchrotron investigations that we present in this thesis.

#### 4. QUANTUM WELL STATES



4.13. [119] (a) n.e. ARUPS spectra for 1-7 ML Ag/V(100). (b) Ag/V(100) CIS spectra.

The d-band QW states were much less investigated, because the detection and the analysis of these states is more complicated. For noble metals there is a large increase of the number of states with film thickness. With the number of atomic layers,  $N$ , the number of d-band QW states is scaled as  $5 \cdot N$ . Also, the broadening of the peaks induced by Coster-Kronig Auger process makes it very difficult to resolve the large number of states. As an example of a d-band quantum well system we have already mentioned silver monolayer on Cu(100) [111]. Up-to-date the silver d-band QW states were also found for Ag/W(110) [114,115] and Ag/Fe(100) [122]. Surprisingly, although the d-electrons have more compact wave functions localised around the atomic core, for these systems the phase accumulation analysis of the d-band QW states was successfully applied to assign the large number of peaks observed. For the uniform silver layer grown on a Fe whisker it has been judged that  $\approx 30 \text{ \AA}$  ( $\sim 15 \text{ ML}$ ) is the phase coherence length for the d-electrons [122].

As already pointed out, for two-dimensional systems the photoemission has a unique ability to directly probe the photohole spectral function. In section 2.2.4 we have discussed the importance of high resolution experiments in bypassing the instrumental Gaussian broadening and accessing the actual spectral function. When knowing the spectral function one can determine the self energy and thus the quasiparticle lifetime and interaction parameters of the system. STS is also a suitable technique to investigate the quasiparticle properties (at surfaces) since it also measures the lifetime. On the other hand the reduced dimensionality of the system means a reduced phase space which can, consequently, enhance or suppress the interactions in the system. This has been, indeed, confirmed by HRARPES and STS experiments. These experiments have been focused to the energy range

#### 4. QUANTUM WELL STATES

of several eV around the Fermi level. Especially the states very near to the Fermi level are of particular interest, since these states dictate important material properties like transport for example. Close to the Fermi level the electron-electron scattering probability is small due to the phase space arguments and the electron-phonon scattering becomes dominant, even at low temperatures. In such cases the measurement of electron correlations close to the Fermi level are difficult due to small contributions, whereas from the temperature dependence of quasiparticle lifetimes one can straightforwardly measure the electron/hole-phonon coupling parameter  $\lambda$  (see section 2.2.6).

The s-p QW states in the limit of ultra thin thicknesses serve as a perfect two-dimensional system where the degree of localisation and binding energy is varied by the change of the film thickness. However, up-to-date one finds only several investigations that explore the quasiparticle interactions in these systems.

Alkali metals on a Cu(111) surface have been investigated by the Chalmers group. The photoemission measurements for Na/Cu(111) [123,124] have shown that the hole-phonon coupling parameter for the 1 and 2 ML QWS ( $\lambda = 0.24$  in each case) is about two times higher than bulk Na or Cu. This enhancement is explained with the reduced dimensionality of the film. The results of photoemission measurements of the Ag/V(100) s-p QW states quasiparticle interactions for the ultra thin silver films are an integral part of this thesis and will be discussed in great detail throughout the thesis. Some of the data has been already published [125,126] where for the first time we reported the strong and oscillatory hole-phonon interaction in the ultra thin silver films. For Ag/Fe(100) Paggel et al. [127,128] have measured the temperature dependence of the s-p QWS photoemission peaks of 12 and 19 ML thick films and proposed that the measured hole-phonon coupling constants ( $\lambda = 0.29$ ) for these films can be attributed to the silver bulk coupling parameter. Similarly, the hole-phonon interaction has been studied for quantum well states in thick Ag films grown on Cu(111) surface by Takahashi et al. [129] where the  $\lambda$  was found to be in the range 0.10-0.15. Very recently Luh et al. [130] reported measurements of the hole-phonon coupling parameter for Ag/Fe(100) for smallest Ag thicknesses. The observed behaviour is quite similar to what we find for Ag/V(100). However, the measured enhancement of the hole-phonon interaction is ascribed to the silver-iron interface contribution which opposes the models proposed for Na/Cu(111) [124] and Ag/V(100) [125,126].

Related to the theoretical work only recently a more serious progress has been made in modelling the electron-phonon interaction at metal surfaces and in quantum wells [48,131,132]. As an input parameter, these studies include the full phonon structure of the system (surface + film + bulk) which requires a lot of computational effort. In Fig 4.14 as an example the calculated phonon dispersion for Cu(111) taken from Ref. [131] is shown.

#### 4. QUANTUM WELL STATES

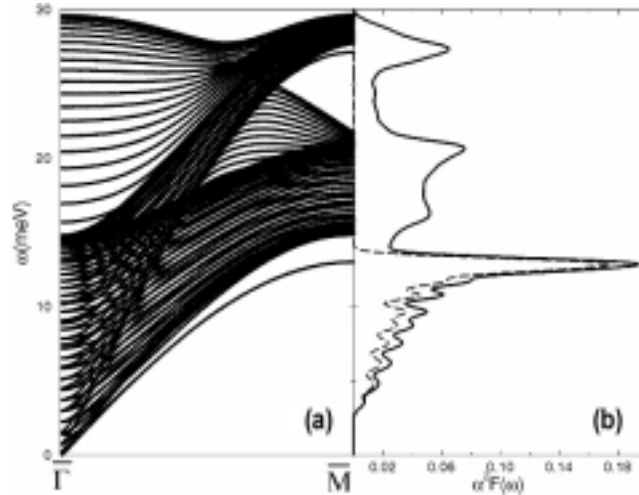


Fig. 4.14. [131] (a) The calculated phonon dispersion for Cu(111). (b) The Eliashberg function of the hole state at the centre of the Brillouin zone (solid curve) and the contribution from the Rayleigh mode to the Eliashberg function (dashed curve).

In contrast to the number of investigations found for quasiparticle properties of s-p QW states, surface states have been more extensively investigated, in particular the L-gap Shockley surface states on the (111) faces of noble metal surfaces [8,9,43,133,134,135,136,137]. We mention the photoemission experiment of Reinert et al. [43] where the measured linewidths perfectly matched the theoretically predicted linewidths (lifetimes) of Ag, Cu and Au (111) surface states. This was due to the combination of the highest resolution analyser and the sample preparation procedure that resulted in an almost perfect, defect-free surface. McDougall and co-workers [133] found that  $\lambda$  for the Cu(111) surface state is 0.14 which is in accordance with values for bulk copper.

A general problem of the area-integrated information in the photoemission and thus inevitable hole-defect scattering contribution was, in fact, the reason for the substantial theory estimates vs. experimental values discrepancy about the lifetime of the noble metal surface states. In contrast to the photoemission, the atomic scale lateral resolution of the STM gives the unique advantage to locally study electronic properties of the surfaces. In the investigations of the quasiparticle interactions STS measurements for the first time enabled to properly study changed electron correlation effects on the surface of a metal [28].

The other surface states have been also investigated. In a study of the Mo(110) surface state [45] it was shown that all three quasiparticle interaction terms (hole-electron, hole-phonon and hole-impurity) can be deduced from the temperature and the binding energy dependence of the photoemission peak width. The hole-electron contribution to the measured photoemission line width was found to be an order of magnitude larger than for the s-p derived surface states. The hole-phonon coupling strength was found to be in the range of the value for bulk molybdenum ( $\lambda = 0.42$ ). Some other studies, like the one on Cu [138], Be [139],

#### 4. QUANTUM WELL STATES

140,141], or Ga [142] surface were focused on the hole-phonon coupling term alone. For the Tamm surface state on the Cu(100) surface Matzdorf et al. [138] have measured  $\lambda = 0.09$ . Other studies have shown that the hole-phonon coupling parameter,  $\lambda$ , for the surface state can be significantly different from that obtained in the bulk from transport measurements. This particularly refers to the example of the Be(0001) surface investigated by Balasubramanian et al. [139]. The measured value for the surface state,  $\lambda_{\text{surface}} = 1.15$ , is found to be 4 times larger than in the bulk Be ( $\lambda_{\text{bulk}} = 0.25$ ). A simple estimate of the superconducting transition temperature ( $T_{\text{C}}^{\text{surface}} = 70$  K) predicted a significant increase with respect to the bulk transition temperature ( $T_{\text{C}}^{\text{bulk}} = 0.02$  K). However, the measurements that followed [141] showed that at 10 K this beryllium surface still exhibits normal metallic behaviour. We also mention that the significantly enhanced electron-phonon coupling strength was measured for the hydrogenated W(110) surface (H/W(110) and D/W(110)) [143]. This is an example where higher energy internal and adsorbate-surface vibrations couple to the electron gas of the substrate. A value  $\lambda \sim 0.7 \pm 0.3$  was obtained, which is significantly larger than the value for bulk tungsten of 0.2.



## 5. The substrate

### 5.1. Introduction

#### 5.1.1. Clean V(100) surface

The vanadium (100) surface itself has been the subject of a number of experimental and theoretical studies [144]. There are several reasons for this. The first one is related to the theoretically predicted magnetism of the topmost V(100) layer as well as of ultra-thin vanadium films [145] of the same or similar structure. The second one is connected with the use of vanadium oxides in the design of various catalysts, whereas clean vanadium surfaces are a prerequisite for the preparation of the so-called “inverted” catalysts which in turn serve to study and model more complex systems. Vanadium has also been frequently studied with respect to trends in electronic properties of the first-row transition metals. It is worth to mention that a study of vanadium Auger transitions [146], within its valence band, has shown how important it is to perform experiments on clean surfaces of transition metals. Impurities, even at very small concentrations, can severely affect electronic and magnetic properties of a transition metal. Moreover, the structural properties may also be significantly affected by impurities and are sometimes misinterpreted as the features of clean surfaces. Vanadium (100) is also an example in this respect [147,148]. And finally, the vanadium (100) surface has proven to be an excellent substrate for studying QW states in Cu and Ag ultra thin films [112].

Getting a clean and ordered surface is a particularly difficult task when it comes to the case of low index surfaces of early transition metals. The reason is a very high reactivity of those surfaces, which results in a high sticking coefficients ( $\cong 1$ ) for the impurities like oxygen or carbon-monoxide. Even more than that, there is a bulk impurity content and diffusion processes that, usually during the annealing of the crystal, contaminate the surface of the sample. In order to be able to get a clean and at the same time ordered surface one has to lower and deplete the concentration of contaminants deep below the near surface region. Regarding the mentioned problems there are very strict demands on the ultra high vacuum base pressure, as well as a pressure during the operations that are applied in order to clean the surface (sputtering, annealing). Additional burden to the process of cleaning the surface is the history of the sample. Namely, it is possible that during the time of hundreds and thousands of hours of different treatments performed on the sample some macroscopic defects are formed at the surface. These then make the local environment suitable for pinning of clusters of impurities at the surface, which complicates the process of sample cleaning.

## 5. THE SUBSTRATE

According to the literature, there are generally two possible ways to clean the early transition metal surface (including the vanadium V(100) surface). The “tricky” way is to apply a long annealing (~ hours) to a very high temperature, some 100 K close to the melting point ( $T_{\text{melt}} \cong 2180$  K for the vanadium) [149,150]. In this process it is necessary not to allow that the total pressure exceeds  $1 \cdot 10^{-9}$  mbar. This requires a construction of a very special sample holder that can stand such sample temperatures and that does not degas much during the annealing. A more conventional way is to follow a lengthy step-by-step sputtering – annealing procedure applied in order to remove standard impurities. This process is, however, very time consuming. Several groups reported clean V(100) surfaces [151,152,153,154]. The clean and ordered V(100) surface is unreconstructed with respect to the surface lattice constant, V(100)-(1×1). According to the LEED measurements the first two layers are relaxed [151] (see Fig. 5.1).

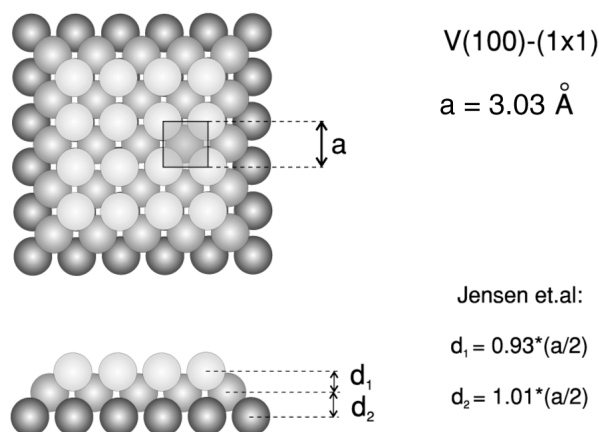


Fig. 5.1. V(100)-(1×1) clean and unreconstructed vanadium surface – structural model.

### 5.1.2. The 5×1 reconstructed V(100) surface

In this study we have used instead the reconstructed V(100)-(5×1) surface as a substrate for the silver films. The (5×1) vanadium (100) reconstruction is oxygen induced. This surface is particularly interesting for two important reasons. First, high annealing temperatures in the last stage of the substrate preparation lead to the formation of large terraces. This is important regarding the quality of the deposited silver film. Second, most of the photoemission results from this thesis were obtained at synchrotrons, where even if the vacuum conditions are perfect the available time is the limiting factor which makes it difficult to prepare clean and ordered V(100) surface. On the other hand the preparation procedure for the well ordered reconstructed V(100)-(5×1) surface is much less time consuming. The results from a previous investigation [155] of silver interaction with oxygen preadsorbed on the V(100) surface indicate that silver deposition on the reconstructed V(100)-(5×1) surface may result in a complete removal of oxygen from the surface and eventually a lifting of the (5×1) reconstruction.

## 5. THE SUBSTRATE

The (5×1) reconstruction of the vanadium (100) surface was first reported more than 20 years ago and interpreted as a reconstruction of the clean surface [147]. Soon after, it had been found that the (5×1) structure is always accompanied by the “presence of a substantial fraction of a monolayer (ML) of oxygen” which was roughly estimated to 0.2 ML [148,151] and that the initial attribution of the observed structure to the clean surface was caused by inadequate resolution of the Auger electron spectrometer. In order to explain the observed (5×1) low energy electron diffraction (LEED) pattern a simple structural model with 0.2 ML of subsurface oxygen was proposed [152]. Recent studies [156,157,158,159,160,161] showed that the (5×1) LEED pattern is obtained with samples containing substantially larger quantities of oxygen. In those cases, as the scanning tunnelling microscopy (STM) results show, the (5×1) pattern is a consequence of the V(100) surface reconstruction. In addition, those surfaces show a rather complex set of structural details, some of which are described here.

Krenn et al. [156] studied the V(100)-(5×1) surface containing ~ 0.6 ML of oxygen and a significant amount of carbon (~ 0.25 ML). In a LEED and STM study Koller et al. [157] calculated that the energetically most favourable oxygen coverage for the observed reconstruction was about 0.76 ML, where oxygen atoms occupied 100% of bridge positions along every fifth V-atom row and 70% of four-fold sites between the rows. According to the calculation there is a distance of 3.8 Å between vanadium atoms sharing bridge bonded oxygen, which is much more (27 %) than the unreconstructed in plane vanadium-vanadium distance. Recently, Konvicka et al. [158] reported that for a higher total coverage of oxygen and carbon (more than 0.8 ML) the (5×1) reconstruction is also observed. Apart from the single-crystalline bulk vanadium substrates, the V(100)-(5×1) surface was investigated for a thick vanadium layer (~100 nm) grown epitaxially on a MgO(100) substrate [159,160]. Such layers are free of bulk impurities, which are always present in the bulk vanadium and the oxygen surface concentration is in that case influenced and controlled by the vanadium deposition rate. Dulot et al. [159] have, based on the combination of reflection high-energy electron diffraction (RHEED) and STM results, proposed that the oxygen induced compressive strain of the topmost layer leads to the observed (5×1) reconstruction of the surface. The oxygen surface concentration was estimated to vary in the range of 1 ML and the carbon concentration was below 0.1 ML.

Most of the work reported to date has been oriented towards the structural properties of the V(100)-(5×1) surface while much less has been done on the issue of the electronic properties. This particularly relates to the valence band structure of the V(100)-(5×1) surface. The only ultraviolet photoemission (UPS) investigation is found in the work of Foord et al. [152] who monitored changes in the UPS spectra accompanying the (1×1) to (5×1) change in the LEED image that occurred upon annealing of the V(100) sample over 750 K. Unfortunately, the data do not provide conclusive information about the valence band

structure of the samples. The influence of oxygen on the electronic structure of the clean V(100) surface was investigated [52,153,155] by means of angle-resolved ultraviolet photoemission spectroscopy mainly in the context of the investigation of the nature of the vanadium band structure and in particular, a vanadium surface state. Locally, the electronic structure of the V(100)-(5×1) surface has been investigated by scanning tunnelling spectroscopy (STS) in the context of oxygen (and/or carbon) influence to the vanadium d-surface state close to the Fermi level [161].

In the next parts of this chapter we describe the preparation procedure for getting a well ordered V(100)-(5×1) surface that we use as a substrate for silver film growth. We characterise the surface by means of combined scanning electron microscopy (SEM) – high-resolution Auger electron spectroscopy, STM and ARUPS techniques. Here we present some results of this study, whereas a more thorough analysis can be found in a paper of Kralj et al. [162].

## **5.2. Preparation and characterisation of the surface**

### **5.2.1. Preparation procedure**

A well ordered (5×1) reconstructed surface was prepared by cycles of sputtering, long annealing and flashing of the sample to temperatures of up to 1200 K. After we have removed hydrogen, phosphorus and sulphur impurities by standard procedures, carbon and oxygen were detected on the surface. Various conditions of surface cleanliness, influenced by the segregation of different impurities, are sometimes characterised by a well defined superstructure or reconstruction. For instance, for a sulphur coverage of  $\approx 0.7$  ML a  $(\sqrt{2}\times\sqrt{5})R27^\circ$  superstructure is detected, while for a sulphur coverage of  $\approx 0.5$  ML a c(2×2) superstructure is observed [163]. The c(2×2) superstructure is also attributed to the presence of carbon. Figs. 5.2a and b show a LEED and STM image of a carbon covered V(100) surface, that were obtained during the early stages of the surface preparation. Although it is known that carbon and oxygen have different temperature – segregation profiles, their segregation may depend on the history of the sample. Further, prolonged cycles of sputtering at elevated temperature (600-650 K) were applied in order to reduce the total carbon quantity in the surface area.

In rare cases the preparation procedure led to carbon quantities higher than 0.2 ML. The quality of the (5×1) LEED pattern is not very sensitive to small variations of the carbon concentration in the range of 0.2-0.4 ML. Above these values the formation of the c(2×2) pattern takes place. It is important to point out that the areas of c(2×2) structure are not homogeneously distributed across the surface indicating inhomogeneous distribution of carbon. By moving the LEED electron spot across the surface one observes the areas that

are locally enriched by carbon showing a superposition of  $c(2\times 2)$  and  $(5\times 1)$  diffraction spots (Figs. 5.2c and d). The inhomogeneity in the carbon as well as in the oxygen distribution is also corroborated by our SEM-HRAES measurements described in the next section.

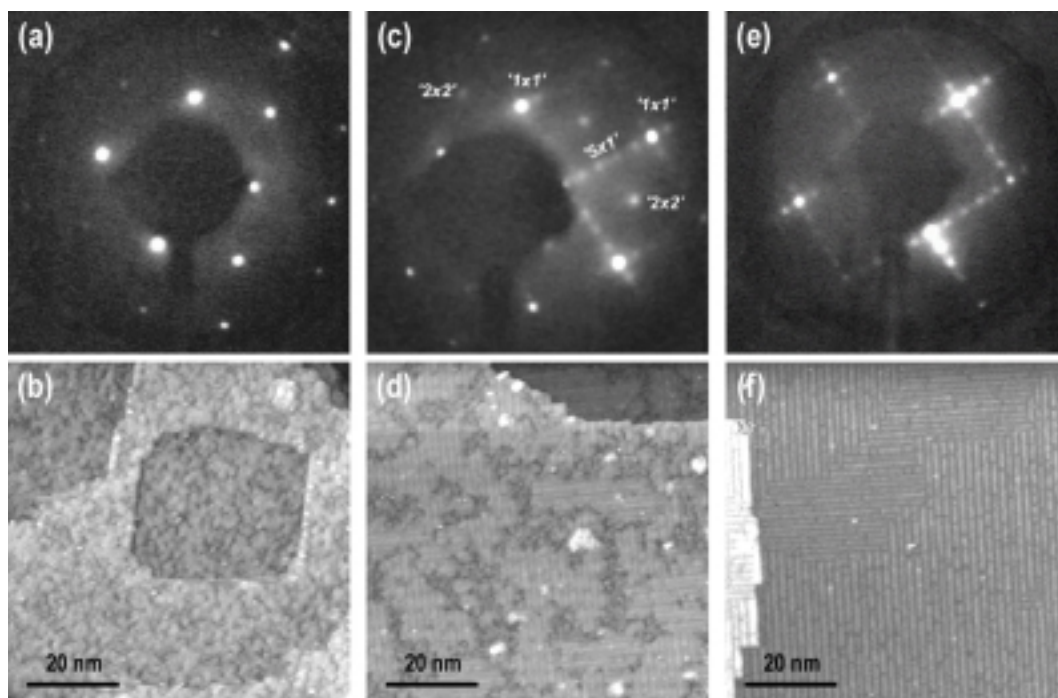


Fig. 5.2. LEED and their STM counterparts related to different structures observed on the vanadium (100) surface during the preparation procedure. (a) and (b):  $c(2\times 2)$  phase related to dominant carbon presence. (c) and (d): mixture of  $c(2\times 2)$  and  $(5\times 1)$  structures related to relatively high concentrations of both oxygen and carbon. (e) and (f):  $V(100)-(5\times 1)$  oxygen induced reconstruction. For each STM image  $U_B = 0.5$  V,  $I_T = 1.1$  nA.

### 5.2.2. Intrinsic chemical composition of the $(5\times 1)$ reconstructed surface

For the characterisation of the chemical composition of the surface from the millimetre- down to the nanometer-scale, we performed combined SEM-HRAES measurements using an electron beam of 10 nm spot size. The same sample that had previously been used for the STM and ARUPS studies of the  $(5\times 1)$  reconstructed  $V(100)$  surface clearly shows inhomogeneous chemical structure on the nanometer scale. A typical example is illustrated in Fig. 5.3a which shows a part of the reconstructed surface taken by SEM at 150000 magnification. The topographic differences are seen as white and dark regions. The Auger spectra taken at the indicated points are shown in Fig. 5.3b. The inset shows the energy region corresponding to the carbon signal. The spectra differ significantly with respect to the carbon and oxygen Auger intensities. Clearly, the carbon to oxygen ratio changes even when one moves by only 10-100 nm across the surface. This is not an effect of some dirt particles but rather an effect of an intrinsic variation in the chemical composition. In order to obtain an averaged information on the chemical composition of the surface we took

the Auger spectrum from a large surface region ( $400 \times 300 \mu\text{m}^2$ ). Note that the typical spot size in the case of a well focused "usual" AES electron beam is about  $500 \times 500 \mu\text{m}^2$ . The corresponding AES spectrum is shown in Fig. 5.3b together with the spectra from the 10 nm areas. The total oxygen and carbon concentration for this particular large area is higher than in any of the 10 nm areas. In Fig. 5.3c the AES spectra are zoomed into the region of the carbon signal.

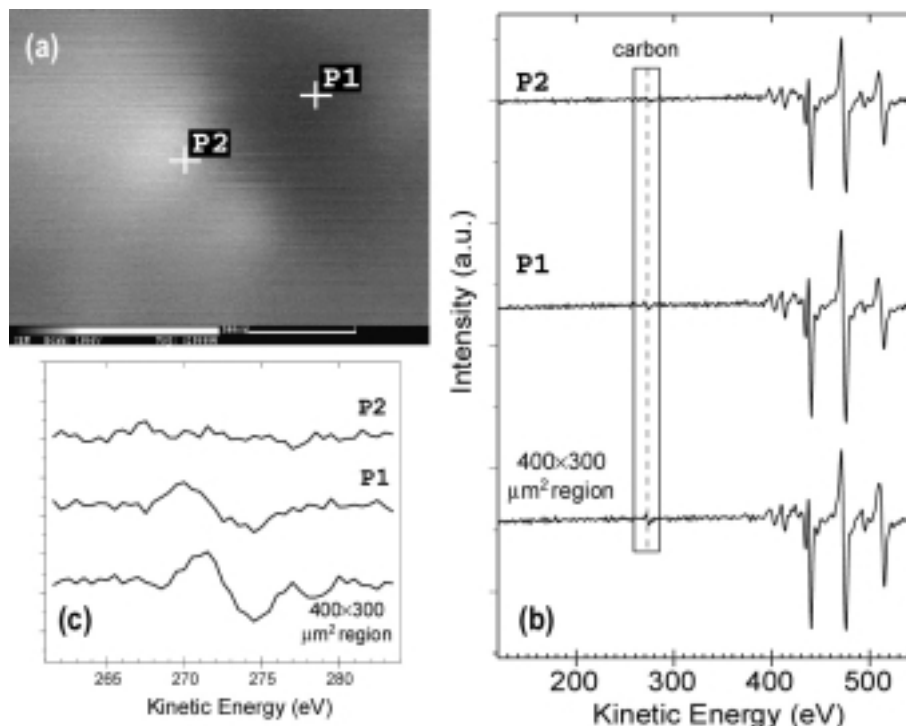


Fig.5.3. (a) SEM image of the V(100)-(5 $\times$ 1) surface at magnifications of 150000. (b) AES spectra taken from different regions of the V(100)-(5 $\times$ 1) surface. (c) Same AES spectra as in (b) zoomed into the region of carbon signal.

### 5.2.3. Atomically resolved STM characterisation

Fig. 5.4 shows typical STM images taken from the V(100)-(5 $\times$ 1) surface characterised with a sharp LEED pattern. On larger scales over the terraces in Fig. 5.4a (and 5.2f) we notice bright stripes equidistantly separated by thin dark lines. The appearance of this feature is particularly sensitive to the applied bias voltage; it is mostly pronounced for bias voltages in the range 0.4-0.6 eV. The average distance between the neighbouring dark lines corresponds approximately to five times the vanadium (100) plane interatomic distance ( $\cong 15 \text{ \AA}$ ). Two orientations of these domains are present, rotated by  $90^\circ$ . They are either parallel or perpendicular to the terrace step orientation and they are clearly correlated to the symmetry of the observed diffraction pattern. The particular domain sizes vary vastly. Within the same domain the individual white stripes might be frequently intercepted by dark lines. Typical atomically resolved images are shown in Figs. 5.4b, c and d. Again, the pronounced feature is the existence of dark lines that separate in most cases 5 and only occasionally 6 and 4 atoms

in between, which was also observed earlier by other authors [156-160]. A value measured for the distance between the corrugation maxima across the dark lines is  $3.5 \pm 0.1 \text{ \AA}$ , which is 17% higher than the nearest neighbour distance of the vanadium atoms in the (100) plane. In Fig. 5.4b the corrugation maxima on each side of the dark line are aligned. On the other hand, Figs. 5.4c and d show a somewhat different structural arrangement where the maxima are shifted in such a way that they form arrangements of triangular symmetry, as indicated in the Figs. 5.4c and d by the zigzag line. For the triangular-like arrangements a shift among the neighbouring (5×1) cells within the domain is locally present. This is found as a somewhat less frequent structural arrangement on the V(100)-(5×1) surface. The same structural details are present in the STM images of Dulot et al. (Ref. 159, Fig. 3d), but the authors did not comment on that matter.

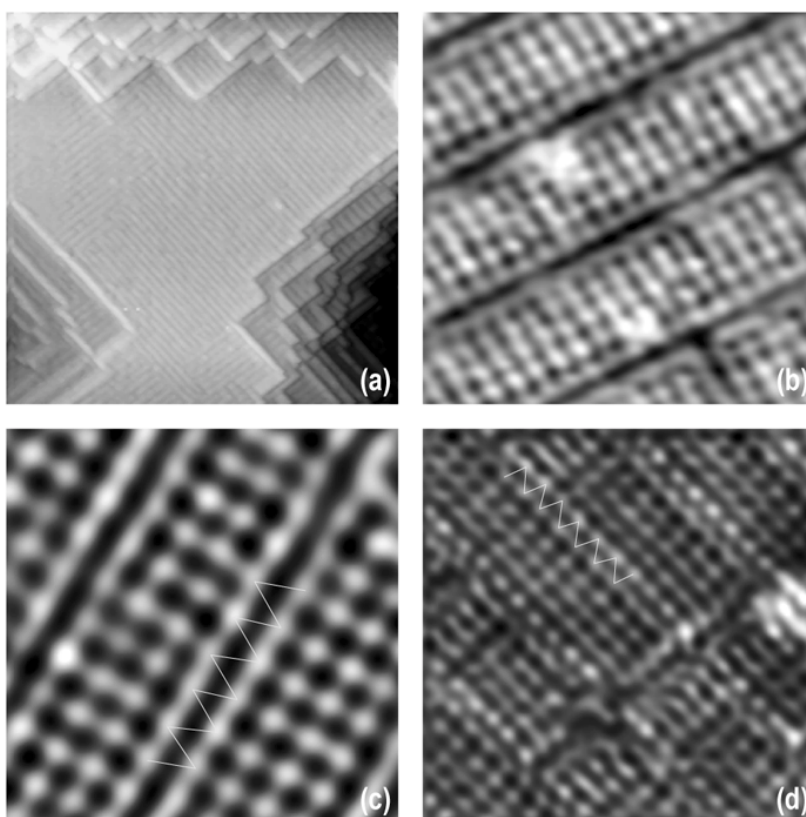


Fig. 5.4. STM images of V(100)-(5×1) surface. (a)  $74 \times 74 \text{ nm}^2$ ,  $I_T = 1.5 \text{ nA}$ ,  $U_B = 0.54 \text{ V}$ . (b)  $4.6 \times 4.6 \text{ nm}^2$ ,  $I_T = 3.5 \text{ nA}$ ,  $U_B = -2 \text{ mV}$ . (c)  $3.2 \times 3.2 \text{ nm}^2$ ,  $I_T = 5.0 \text{ nA}$ ,  $U_B = 15 \text{ mV}$ . (d)  $4.5 \times 4.5 \text{ nm}^2$ ,  $I_T = 4.0 \text{ nA}$ ,  $U_B = 2 \text{ mV}$ . Figs. c and d are suggesting triangular like symmetry in the position of maxima nearest to the dark lines which is indicated with zigzag lines.

### 5.3. Discussion

It is accepted that the dark lines in the STM images are a result of a significant increase of every fifth vanadium inter-atomic distance which, in turn, is induced by oxygen bonded to the vanadium atoms. According to a calculation of Koller et al. [157] the dark lines are associated with oxygen atoms in the vanadium bridge positions. The existence of the

## 5. THE SUBSTRATE

triangular arrangement of vanadium atoms along dark lines indicates that different bonding of oxygen to the vanadium atoms is also possible. In the bridging position as calculated by Koller et al. [157] the oxygen bond length is already almost at its maximum value. Any lateral shift of vanadium atoms would further increase the bond length which would make the oxygen bridge position unfavourable. Therefore, we believe that in the case of triangular symmetry (Figs. 5.4c and d) oxygen occupies the three-fold co-ordinated sites.

A direct interpretation of the STM images of the V(100)-(5×1) surface is burdened with the fact that the oxygen (and carbon) atoms are not directly imaged on the surface. In an experiment, Koller et al. [157] under particular imaging conditions managed to image unoccupied four-fold hollow sites as large bright spots and occupied sites as small dark spots between the lines. Under such imaging circumstances they observed locally differently ordered structures between the dark lines. Those imaging conditions, however, did not give a conclusive distinction between the oxygen or carbon atom in the structure. Accordingly, the interpretation of the STM and LEED results should strongly depend on the information about the chemical composition provided by the AES data. However, one should bare in mind that this chemical information is averaged over the electron beam spot. Our nano-spot electron beam Auger analysis suggests that the intrinsic chemical composition of the surface contains variations on the scale of 10 nm. This in turn may give rise to the variations in the local structure, i.e. the appearance of (4×1), (6×1), three-fold arrangements, etc. Different concentrations of oxygen and carbon may be responsible for the presence of domain boundaries and the occurrence of defects on the surface that influence the local structure. A drastic example of that kind in our case is presented in Fig. 5.4d (which is accompanied by quite a lot of domain interceptions), where the local three-fold positions are observed. Obviously, though the calculated structure proposed by Koller et al. [157] may be energetically the most favourable one for the chemical composition they have considered, the existence of other local minima must be taken into account.

We also point out the possibility that some of the oxygen (and/or carbon) atoms are positioned in the subsurface region. The possibility of subsurface oxygen in the case of oxidised vanadium surface was addressed by the work function results of Valla et al. [155] who dosed oxygen on the clean and ordered V(100) surface and annealed the surface at different temperatures. The importance of the subsurface oxygen was also recognised by Todorova et al. [164] in the case of the oxide formation at late 4d transition metals. These calculations have shown that the energy balance in the system may favour the presence of subsurface oxygen for certain on-surface coverages.

## 6. Ag/V(100) measurements

In this chapter the Ag/V(100) experimental results are presented. First, the structural and growth properties of silver layers deposited on the reconstructed V(100)-(5×1) are investigated. The characterisation mainly includes STM measurements but also AES, ARUPS and LEED measurements. The central point of this structural study is to establish a well defined procedure for obtaining well ordered silver films of atomically uniform thickness. We will demonstrate that well annealed silver films deposited on V(100)-(5×1) have the same structure as Ag/V(100).

Next we use the HRARPES technique to characterise the s-p QW states for 1-8 ML thick Ag films. Their dispersions are measured. From data near the Brillouin zone center the s-p QWS effective masses are determined, while the data away from the Brillouin zone center are used to investigate the hybridisation effects with the substrate states. The photoemission lineshape analysis is used to determine the parameter of the hole-electron coupling strength ( $\beta$ ) for the s-p QW states, and the contribution of the hole-impurity scattering in the photoemission linewidth. Measurements of the temperature dependence of photoemission spectra in the Brillouin zone center enable straightforward determination of the hole-phonon coupling parameter ( $\lambda$ ) and the temperature dependent data away from the zone center are used to investigate the nature of the phonon spectrum of the system. HRARPES is also used to characterise and investigate properties of the d-band QW states. Due to the large increase of the number of d-derived QW states with the number of layers we concentrate on the 1-5 ML thickness range.

Finally, we present constant current room temperature STM measurements where the tunnelling parameters are adjusted to optimise the observation of standing wave features. Those data enable the quantitative investigation of electronic properties of the Ag/V(100) surface, around the Fermi level.

### 6.1. Structural characterisation

#### 6.1.1. Preparation of silver layers

The overlayer film is formed by silver deposition on the well ordered V(100)-(5×1) substrate kept at room temperature, where the silver deposition rate was adjusted to be approximately 0.2-1 ML·min<sup>-1</sup>. After deposition of a certain amount of silver the Auger spectrum reveals that besides the silver signal the vanadium, oxygen and carbon signals are still present. Interestingly, we find that the substrate related AES signals are still detected after the deposition of the quantity of up to  $\cong$  10 ML of silver. According to the in situ

## 6. Ag/V(100) MEASUREMENTS

measurements of Valla and Milun [165], who deposited silver on the clean and ordered V(100) surface we find that the increase of the silver signal intensity, i.e. an increase of the silver to vanadium intensity ratio, is less pronounced for the silver deposition on the V(100)-(5×1) surface. The deposition of silver on the clean V(100) substrate at RT or above does not produce a perfect layer by layer growth, but rather two completed silver layers with further growth of three-dimensional clusters (Stranski-Krastanov growth mode). Thus, we conclude that the deposition of silver on the reconstructed V(100)-(5×1) substrate at RT most probably leads to the three-dimensional growth of silver islands from the beginning (Volmer-Weber growth mode).

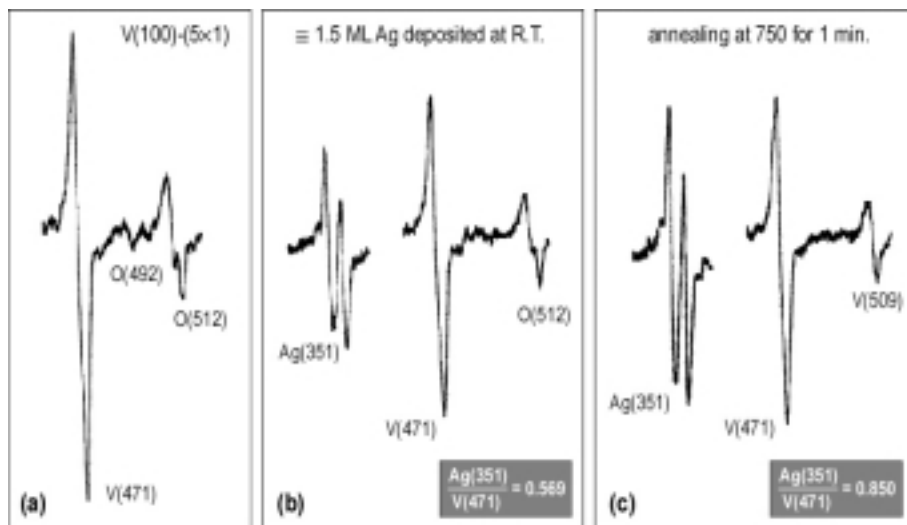


Fig. 6.1. The AES spectra corresponding to: (a) the substrate – V(100)-(5×1), (b) the deposition of approximately 1.5 ML of silver on this substrate at RT, and (c) the annealing of the same sample for 1 min to 750 K.

In Fig. 6.1 three AES spectra are shown that are related to three steps of the formation of a silver film. For the reconstructed V(100)-(5×1) surface that is precovered by 1.5 ML of Ag and annealed to 750 K, several drastic changes are observed in the AES spectra (Fig. 6.1c). First of all, the silver to vanadium intensity ratio is substantially increased and has a value of  $\cong 0.85$  (0.57 prior to the annealing), which is typical for the 1.5 ML thick ordered silver layer. Second, we find no oxygen traces in the Auger spectrum. This means that the oxygen has segregated out of the near surface region, most probably deep into the bulk. This result is consistent with the measurements of Valla et al. [155] who investigated interaction of oxygen and silver on the oxygen preadsorbed or clean V(100) surface. However, we point out that the difference compared to the situation described in Ref. [155] is that from the beginning we are dealing here with the strongly bound chemisorbed oxygen incorporated in the (5×1) reconstruction. This suggests a very strong character of the silver – oxygen interaction. We should mention that the same behaviour is observed for the carbon (not shown in the Auger spectra).

## 6. Ag/V(100) MEASUREMENTS

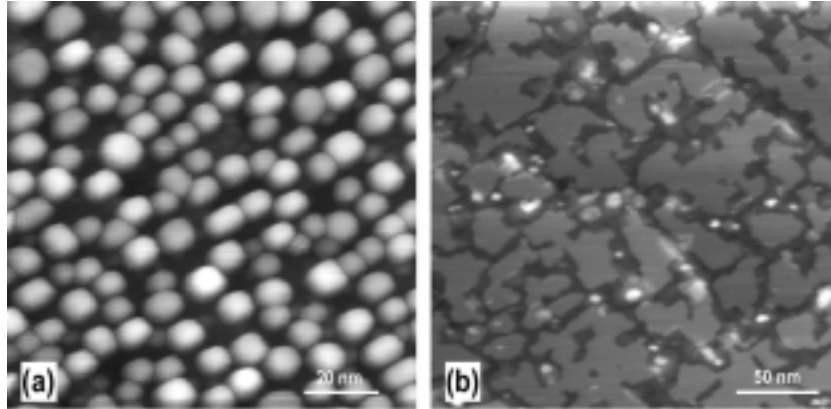


Fig. 6.2. (a) the STM image obtained after the RT deposition of approximately 1.5 ML of silver on the V(100)-(5 $\times$ 1) substrate.  $U_B = 840$  mV,  $I_T = 0.1$  nA. (b) The STM image of the same surface after a flash to 750 K.  $U_B = -56$  mV,  $I_T = 0.1$  nA.

A straightforward confirmation of the Volmer-Weber silver growth on the V(100)-(5 $\times$ 1) reconstructed surface comes from the STM experiment. Fig. 6.2 shows the topology of the surface after the RT deposition of approximately 1.5 ML of silver (can be correlated to the AES spectrum in Fig. 6.1b), and after the annealing of such film (can be correlated to the AES spectrum in Fig. 6.1c). Our investigations show that an annealing or flashing of the sample is always necessary to produce an ordered and smooth silver film. The flashing temperatures were chosen from the thermal desorption (TDS) results as well as from the in situ AES measurements for the silver on the clean V(100) surface [165].

### 6.1.2. Photoemission characterisation

The steps of preparation of smooth and well ordered Ag films described in the previous section are reproduced for ARUPS measurements. Fig 6.3. shows the results of the photoemission experiment. The bottom spectrum is taken from the V(100)-(5 $\times$ 1) substrate. Room temperature silver deposition strongly modifies the region previously dominated by the O 2sp valence band and reduces the intensity at the Fermi level. Flashing to 750-800 K or 900 K leads to the formation and ordering of 2 or 1 ML of silver, respectively. The obtained spectra exhibit the same structure as the ARUPS spectra of ordered silver layers grown on the clean V(100) surface [112]. The key evidence that the silver layers are well ordered is the appearance of the s-p and the d-quantum well states. Not only their existence, but also the well developed intensities of the photoemission peaks indicate that the smoothness of the silver layer is as good as for silver layers grown on the clean and well ordered V(100) substrate.

We summarise that for the obtaining 2 ML thick ordered silver layer a flash to  $\cong 700$ -800 K is applied and for 1 ML thick film a flash to  $\cong 900$  K is applied. Naturally, for the specified film thicknesses the deposited silver quantity has to be larger than 2 or 1 ML,

respectively. Depending on the exact flashing or annealing temperatures the rest of the silver either desorbs from the surface or clusters in such way that does not contribute significantly to the AES, ARUPS or LEED intensities. Indeed, such clusters that are distributed over the small surface area but contain a lot of material are sometimes found in large-scale STM images. Higher silver thicknesses are obtained by the subsequent room temperature silver deposition on well ordered 2 ML thick silver layer.

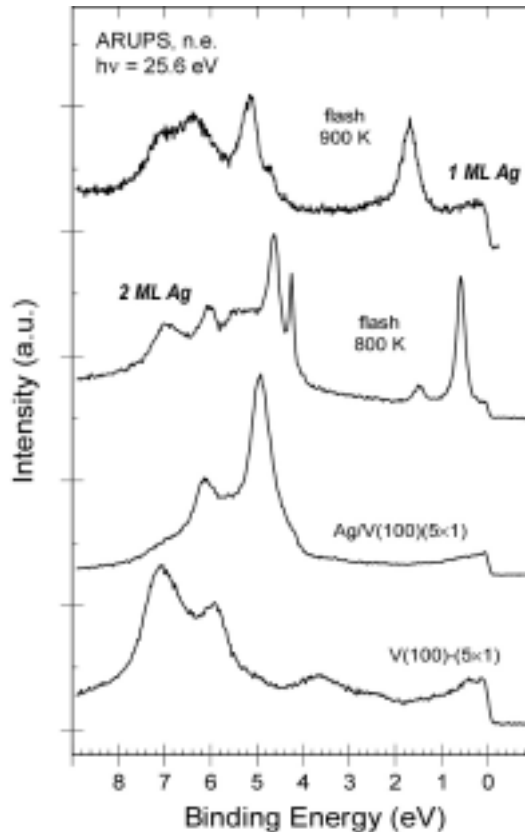


Fig. 6.3. Photoemission spectra characterising the silver film formation on the V(100)-(5×1) substrate. From the bottom to the top: the substrate, Ag deposited at RT on that surface, flashed to 800 K, or flashed to 900 K, respectively.

### 6.1.3. LEED measurements

To investigate the long range order of the overlayer films a LEED experiment was performed. As expected, the LEED pattern of films prepared in the described way shows the (1×1) symmetry. This is in line with the (1×1) symmetry of the unreconstructed vanadium surface. The same LEED images were obtained for 1 as well as for 2 ML thick films. Comparison of the distance between the diffraction spots from 1 and 2 ML thick silver layer with the distance between the integral points of the V(100)-(5×1) diffraction pattern suggests that, within the limit of accuracy of our measurement, the surface lattice constant of the silver layer is identical to the vanadium (100) plane lattice constant. The same result was obtained for the silver grown on the clean V(100) surface [165,166].

## 6. Ag/V(100) MEASUREMENTS

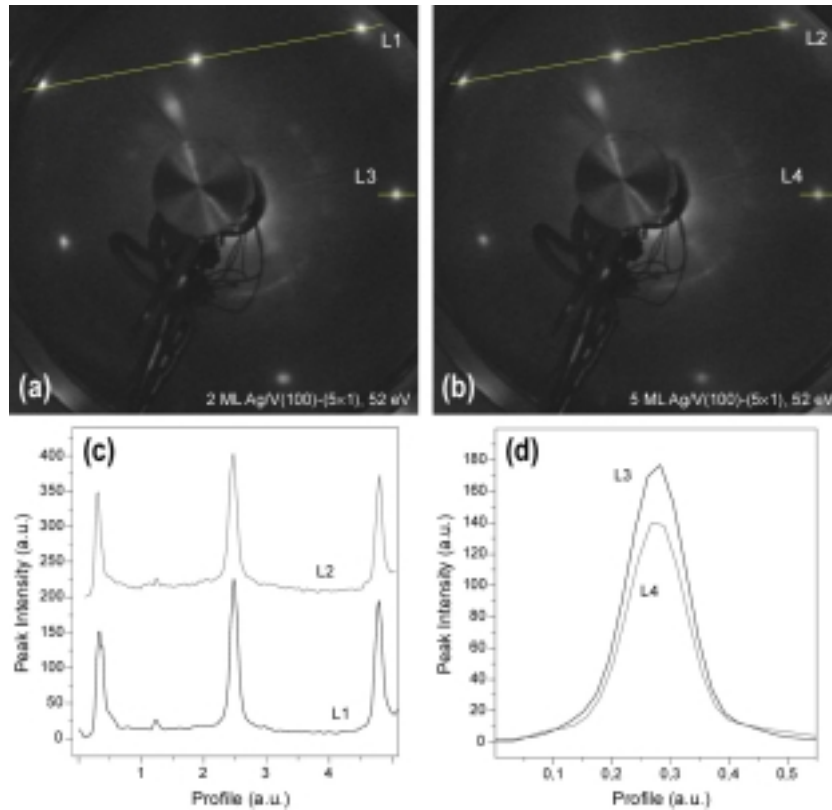


Fig. 6.4. LEED patterns obtained from a 2 ML (a) and 5 ML (b) thick silver layer. (c) and (d) are the profile scans over the lines as indicated in the LEED images.

With growing thickness up to 5 ML the quality of the LEED pattern deteriorates somewhat. For the 5 ML thick film, at the same electron energy, there is a decrease in the spot intensity of about 20 % compared to the 2 ML film. At the same time this is accompanied with a small increase of the background intensity, whereas the spot width does not change up to 5 ML. This is illustrated in Fig. 6.4 where along with LEED images profile scans along the indicated lines over the spots are given. Supposing the simplest linear dependence between the LEED spot intensity and the relative order in the system one can conclude that, after the deposition of additional 3 ML of silver, the number of defects has grown roughly by 20 % compared to the 2 ML film. For higher silver coverages the background intensity is increased and the width of diffraction spots starts to increase which eventually results in rather poor LEED pattern for the 10 ML thick silver film.

### 6.1.4. STM characterisation

In the regime where silver only partly covers the reconstructed V(100)-(5x1) surface some important information can be extracted from the STM images. In the large scale images where the atomic resolution is not achieved the shape as well as the height of individual silver islands can be studied.

## 6. Ag/V(100) MEASUREMENTS

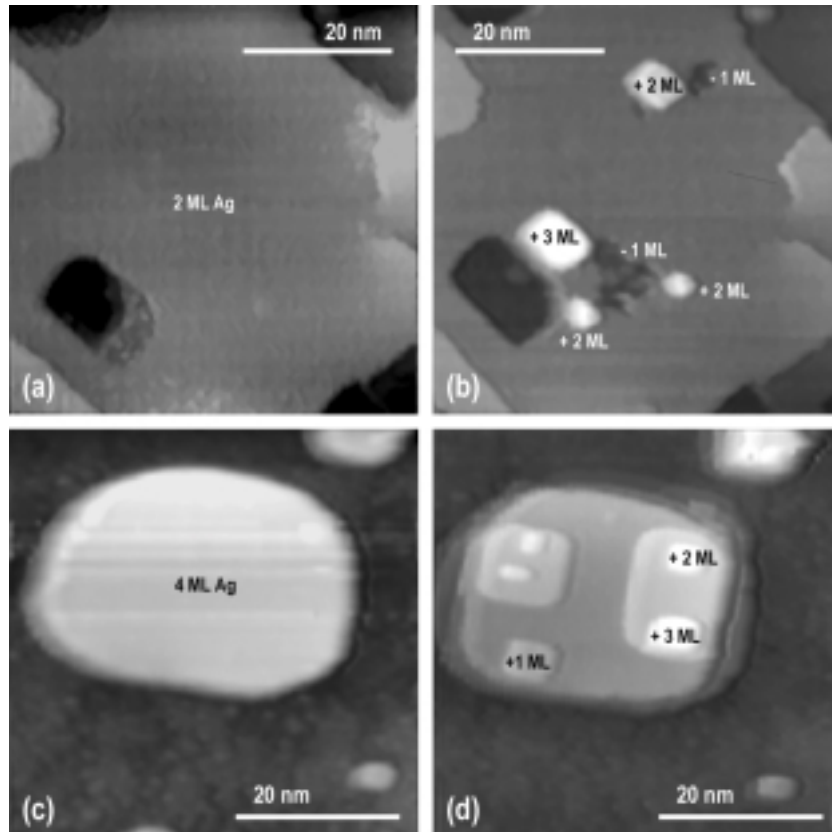


Fig. 6.5. The stability of the silver layer – before and after performing few scans. (a) and (b)  $U_B = 0.45$  V,  $I_T = 0.8$  nA, (c) and (d)  $U_B = 0.4$  V,  $I_T = 0.9$  nA.

The experiments have shown that the imaging of islands is a quite delicate procedure. During the scan an island is sometimes shifted in position or damaged in a way that holes are created in islands along with the appearance of new terraces. Fig. 6.5 illustrates two examples how the scanning process can influence the silver layers. In both examples, the areas were scanned tens of times using different tunnelling parameters. Also, the contrast around the silver island is altered by the scanning process with respect to the scanning direction, which may vary depending on the tunnelling parameters used. These experiments indicate that one has to find out optimal tunnelling parameters in order not to perturb the silver overlayers. For reliable determination of the silver island height it is best to use small tunnelling currents (below 0.5 nA) and bias voltages in the range 0.2-0.5 V.

For a submonolayer silver coverage no preferential nucleation regions are found, i.e. some islands are formed in the middle of the terraces and some are aligned by the vanadium step edges. In Fig. 6.6 two situations are shown. The dominant island height is 1 ML in (a) and 2 ML in (b), which was obtained through different annealing treatments. The distinction between the silver and vanadium is quite obvious. The edges of silver islands do not follow the reconstruction of the vanadium surface which indicates the change in the structure of the underlying vanadium (removal of the reconstruction below the silver islands). A different

## 6. Ag/V(100) MEASUREMENTS

contrast appearance of the two images in Fig. 6.6 is a result of different image filtering procedures.

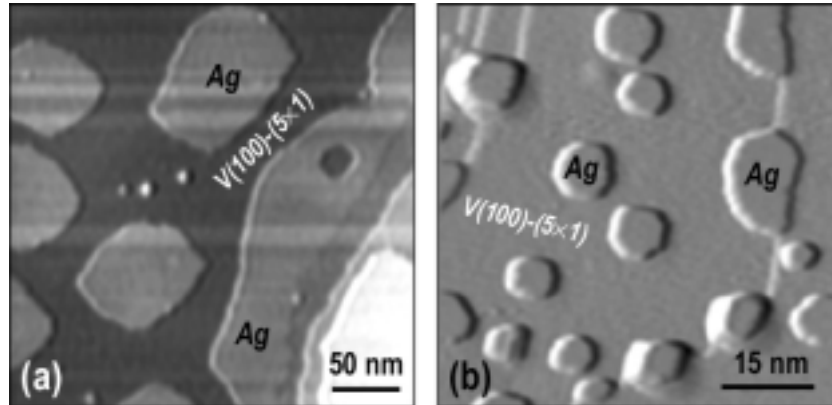


Fig. 6.6. STM images obtained after deposition of a submonolayer silver quantity and annealing to different temperatures. (a)  $U_B = 0.2$  V,  $I_T = 0.5$  nA, (b)  $U_B = 0.4$  V,  $I_T = 0.5$  nA.

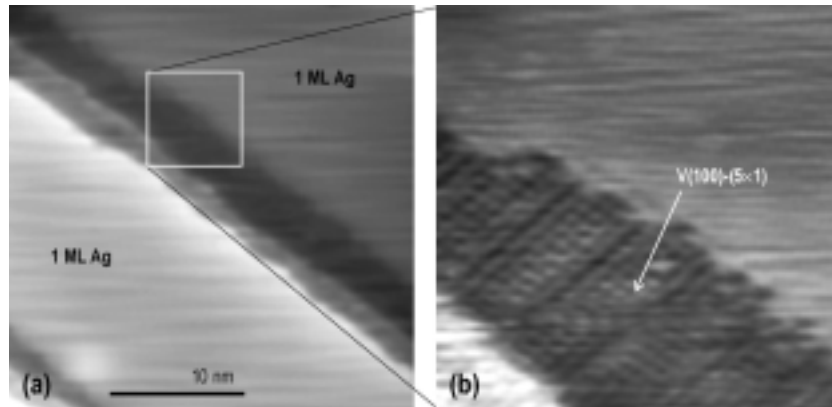


Fig. 6.7. (a) STM image of 1 ML Ag/V(100)-(5 $\times$ 1).  $U_B = 0.05$  eV,  $I_T = 1.6$  nA (b) Zoom into the region of the uncovered vanadium part.  $U_B = 15$  mV,  $I_T = 2.8$  nA

For ordered silver layers and higher silver coverages one can always find statistically small parts at the surface still uncovered with silver. We have established that those uncovered parts always exhibit the (5 $\times$ 1) structure. For the illustration in Fig. 6.7 an STM image of approximately 1 ML Ag/V(100)-(5 $\times$ 1) is shown. The uncovered parts are found here at the edges of terraces. Zooming into this region reveals the (5 $\times$ 1) reconstruction that is clearly seen in the STM image. With increasing coverage such areas are found in the small holes (up to  $\sim 20$  nm in diameter) in the silver film. Statistical insignificance of such regions is proofed from STM, LEED and AES results.

The height of the 1 ML silver island is higher than the vanadium step height when measured with STM, which suggests a tetragonal silver structure. The single silver layer height we measure to be  $1.8 \pm 0.2$  Å (Fig. 6.8), which is  $\cong 0.3$  Å higher compared to the measured vanadium step height  $1.5 \pm 0.1$  Å. This result is consistent with the simple hard

## 6. Ag/V(100) MEASUREMENTS

sphere picture [5] where the interlayer separation between the topmost vanadium and the first silver layer is 1.71 Å, which is higher than the unrelaxed vanadium interlayer distance (1.51 Å), because of the larger diameter of silver atom. Within this model further silver layer separations are 1.94 Å. From STM measurements we find that the height of every next silver layer on top of the 1 ML contributes with  $2.0 \pm 0.2$  Å. One should, however, be careful when taking an STM result as a reference for the actual interlayer distance.

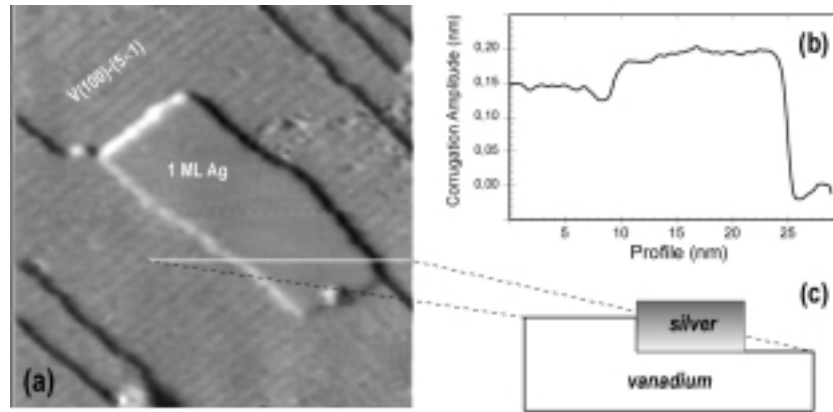


Fig. 6.8. (a) STM image of the 1 ML thick silver island.  $U_B = 0.45$  V,  $I_T = 1.2$  nA. (b) Profile scan over the 1 ML silver island as indicated by the white line. (c) Schematic of the vanadium surface and silver island along the white line in (a).

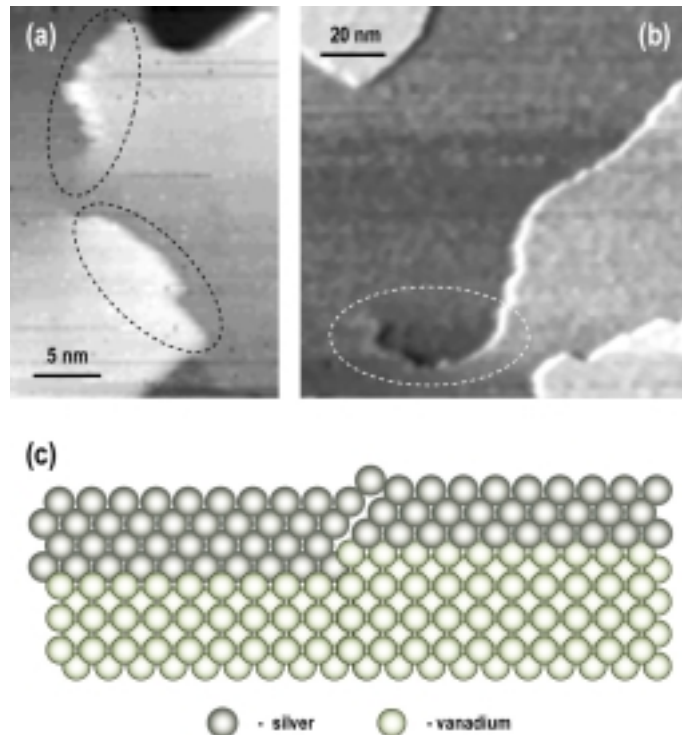


Fig. 6.9. (a) and (b): Examples of Ag/V(100)-(5x1) line dislocations indicated with ellipses. (c) Schematic overview of a dislocation occurrence in this case induced by a mismatch between the tetragonal silver film height and the vanadium step height.

## 6. Ag/V(100) MEASUREMENTS

For thicknesses higher than 1 ML STM images show line defects that point to the stress present in the tetragonal structure of silver layers (Fig. 6.9). We believe that, among other reasons, the mismatch between the vanadium substrate and the deposited silver step heights might be the reason for such observations (Fig 6.9c). As it was measured, the ordered silver film covers almost the whole area of the substrate. This means that eventually, for more than 1 ML Ag it also has to cover most of the vanadium steps. In the STM images we have also observed a somewhat milder manifestation of a stress in the system through the small ( $\leq 0.2 \text{ \AA}$ ) variations in the height of the silver film without the existence of line-like dislocations.

To obtain atomically resolved images from the silver film the stable experimental conditions (the total level of noise, noise frequencies, thermal drift, ...) are very crucial. We could achieve atomic resolution for a relatively narrow range of tunnelling parameters, i.e. for tunnelling currents higher than 3 nA and absolute bias voltages in the region 5-30 meV.

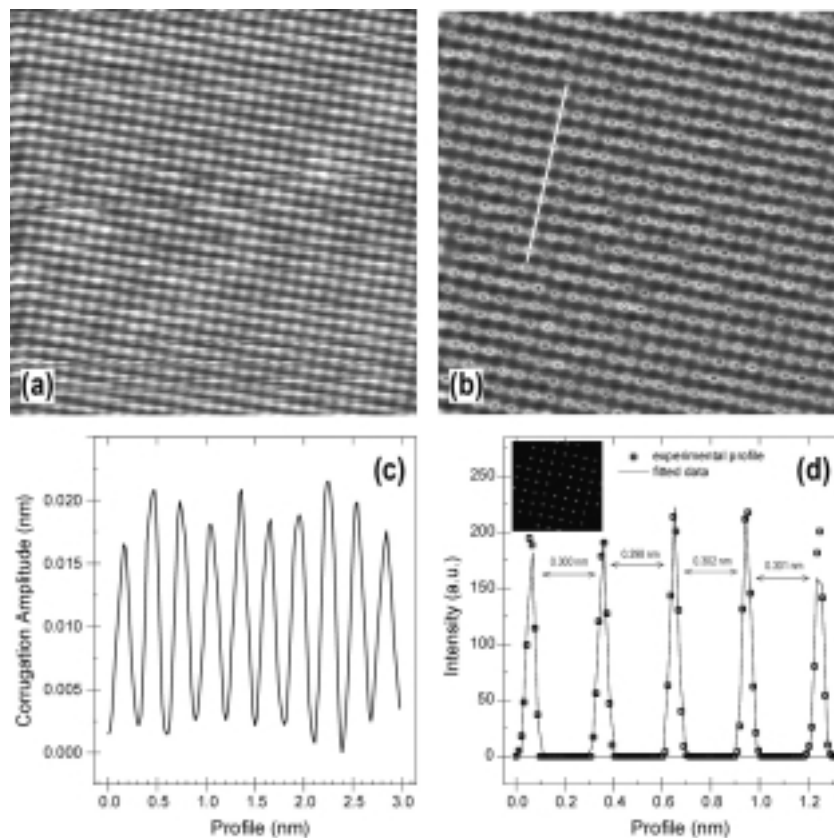


Fig. 6.10. (a) Unprocessed atomically resolved image from a 2 ML Ag/V(100)-(5 $\times$ 1) surface. Image size: 7.8 $\times$ 7.8 nm<sup>2</sup>.  $U_B = 25 \text{ mV}$ ,  $I_T = 19 \text{ nA}$  (b) Drift corrected and Fourier filtered image. (c) Profile scan along the white line in (b). Circles mark the atomic positions. (d) The Ag-Ag interatomic distance is obtained from pair-correlation analysis (see the inset).

In Fig 6.10a an unprocessed STM image from 2 ML Ag/V(100) is shown. In Fig. 6.10b

the experimental drift is corrected and the image slightly Fourier filtered. A profile scan along the white line in Fig. 6.10b is shown in Fig. 6.10c. Note that the typical atomic corrugation amplitude is about 0.2 Å. To determine the interatomic distance for this square unit cell a pair-correlation for atomic positions is calculated. In Fig. 6.10.d a profile scan over the angular correlation image (shown in the inset) is given. The Ag-Ag in-plane interatomic distance measured from many pair correlation images is  $3.0 \pm 0.1$  Å. This value is measured for 1-5 ML thick silver layers, while for higher silver coverages due to the insufficient number of high quality images we were not able to perform such statistical analysis.

## 6.2. HRARUPS measurements

In this section high resolution ultraviolet photoelectron spectroscopy is used to investigate in great detail the electronic structure of the Ag/V(100) quantum well system. In Fig. 6.11. two energy distribution curve photoemission spectra for 1 and 2 ML Ag/V(100) are shown. In a relatively wide range of binding energies two regions are shaded that denote the hybridisation gaps within which the s-p and d- QW states are formed. The bandstructure and hybridisation band gaps for silver on vanadium (100) are also shown and discussed along with Fig. 4.5 (see section 4.1.1).

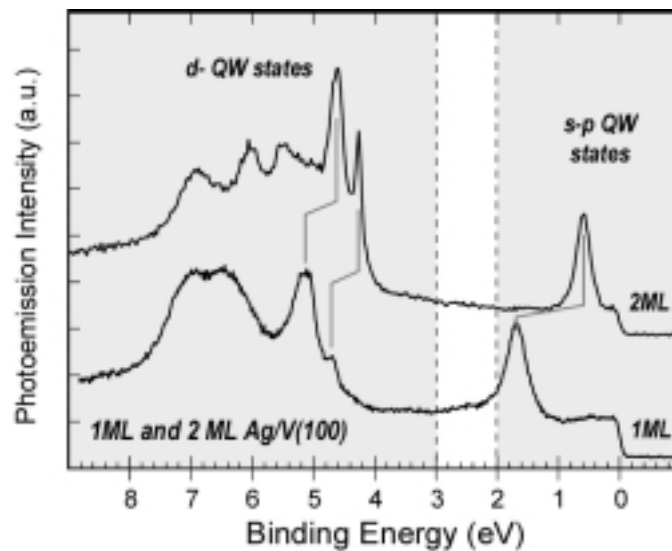


Fig. 6.11. Normal emission photoelectron spectra (recorded at a photon energy of 24 eV) of 1 ML and 2 ML Ag films on V(100). The shown energy window includes the s-p and the d-hybridisation band gap regions. The QW states of s-p and d-symmetry are formed within these gaps in silver overlayer film.

### 6.2.1. s-p QW states: angle resolved measurements

To study dispersions of QW states we used a SES-200 analyser with multichannel 2-D detector (see section 2.2.5 and chapter 3). For comparison in Fig 6.12 four such spectra for 1, 2, 4 and 5 ML Ag/V(100) are aligned, as indicated in the figure. The polar angle goes along

## 6. Ag/V(100) MEASUREMENTS

the x-axis, while the energy is along the y-axis. Spectra were obtained approximately  $\pm 6^\circ$  (analyser acceptance angle) around the Brillouin zone center and up to 2.5 eV in binding energy. A thick dashed line indicates the position of the Fermi level. Visual inspection of such spectra immediately provides qualitative information about the electronic states. For instance, in these spectra one notes that the curvature of recorded s-p QW states dispersions varies from state to state. It is easy to obtain EDC spectra from 2-D intensity maps by performing a slice cut around the certain angle, i.e.  $k_{||}$ . In Fig 6.13. for 5 ML Ag/V(100) six slice cuts are shown. They were taken along thin dashed lines drawn in Fig. 6.12.

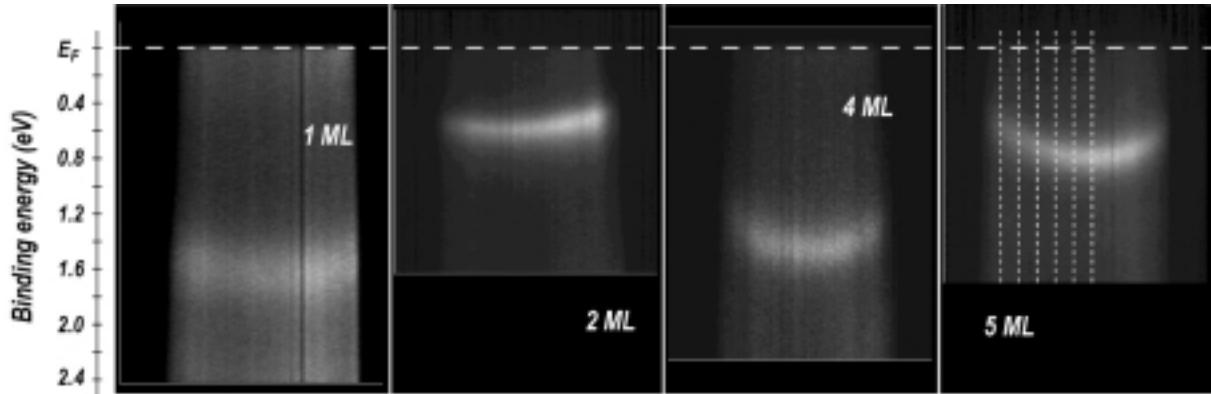


Fig. 6.12. Experimental photoemission intensity gray-scale maps for 1, 2, 4 and 5 ML Ag/V(100) as a function of photoelectron polar emission angle and binding energy. Spectra were collected directly from the 2-D detector of the SES-200 hemispherical analyser. The arced intensities correspond to the emission from the QW states. A thick dashed line indicates the position of the Fermi level, while thin dashed lines indicate polar angles for 5 ML Ag/V(100) along which slice cuts were taken (see Fig. 6.13).

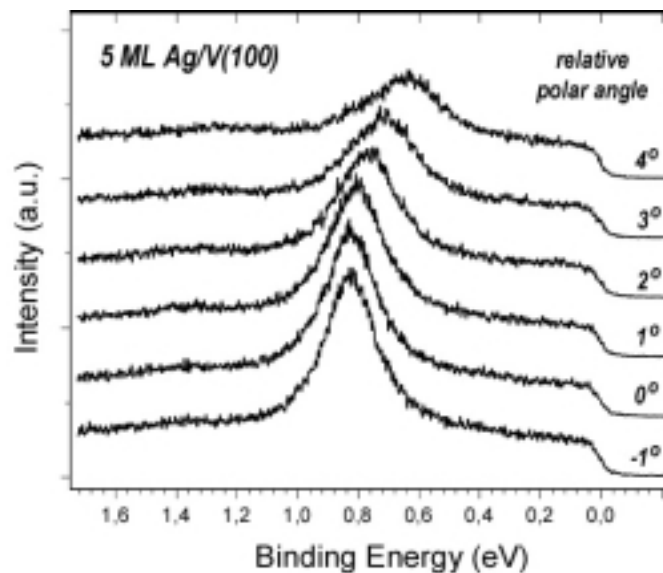


Fig. 6.13. 5 ML Ag/V(100): The photoemission spectra obtained at different polar angles (indicated with thin dashed lines in Fig. 6.12) by slice cuts from 2-D grey-scale intensity maps.

## 6. Ag/V(100) MEASUREMENTS

Dispersions of s-p QW states for 1-8 ML thick Ag layers have been characterised systematically  $\pm 0.25 \text{ \AA}^{-1}$  around the Brillouin zone center, which corresponds to the k-space region accessible from a single 2-D intensity map. We have also investigated the s-p QW states dispersions behaviour in a more extended region within the Brillouin zone. Fig. 6.14 shows two combined 2-D intensity maps for 2 ML Ag/V(100). Note that the QW state dispersion changes its curvature which is accompanied with the increase of the intensity at the Fermi level (indicated with dashed line). A closer inspection of the 2-D intensity map reveals that the increase of the photoemission intensity at the Fermi level is due to the dispersion of a state that enters the Fermi level at about  $0.22 \text{ \AA}^{-1}$ . Fig. 6.14 also shows several EDC spectra obtained at noted  $k_{\parallel}$ . From a denser set of data points the dispersion curve for this QW state is obtained (shown in the figure inset). At larger values of  $k_{\parallel}$  the actual peak position is not so easy to determine since the photoemission peak broadens and gains some asymmetry, whereas the peak position was determined from the Lorentzian fit. Note that the data points agree nicely with the parabolic fit up to  $\cong 0.22 \text{ \AA}^{-1}$ , whereas after this point the dispersion curve starts to slow down, and eventually at  $\cong 0.35 \text{ \AA}^{-1}$  it changes sign. A more complicated situation is shown in Fig. 6.15 – the silver film thickness was 5.5 ML and in the 2-D photoemission intensity spectra dispersion curves of s-p QW states corresponding to 5 and 6 ML were recorded. Both peaks show similar behaviour as in the previously described example: The dispersion changes for higher  $k_{\parallel}$ , which is accompanied by the increase of the photoemission intensity at the Fermi level. The dispersion curve of QWS corresponding to 6 ML (state closer to the Fermi level) changes sign at  $\cong 0.35 \text{ \AA}^{-1}$ , whereas the state characteristic for 5 ML thickness seems to change sign at about  $0.45 \text{ \AA}^{-1}$ .

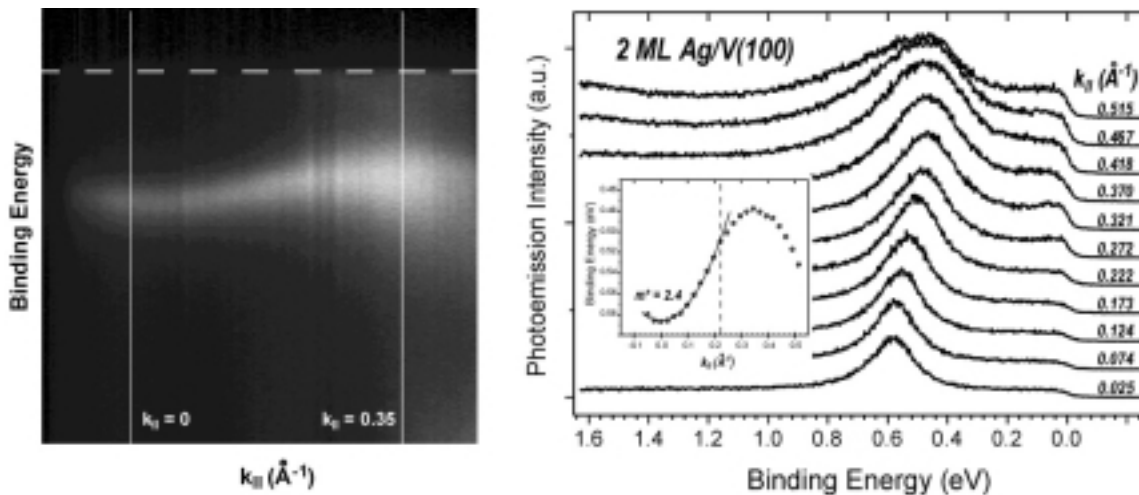


Fig. 6.14. 2 ML Ag/V(100): Two combined photoemission 2-D intensity gray-scale maps obtained in a successive measurement where only the polar angle has been changed. The EDC spectra obtained at different  $k_{\parallel}$  values (or equivalently polar angles) are also shown. The dispersion curve obtained from a denser set of spectra is shown in the inset.

## 6. Ag/V(100) MEASUREMENTS

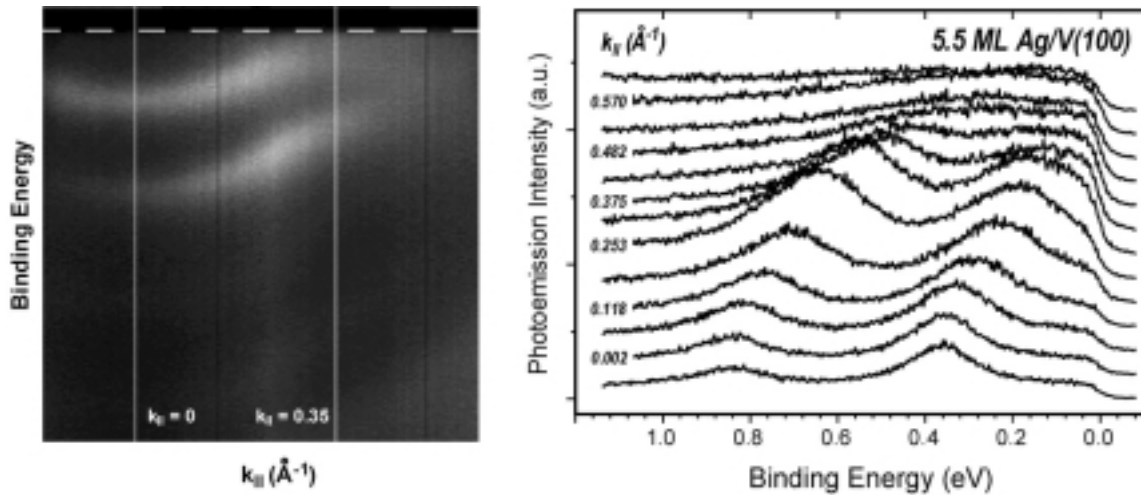


Fig. 6.15. 5.5 ML Ag/V(100): Two combined photoemission 2-D intensity maps obtained in a successive measurement. The s-p QW state dispersion curves characteristic for 5 and 6 ML thick silver film are visible in the intensity map. The EDC spectra obtained at different  $k_{||}$  values are also shown.

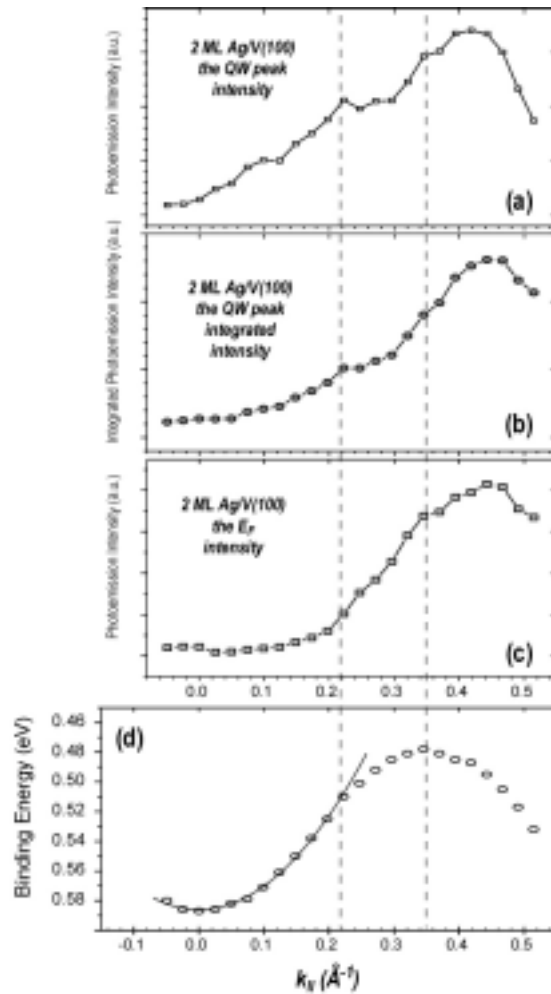


Fig. 6.16. 2 ML Ag/V(100). (a) Photoemission intensity of the s-p QW state peak. (b) Integrated photoemission intensity of the s-p QW state peak. (c) Photoemission intensity at Fermi level + 0.05 eV. (d) Dispersion curve. For details about the vertical dashed lines see text.

## 6. Ag/V(100) MEASUREMENTS

For 2 ML Ag/V(100) we have analysed the peak photoemission intensity and the photoemission intensity at the Fermi level. We note that for this purpose each ECD curve is obtained from a slice cut of the same width which allows the photoemission peak intensity analysis. The results are shown in Fig. 6.16. In (a) the QW peak photoemission intensity and in (b) the integrated QW peak photoemission intensity vs.  $k_{||}$  are plotted. In (c) the photoemission intensity is measured at the Fermi level + 0.05 eV. In (d) the QW state dispersion curve is aligned for comparison. Two characteristic points ( $0.22 \text{ \AA}^{-1}$  and  $0.35 \text{ \AA}^{-1}$ ) related to the QW state dispersion are indicated with vertical dashed lines.

For all studied s-p QW states in the region of approximately  $\pm 0.25 \text{ \AA}^{-1}$  around the Brillouin zone center we find that the photoemission peak binding energy (measured and fitted from slice cut spectra) versus  $k_{||}$  shows a parabolic behaviour. The curvature of a parabola is a direct measure of the electron effective mass in the nearly free electron model. The parabolic dispersion curves obtained from the 2-D intensity maps for s-p QW states are shown in Fig. 6.17. The change of the polar angle in the experiment follows approximately the  $\Gamma M$  direction in the surface Brillouin zone. Table 6.1 summarises binding energy and effective mass of each s-p QW state characterised in this study.

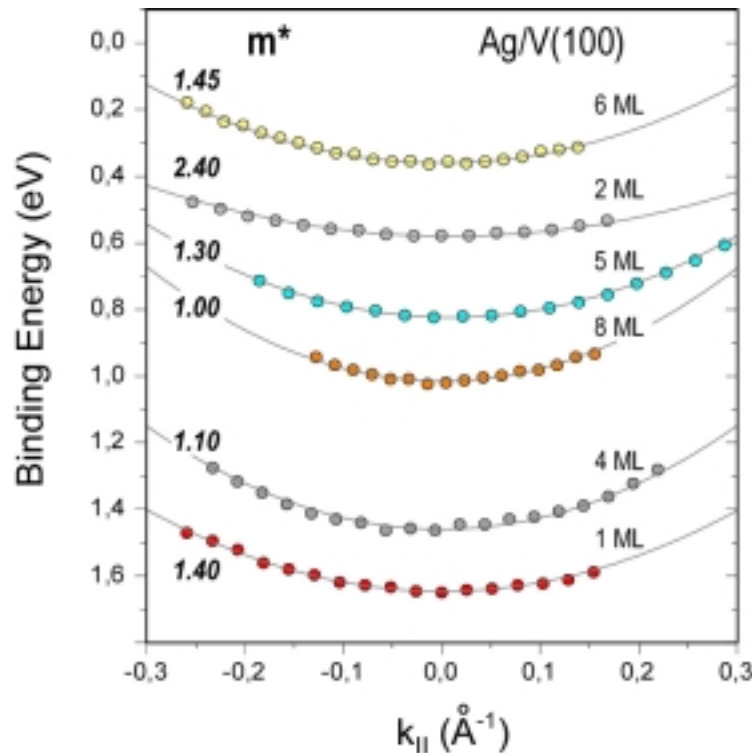


Fig. 6.17. Dispersions of the Ag/V(100) s-p QW states. Experimental points are extracted from the photoemission spectra. Nearly free-electron parabola fits of the experimental points give the electron effective masses noted for each state.

## 6. Ag/V(100) MEASUREMENTS

Film thickness (ML)	Binding energy (eV) at 90 K	Effective mass $m^*$ at 90 K
1	$1.65 \pm 0.01$	$1.40 \pm 0.05$
2	$0.58 \pm 0.01$	$2.40 \pm 0.05$
3	no occupied state	–
4	$1.43 \pm 0.01$	$1.10 \pm 0.05$
5	$0.82 \pm 0.01$	$1.30 \pm 0.05$
6	$0.36 \pm 0.01$	$1.45 \pm 0.05$
7	$1.44 \pm 0.01$	–
8	$1.02 \pm 0.01$	$1.00 \pm 0.05$

Table. 6.1. Ag/V(100) s-p QWS binding energies and effective masses measured at  $T = 90$  K in this HRARPES characterisation.

### 6.2.2. s-p QWS lineshape analysis

As it has been shown in section 2.2.6, the lineshape of the peak from the two-dimensional electronic state (QW state in this case) is completely determined by the photohole self-energy  $\Sigma(\mathbf{k}, \omega)$  [46]. The experimental spectra are most accurately fitted with the Fermi liquid line shape (see Eq. (2.20) and (2.24)) that reflects the QW state Fermi liquid nature. The Fermi liquid formalism can be extended to the region a few eV away from the Fermi level and to temperatures above 0 K [47]. At fixed temperature the energy independent term  $\Gamma_0$  contains the superposition of the hole-impurity and the hole-phonon scattering contributions. For the illustration in Fig. 6.18 we compare the Fermi liquid, Lorentzian and Gaussian fits for the 2 ML Ag/V(100) s-p QW state. Note that the Fermi liquid shape provides the best fit.

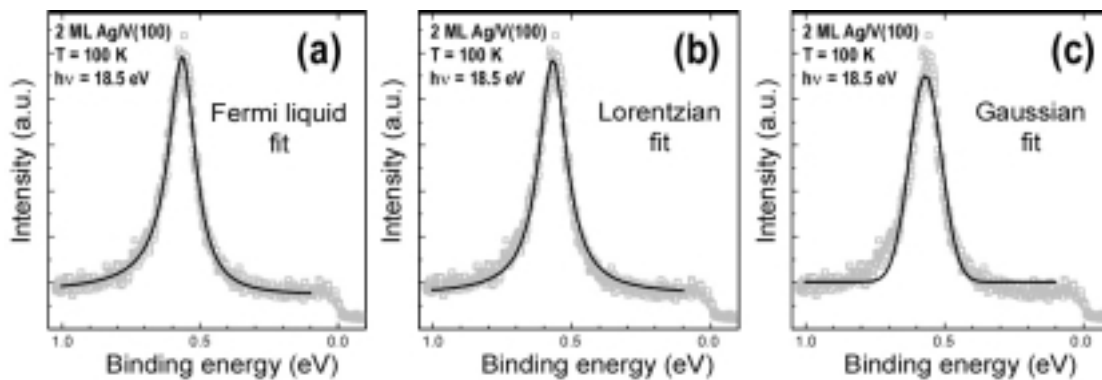


Fig. 6.18. HRARPES 2 ML Ag/V(100),  $T = 100$  K. Results of different fitting procedures: (a) Fermi liquid, (b) Lorentzian, (c) Gaussian.

## 6. Ag/V(100) MEASUREMENTS

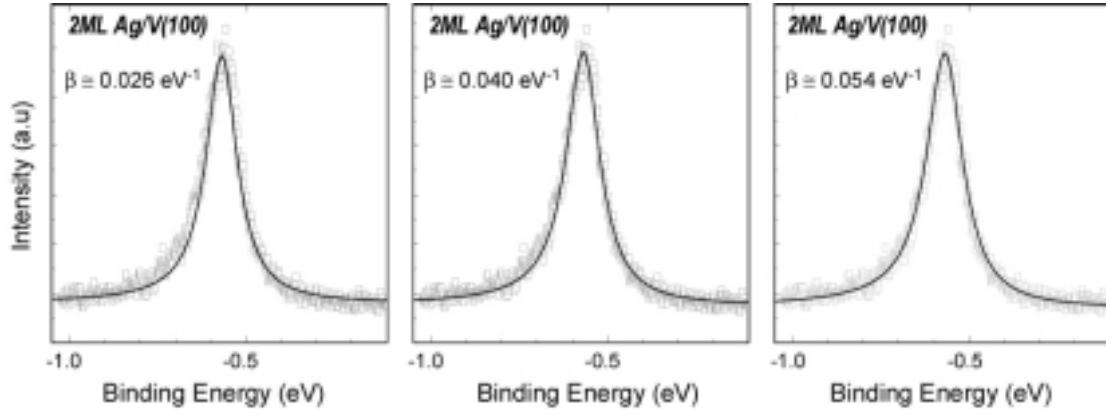


Fig. 6.19. 2 ML Ag/V(100), Fermi liquid fit with various hole-electron coupling parameters.  $\beta = 0.026, 0.04$  and  $0.054 \text{ eV}^{-1}$ , as indicated in the figure. The energy independent term  $\Gamma_0$  is in each case 90 mV.

In the Fermi liquid lineshape the whole hole-electron scattering contribution is contained in the quadratic term of the self-energy (Eq. (2.24)). For Ag/V(100) we note, however, that the fits are moderately sensitive to the relative values of  $\Gamma_0$  and  $\beta$ , making the separation of the hole-electron coupling less accurate. This we demonstrate in Fig. 6.19 for 2 ML Ag/V(100) by varying the hole-electron coupling strength  $\beta$  and keeping the  $\Gamma_0$  term constant (90 meV). However, a systematic analysis gives  $\beta \cong 0.04 \text{ eV}^{-1}$  for 1 and 2 ML silver film, and  $\beta \cong 0.045 \text{ eV}^{-1}$  for 5 ML silver QW state. This is significantly larger than in the bulk-like silver film [128]. These fits lead to values for the constant term  $\Gamma_0$  of approximately 150 meV for the 1 ML QW state, 80-100 meV for the 2 ML QW state and 150-180 meV for the 5 ML QW state. For the 2 ML thick film our calculations give an hole-phonon coupling term of  $\cong 40 \text{ meV}$  for the temperature and the binding energy (see discussion in chapter 7). This leaves 40-60 meV for scattering on defects and for a contribution from the finite transmission into the substrate. We believe that in the present case, the interaction of electrons with impurities plays the dominant role.

### 6.2.3. *s-p* QWS temperature dependence

Temperature induced changes in the photoemission spectra are shown in Fig. 6.20 for 2 ML Ag/V(100) for three different temperatures. The left hand side panel shows 2-D intensity spectra obtained at indicated temperatures. For the reference, the binding energy of this QW state in the Brillouin zone center at 100 K (0.6 eV) is indicated by a thin black line. From each 2-D map we obtain three EDC spectra shown in the middle and the right hand side panels. The middle panel corresponds to slice cuts at the surface Brillouin zone center ( $k_{||} = 0$ ). The right hand side panel shows EDC spectra obtained at approximately  $0.1$  and  $0.2 \text{ \AA}^{-1}$  ( $k_{||}^1$  and  $k_{||}^2$ , respectively).

## 6. Ag/V(100) MEASUREMENTS

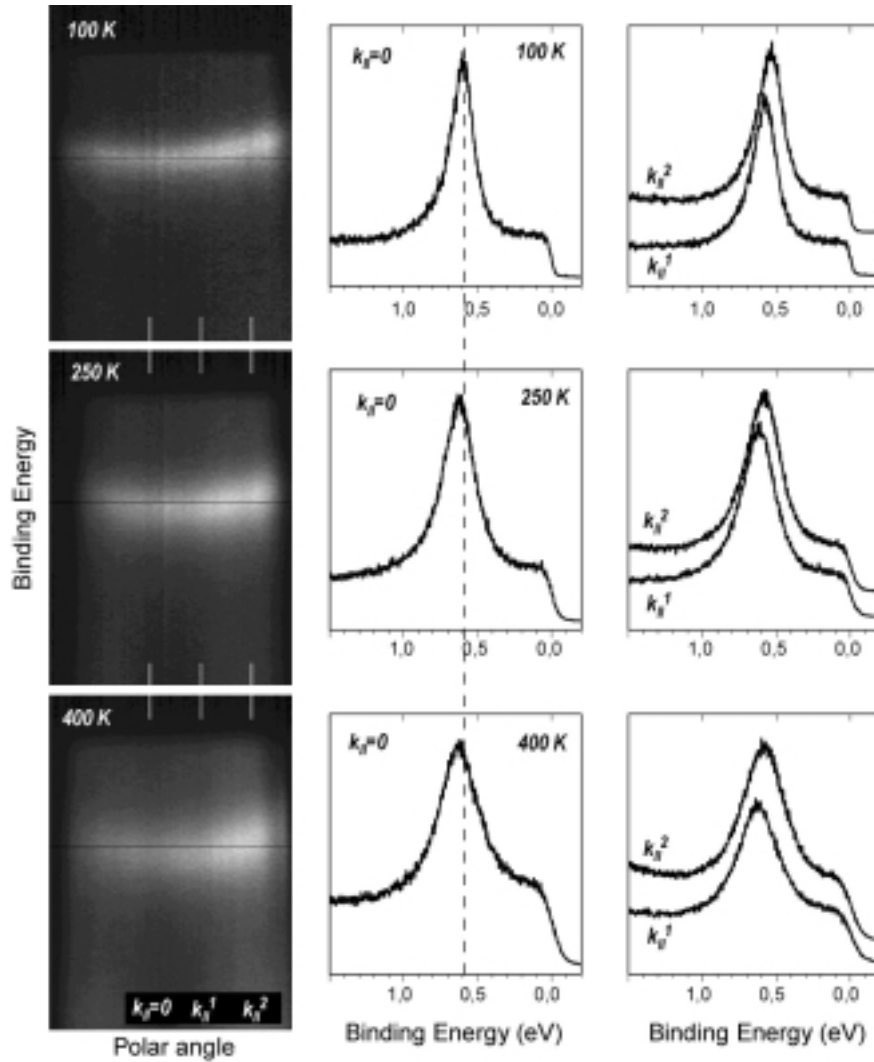


Fig. 6.20. The s-p QW state temperature induced changes in the photoemission spectra for 2 ML Ag/V(100). Left panel shows 2-D grey-scale intensity maps recorded at 100, 250 and 400 K. The thin black line denotes the photoemission peak position at the bottom of the s-p QW state dispersion for 100 K. Along the short thin white lines EDC cuts are taken and shown in the middle and right panel. For details see the text.

Temperature induced changes at  $k_{||} = 0$  are also shown in Fig. 6.21, 6.22 and 6.23 for the 1, 2 and 5 ML s-p QWS, respectively. In each figure in (a) few normal emission HRARUPS spectra obtained at different temperatures are shown. The photoemission peak width and the binding energy vs. temperature dependencies are additionally plotted in (b) and (c), respectively. Fig. 6.24 shows temperature induced changes of effective masses for 1, 2 and 5 ML Ag/V(100). Table 6.2 summarises the obtained results. For all studied thicknesses with increasing temperature we observe:

1. increase of the spectral width,
2. reduction of the spectral intensity,
3. binding energy shift towards higher binding energies,
4. decrease of the electron effective mass.

## 6. Ag/V(100) MEASUREMENTS

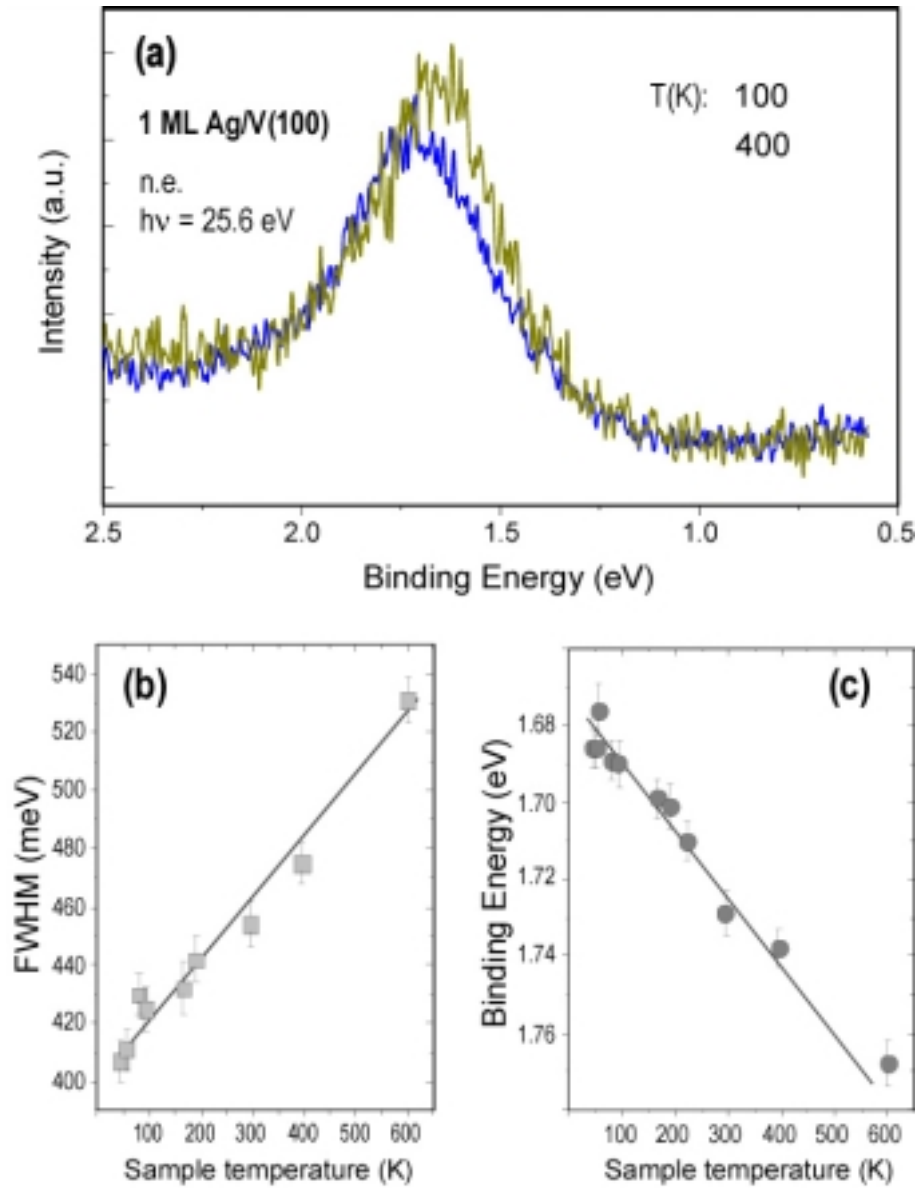


Fig. 6.21. (a) Normal emission photoemission spectra from the QW state corresponding to 1 ML of Ag on V(100) recorded at several different substrate temperatures. These data are extracted from a series of two-dimensional detector output maps similar to that shown in Fig. 6.20. (b) Photoemission peak width as a function of temperature deduced from a more extensive set of similar spectra. (c) Photoemission peak energy as a function of temperature deduced from a more extensive set of similar spectra.

6. Ag/V(100) MEASUREMENTS

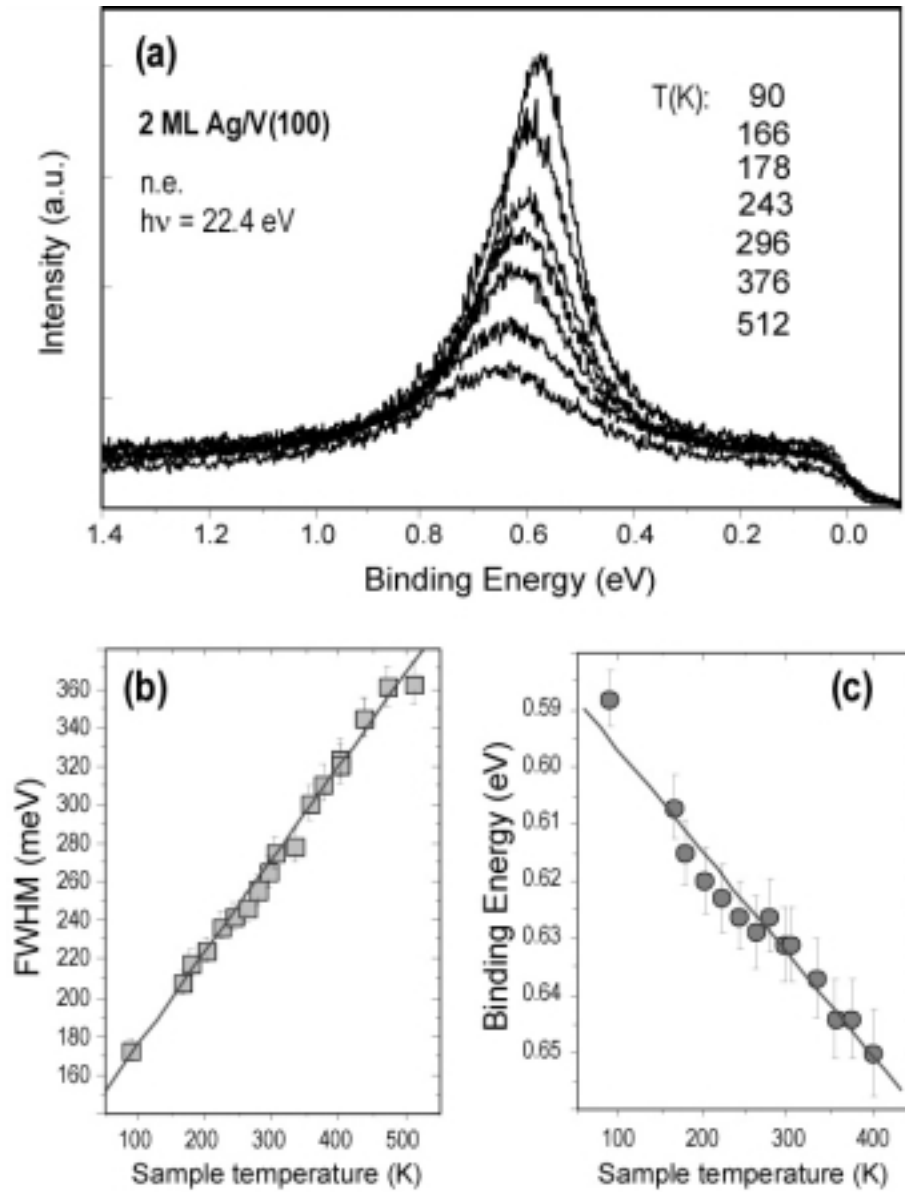


Fig. 6.22. (a) Normal emission photoemission spectra from the QW state corresponding to 2 ML of Ag on V(100) recorded at several different substrate temperatures. These data are extracted from a series of two-dimensional detector output maps similar to that shown in Fig. 6.20. (b) Photoemission peak width as a function of temperature deduced from a more extensive set of similar spectra. (c) Photoemission peak energy as a function of temperature deduced from a more extensive set of similar spectra.

## 6. Ag/V(100) MEASUREMENTS

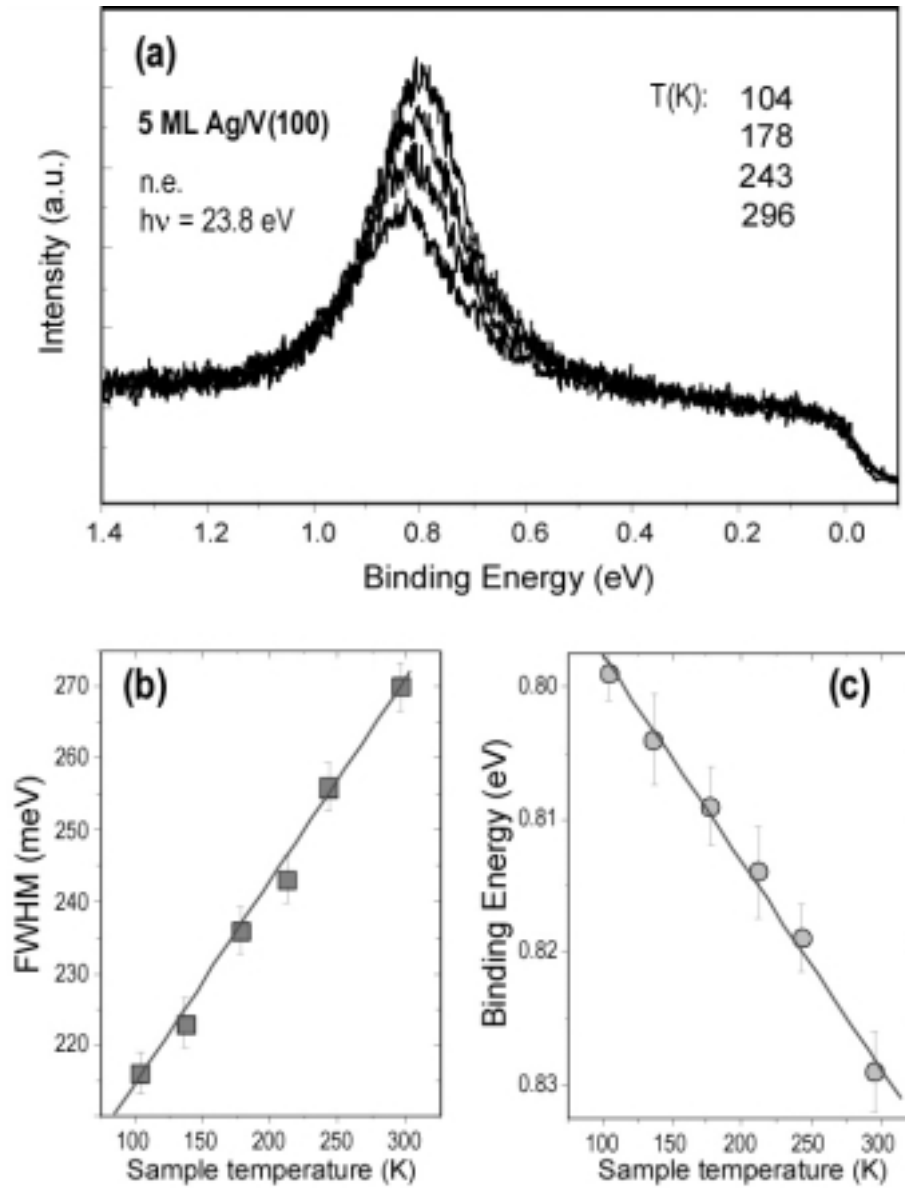


Fig. 6.23. (a) Normal emission photoemission spectra from the QW state corresponding to 5 ML of Ag on V(100) recorded at several different substrate temperatures. These data are extracted from a series of two-dimensional detector output maps similar to that shown in Fig. 6.20. (b) Photoemission peak width as a function of temperature deduced from a more extensive set of similar spectra. (c) Photoemission peak energy as a function of temperature deduced from a more extensive set of similar spectra.

## 6. Ag/V(100) MEASUREMENTS

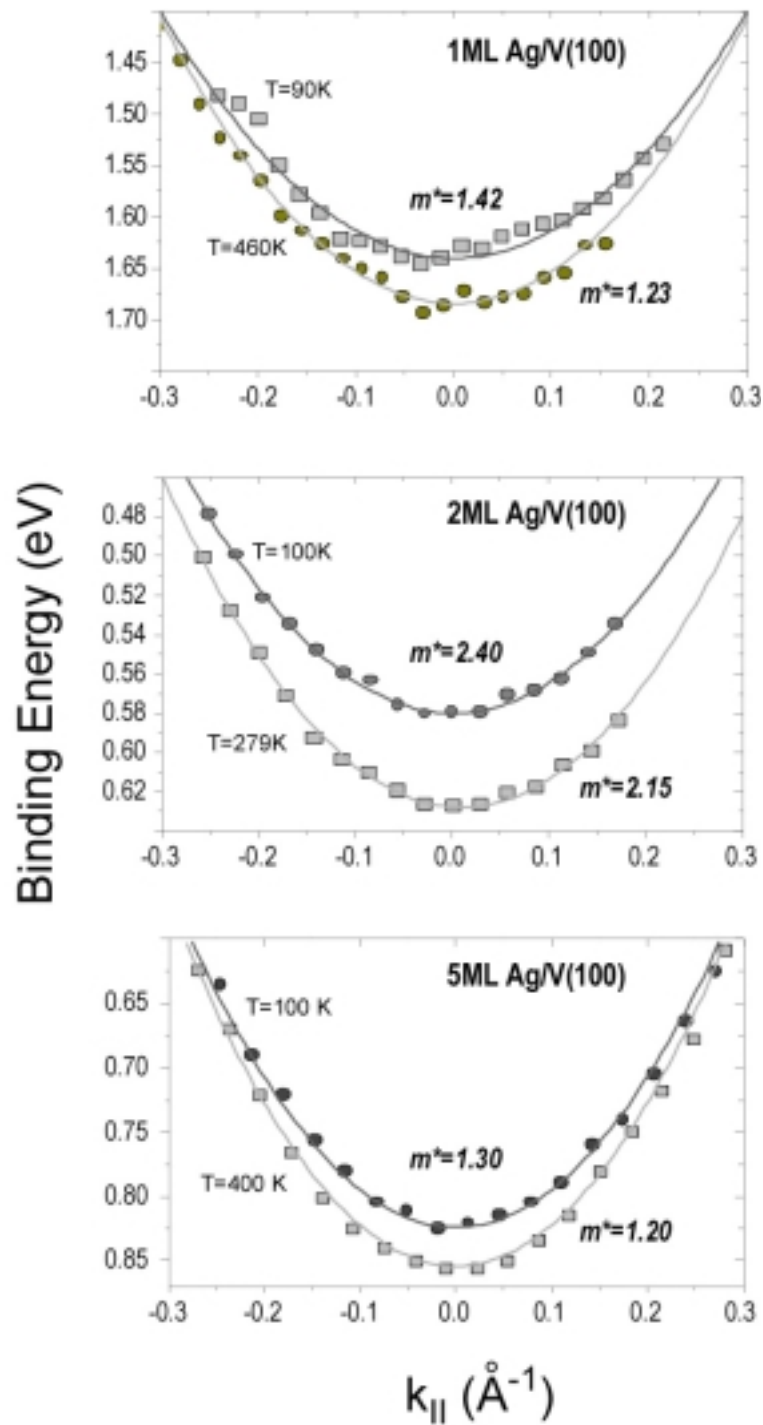


Fig. 6.24. Temperature dependence of the s-p QWS effective mass illustrated for two different temperatures for 1 ML Ag, 2 ML Ag, and 5 ML Ag. Note that in the shown dispersions also a shift in binding energy is clearly visible.

## 6. Ag/V(100) MEASUREMENTS

Film thickness (ML)	Thermal shift ( $\text{eV}\cdot\text{K}^{-1}\cdot 10^{-4}$ )	Electron-phonon coupling parameter $\lambda$
0 (surface state)	–	$1.45 \pm 0.15$
1	1.5	$0.21 \pm 0.05$
2	1.6	$1.00 \pm 0.03$
3	–	–
4	1.0	$0.28 \pm 0.12$
5	1.6	$0.52 \pm 0.07$
6	1.8	$0.44 \pm 0.07$
7	–	–
8	1.1	$0.25 \pm 0.15$

Table 6.2. Summary of the data acquired from the HRARPES temperature dependence. The electron-phonon coupling parameter is obtained from the slope of the photoemission peak widths vs. temperature dependence and is discussed later in the text.

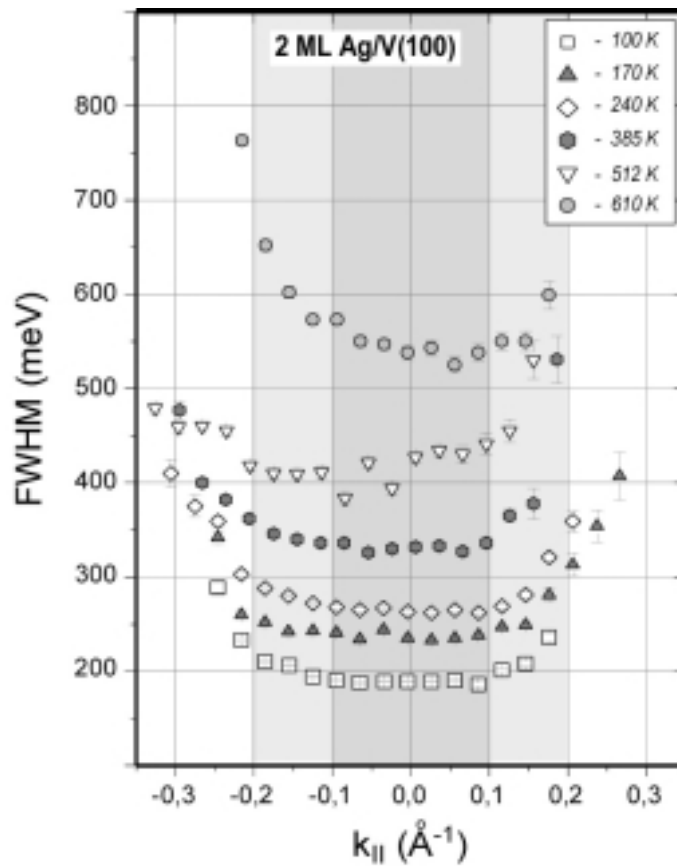


Fig. 6.25. The  $k_{||}$  dependence of the measured photoemission line width for 2 ML Ag/V(100) at different temperatures as indicated in the figure. Note that this is the total line width which includes all contributions to the lifetime. Central shaded area  $\pm 0.1 \text{ \AA}^{-1}$  around the centre of the surface Brillouin zone indicates the region of minor changes, while out of this area the linewidth starts to increase significantly.

For 2 ML Ag/V(100) we have also analysed temperature induced effects away from  $k_{||} = 0$ . The studied range included the region of  $\cong \pm 0.25 \text{ \AA}^{-1}$  around the surface Brillouin zone center. This region was chosen since it is characterised by the parabolic behaviour of the QW state dispersion (see previous section and Fig. 6.14). Analysis outside this region could possibly include more than just temperature induced effects. We believe that within the studied region the hole-phonon coupling effects are dominantly determining the temperature dependence in the photoemission spectra. The 2 ML s-p QW state has the largest effective mass and it is fairly close to the Fermi level. Thus the possible hole-electron contributions to the photoemission line width are negligible compared to the observed effects. In Fig. 6.25 the results of the analysis of the photoemission peak widths are summarised. We note that for each temperature, the sets of analysed spectra are similar to the one shown in Fig. 6.14 (up to  $k_{||} = 0.25 \text{ \AA}^{-1}$ ). The error bars are determined from the Lorentzian fit uncertainty. Up to the temperature of 385 K and  $\cong \pm 0.08\text{-}0.10 \text{ \AA}^{-1}$  around the Brillouin zone center the widths do not change. After that point and up to  $\pm 0.20 \text{ \AA}^{-1}$ , an increase of the photoemission width takes place and behind that point an even steeper increase is observed within the studied  $k_{||}$  region. For temperatures above 400 K the spectra have more intensive background which makes the measured data points more scattered.

#### 6.2.4. Electron-phonon coupling analysis

The ambiguity in separating the various contributions to the peak widths present in section 6.2.2 does not, however, extend to the hole-phonon scattering which is of primary interest here and which can be obtained directly from the dependence of the measured HRARPES peak widths on temperature with great precision. Within the studied temperature range the temperature dependence is approximately linear with a slope  $2 \cdot \pi \cdot \lambda \cdot k_B$  (see Eq. (2.26)), where  $\lambda$  is the hole-phonon coupling constant. For this analysis we focus on the  $k_{||} = 0$  point. The linear fits superimposed in the data shown in Fig. 6.26 show that the gradient changes strongly with film thickness. The obtained coupling parameters are shown in Table 6.2. In Fig. 6.27 we plot the photo hole-phonon coupling strength as a function of the Ag film thickness,  $d$ . The most prominent feature of the  $\lambda(d)$  plot is the change in the coupling strength when the thickness of the silver film is increased from 1 to 2 ML – the corresponding value of  $\lambda$  for the 2 ML Ag film is almost five times larger than that for the 1 ML QW state and 3-4 times larger than the recently reported value measured for a 19 ML Ag film grown on Fe(100) [128] and 6-10 times larger than for 3-5 nm thick Ag(111) layers grown on the Cu(111) substrate [129]. Apart from the prominent maximum in  $\lambda$  at 2 ML, the Ag/V(100) system shows an additional maximum of the coupling constant for 5 ML. A very similar h-p coupling strength variation has been only recently measured for ultra thin Ag on Fe(100) [130]. In Fig 6.27 we also plot  $\lambda \cong 1.45$  obtained for the V(100) surface that we have derived from the mass enhancement of the surface state near the Fermi level in the same manner as in the earlier surface state studies of Mo(110) [45] and Be(0001) [139].

## 6. Ag/V(100) MEASUREMENTS

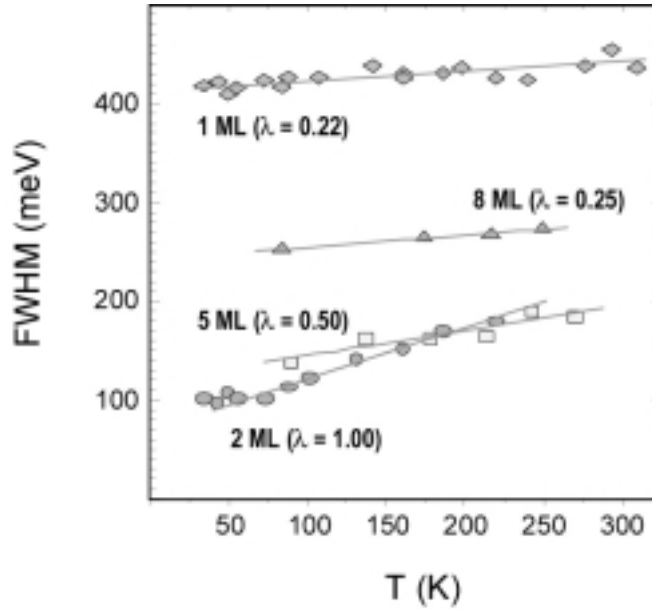


Fig. 6.26. The QWS peak widths plotted as a function of substrate temperature. From the linear fit of each set of data the corresponding e-p coupling constant ( $\lambda$ ) was calculated and is shown in brackets. For the sake of clarity not all sets of data are shown.

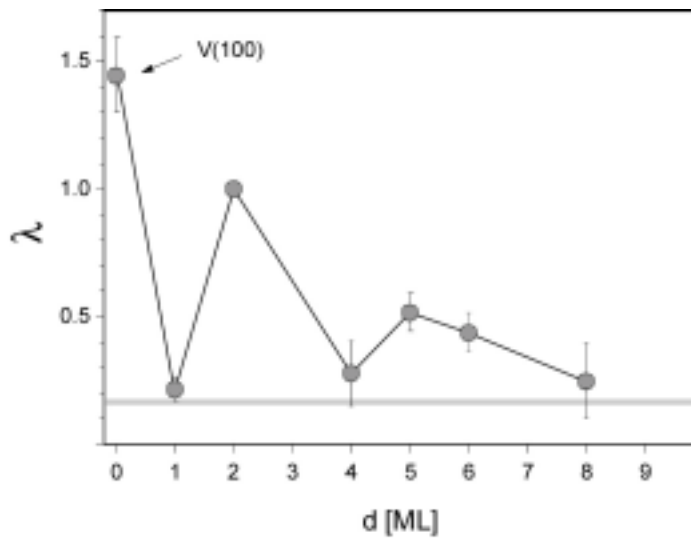


Fig. 6.27. The measured h-p coupling constant ( $\lambda$ ) values obtained from temperature dependent HRARPES measurements as a function of silver film thickness. The experimental value of  $\lambda$  for the surface state on V(100) is shown at zero film thickness while  $\lambda$  for bulk silver is indicated by the thick grey line parallel to the abscissa.

Fig 6.28 shows the results of another experiment conducted on a 5 ML Ag film deposited at 100 K without annealing. As the temperature is subsequently increased through the range 250-300 K it is clear that some ordering of the film occurs. However, the gradient of the peak width with increasing temperature is the same before and after restructuring. In all cases, for all film thicknesses, the temperature dependence is approximately linear and does not change the gradient for the particular film thicknesses.

## 6. Ag/V(100) MEASUREMENTS

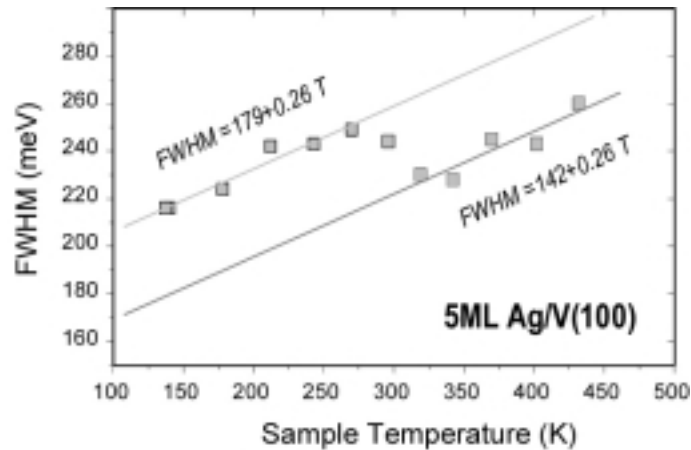


Fig. 6.28. Plot of the HRARPES peak width as a function of substrate temperature recorded at normal emission from the QW state corresponding to 5 ML of Ag on V(100). In this experiment the original film was apparently not well ordered and the film morphology and ordering changes around 250-300 K. The slope of the temperature dependence, however, does not change.

### 6.2.5. *d*-band QW states

The spectral intensity at energies below 3.5 eV binding energy corresponds to the photoemission from QW states of *d*-symmetry. In Fig. 6.29 the 2-D intensity grey-scale maps for 1, 2 and 2.5 ML Ag/V(100) are shown. Note a systematic shift towards lower binding energies. Also note how the dispersion for *d*-band QW states is slower than for *s*-*p* QW states which is expected, since the *d*-symmetry states should be more localised. The states are dispersing away from the Fermi level (negative effective masses). In Fig 6.30 several EDC spectra for 2 ML Ag/V(100) obtained as slice cuts along dashed lines drawn in Fig. 6.29 are shown.

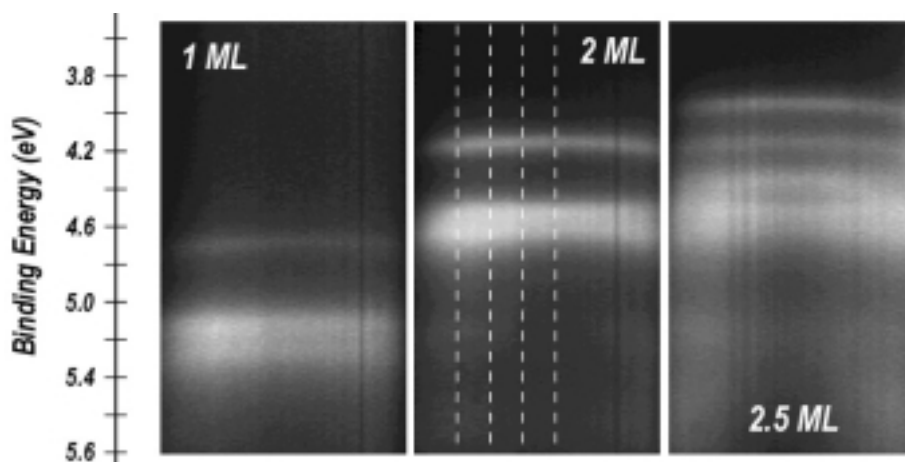


Fig. 6.29. Experimental 2-D photoemission intensity grey-scale maps for 1, 2, and 2.5 ML Ag/V(100) as a function of photoelectron polar emission angle and binding energy. The binding energy region captures the *d*-band QW state intensities.

## 6. Ag/V(100) MEASUREMENTS

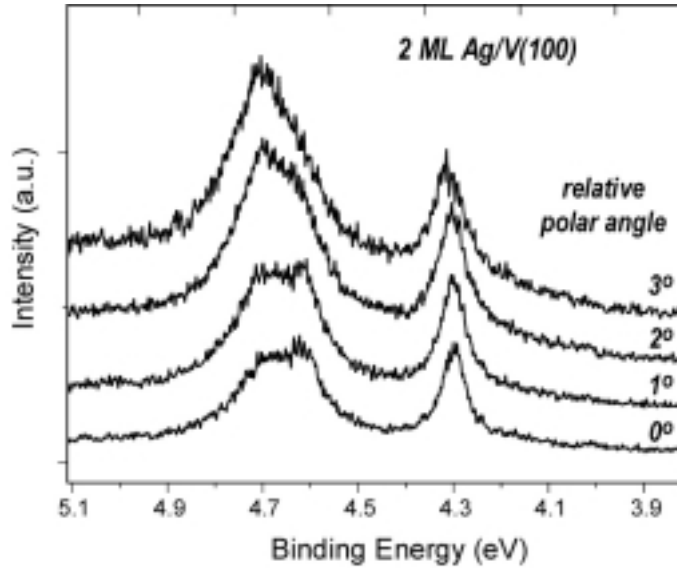


Fig. 6.30. 2 ML Ag/V(100): The photoemission spectra obtained at different polar angles (indicated with thin dashed lines in Fig. 6.29) by slice cuts from 2-D grey-scale intensity map. The binding energy region corresponds to d-band QW states.

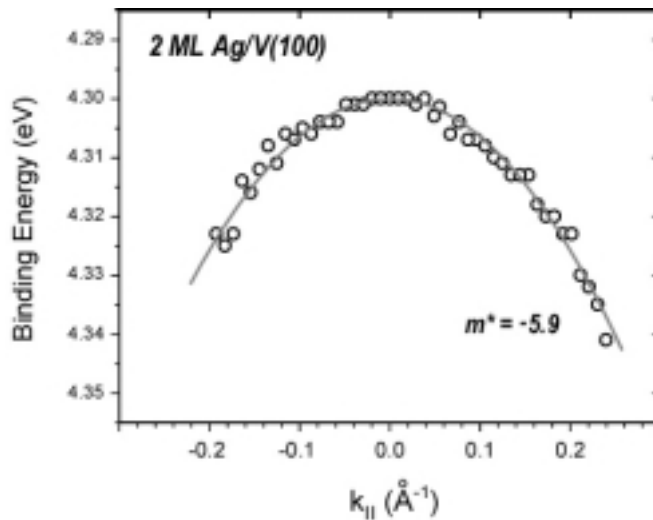


Fig. 6.31. Dispersion curve of the lowest binding energy 2 ML Ag/V(100) d-band QW state. Nearly free electron parabola fit gives a value of  $-5.9m_e$ .

In Fig 6.31 for 2 ML Ag/V(100) we have also extracted the effective mass of the d-band QW state ( $-5.9m_e$ ) for the state with lowest binding energy. Namely, in the region near the Brillouin zone center the state exhibits parabolic dispersion. Generally, the number of d-QWS that increases with film thickness as  $5N$  ( $N$  is number of silver layers), and the broadening of the peaks induced by Coster-Kronig Auger process makes it very difficult to resolve all the QW states even for the very thinnest film. Using an extensive range of photon energies, four QW states were resolved for 1 ML film (see Fig. 6.32), where every peak corresponds to a QW state derived from a silver band of different symmetry (the symmetry assignment will be made later in the discussion). In this special case all QW states have the

## 6. Ag/V(100) MEASUREMENTS

same quantum number,  $n = 0$ . The spectra shown exhibit independence of the peak position with photon energy. This appears to be a consequence of the fact that  $k_{\perp}$  of the d-QW states is not yet good quantum number and no dispersion perpendicular to the surface is possible.

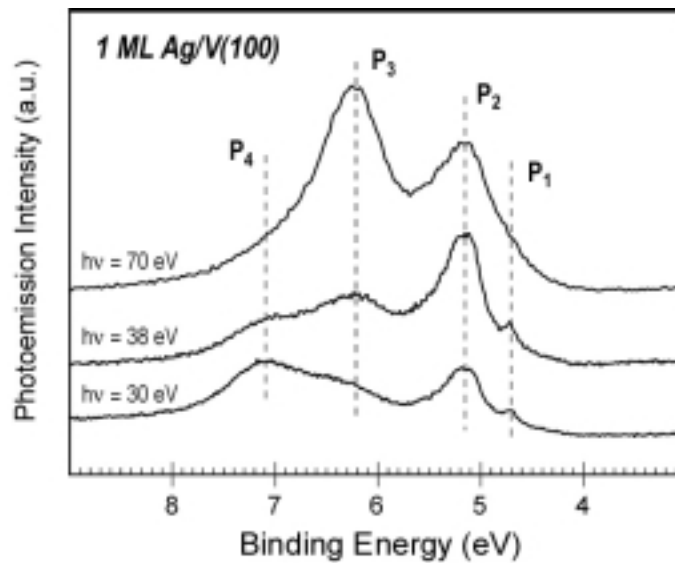


Fig. 6.32. Normal emission photoelectron spectra recorded at different photon energies from 1 ML Ag film.

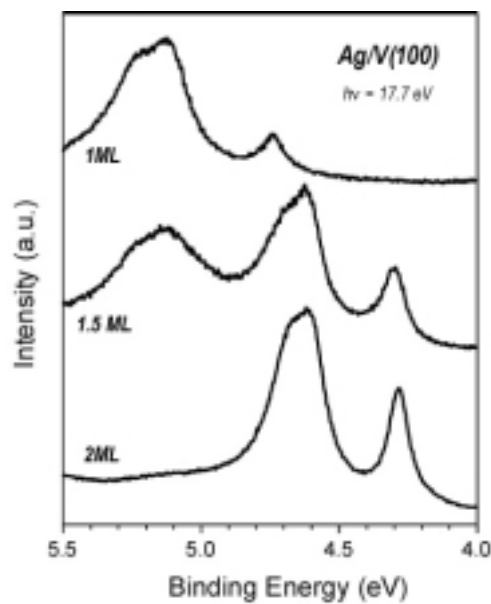


Fig. 6.33. Normal emission EDC photoemission spectra for 1, 1.5 and 2 ML Ag/V(100).

We can follow the d-band region development by changing the film thickness. Fig. 6.33 illustrates how the peak appearance is very sensitive to the silver coverage. This particularly refers to the leading peak (the one at lowest binding energy). This peak is usually well separated from any other photoemission intensity, so it can also be used for reliable identification of the silver coverage.

## 6. Ag/V(100) MEASUREMENTS

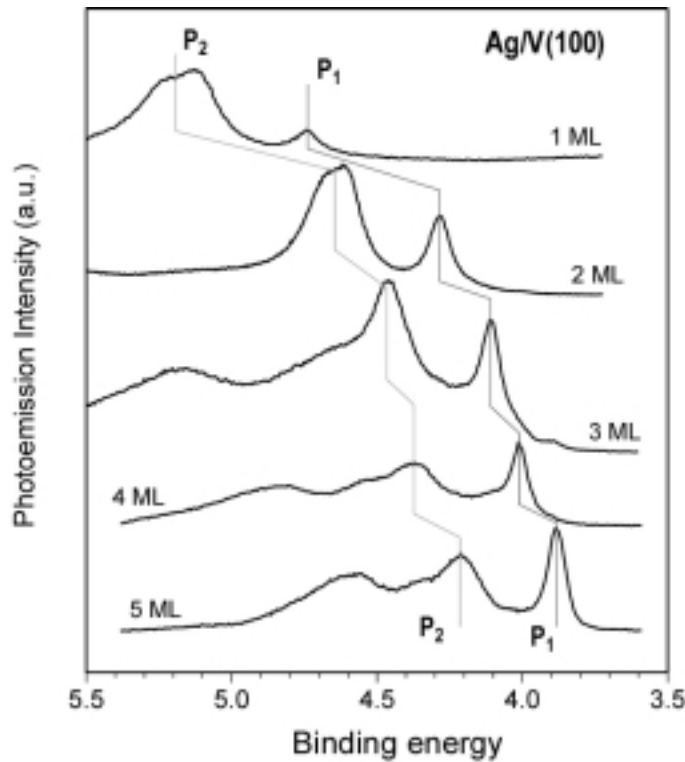


Fig. 6.34. Normal emission photoelectron spectra of d-QWS recorded at photon energy of 18 eV from Ag films of different thicknesses.

The analysis of peaks in the photoemission spectra from d-QW states is much more delicate already for the 2 ML film. Two QW states are derived from each d-band ( $n = 0, 1$ ). A identification of a particular peak can be rather difficult and sometimes conflicting. For this reason we have restricted our analysis of QWS in thicker films to a small number of states in the reduced binding energy range between 3.5 and 5.5 eV. This energy range includes the leading peak ( $P_1$ ) which is not affected by the Auger broadening and consequently it is the narrowest state in the d-band manifold and the  $P_2$  state. Fig. 6.34 shows a set of the normal emission photoemission spectra of the d-band QWS taken from 1-5 ML silver films. These spectra were taken by a high energy resolution spectrometer which enabled us to observe some additional structure. The spectra exhibit a pattern typical for the QW states: a shift to lower binding energy with increasing film thickness [167]. The peak  $P_1$  shifts from 4.75 eV (1 ML) up to 3.85 eV (5 ML) with respect to the Fermi level. A total shift of the same order (0.9 eV) was observed for  $P_2$  state as well. The biggest shift of 0.55 eV was observed between 1 and 2 ML peaks. The leading  $P_1$  peak is well separated from the other photoemission peaks making the lineshape analysis rather reliable. For all film thicknesses the peak was well fitted by a Lorentzian lineshape. The width of the peak increases from 61 meV to 95 meV as the film thickness was reduced from 5 ML to 1 ML, respectively. The peak  $P_2$  clearly shows splitting, which reduces with increasing film thickness. For the 1 ML spectrum the peak splitting is 120 meV and 80 meV for the 2ML spectrum (see Fig 6.35a, b). No splitting of this

peak could be resolved in the spectra from films of 3 ML or more, although for the thicker silver films the peak is broader.

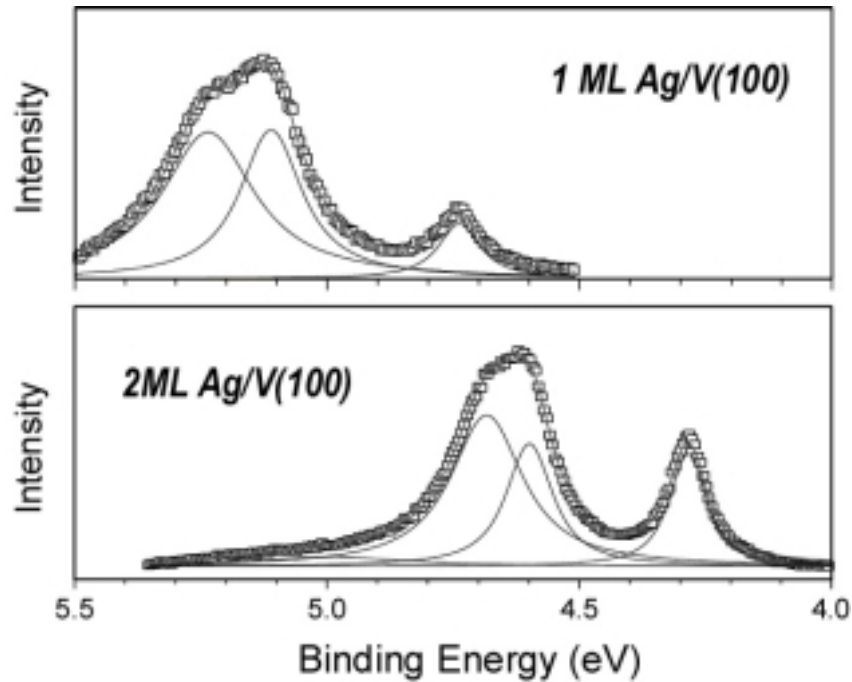


Fig. 6.35. (a) and (b): Deconvoluted normal emission photoelectron spectra of d-QWS from 1 ML and 2 ML Ag films showing a decrease of the  $P_2$  peak splitting.

### 6.3. Ag/V(100) electronic structure probed by STM

In the section 6.1.4 the (geometric) structure of the Ag/V(100) system has been characterised using direct STM imaging. This section deals with the electronic properties of Ag/V(100) probed in the STM measurements. For 1-5 ML thick silver films we perform constant current room temperature STM experiments, where the tunnelling parameters are (carefully) adjusted to optimise the observation of the standing wave features. Those features are then analysed based on the principles of the Fourier transform STM method described in section 2.1.9.

#### 6.3.1. Characterisation of standing wave patterns

The “quality” of the atomically resolved images is particularly altered in the presence of surface impurities. For the illustration in Fig 6.36 for a 5 ML thick silver film a set of successive measurements is presented where the tunnelling current was kept at the constant value of  $I_T = 19$  nA and only the bias voltage was varied. The obvious difference between the images is the existence (Fig. 6.36a and c) or (almost) non-existence (Fig. 6.36b) of surface standing wave features.

## 6. Ag/V(100) MEASUREMENTS

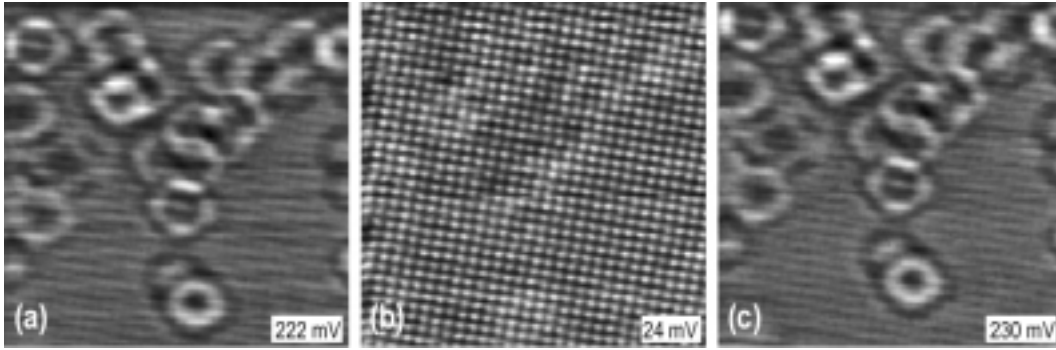


Fig. 6.36. 5 ML Ag/V(100). A successive set of STM measurements where only the bias voltage is varied: (a)  $I_T = 19$  nA,  $U_B = 222$  mV; (a)  $I_T = 19$  nA,  $U_B = 24$  mV; (a)  $I_T = 19$  nA,  $U_B = 230$  mV. Image size:  $7 \times 7$  nm<sup>2</sup>.

We observe that the surface standing wave vs. atomic corrugation amplitude ratio heavily depends on the precise tunnelling parameters, which actually makes the appearance of good atomically resolved or good surface waves images. When measured separately the surface wave corrugation can reach the value of  $\cong 0.015$  nm. Unfortunately, we were not able to perform an extensive set of measurements to investigate the detailed bias voltage dependence of surface waves. However, we note that the bias voltages in the range 100-300 mV are particularly suitable for surface waves and that the polarity of the bias voltage did not make a difference on the surface wave appearance; only the absolute value was important for the observation of this effect.

We can make an estimate of the phonon contribution to the electron mean free path at room temperature, taking into account the measured phonon contribution to the s-p QW state photoemission line width. For example, for 2 ML s-p QW state ( $\Gamma_{e-p}(300\text{ K}) \cong 150$  meV,  $m^* \cong 2.4$ ,  $E_B \cong 0.6$  eV) we obtain the mean free path of  $L_{e-p} \cong 12-15$  Å. In an ideal room temperature experiment this contribution would basically determine the region around the single imperfection that exhibits a standing wave feature. In fact, this rough estimate matches quite well the imaged surface wave features appearance.

We have, generally, identified two types of scattering centers for surface waves (Fig. 6.37): point scatterers and steps. Among point scatterers we distinguish the ones that appear like protrusions (Fig. 6.37a) and the ones that appear like depressions (Fig 6.37b and c). The other type of scattering centre is the edge of the terrace (Fig. 6.37d) as a line scatterer. In this room temperature experiment we do not observe much oscillations far from the scattering centres. However, the interference between the surface standing waves, if the centres are close enough (see for example Fig. 6.37d and Fig. 6.36a and c) is observed. We measure that an average concentration of point scatterers reaches the value of about  $10^{-2}$  per surface atom.

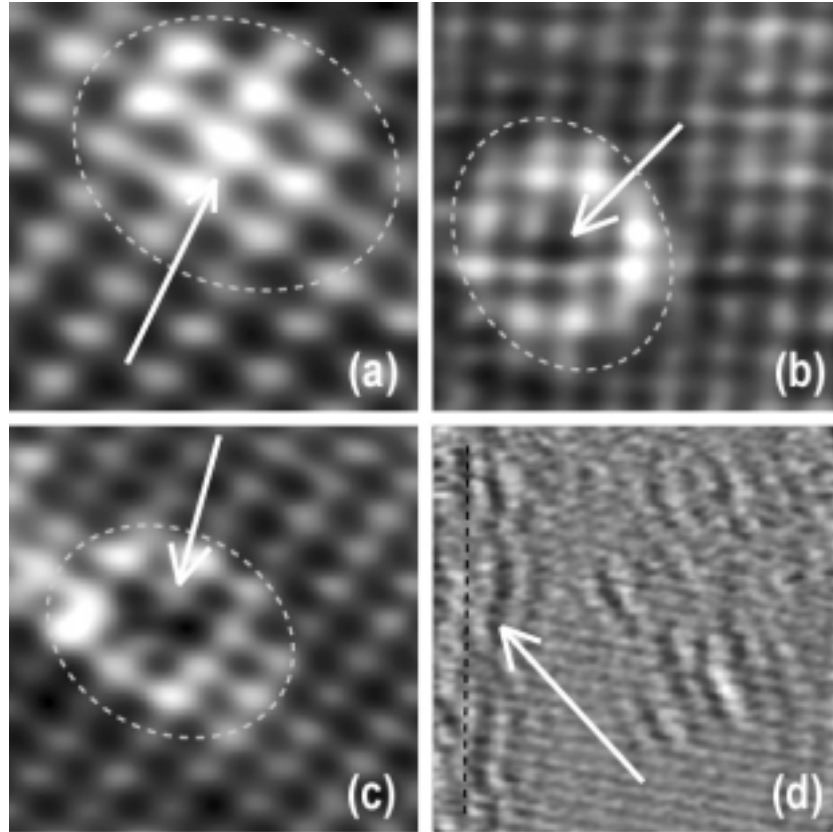


Fig. 6.37. Identification of scattering centres for the surface waves: (a) the protrusion, (b) the depression, (c) the depression, and (d) the edge of the terrace (in order to emphasise the contrast in the image the step itself and the lower terrace are not shown). Sizes and tunnelling parameters: (a)  $1.5 \times 1.5 \text{ nm}^2$ ,  $U_B = 130 \text{ mV}$ ,  $I_T = 4 \text{ nA}$ , (b)  $2.4 \times 2.4 \text{ nm}^2$ ,  $U_B = -150 \text{ mV}$ ,  $I_T = 4.5 \text{ nA}$  (c)  $2.7 \times 2.7 \text{ nm}^2$ ,  $U_B = 130 \text{ mV}$ ,  $I_T = 4 \text{ nA}$  (d)  $6.9 \times 6.9 \text{ nm}^2$ ,  $U_B = -55 \text{ mV}$ ,  $I_T = 5 \text{ nA}$ .

### 6.3.2. Fourier transform analysis

The best way to analyse surface wave features it to perform the FTSTM analysis, where surface wave wavelengths, i.e. the wave vectors that they constitute are measured. We find this as a much more reliable and accurate method than direct image analysis. Since in the room temperature STM experiments there is always some drift, as a secure reference point we use an inverse of the atomic periodicity. In other words, the images where both, the surface waves and the atomic positions are visible, are analysed.

For 1 ML thick silver film we demonstrate the steps of data analysis (Fig. 6.38). Fig 6.38a shows a slightly smoothed FT of the original STM image shown in the inset. In the real space STM image two white dashed lines are drawn in order to indicate high symmetry directions ([010] and [001]). White arrows in Fig. 6.38a denote the atomic periodicity contributions. In Fig. 6.38b the same Fourier transform is shown. The white dashed lines are now aligned along the high symmetry directions in the inverse space. The distance between

## 6. Ag/V(100) MEASUREMENTS

the center of the Fourier transform image ((0,0) point) and atomic periodicity points ((1,0) and (0,1)) is calibrated using the lattice parameter: the (100) bcc plane is of a square symmetry with a lattice parameter of  $\cong 3 \text{ \AA}$  and this distance is in each case  $2 \cdot \pi/a \cong 2.094 \text{ \AA}^{-1}$ . The mesh of white dashed lines is not perfectly quadratic which is due to the experimental drift. The feature that is induced by the surface waves presence for 1 ML thick silver film clearly contains two ring-like structures. They are indicated with black dashed circles. The radius of each circle is indicated with an black arrow and indexed as  $k_1$  and  $k_2$  for the inner and the outer ring, respectively. Additionally, in the centre of the FT image one can notice small circular bright area. Fig. 6.38c shows profile scans along high symmetry direction through the center of the FT image in Fig. 6.38b. With the thin dark line the  $\pm 2 \cdot \pi/a$  positions are noted. We read  $k_1 = 0.64 \pm 0.15 \text{ \AA}^{-1}$  and  $k_2 = 1.10 \pm 0.15 \text{ \AA}^{-1}$ . Note that the ring intensities (see Fig. 6.38a) mildly vary with the angle. This is not an intrinsic property but rather is an effect of the quality of the original STM image. In the linescans we have shaded the central region  $\approx \pm 0.4 \text{ \AA}^{-1}$ , around  $k = 0$ . In Fourier transforms of the surface wave images we always observe such high-intensity contributions. At the end, each identified contribution ( $k_1$ ,  $k_2$  and bright area) is separately FT filtered out of the real space STM image and shown in Fig 6.38d.

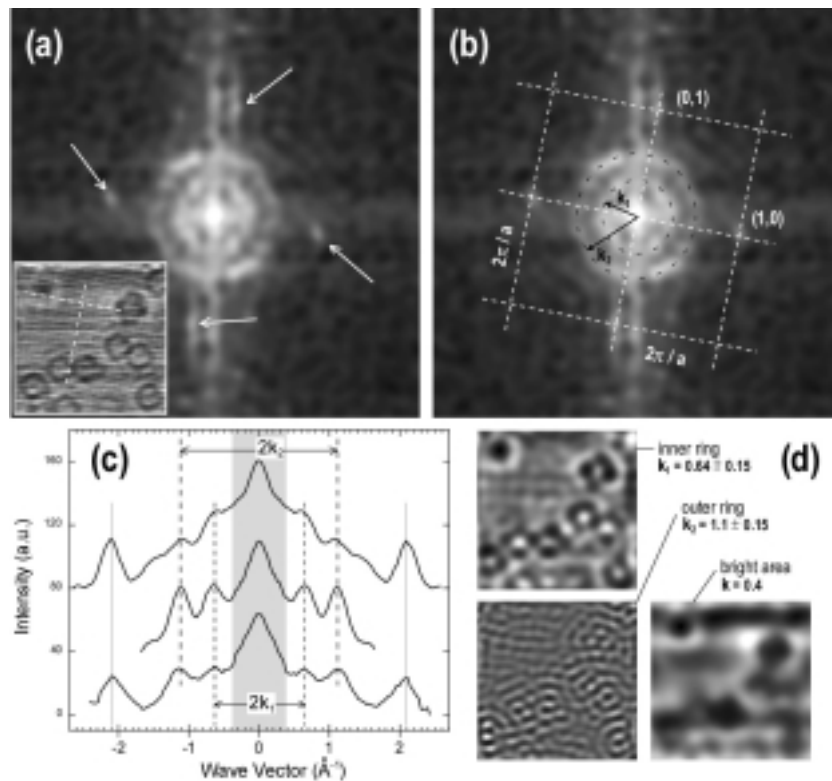


Fig. 6.38. 1 ML Ag/V(100)-(5×1). (a) Fourier transform of the STM image that is shown in the inset. Tunnelling parameters:  $U_B = 252 \text{ mV}$ ,  $I_T = 4.5 \text{ nA}$ . Image size:  $7.9 \times 7.9 \text{ nm}^2$ . (b) The same Fourier transform. Details are explained in the text. (c) Three profile scans over the ring-like features from the image in (a). (d) Separately filtered direct space images originating from the inner ring and from the outer ring.

## 6. Ag/V(100) MEASUREMENTS

For a 2 ML thick silver film the FT images are quite similar to what was obtained for 1 ML, though the intensity of the outer ring feature and consequently the ring separation are less pronounced. In Fig. 6.39a a Fourier transform from a  $11 \times 11 \text{ nm}^2$  real space STM image is shown. Note that the ring in Fig. 6.39 looks more like an ellipse which is due to a relatively higher experimental thermal drift for this image. In Fig. 6.39b profile scans are given where we indicate the position of the visible rings. In the case of a 3 ML thick film we are again able to resolve two dominant contributions in the Fourier spectrum. We should note that the visual inspection of the Fourier transform images plays an important role in the identification of the actual rings, especially when FT images contain some background noise. In Fig. 6.40 the FT and profile scans over several 3 ML Fourier transforms are shown.

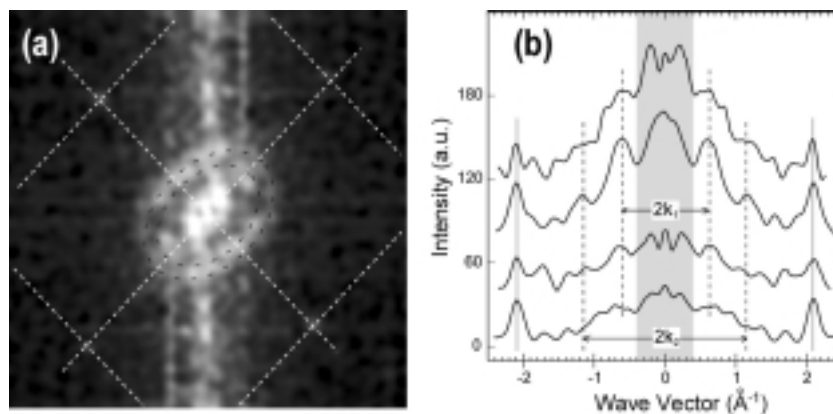


Fig. 6.39. 2 ML Ag/V(100)-(5 $\times$ 1). (a) Fourier transform of the surface wave STM image. (b) Profile scans over the ring-like feature from several 2 ML images along the high symmetry direction.

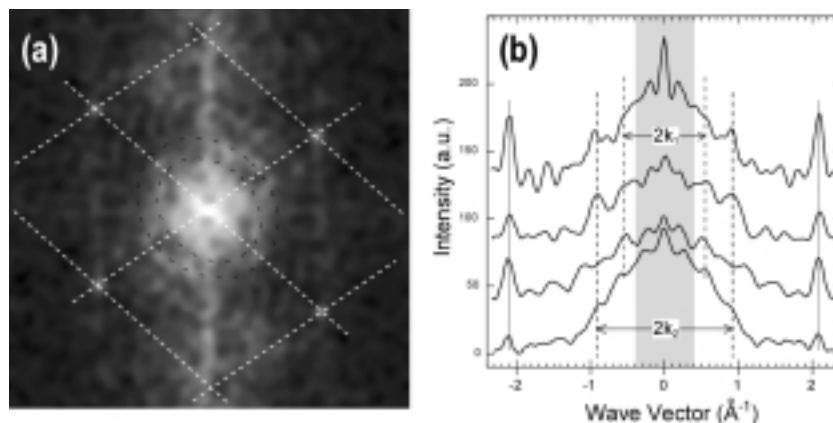


Fig. 6.40. 3 ML Ag/V(100)-(5 $\times$ 1). (a) Fourier transform of the surface wave STM image. (b) Profile scans over the ring-like feature from several 3 ML images along the high symmetry direction.

For relatively small silver islands we notice the “anisotropy” effect. A nice example is already illustrated in Fig. 6.37d. The image is taken from the small island. The black dashed line indicates the orientation of the island edge. There one can see a wave perpendicular to

## 6. Ag/V(100) MEASUREMENTS

the line exhibiting a few wavelengths visible effect. A bit further away one notes that the point scatterers are sources not for circular waves but for something that looks more like a scattering from the step. However, the direction of those lines does not coincide with the silver terrace edge orientation. In fact, we believe that there we observe the influence of the underlying vanadium step. In this image it is included as a defect with respect to the homogeneity of the silver thickness and the electronic states within the silver island. What one sees on the surface with STM is an interference from waves induced by point scatterers on the surface and oscillations induced by the underlying step. A rather complicated situation is also illustrated in Fig. 6.41. A quantity of approximately 3 ML of silver was deposited, but the annealing temperature was below 600 K. This resulted in small silver islands and non-uniform silver thickness as illustrated in Fig. 6.41a – relatively small islands and many island heights. Additionally, the imaged region is probably positioned above a rather dense vanadium steps structure which we conclude from the fact that the absolute height is increased much in the image from the left to the right hand side. Regardless of this anisotropy we again clearly identify two important Fourier contributions that now are not distributed spherically in the reciprocal space, but they exist dominantly in the direction of propagation of the surface waves. This we confirm with linescans that clearly show that the Fourier components are dominantly positioned only in one direction. From the STM image we filter out the inner and the outer ring contributions (Figs. 6.41e and f).

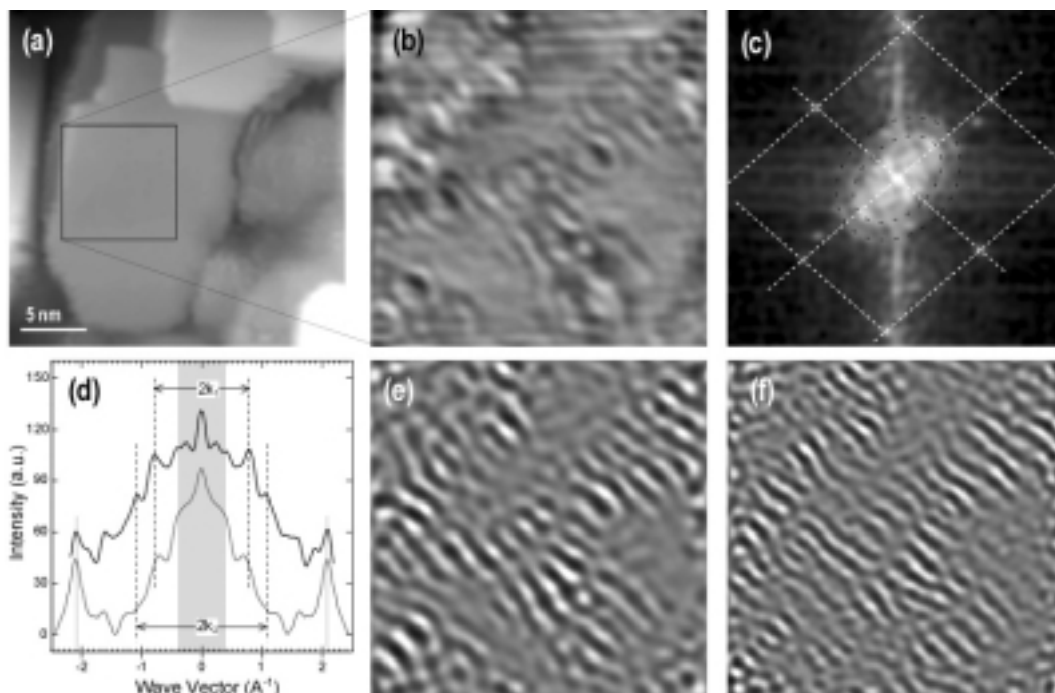


Fig. 6.41. (a) STM image in the region of a not perfectly ordered silver film, characterised by many small islands and in the region of rather dense vanadium steps. (b) Surface wave image of indicated region in (a).  $U_B = 22$  mV,  $I_T = 5$  nA,  $8.1 \times 8.1$  nm<sup>2</sup>. (c) Fourier transform of (b). (d) Profile scans over Fourier transform. (e) Filtered inner ring contribution in the STM image (b). (f) Filtered outer ring contribution in the STM image (b).

## 6. Ag/V(100) MEASUREMENTS

For higher coverages and ordered silver layers it is hard to estimate the actual thickness of the silver film barely from the STM experiment. One has to put trust in other methods to determine the thickness (AES, ARUPS). To be sure, we searched for such regions that enabled also an STM confirmation of the silver thickness. Fig. 6.42 shows the Fourier transform and the profile scans for 5 ML Ag/V(100). The corresponding real space image is already shown in Fig. 6.36c. Along with profile scans over the FT of the surface wave image we show also a profile scans over the FT of the atomically resolved image that is shown in Fig. 6.32b. These profiles are coloured in grey. For 5 ML thick silver, apart from  $k_1$  and  $k_2$  rings, an additional ring-like feature is detected ( $k_3$ ).

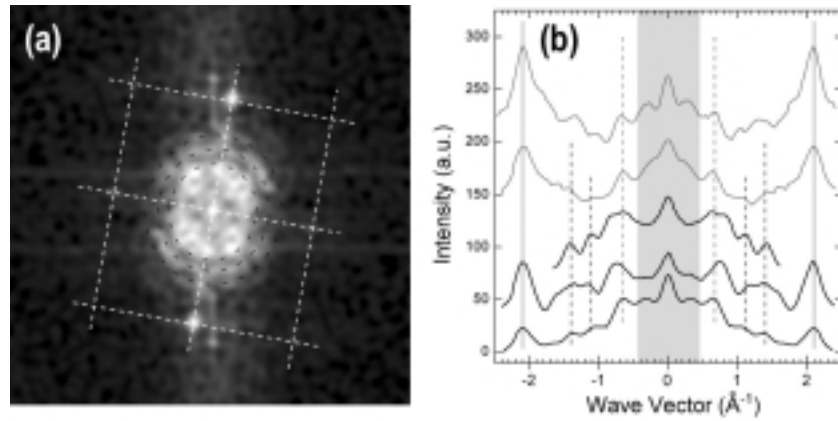


Fig. 6.42. 5 ML Ag/V(100)-(5×1). (a) Fourier transform of the surface wave STM image (shown in Fig. 6.12a). (b) Profile scans over the ring-like feature in (a) and in addition coloured in gray two profile scans over the Fourier transform of the corresponding "atomically resolved" image.

As explained in section 2.1.8 the standing wave in the LDOS extends from the defect basically with a wave vector  $q = 2 \cdot k_F$ , where  $k_F$  is the Fermi surface wave vector. Thus, we have to divide the measured radii by 2 in order to obtain proper  $k_F$  vectors. For the studied layers the data are summarised in table 6.3.

Silver layer thickness	$k_F$ radii of ring-like features in Fourier transformed STM images in $\text{\AA}^{-1}$				
	Bright region	$k_1^F$	$k_2^F$	$k_3^F$	$\Delta k$
1 ML	$\cong 0.2$	<b>0.32</b>	<b>0.55</b>		0.1
2 ML	$\cong 0.2$	<b>0.35</b>	<b>0.58</b>		0.1
3 ML	$\cong 0.2$	<b>0.30</b>	<b>0.48</b>		0.1
5 ML	$\cong 0.2$	<b>0.35</b>	<b>0.55</b>	<b>0.7</b>	0.1
3 ML Aniso.	$\cong 0.2$	<b>0.38</b>	<b>0.55</b>		0.1

Table 6.3. Measured radii of ring-like features in analysed Fourier transforms of surface wave STM images.



## 7. Ag/V(100) discussion

### 7.1. Formation of an ordered silver film

#### 7.1.1. Removal of the (5×1) vanadium reconstruction

STM results show the cluster-like topography of the silver deposited onto the well ordered V(100)-(5×1) substrate at RT. From the AES measurements we conclude that the three-dimensional character of the RT silver growth is pronounced on the V(100)-(5×1) substrate. To acquire ordered and uniform silver layers that are formed as wide islands and terraces a temperature treatment (annealing) is needed. This investigation included only chosen annealing temperatures which are rather high, always higher than 700 K. This is the key step to obtain the ordered silver film of such quality. The adsorption sites of the V(100)-(5×1) substrate are mostly occupied with oxygen (and carbon) atoms. We believe that the annealing of the adsorbed silver removes oxygen and carbon atoms, which is accompanied by the local lifting of the (5×1) reconstruction of the vanadium substrate and eventually the formation of ordered (1×1) silver islands.

Konvicka et al. [158] studied Pd growth on the V(100)-(5×1) surface. From the STM and AES results they found that for submonolayer coverage (0.15 ML) and room temperature single Pd atoms are trapped (stabilised) in the four-fold co-ordinated hollow sites unoccupied by oxygen or carbon. This is explained with stronger affinity, i.e. bonding energies of palladium to vanadium in the clean four-fold hollow sites compared to other available sites on the surface. Further they found that annealing at 470 K leads to the formation of small Pd islands and that the mobilised O and C atoms are compressed at the surface to a denser adlayer, resulting in a clean Pd – V interface. For higher coverages they found that the Pd growth proceeds only on areas free of oxygen which limits the size of the Pd islands and leaves the parts of the surface covered with the dense (1×1) oxygen layer that is acting as anti-surfactant for the growth of the Pd islands.

On the other hand, Valla et al. [155] studied the effects of silver deposition on the oxygen precovered clean and ordered V(100) surface with large doses of oxygen (~ 10 L). The main tool in this investigation was the photoemission which has proven to be the most sensitive method to probe the effects due to the presence of oxygen. At RT and below they found the effects of disordering of the silver film. Moreover, they concluded that not only oxygen disorders the silver film, but most probably it occupies the Ag/V interface sites which is driven by the high affinity towards atomic oxygen of both, vanadium and silver. Investigating the effects of annealing they found that up to 570 K no significant changes are present. At higher annealing temperatures the ordered structure of the silver layer is gradually restored

and finally after annealing at 710 K no oxygen-derived emission is found in the ARUPS, XPS or AES spectra and the order in the silver film is completely restored. This experiment also included TDS measurements which showed that during the annealing there is no desorption of oxygen, which means that it probably diffuses into the bulk. However, diffusion of oxygen into the bulk upon annealing does not seem to be a regular behaviour of all noble metals on oxygen precovered transition metals systems. As an opposite example we mention the Cu/O/Ru(0001) system [168,169], where upon annealing oxygen diffuses on top of the Cu film and even forms an oxidised topmost Cu layer.

Obviously, in each of the mentioned cases (Pd/V(100)-(5×1) and Ag/O<sub>2</sub>/V(100)), the annealing temperature plays an important role. A silver atom has a strong affinity to occupy four-fold clean vanadium site, which we believe is the reason that the oxygen and carbon atoms are removed from those sites. Further, for the annealing temperatures that we use (> 700 K) the diffusion of oxygen out of the near surface region is initiated, most probably into the bulk. The formation of large silver islands takes place. At the same time (same annealing temperatures) on the bare parts of the substrate we find no structural changes – it maintains the (5×1) structure and, in contrast to Pd/V(100)-(5×1) no traces of the compressed (1×1) oxygen areas are found.

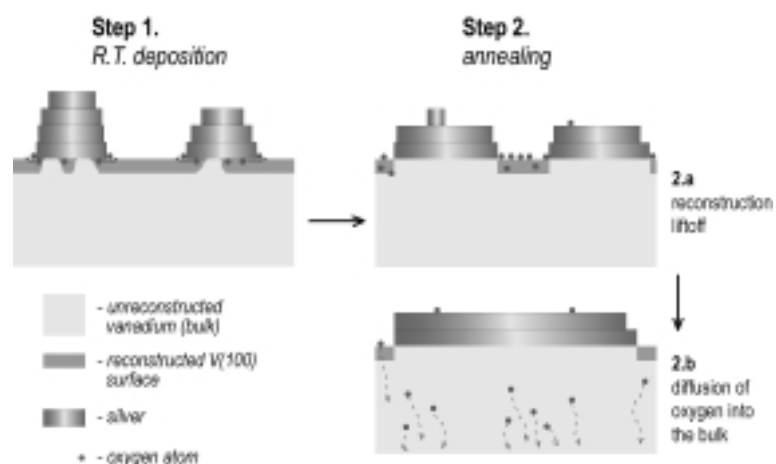


Fig. 7.1. Schematic overview of the silver film ordering process. Step 1 – formation of silver clusters, step 2 – annealing that eventually leads to the diffusion of oxygen into the bulk.

We suspect that the optimisation of the system free energy and the dynamics of the whole process may be rather complicated on the microscopic level. This may include a lot of energy parameters (oxygen-vanadium and silver-vanadium bonding energies, surface free energies of vanadium, silver, silver-vanadium, silver-oxygen and oxygen-vanadium interface) as well as a lot of dynamical steps (lateral diffusion of oxygen + vertical diffusion into the bulk, or direct vertical diffusion). According to the results of Konvicka et al. [158], that used much smaller annealing temperatures, the results of Valla et al. [155] and our own investigations of

the Ag/V(100)-(5×1) surface we propose a schematic sketch that describes the creation of an ordered silver film as illustrated in Fig. 7.1. Small dark oxygen atoms that are drawn in the figure represent those oxygen atoms that were part of the (5×1) reconstructed surface. During the annealing process these atoms eventually diffuse into the bulk. The order of the silver film is evidenced not only with STM, but as well with LEED, AES and most importantly with ARUPS, that all proved the identicalness with the Ag/V(100) system.

The differences in the properties of Ag/V(100)-(5×1) and Pd/V(100)-(5×1) can be explained if one takes simple geometry and energy considerations into account. First of all, the lattice mismatch between the vanadium bcc(100) lattice is much smaller for silver fcc(100) (4 %) than for palladium fcc(100) (9%). Another point of difference is the surface free energy balance which again favours the ordered silver film. The surface free energy is  $\approx 3 \text{ J/m}^2$  for vanadium,  $\approx 1.9 \text{ J/m}^2$  for palladium and  $\approx 1.3 \text{ J/m}^2$  for silver, which means that the silver layer minimises the surface free energy better than palladium. This is in agreement with thermal desorption measurements of Valla et al. [165] which show that the stability of the first silver layer is very high reflecting the strong silver–vanadium bonding that is in this case much stronger than the silver–silver bonding. To our opinion these are the arguments for the origin and the driving force for the much better epitaxial formation of the ordered silver layer on the V(100)-(5×1) surface. For comparison we note that the copper–oxygen or silver–oxygen interaction for Cu/O/V(100), Ag/O/V(110) and Cu/O/V(110) surfaces is quite different leading to the clustering and disordering of the copper or silver layer, i.e. no temperature induced ordering as for the Ag/V(100)-(5×1) system can be accomplished [170].

### 7.1.2. Tetragonal silver

STM measurements of silver layer heights and the lattice parameter obtained from LEED and atomically resolved STM images are in agreement with the simple hard sphere picture for the structure of a tetragonal silver which is grown in registry with the bcc V(100) substrate. From the symmetry point of view the structure of the silver film is (100) face centred tetragonal (fct), or equivalently (100) body centred tetragonal (bct), where the (100) unit cell contains 2 atoms or 1 atom, respectively. Our measurements show that the in plane lattice parameter, at least for the thickness up to  $\approx 8 \text{ ML}$ , is not relaxed to the silver fcc(100) bulk parameter, i.e., that the tetragonal structure is preserved within this thickness range.

The ordered bcc, bct or hcp growth of bulk fcc material has been already observed for several systems, especially for copper [171,172] and palladium films [172]. According to the calculations for copper a nonequilibrium thin crystal structure is stable due to the only slightly larger volume energies of the equilibrium fcc structure. On the other hand, for Pd/W(100) atomic radii of W and Pd are almost identical and Pd epitaxially follows the substrate. In the limit of very thick films its structure is determined by the difference in the volume energy and

## 7. Ag/V(100) DISCUSSION

will always prevail towards the bulk structure. In the situation where a nonequilibrium crystal structure provides a much better fit to the substrate lattice than any other orientation of the bulk crystal structure, the smaller stress can make a nonequilibrium structure energetically more favourable than the bulk structure over a quite large thickness range. Our results show that the tetragonal silver grown on the V(100)-(5×1) substrate is stable in the range of 1-8 ML. We believe that such a good epitaxy has to do with both, the small difference in the volume energies of bct (fct) and fcc silver (compared to the lattice mismatch induced strain energy), as well as relatively good matching of the lattice parameters (4% mismatch) [173]. The structure and parameters are given in Fig. 7.2.

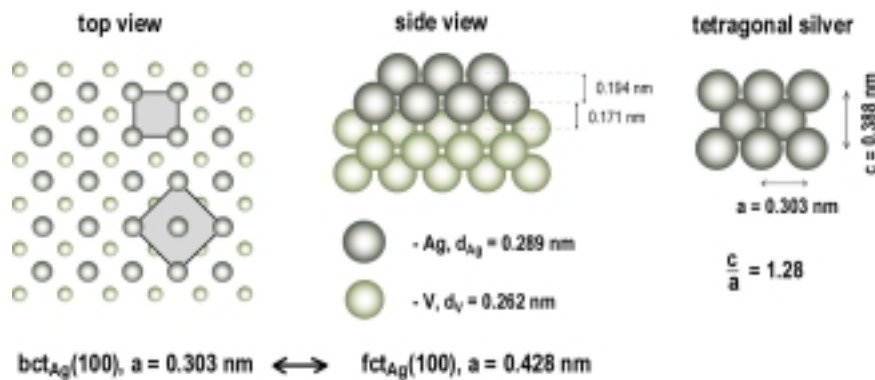


Fig. 7.2. The parameters of tetragonal (bct or equivalently fct) silver grown in the registry with the (100) vanadium substrate.

Although the tetragonal silver seems to be rather stable there must be some stress present and it should lead to the formation of some dislocations in the silver film. We indeed observe some, but their origin is not quite clear (see Fig. 6.9). Namely, as we have already noted, the influence of the substrate step structure might be important. If this is the case one should prepare a well ordered substrate with large terraces and small number of steps in order to minimise the number of dislocations/imperfections. In that sense V(100)-(5×1) is an ideal substrate since the final preparation step includes annealing to high temperature which produces wide terraces. On the other hand, the accumulated stress itself due to the tetragonal structure will lead to the formation of the observed dislocations. Although STM can reveal atomic-scale structure of surface dislocations, it is unfortunately blind with respect to the region beneath the topmost layer and no conclusive explanation regarding the origin of each particular dislocation can be given.

In conclusion, the procedure that leads to the formation of ordered and uniform silver layers grown on the reconstructed V(100)-(5×1) substrate has been investigated. We found that the deposition of silver on the substrate kept at room temperature results in the formation of silver clusters. Annealing to well defined temperatures leads to the formation of a uniform 1 or 2 ML thick silver film. Larger thicknesses are obtained by the subsequent RT deposition. During the temperature treatment the (5×1) vanadium reconstruction underneath the silver

layer is removed by the displacement of oxygen (and carbon) atoms. This enables unsuppressed increase of the silver islands diameter and almost complete lifting of the vanadium reconstruction and eventually the formation of the uniform (1×1) silver layer. According to the results, for thicknesses up to 10 ML, silver grows in registry with the substrate, i.e. the silver has tetragonal structure. We believe that such structure is stable due to the relatively small vanadium (100) – silver (100) mismatch and, probably, the small difference in the volume energies of tetragonal and fcc silver. Since the ordered silver layer lifts the (5×1) reconstruction of the V(100) surface, Ag/V(100)-(5×1) is completely equivalent to the ordered Ag/V(100).

## **7.2. s-p derived QW states**

### *7.2.1. Dispersions and effective masses*

The analysis of the in-plane effective masses of the s-p QW states,  $m_{xy}$ , reveals that there is a strong variation of  $m_{xy}$  with film thickness. We note that this high-resolution characterisation shows that some of the previously measured data should be substantially corrected. For instance, the effective masses published in a study of Valla et al. [112] differ significantly from what we report here. For the 1 and 2 ML s-p QW states they reported 2.2 and 3.1  $m_e$ , respectively. We believe that the difference between the present study and the results of the previous investigation [112] originates from several reasons. First of all, both the energy and angular resolution used in the present measurements are an order of magnitude better than those used in the earlier studies. Further, the best results are obtained if one performs a parabolic fit in a narrow region around the Brillouin zone centre since the studied quantum well states tend to level off away from the center of the Brillouin zone, thus increasing the effective mass on moving away from the gamma point (as we have measured for the 2 and 5.5 ML thick silver film and as it was observed in some previous measurements [174]). The use of only a small number of experimental points can therefore lead to an erroneous estimate of the effective mass, as we believe was the case in the measurements in Ref. [112]. We conclude that the present results of much more accurate measurements give more reliable s-p QWS binding energies and effective masses.

Large values of  $m_{xy}$  are typically associated with more localised states and it was argued previously [112,175] that the larger values seen in the thinnest films must be related to hybridisation of the QW states with the substrate d-bands. Recently, Ernst et al. [176] performed ab initio calculations for the Ag/V(100) system. The obtained results suggest a pronounced effect of hybridisation between Ag s-p states and V d states, although they did not calculate the actual s-p QW states effective masses (dispersions). We believe, however, that one should take this calculated hybridisation strength with some reservation. The hybridisation is evaluated from the charge redistribution at a Ag-V interface. In this calculation

## 7. Ag/V(100) DISCUSSION

the V and Ag lattice parameters perpendicular to the surface were taken to be fixed, i.e. without self consistent relaxation of lattice parameters and charge transfer, which may lead to an inaccurate charge transfer estimate. Charge transfer effects influence the work function. According to the calculation there is an increase of the work function by 1.2 eV for 1 ML Ag. On the other hand, we find that experimentally measured value changes are less than 0.2 eV.

From HRARPES measurements for 2 and 5.5 ML Ag/V(100) we observe that the QW states levelling off coincides with the increase of the photoemission intensity at the Fermi level associated with the dispersion of an electronic band that crosses the Fermi level. The QW states dispersions that we measure (see Fig. 6.14-6.16) exhibits typical characteristics of the so-called avoided crossing [177] indicating hybridisation. Moreover, according to the unpublished data by Pervan and Milun [174], the electronic structure of the V(100) surface measured by ARPES along the  $\Gamma M$  direction in the surface Brillouin zone exhibits the dispersion of the  $G_3$  vanadium bulk band that crosses the Fermi level at about 1/3 of the Brillouin zone (Fig. 7.3).

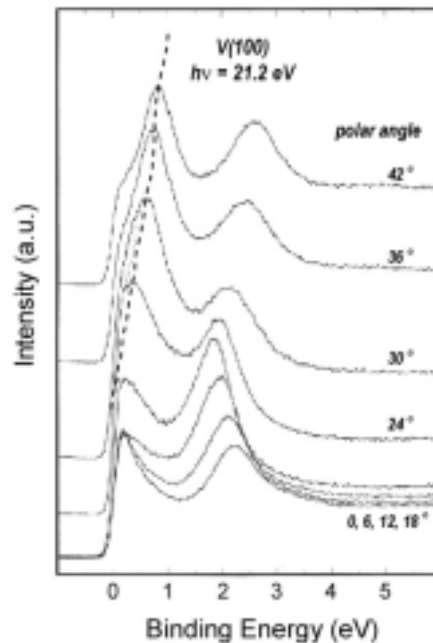


Fig. 7.3. [174] The photoemission spectra taken from the clean V(100) surface obtained at different polar angles (along the  $\Gamma M$  direction in the surface Brillouin zone). The dashed line indicates a dispersion of the bulk band  $G_3$  that crosses the Fermi level at about 20-24°.

We argue that this vanadium bulk electronic band may be responsible for the dispersion behaviour measured for the 2, 5 and 6 ML s-p QW state. If the actual avoided crossing takes place the  $G_3$  band would comprehend some of the s-p character, i.e. hybridise with silver film s-p states and would disperse back towards the Fermi level, whereas the QW state would comprehend some of the d character and would disperse in a direction away from the Fermi level, as it is observed in the experiment. For 2 ML Ag/V(100) from the

photoemission spectrum taken at  $\cong 0.35 \text{ \AA}^{-1}$  we judge that the width of the region that characterises the avoided crossing is about  $\Delta \cong 0.4 \text{ eV}$  (see Fig. 6.15). Such hybridisation could, in turn, explain a relatively high QW state effective mass measured in the Brillouin zone center. On the other hand, for 5 and 6 ML QW states the hybridisation parameter  $\Delta$  is smaller and for 6 ML QW state it is about  $\Delta \geq 0.1 \text{ eV}$ , indicating less pronounced hybridisation.

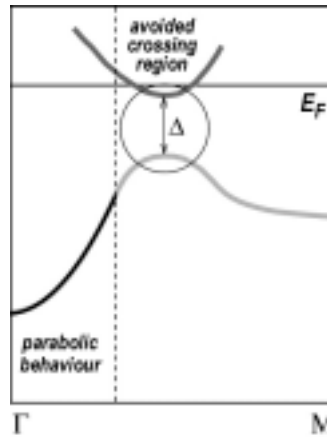


Fig. 7.4. Schematic drawing of the proposed QW s-p –  $G_3$ -d hybridisation.

The proposed hybridisation scheme is illustrated in Fig. 7.4. It is reasonable to expect that the hybridisation is favoured for QW states in thinnest films with smallest binding energies that would sense the presence of the substrate state most intensively. Within this picture we can explain the mostly pronounced enhancement of the effective mass for the 2 ML s-p QWS:

- It is highly localised, thus having a large amplitude at the interface allowing substantial overlap with the substrate electronic structure
- It is located relatively close to the Fermi level thus strongly sensing the  $G_3$  band presence and dispersion.

According to the dispersions and masses measured in the photoemission experiment it seems that all s-p QW states included in this study hybridise with the substrate. The correlation is evident from the data of Fig. 6.17. The special case is the 1 ML QW state which is spatially mostly localised, but the combined effects of an amplitude at the interface and the binding energy position compared to the  $G_3$  band are much smaller than for 2 ML Ag/V(100). Further work, both experimental and theoretical, is clearly warranted to investigate these hybridisation effects more detailed.

### 7.2.2. Temperature induced static effects

In the next two sections simple theoretical models that tend to qualitatively and quantitatively explain the measured temperature induced behaviour are introduced. The s-p quantum well state is the bound-state solution of the one-dimensional Schrödinger equation

## 7. Ag/V(100) DISCUSSION

where the well potential is determined by the substrate band gap on one side and the solid-vacuum interface on the other. Within this description, it is clear that the width of the well is reflected directly in the energy of the QW bound states – there must be a matching of the electron wavelength to the well width. The width corresponds to an integral number of half-wavelengths of the QW state wave function modified by the presence of an evanescent tails extending into the substrate and the vacuum. Consider, now, the influence of thermal expansion on this system. Heating will lead to an increase in the film thickness and thus a widening of the potential well. The associated increase in the QW state wavelength results in a lower energy relative to the bottom of the well (Fig. 7.5). If the Fermi energy remains fixed, the net effect is to increase the binding energy of the QW state relative to the Fermi level, as observed in the present experiments.

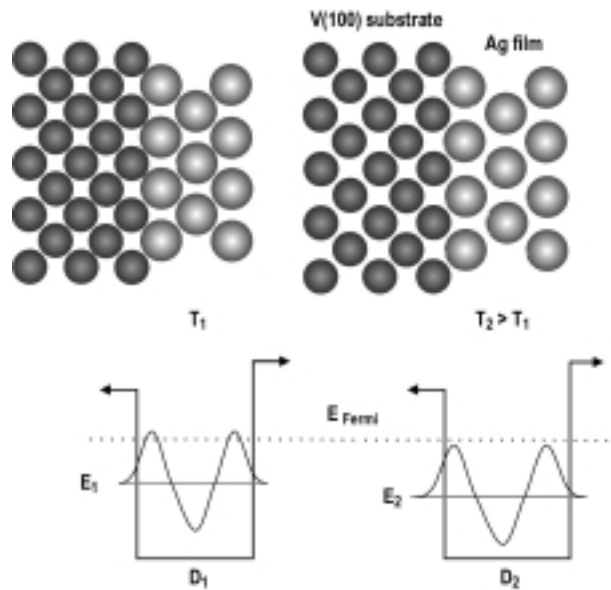


Fig. 7.5. Static temperature dependent width of the QW state potential and the accompanying QW state binding energy change. Note that in this illustration the Fermi level does not change its position, which is generally not true.

Of course, the complete picture will reflect not only the changes in the film, but also the temperature induced changes in the substrate Fermi energy. The relative importance of these two contributions can be deduced from the thermal expansion coefficients of the two materials;  $17 \times 10^{-6} \text{ K}^{-1}$  for Ag and  $8 \times 10^{-6} \text{ K}^{-1}$  for V, respectively [178]. The relative difference clearly favours the dominance of the increasing Ag film thickness over the expanding substrate. The value for Ag is not strictly the one relevant to the present situation, because the Ag film is pseudomorphic centred tetragonal. The large difference in linear expansion coefficients is consistent with the fact that the cohesive energy of bulk V is almost twice as large as that of bulk Ag [81]. Indeed, if we note that for a pseudomorphic Ag film on V(100) the thermal expansion of the film parallel to the surface is constrained to the low value dictated by bulk V, we can anticipate that the expansion coefficient in the Ag film perpendicular to the surface will be even larger than that in bulk Ag.

## 7. Ag/V(100) DISCUSSION

This explanation of the binding energy shift is also consistent with the quantitative behaviour for the QW states in films of different thickness. As the film thickness increases, the number of nodal planes in the QW state wave-function also increases. Thus, the wavelength of the different quantum well states is very similar and the increase in wavelength induced by the thermal expansion of the film thickness must also be approximately constant. The exception to this simple generalisation is the behaviour of the 1 ML Ag film. In this case it is clear that the bulk Ag thermal expansion behaviour cannot be an accurate guide to the expected temperature dependence of the film thickness. Indeed, the V-Ag bonding at the interface is stronger than the Ag bulk cohesive energy (as implied by the high-temperature stability of this layer [165,166]). As such we might anticipate a lower thermal expansion of this bond than the equivalent in a bulk alloy. On the other hand, the asymmetry of the forces experienced by an atom in the outermost layer of a surface can be expected to lead to an enhanced thermal expansion coefficient (e.g. the enhanced vibrational amplitudes perpendicular to the surface [179]), as was recognised many years ago [180].

It is rather straightforward to quantify these arguments. In the case of a simple free-electron metal the Fermi energy,  $E_F$ , is proportional to the reciprocal of the square of the lattice parameter. It is therefore easy to show that the temperature dependence of the Fermi energy due to thermal expansion of the crystal is given by

$$dE_F/dT = -2E_F\alpha_B \quad (7.1)$$

where  $\alpha_B$  is the coefficient of linear expansion of the solid. Applying this model to the vanadium substrate, with a value for  $E_F$  of 5.2 eV, we obtain a temperature dependence of the Fermi energy of  $-8.3 \times 10^{-5}$  eV  $K^{-1}$ . The fact that vanadium is a transition metal rather than a free-electron metal, will have the effect of reducing the temperature dependence of the Fermi energy by a factor determined by the effective masses of the bands which cross the Fermi level. If the overlayer film thickness has a coefficient of thermal expansion of  $\alpha_F$ , a QWS with an energy (relative to the bottom of the well) of  $E_{QW}$  will have a temperature dependence of

$$dE_{QW} / dT = -2E_{QW}\alpha_F \quad (7.2)$$

and taking  $E_{QW}$  as 4 eV (i.e. a binding energy relative to the Fermi level of 1.2 eV) and equating the expansion coefficient of the film thickness to the linear coefficient of bulk silver yields a result of  $-13.6 \times 10^{-5}$  eV  $K^{-1}$ . This would predict an increase of the QW state binding energy relative to the Fermi level of  $0.53 \times 10^{-4}$  eV  $K^{-1}$ , about a factor of 2-3 smaller than the experimentally measured values. However, the presence of the d-band crossing of the Fermi level in the vanadium substrate will increase this value. Further, the tetragonal distortion in the silver overlayers will result in an increase to  $2.0 \times 10^{-4}$  eV  $K^{-1}$ , slightly larger than the experimental values. Note that the trends in the experimental energy shifts for the different film thickness are consistent with this model. Specifically, the shifts should be smallest for the QW states with the lowest energy relative to the bottom of the well (i.e. the largest binding energies relative to  $E_F$ ), and largest for the smallest binding energy QW states. This correlation is seen in Table 6.2 and 6.1, which include both the thermal shift coefficients and

the QW state binding energies.

All previous studies of the temperature dependence of bulk valence-state binding energies (e.g. Refs. [181,182,183,184]) have shown a decrease in binding energy with increasing temperature as noted above, and indeed the same behaviour has been observed for Shockley surface states on surfaces of Cu [133], Ag [135], Au [135] and Ga [142]. In contrast, an increase in binding energy with increasing temperature has been observed for d-like Tamm surface states on Cu(100) and Cu<sub>3</sub>Au(100) [185]. However, no simple quantitative description of Tamm states, such as the phase model exists, so that direct comparison is not possible. Indeed, the authors of Ref. [185] note that the shift “most probably reflects the variation of the surface potential within the outermost layer” and that “quantitative estimates based on realistic three-dimensional models are not available yet”.

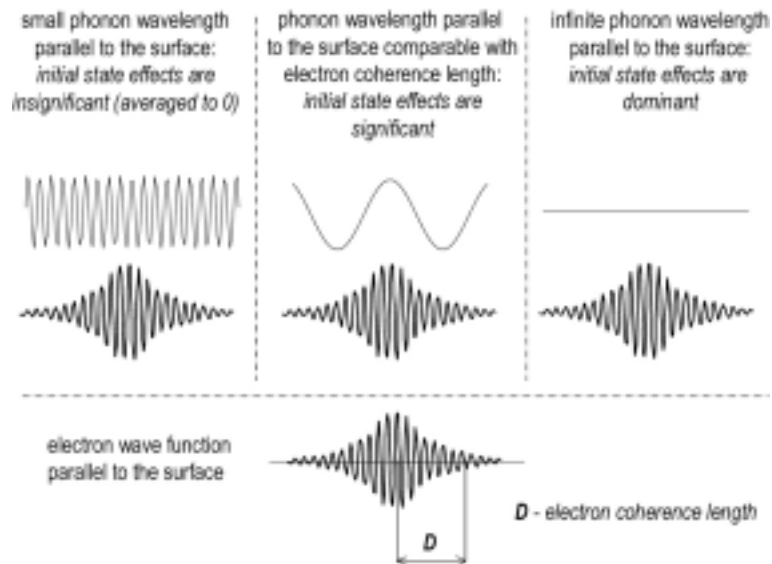


Fig. 7.6. Possible initial state influence to the QW state peak width.

In view of the success of the simple model in describing the temperature-dependent binding energies of the QW states, we have considered an extension to account for the observed temperature dependence of the ARPES peak widths. However, while the thermal expansion at the surface influences the well-width statically, in the same way across the whole surface, the surface phonons produce local variations in the well width which will only influence the apparent well width if the phonon wavelength is large compared with the coherence length of the QW states parallel to the surface (Fig 7.6). Such states make up only a small component of the full spectrum of surface phonons. The resulting effect on the QW state broadening is therefore negligible and we discuss this broadening only in terms of final-state electron/photohole-phonon coupling.

### 7.2.3. Temperature induced dynamic effects

We find strong variation in hole-phonon coupling as a function of film thickness, and some of these coupling constants are very large relative to the values for bulk Ag ( $\lambda = 0.23$  [128] and  $\lambda = 0.13$  [47,129]). Within these films we expect that the largest vibrational amplitudes will be associated with the soft modes of the outermost surface layer, and as there is a large potential step at this surface-vacuum interface, it seems likely that the coupling of the photohole to this surface vibrational mode should be particularly strong.

We assume that as the surface atoms move, they locally deform the potential well seen by the electrons in the film. It is convenient to assume that the total effective potential,  $V$ , can be written as a pairwise sum of the interactions between the electron at  $\mathbf{r}$  and a particular crystal site  $j$  positioned at  $\mathbf{r}_j$ :

$$V(\mathbf{r}) = \sum_j v(\mathbf{r} - \mathbf{r}_j) \quad (7.3)$$

The change of the effective potential introduced by the time dependent oscillation of the atoms in the sample can be written as

$$\Delta V(\mathbf{r}) = - \sum_j \nabla v(\mathbf{r} - \mathbf{r}_j) \cdot \mathbf{u}_j \quad (7.4)$$

where  $\mathbf{u}_j$  represents the deviation of the atom at crystal site  $j$  from its equilibrium position. By expanding the atomic displacements as a superposition of normal modes characterised by the mode number,  $s$ , and parallel wave vector  $\mathbf{Q}$ , we can evaluate the state-to-state transition amplitude per unit time,  $w_{fi}$ , which is defined in the first order perturbation treatment (one phonon created or destroyed in the final state of the system) by the Fermi golden rule as

$$w_{fi} = \frac{2\pi}{\hbar} |M_{fi}|^2 \delta(E_f - E_i \pm \hbar\omega(\mathbf{Q}, s)). \quad (7.5)$$

Here,  $M_{fi}$  is the matrix element of the perturbation defined by Eq. (2.14) now calculated with the wave functions of the whole system (electrons + phonons).  $E_f$  and  $E_i$  are the final and initial energies of the electronic system. For the matrix element,  $M_{fi}$ , we can write

$$M_{fi} = \sum_j \int d^3r \Psi_f(\mathbf{r}) \nabla v(\mathbf{r} - \mathbf{r}_j) \Psi_i(\mathbf{r}) \langle n_i(\mathbf{Q}, s) \pm 1 | \mathbf{u}_j | n_i(\mathbf{Q}, s) \rangle, \quad (7.6)$$

where  $\Psi_f$  and  $\Psi_i$  are the final and initial wave functions of the electronic system and  $|n_i(\mathbf{Q}, s)\rangle$  is the wave function pertaining to phonons in the crystal initial state. For the electronic wave-functions we take

$$\Psi(\mathbf{r}) \sim e^{i\mathbf{K}\cdot\mathbf{R}} \phi(z) \quad (7.7)$$

where  $\mathbf{K}$  is the wave vector of the electron parallel to the surface plane and  $\mathbf{r}=(\mathbf{R}, z)$  where  $\mathbf{R}$  is the projection of vector  $\mathbf{r}$  onto the surface plane and  $z$  is the component perpendicular to the surface plane.  $\phi(z)$  is the solution to the one-dimensional Schrödinger equation in the effective potential profile in the  $z$ -direction. The single particle lifetime,  $\tau$ , is generally given by

$$\frac{1}{\tau} = \sum_f w_{fi} \quad (7.8)$$

and we can calculate the effective phonon-induced width of the initial state as  $\Delta E = \hbar/\tau$ . The final formula for the phonon-induced lifetime of the photo-hole created in the QW band  $i$  is:

$$\frac{1}{\tau} = \frac{A_c}{M\hbar^2} \left[ \sum_f \{m_{xy}^f |T_{fi}|^2 (2n(\omega_0) + 1) \frac{Y^2(Q_{f,i})}{\omega_0}\} + m_{xy}^i |T_{ii}|^2 (n(\omega_0) + 1) \frac{Y^2(Q_{i,i})}{\omega_0} \right] \quad (7.9)$$

where  $Q_{f,i}$  is the wave-vector of the phonon emitted (or absorbed) given as

$$Q_{f,i} = \frac{\sqrt{2m_{xy}^f}}{\hbar} (E_i(\mathbf{K}=0) - E_f(\mathbf{K}=0) \pm \hbar\omega_0), \quad (7.10)$$

where  $E_i(\mathbf{K}=0)$  and  $E_f(\mathbf{K}=0)$  are the energies of the quantum well states at the bottom of the  $i$ -th and  $f$ -th QWS band, respectively.  $A_c$  is the area of the surface Wigner-Seitz cell,  $M$  is the mass of the surface atom and  $n(\omega_0)$  is the Bose-Einstein distribution function.

Equation (7.9) was derived assuming that the surface atoms vibrate in the  $z$  direction with only one characteristic frequency,  $\omega_0$ . The effect of longitudinal surface phonons on the hole lifetime was investigated numerically and found to be much smaller than the corresponding effect from the  $z$ -polarised surface phonons. The coupling of holes to the vibrations of the atoms located in the crystal planes below the surface plane was neglected. The dispersions of the QW states were taken to be isotropic and parabolic parallel to the surface plane with a mean effective mass,  $m_{xy}^f$  which depends on the particular QW state,  $f$ , in question. ‘‘Recoil’’ of the hole in the process of phonon emission or absorption was neglected. It was assumed that the change of the potential is uniformly distributed over the particular Wigner-Seitz cell. This assumption leads to  $Y$ -factors of the form

$$Y(Q) = 2A_c \frac{J_1(x_{WS})}{x_{WS}} \quad (7.11)$$

where  $x_{WS} = QR_{WS}$ , and  $R_{WS}$  is the effective radius of the Wigner-Seitz cell.  $J_1$  is the first-order Bessel function. If we represent the one-electron effective potential profile in the direction perpendicular to the surface with the asymmetric square well, the transition matrix element  $T_{fi}$  acquires a particularly simple form:

$$|T_{fi}|^2 = V_R^2 |\phi_f(z=0)|^2 |\phi_i(z=0)|^2. \quad (7.12)$$

Here,  $V_R$  is the height of the film/vacuum interface potential step located at  $z=0$ .

Note that there are two types of possible matrix element transitions (Fig. 7.7):

- intra-band, and
- inter-band.

The first one is related to the transitions originating from a single QW state band and the other one includes the transitions between the QW state bands. For intra-band transitions the

electron can relax the hole from the bottom of the dispersion only accompanied by phonon emission, while for inter-band transitions, in principle, the other way around is also possible.

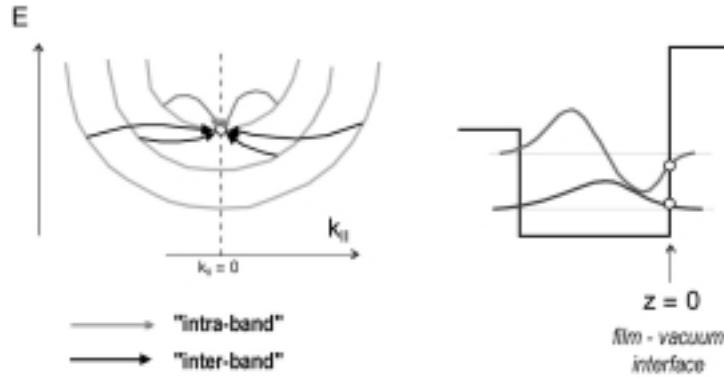


Fig. 7.7. Intra- and inter-band phonon assisted electron-hole transitions.

#### 7.2.4. Temperature induced effects - discussion

The significance of the derived equations is that if an electronic state of interest is localised near the surface, and thus has a significant wave function amplitude in the region of rapid change in potential at the surface-vacuum interface, and further if there are also final states, similarly localised, to which energy- and momentum-conserving transitions are possible, then one can expect the influence of the surface layer vibration to be strong. This argument, of course, should also be relevant to intrinsic surface states of clean surfaces and may account for the widely observed electron-phonon coupling enhancement for such states. It should be noted that Eq. (7.9) is equivalent to Eq. (5) from the paper by Hellsing et al. [124]. Although the final expressions are the same, the present approach is simpler in the parameterisation of the interaction matrix elements and does not rely on the results produced by the density functional calculations.

Our theory also reproduces the Q-dependence of the matrix elements, accounting for the finite size of surface atoms, in a very simple and straightforward fashion, which is a consequence of the assumption of the pairwise additivity of the electron-site potentials (Eq. (7.3)). In order to evaluate Eq. (7.9) we have assumed that the characteristic frequency,  $\omega_0$ , is independent of film thickness in the range that we have explored experimentally. In the calculations we have taken  $\hbar\omega_0=8.0$  meV (the Rayleigh wave phonon frequencies of Ag(111) and Ag(100) at the edge of the surface Brillouin zone are  $\hbar\omega_0\sim 8.0$  meV [186,187]). The asymmetric square well potential profile has a step at the film-substrate interface, which is 7.6 eV high, and another step at the film-vacuum interface ( $V_R$ ) which has a height of 9.7 eV. The Fermi level is positioned at 5.6 eV above the bottom of the quantum well. We have assumed that each monolayer of Ag contributes 1.96 Å to the well width [112,165,166]. This potential profile reproduces both the measured binding energies of quantum well states and the magnitude of the s-p propagation gap into V(100).

## 7. Ag/V(100) DISCUSSION

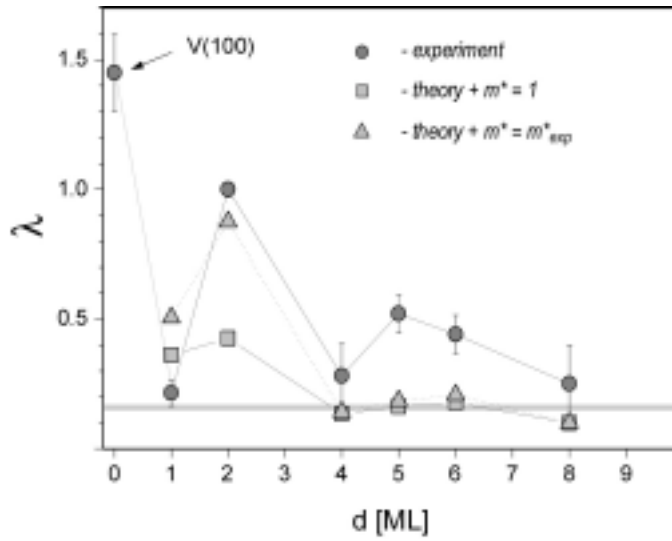


Fig. 7.8. The h-p coupling constant ( $\lambda$ ) as a function of Ag thickness. Solid circles are experimentally obtained values. Calculated values of  $\lambda$  assuming an effective mass  $m^* = 1$  for all QW states are shown as squares, while calculated values that include experimentally determined values of effective mass for each QW state are shown as triangles. The experimental value of  $\lambda$  for the surface state on V(100) is shown at zero film thickness while  $\lambda$  for bulk silver is indicated by the thick grey line parallel to the abscissa.

Fig. 7.8 shows values of the h-p coupling constant derived from the slope of the calculated widths ( $\hbar/\tau$ ) in the high temperature range. The open squares correspond to values of  $\lambda$  calculated assuming that the effective mass of all the QW states around the centre of the Brillouin zone is equal to one. For comparison, full circles are experimentally obtained values. These theoretical results reproduce the experimentally-observed oscillation of the coupling constant, even if free-electron like dispersion of all the QW states is assumed. In this case changes in the coupling appear to arise mainly from the different localisation of the states, and specifically, the amplitude of the associated wave-functions at the surface barrier. These amplitudes are influenced by the QW state binding energy, the more shallow states extending further into the vacuum, and by the degree of localisation as determined by the film thickness, thicker films having more extended states which (when normalised) have lower amplitudes at the surface. There is also some influence on the coupling in this simple model associated with differences in the available phase space for the photo-hole decay. In particular, only a single QW state exists in the 1 ML Ag film so only intra-band transitions are possible. For the thicker films both inter- and intra-band transitions can occur. However, calculations allowing only intra-band transitions in all films produce results similar to those shown in Fig. 7.8, indicating that the inter-band phase space consideration is secondary.

Notice however that the above equations contain a dependence on the mean effective electron mass,  $m_{xy}$  of each QW state, and this parameter could be extracted from

our experimental determination of the dispersion of the QW state energies around normal emission. As it was already discussed, the electron effective mass varies significantly for different states, and incorporating these values into the theoretical calculations gives the triangles in Fig. 7.8. Now significantly better agreement with the experimental  $\lambda$  is accomplished. The fact that this improvement is so marked, however, is a reflection of the fact that the qualitative character of the variation of electron effective mass with thickness is actually very similar to that of  $\lambda$  in our experiments and in the simple theory. Indeed, this correlation is essentially the same as that favouring an important role for the surface phonons in influencing the hole-phonon coupling. Still, our results clearly indicate the importance of the surface phonon coupling for the oscillatory behaviour of  $\lambda$  values seen in our work.

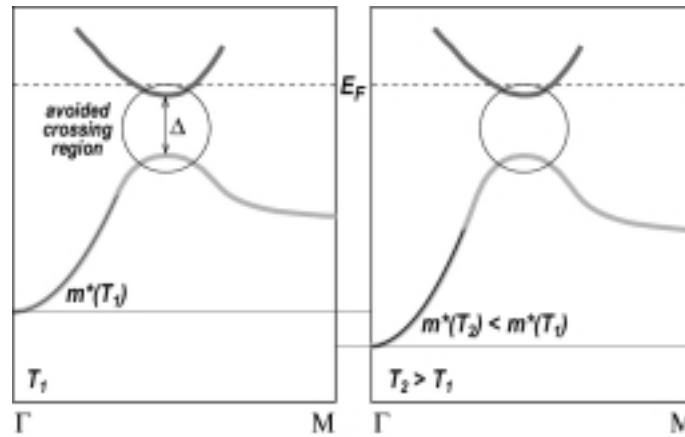


Fig. 7.9. A scheme describing temperature dependent behaviour of the Ag/V(100) s-p quantum well state effective mass.

And finally, we briefly discuss the observed temperature dependence of the QW state effective mass. As argued in section 7.2.1 we believe that the relatively large effective masses are due to the hybridisation effect. On the other hand, the QW state binding energy shifts towards the higher values with increasing temperature. The avoided crossing region is determined by the position of the vanadium  $G_3$  band. From the same argumentation introduced in 7.2.2 for this vanadium bulk band we suppose an insignificant temperature induced shift (compared to the effects in silver), thus making it fixed. We make the further assumption that the width  $\Delta$  of the hybridisation region, or equivalently the hybridisation strength, does not depend on the temperature (also fixed). Under such circumstances the temperature dependent QW state binding energy would allow a modification, i.e. a decrease of the QW state effective mass. It is readjusted with respect to the relative change of its binding energy in the center of the Brillouin zone and fixed hybridisation region. In Fig. 7.9 a scheme is drawn where the s-p quantum well state effective mass behaves according to the described temperature dependence.

## 7.2.5. Temperature induced effects beyond the simple model

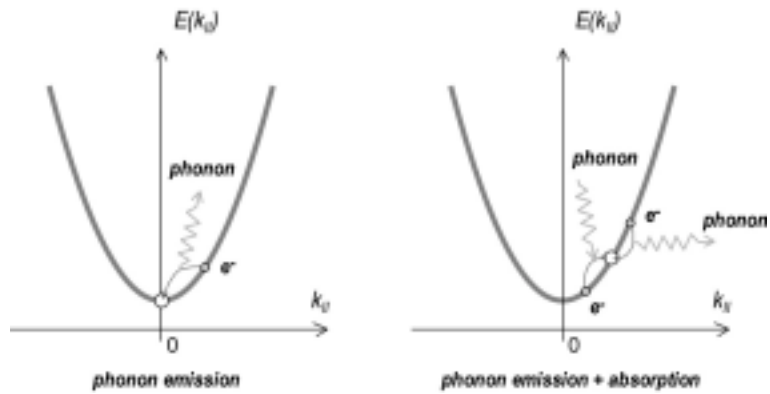


Fig. 7.10. Schematic description of the phonon-assisted intra-band transition channels at  $k_{||} = 0$  (phonon emission) and away from  $k_{||} = 0$  when an additional intra band channel (phonon absorption) opens.

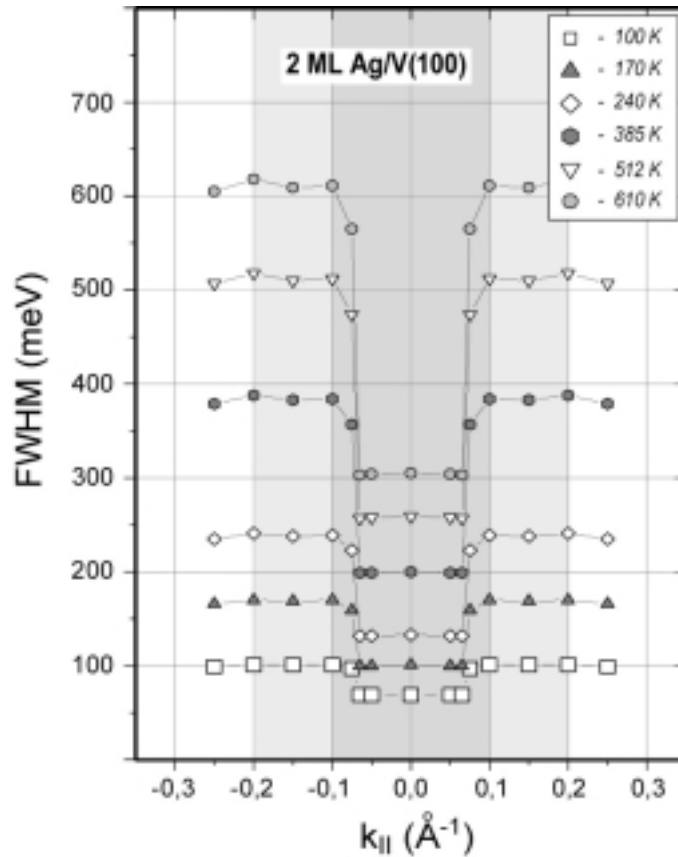


Fig. 7.11. Calculated  $k_{||}$  dependence of the phonon contribution to the photoemission line width for 2 ML Ag/V(100) at different temperatures as indicated in the figure. Shaded regions are the same as in Fig. 6.25.

## 7. Ag/V(100) DISCUSSION

When the photohole moves away from the centre of the surface Brillouin zone an additional channel becomes available for the hole-phonon scattering process. While for intra-band transitions at  $k_{||} = 0$  it is possible for the photohole only to adsorb a phonon, the additional channel enables the intra-band transition if the hole emits a phonon (Fig. 7.10). For 2 ML Ag/V(100) within the region of parabolic dispersion we have measured the increase of the photoemission linewidth as the  $k_{||}$  increases (see Fig. 6.25). Using our simple model (Eq. (7.9)) we calculate the hole-phonon contribution for the 2 ML QW state and plot it as a function of  $k_{||}$  in Fig. 7.11 for the same sample temperatures that we have measured in Fig. 6.25. Note that the calculated values from Fig. 7.11 do not include the hole-impurity or the hole-electron contributions to the linewidth which results in a rigid shift between the points at  $k_{||} = 0$  in Fig. 6.25 and 7.11. One observes that the calculated temperature dependent width is essentially characterised with an abrupt, step-like increase.

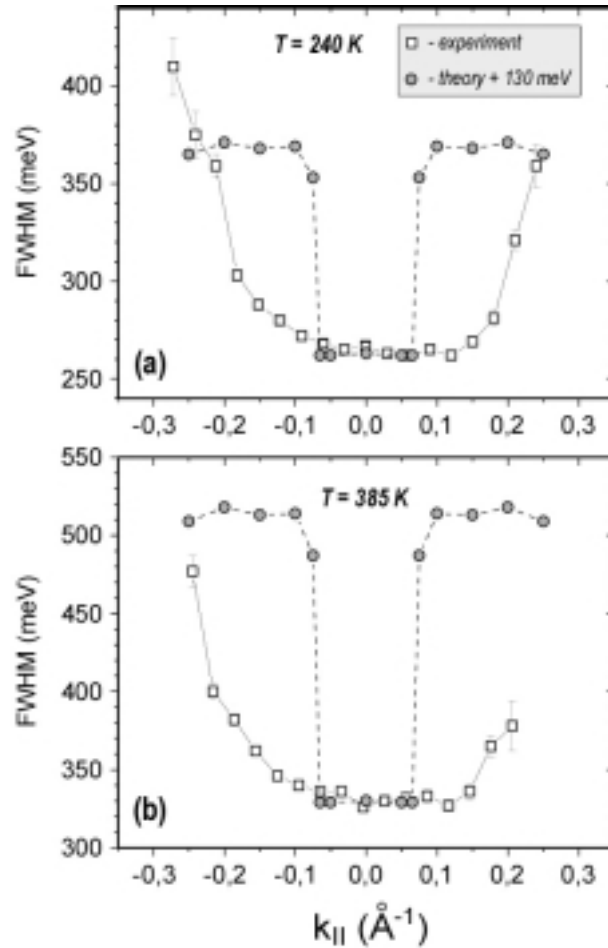


Fig. 7.12. Comparison of measured (squares) and calculated (circles) temperature induced photoemission line widths for (a) 240 K and (b) 385 K. The rigid offset of 130 meV is applied to align measured and calculated data (see the text for details).

For comparison of the experimental and theoretical data in Fig. 7.12 for 240 and 385 K we align the measured and calculated values (which are now shifted for a constant factor to coincide with the measured points in the centre of the Brillouin zone). Although the simple

theory managed to properly quantify the electron-phonon interaction in the centre of the surface Brillouin zone, we find less good agreement going away from that point. The biggest disagreement is in a relatively moderate increase of the photoemission line width found in the experiment vs. an abrupt increase that should take place according to the theory.

This motivates us to revisit the basic suppositions and approximations used in the calculation. The roughest assumption is that there is only one optical phonon frequency (Rayleigh wave) important for the electron-phonon interaction and that the whole phonon density of states is located at the surface. Indeed, taking into account a more realistic phonon system (bulk + surface) Eiguren et al. [48] and Hellsing et al. [131] managed to properly describe lifetime broadening of the Cu(111) and Ag(111) surface state as a function of binding energy (see Fig. 2.10 and 4.14). There is greater importance of electron-electron interaction in these systems than for Ag/V(100), and there was need to incorporate it in the calculation. Note that the binding energy scale that these authors use and the  $k_{||}$  scale that we use are directly related. The observed and calculated behaviour is characterised by a relatively moderate increase of the line width, similarly as for Ag/V(100).

An additional problem related to the simplicity of our model that may cause the discrepancy between the theory and experiment is that the surface Wigner-Seitz cell that appears in the photoemission linewidth integration is spherical, which in combination with the single phonon frequency in the system is responsible for the abrupt step-like increase. And finally, this calculation, as well as more improved theories [48,131,132] do not account for the possible importance of the multi-phonon processes (higher order perturbation) in the electron-phonon interaction.

### 7.2.6. *Film-vacuum vs. film-substrate interface influence*

Recently Luh et al. [130] reported a s-p QW hole-phonon coupling dependence on film thickness for Ag/Fe(100) similar to that we observe for Ag/V(100), i.e.  $\lambda$  exhibits oscillatory variation with film thickness. For a 13 ML thick film characterised by the existence of two QWS they have also measured that  $\lambda$  exhibits a binding energy dependence. A model was developed in order to explain the observed behaviour. Within this model enhancement and the oscillation of  $\lambda$  is due to the fact that  $\lambda/\lambda_{\text{Bulk}}$  is proportional to  $|\Psi(z_i)|^4$ , where  $z_i$  describes the position of the film-substrate interface (Eq. (3) of Ref. [130]). The importance of the film-vacuum interface is completely neglected which was supported by the argumentation that the “potential step at the vacuum side is not as sharp as that at the film-substrate interface”, which makes it unimportant in the scattering probability. In this calculation the QWS wave functions (and their probabilities) end with almost zero amplitude at the film-vacuum interface. This was explained in terms of almost perfect reflectivity at this interface.

In contrast, for Ag/V(100) we calculate that in the limit of ultra thin thicknesses each QW state has a significant amplitude at both interfaces. We have reasonably supposed that the vibrations in the system are mainly located at the topmost silver layer, which accordingly indicates the importance of the film-vacuum interface. Note that our results, summarised through Eq. (7.12), account for the phonon assisted electron transitions whose amplitudes are coupled at the surface – there where the phononic vibrations in the system are expected to be the most intensive and thus initiate transitions. As we have shown, the inter-band processes are more important than the intra-band processes in which case Eq (7.12) becomes similar to the Eq. (3) from Ref. [130], but here evaluated at the film-vacuum interface:

$$|T_{fi}|^2 = V_R^2 |\phi_i(z=0)|^4 \quad (7.13)$$

Interestingly, for two apparently similar systems, silver on a transition metal surface, almost the same electron-phonon coupling strength behaviour is measured, but qualitatively and quantitatively explained based on different assumptions. Additionally we mention that using the theory described in this thesis Šiber [188] has calculated that for Ag/Fe(100) the surface contribution to the hole-phonon coupling plays an important role compared to the bulk-like contribution for thicknesses such as 14 ML (20%) or 19 ML (14%) and that in the limit of ultra thin films it properly reproduces the measured behaviour for Ag/Fe(100) [189].

Recently developed more sophisticated theories that treat the hole-phonon coupling in the systems of reduced dimensionality (surface and quantum well states) [48,131,132] suggest that the hole-phonon contribution to the reduction of the quasiparticle lifetime crucially depends on the localisation of the phonon modes at both, the film-vacuum and the film-substrate interface. Both regions are of particular importance due to the fact that the local deformation potential has the largest values there. Calculating the phonon dispersion for a Cu(111) surface from a 31-layer slab calculation (see Fig. 4.14), Hellsing et al. [131] have shown that taking into account bulk and surface phonon states, the surface Rayleigh mode gives substantial, almost dominating contribution to the hole-phonon coupling in the system. Following such argumentation we summarise that for Ag/V(100) both interfaces should be considered, but expect that the e-p coupling enhancement is dominantly caused by the localisation of the phonon system at the surface, i.e. film-vacuum interface.

### **7.3. d-derived QW states**

#### **7.3.1. Phase accumulation analysis for the d-band QWS**

Despite the inherent simplicity and somewhat crude approximations the multiple reflection model has been successfully used to account for the energy of quantum well states and resonances of s-p (see section 4.1.2) and, recently, d-symmetry [114,115,190]. We remind that the phase accumulation condition has a form written in Eq. (4.3). We used a

standard functions to describe the energy dependence of the phase shift at the vacuum side  $\phi_B(E)$  of the film. In the case of incomplete confinement the phase shift  $\phi_C(E)$  can become a complex function [191] and a proper choice of  $\phi_C(E)$  is less clear. Two types of functions have been used in the literature to generate the energy dependence of the wave vector  $k(E)$ ; one derived from the two-band nearly free electron model [77] and the second one generated by a tight-binding model for the simple linear chain [61,115]. Here we chose the simplest possible assumption and set the value for  $\phi_C(E)$  to  $0.21 \cdot \pi$ . Thus, the change in the total phase is derived entirely from the film thickness and the vacuum barrier. We have found that this approximation reproduces silver 4d energy bands with satisfying accuracy.

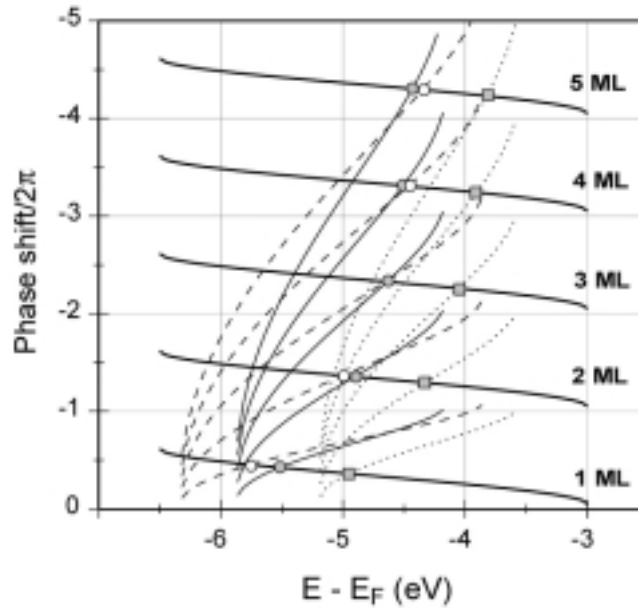


Fig. 7.13. Graphical solution of the phase accumulation model equation for d-QWS in silver films on V(100). The dashed, thin solid and dotted lines represent a phase change associated with the different silver bulk bands  $k(E)$ , while solid bold curves represent a phase change at the vacuum and the interface side. Notice that for each silver film thickness only the highest energy solutions are marked (open and solid circles and solid squares).

Fig. 8 shows a graphical solution of equation (4.3). In order to account for the energy of the QW states,  $P_1$  and  $P_2$ , we have generated three sets of  $k(E)$  functions which are associated with three bulk silver 4d bands ( $\Delta(7)$ ,  $\Delta(6)$  and  $\Delta(7)$ ). To simplify comparison with the photoemission data in Fig. 6.34 we have marked in Fig. 7.13 only the highest energy solutions for each branch of  $k(E)$ , and for each silver film thickness ranging from 1ML to 5 ML. We see that most of the trends observed experimentally are reproduced by the phase accumulation model. The solid squares reproduce reasonably accurately the shift of the  $P_1$  QW state to smaller binding energies with increasing film thickness including the effect we have already remarked upon of a particularly large decrease of binding energy between the 1 ML and 2 ML films. The separation between the solid and open circles accounts for the

observed splitting of the  $P_2$  QW state which decreases with the film thickness in such a way that the splitting collapses for a film thickness of 3 ML. The phase accumulation model clearly demonstrates why this is the case. For thicknesses greater than 3 ML the  $P_2$  peak splitting should increase again. However, due to the increasing number of states generated for each new silver layer, and the width of the peaks, it is no longer possible to trace the splitting experimentally.

### 7.3.2. Reflectivity of the vanadium-silver interface

There are several factors which suggest that the 4d electrons in the silver films are well-confined within the film, despite the fact that barrier at the vanadium-silver interface is not due to an absolute band gap in the substrate along the surface normal, but rather to an energetic offset of states of the same symmetry in the substrate and overlayer. One indication of this is the complete lack of dispersion of the observed QW state energies on perpendicular momentum transfer (achieved at different photon energies); if the states in the Ag film coupled to extended substrate bands some degree of dispersion would be expected. Notice that this statement is not unique to d-states for which even the bulk bands are mainly quite flat – the same absence of any photon energy dependence in the binding energies of s-p QW states (for which the bulk states disperse strongly) has been observed for even thicker silver films (8 ML) [119].

Of course, we should also acknowledge that even in the absence of an energy or symmetry gap at the substrate-film interface, which must result in an incomplete confinement of the electrons in the overlayer film, well-defined QW resonances can still be formed if the interaction across this interface is not too strong. A valuable analogue for describing this situation is the optical Fabry-Perot interferometer model, in which this incomplete confinement can be regarded as a partial reflectivity at the substrate/film interface [127]. This partial reflectivity leads to a broadening of photoemission peak widths of the QW resonances. This kind of broadening, in addition to the lifetime broadening induced by photo-hole interaction with electron and phonon excitations or scattering on the impurities, is reported for d-QW states in silver on Fe(100) [122].

Our analysis of the peak width of the  $P_1$  d-quantum well states (see Fig. 6.34) indicates that the effective reflectivity at the Ag/V(100) interface may well be rather different from that reported for the Ag/Fe(100) interface. Fig 7.14 shows the Lorentzian width of the d-QW states closest to the Fermi level for Ag films on V(100), Mo(110) [192] and Fe(100) [122]. The peak widths for Ag on Mo and V are the Lorentzian widths of the experimental spectra while the widths shown for Ag on Fe are Lorentzian widths with an additional correction for the instrumental broadening. The solid curve is a fit to the Ag/Fe(100) data assuming a value for the reflectivity of  $R=0.69$  (calculated from Eq. (3) in Ref. [122]). Clearly, the peak widths of the QW states in silver films on vanadium and molybdenum are substantially smaller than

those predicted for the same silver film thicknesses on an iron substrate.

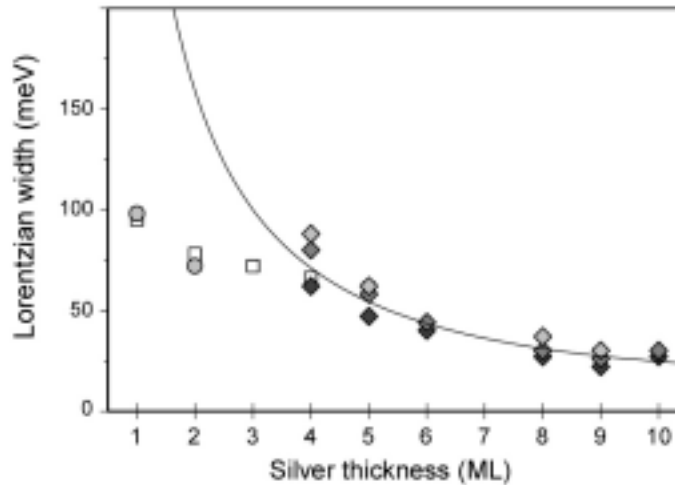


Fig. 7.14. The Lorentzian peak width of the quantum well state  $P_1$  as a function of silver film thickness as indicated in the figure. The data for Ag/Fe(100) (diamonds) and Ag/Mo(110) (circles) are taken from Ref. 122 and 192, respectively. The solid curve is calculated using Eq. (3) in Ref. 122.

In the case of silver films grown on Mo(110), the  $P_1$  QW state falls within a total band gap that exists in the range from 5.0 to 3.7 eV below the Fermi level. It is therefore reasonable to assume that within this energy range the reflectivity is complete, and we use the widths of the QWS of silver films grown on the molybdenum substrate as a gauge of the reflectivity at the vanadium substrate. The fact that the widths of the photoemission peaks from the QW states in films grown on the two substrates are the same, leads us to the conclusion that the reflectivity at the vanadium surface is similar to that at the molybdenum surface. This implies that the symmetry gap of vanadium surface is as efficient a barrier as the total energy gap of molybdenum. The reason for the non-perfect reflectivity of the iron (100) surface for the silver 4d electrons might be in the partial overlap of iron 3d and silver 4d bands that can lead to the incomplete confinement of the silver 4d electrons. The iron  $H_{12}$  critical point is at 4.5 eV and silver  $X_7$  at 3.7 eV. Therefore, all QWS derived in silver films on Fe(100) at energies ranging from 4.5 up to 3.7 eV may fall into the category of QW resonances. The width of the resonance depends on the fraction of the electronic wave function that extend into the substrate and it is not, therefore, surprising that in the case of Fe(100) the photoemission peaks show the tendency of strong increase with decreasing film thickness. For thicker films the influence of the interface is small and the width of the corresponding QW resonances can be as small as for real QW states.

A more definitive evaluation of the importance of the partial reflectivity at the interfaces may be provided by STM measurements. The intrinsic peak widths associated with lifetime broadening also contain contributions from electron scattering at impurities and defects within the film and on the surface, and conventional photoelectron spectroscopy

produces information which is spatially averaged over an area in which the concentration of defects is unknown. STS, on the other hand, can give us the same information but from a selected region which can be identified as being structurally perfect. Such a capability has been demonstrated in the analysis of the surface states on (111) noble metal surfaces [28]. However, recent results from noble metal surfaces show that high energy and angular photoemission in combination with carefully prepared surfaces can provide very narrow photoemission peaks whose peak-widths are comparable to those obtained with STS [43].

### 7.3.3. Silver monolayer

As a special case of 2-D silver we discuss an extreme case – one atomic layer film. In order to model the Ag/V(100) system and to determine the influence of the vanadium substrate on the silver d-QW states a tight binding (TB) calculation has been performed [193]. This is a slab calculation where each layer has 18 orbitals, 9 (5d 3p 1s) for each spin with included spin-orbit interaction. The slab calculation allows determination of a layer-by-layer k-resolved DOS. Fig. 7.15a shows TB calculated silver d-bands of an unsupported monolayer along the (110) direction while in Fig. 7.15b the same band structure is shown for the silver monolayer on V(100). Because Ag has an fcc lattice and V a bcc lattice and because the symmetry is defined with respect to the substrate, the direction (110) for an unsupported silver monolayer corresponds to the (100) direction on vanadium. The energies at the centre of the Brillouin zone ( $k_{||} = 0$ ) are marked  $P_1$ - $P_4$  (Fig. 7.15b) to be easier to compare with the data from Fig. 6.32. The symmetry assignment of the bands  $P_1$ - $P_4$  is as follows:  $P_1$  is made up of the  $d_{xy}$  orbital contributions,  $P_2$  is a mix of  $d_{xz}$  and  $d_{yz}$ ,  $P_3$  is of  $d_z^2$  and  $d_{x-y}^2$  character while  $P_4$  seems to be predominantly s with the most weight going back into the bulk. A tight binding calculation for an unsupported and an adsorbed silver monolayer indicate a strong influence of the vanadium substrate on the 4d electron bands. The energy of the 4d electrons in a monolayer silver film is reduced through the interaction with the vanadium substrate on average by 0.75 eV.

There are several features which characterise the vanadium influences on the band structure of a silver monolayer. There is an overall and significant reduction of the electron energy when the silver monolayer is put on the vanadium surface. In addition, the splitting effect, which is characterised by the broadening of the electronic states around 3.75 eV and 4.30 eV below the Fermi level (Fig. 7.15a) is significantly reduced by the interaction with vanadium (Fig. 7.15b). Notice that the topmost band,  $P_1$ , shows only slight negative dispersion while  $P_2$  is almost constant in energy throughout the Brillouin zone. Note that for 1 ML the  $P_2$  band is splitted for the isolated as well as for the vanadium supported monolayer.

## 7. Ag/V(100) DISCUSSION

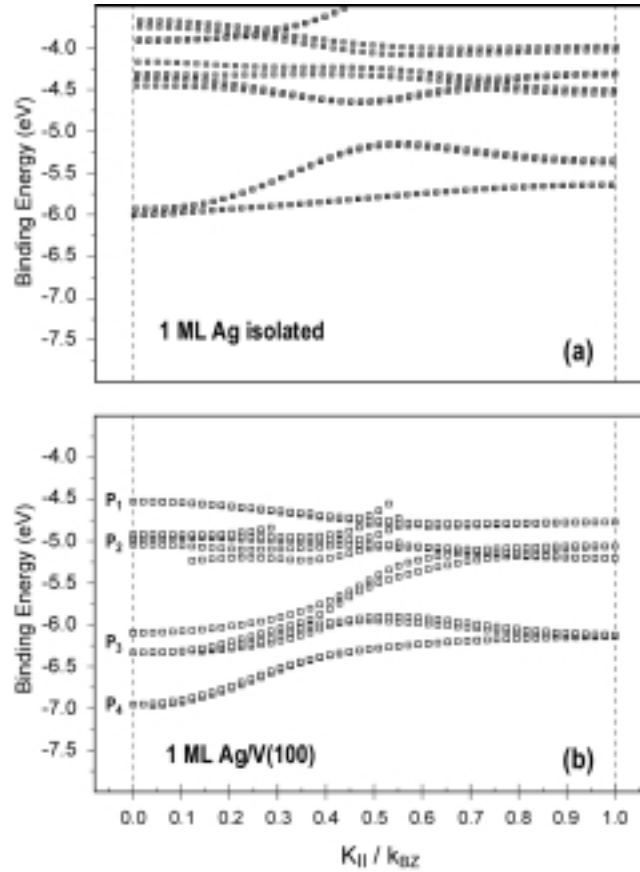


Fig. 7.15. [193] (a) The tight binding calculated band structure of an unsupported silver monolayer along the [110] direction. (b) The tight binding calculated band structure of a silver monolayer on vanadium (100) surface along the [100] direction.

The agreement between the peak positions of normal-emission spectra taken from the silver monolayer film (see Fig. 6.32) and the calculated electron energies in the centre of the Brillouin zone is surprisingly good. Apart from the rigid offset of 200 meV, the calculated energies correspond nicely to the measured ones. The tight binding calculation appears to give a correct estimate of the  $P_2$  band splitting as well, that we argue is mainly spin-orbit interaction. We propose that a combined action of spin-orbit interaction and crystal field induces the measured value of 0.12 eV in the Brillouin zone center. The spin-orbit splitting in the isolated silver atom is 0.224 eV and the same value has been reported for 1 ML Ag/Cu(100) where the interaction of the silver overlayer with the copper substrate is expected to be weak [111]. On the other hand in a study of Aristov et al. [194] for thin silver layers grown on a InSb(110) substrate it has been demonstrated that in the bcc silver the spin-orbit interaction is substantially smaller than in the fcc silver.

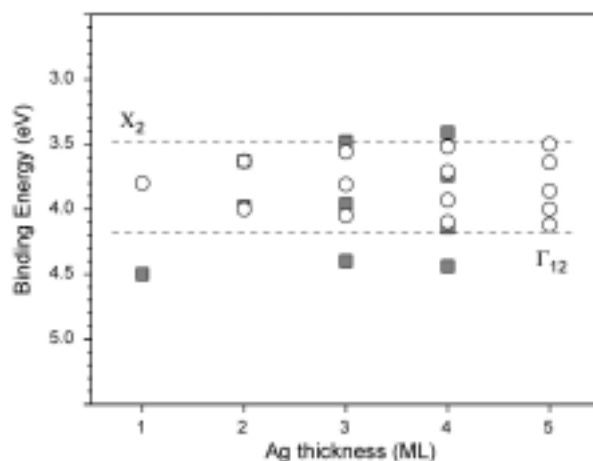


Fig. 7.16. The calculated energies of the  $P_1$  QWS for unsupported silver layers (open circles) and silver layers in contact with vanadium (100) surface (solid squares).

Fig. 7.16 shows the energy dependence of the  $d_{xy}$  QWS in a silver film as a function of film thickness. Open squares show calculated QWS for the unsupported silver film while the solid squares represent the energy of the QW states in the silver film on V(100). As expected, for unsupported silver films, QWS show up symmetrically at higher and lower binding energies around the 1 ML state. The closest realistic system that shows similar behaviour is physisorbed Xe multilayers [58] where the interaction with the substrate is negligible. The strongest influence of the vanadium substrate on the silver  $d_{xy}$  QWS is, not surprisingly, for the 1 ML film. The state is pulled down in energy by 750 meV. It is however surprising that the effect of the substrate decays very quickly with film thickness.

## 7.4. STM and the electronic structure

### 7.4.1. Surface waves and surface electronic structure

Most of the scatterers for surface wave features imaged with STM on Ag/V(100) are point defects. This primarily includes adatoms. If those adatoms are impurity atoms their origin is unknown since their concentration is below the detection limit of our AES spectrometer. The bias-dependent sensitivity for good atomic resolution (smallest biases) and surface waves appearance (generally above 100 mV) may be explained by the arguments that at larger tip-surface separation smaller periodicities are less clearly observed [195]. When increasing the distance (or equivalently the bias voltage) between the surface and the tip small wavelength features are suppressed. In our case the atomic periodicity has smaller wavelength than the surface wave features.

## 7. Ag/V(100) DISCUSSION

However, to determine the origin of the surface waves appearance we will have to make correlations to the detailed electronic structure of silver layers. The waves are the fingerprints of the scattering of the electrons from defects that are assigned by the electron gas in order to minimise the influence of imperfection potentials. As described in section 2.1.8, in principle, the low bias constant current STM image is proportional to the local density of states (LDOS) at  $E_F$  and in the presence of surface waves in the Fourier transformed image it is a surface Fermi contour, scaled by the factor of two.

Most of up-to-date results based on the FTSTM method rely on the data obtained at low temperatures, where the standing wave pattern is clearly visible. Only recently, at room temperature on a NiAl(110) surface a pronounced surface wave pattern was observed [196]. By the use of the  $dI/dV$  technique Hasegawa et al. [21] imaged a standing wave on Au(111) surface at RT, but the NiAl(110) study is the first report of that kind in the constant current mode and room temperature. Interestingly, the strong surface waves were also obtained at relatively high bias voltages ( $\cong 700$  meV). Neither the temperature broadening ( $[E_F, E_F \pm kT]$  contribution) nor the bias voltage broadening ( $[E_F, E_F + U_B]$ ) destroyed a strong standing wave pattern. It is important to notice that the detailed tip character was decisive for the good surface waves imaging. The DOS calculations revealed that the surface wave pattern has two origins: surface and bulk electron states. The measured radii of the observed ring sections were attributed to the  $k$ - position where the surface and the bulk band states cross the Fermi level. The asymmetric angular distribution of the ring sections implies some anisotropy in the electronic structure which makes the surface state contributions vanishing in the [1-10] direction in the real space. Indeed, in this direction the surface state actually does not exist. The coherence length ( $l_c$ ) of the standing waves is of the order  $\sim 1/\Delta k$ , where  $\Delta k$  is the width of each ring. This explains the faster decay of the surface wave contributions due to the faster dispersion of the surface state compared to the edge of the projected bulk band. In a more recent STS study of the same NiAl surface ( $T = 4-5$  K) Song et al. [197] have additionally demonstrated that the states of  $d$ -character can be imaged with STM in spite of their highly localised nature.

The only QW state study that exhibited the surface wave features and which included the FTSTM approach is found in a recent work of Breitholtz et al. [105]. Use of a low temperature STM revealed that the wavelengths of the oscillations, i.e. the radii of the ring-like FT features depend on the film thickness. Besides the impurity (step edges) screening effect the wave vector characteristic of the buckled surface was identified. The QW state contributions were attributed to the regions where the supposed free-electron like QW state dispersions cross the Fermi level.

To correlate the ring-like features in FT images to the electronic structure of silver layers we have to search for the features in the Ag/V(100) electronic structure that cross or

are very close to the Fermi level and which have high density at the surface, i.e. the topmost silver layer. We can suppose that for Ag/V(100) the s-p quantum well states are a major contributor to the observed wave patterns. Since up-to-date there is virtually no ab initio information on the electronic structure of the surface we can only rely on the photoemission data. We can make an assumption that throughout the Brillouin zone the s-p QW electrons have free electron-like behaviour (parabolic dispersions). In Fig. 7.17 the extension of a free electron behaviour measured in the photoemission experiment  $\pm 0.2 \text{ \AA}^{-1}$  around the centre of the Brillouin zone is shown. If all s-p QW bands would cross the Fermi level for each thickness we should measure this at different  $k_F$ .

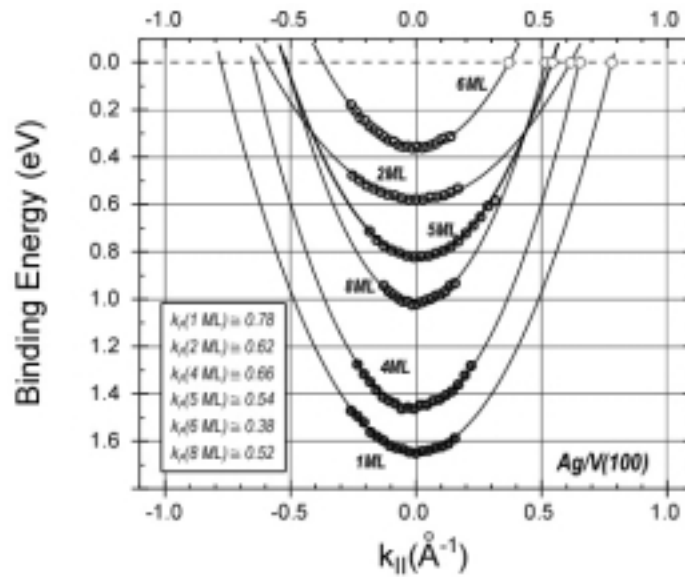


Fig. 7.17. Extension of the measured parabolic dispersion behaviour (circles) for the s-p QW states. For each state the wave vector  $k_F$  is determined according to this parabolic behaviour.

However, the assumption of parabolic dispersions of s-p QW states is in our case not justified, since from the photoemission we observe the hybridisation effect that influences the QW state dispersion, which is discussed in section 7.2.1. The effect is clearly seen in the 2-D intensity grey-scale photoemission spectra shown in Fig. 6.14 and 6.15. In the photoemission experiment we observe a levelling off and change of curvature of the QW state dispersions due to the hybridisation with the  $G_3$  vanadium d-band that crosses the Fermi level at about  $0.25\text{-}0.30 \text{ \AA}^{-1}$ . This point can be correlated to the  $k_1$  ring observed in the FT-STM images and the corresponding  $k_1^F$  Fermi wave vector (see table 6.3). Due to the avoided crossing the s-p – d hybridised  $G_3$  band again crosses the Fermi level at the corresponding  $k_2^F$  point, which we attribute to the outer ring. Fig 7.18 illustrates the proposed correlation between the ring-like features in the FT-STM images and the electronic structure at the Fermi level. Note, however, that for 5 ML thick silver film we observe additional  $k_3^F$  ring-like contribution that we cannot explain within this model with the  $G_3$  d-band crossing the Fermi level. As for the bright region in the centre of the FT images from our experimental data we are not able to correlate it to

some feature in the Ag/V(100) electronic structure. We believe that this region might contain also some geometric information about the adsorbate atoms or molecules that are inducing the surface wave phenomenon.

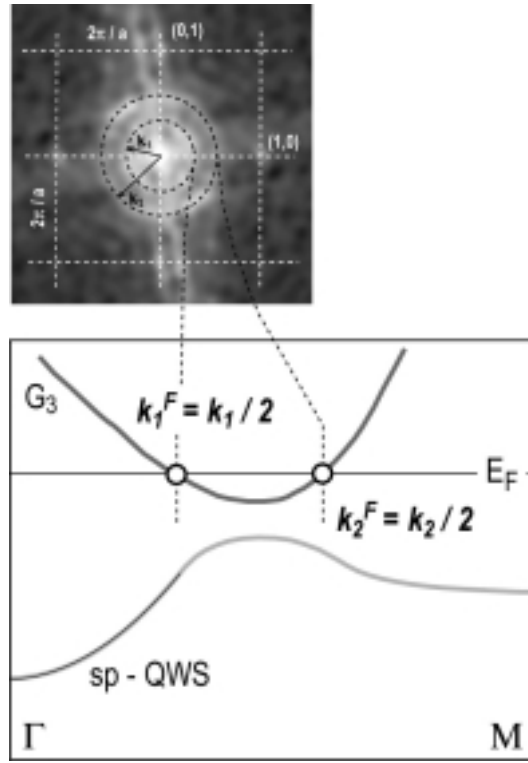


Fig. 7.18. Correlation between the Ag/V(100) surface electronic structure at the Fermi level and the ring-like features measured in the FTSTM images.

In conclusion we point out that we basically observe the same surface Fermi contour for 1-5 ML thick silver layers, within the accuracy of our measurements ( $\approx 0.1 \text{ \AA}^{-1}$ ). In a simple consideration we have correlated the hybridised substrate band to the observed contour. The issue that can not be resolved at the moment, but which is important and is of fundamental interest is to for what range of silver thicknesses in Ag/V(100) this hybridisation is strong enough that it can make a significant contribution to the surface LDOS( $E_F$ ) and that it can be observed in the STM measurements? A lack of a simple consideration is also that we have relied here only on the photoemission data. However, some d-symmetries that may also contribute to the measured Fermi contour (like  $d_{xy}$ ) are forbidden in the photoemission process and a more detailed information is definitely necessary to in detail explain all the observed features.

## 8. Summary and conclusions

In this thesis we have investigated the valence band electronic structure of ultra thin silver layers that are supported by a vanadium (100) substrate. The ultra thin silver valence electronic structure is dominantly influenced by the existence of two hybridisation band gaps which are a consequence of the mismatch between the electronic states of vanadium and silver. Structural and electronic properties were characterised and studied by means of AES, LEED, STM and HRARUPS techniques.

We have established a rather simple, fast and reproducible procedure to prepare a well ordered ( $5\times 1$ ) reconstructed surface that serves as a substrate for ultra thin silver films. The key step of the substrate preparation includes annealing to high temperatures (up to 1200 K) which results in a relatively flat surface with numerous wide terraces. We have also found that the chemical composition of the substrate intrinsically varies on the nanoscopic scale, which is in agreement with the variety of local atomic arrangements that are observed on the surface. Next, we have studied the procedure that leads to the formation of ordered and atomically uniform ultra thin silver films. We found that the deposition of silver on the substrate kept at room temperature results in the formation of 3-D silver clusters, whereas annealing to well defined temperatures leads to the formation of a uniform 1 or 2 ML thick silver film. During the temperature treatment the ( $5\times 1$ ) vanadium reconstruction underneath the silver layer is removed by the displacement and diffusion of oxygen (and carbon) atoms. This enables unsuppressed increase of the silver islands diameter and almost complete lifting of the vanadium reconstruction and eventually the formation of the uniform ( $1\times 1$ ) silver layer. For thicknesses up to 10 ML silver grows in registry with the substrate, i.e. the silver has tetragonal structure which is corroborated with our STM, LEED measurements. We believe that the tetragonal silver structure is stable due to the relatively small vanadium-silver mismatch and, probably, the small difference in the volume energies of tetragonal and fcc silver.

For 1-8 ML thick silver we have characterised s-p quantum well states by measuring their dispersions along the  $\Gamma M$  direction in the surface Brillouin zone. We find that approximately  $\pm 0.25 \text{ \AA}^{-1}$  around the Brillouin zone center each s-p QW state exhibits nearly free electron-like behaviour (parabolic dispersions). The in plane effective masses,  $m_{xy}$ , are found to vary with film thickness in the range from almost free electron mass (for 8 ML Ag/V(100)) to  $2.4 \cdot m_e$  for 2 ML Ag/V(100). We find that the variation and relatively large s-p electron effective masses are due to the hybridisation with the substrate d-symmetry state. This is evidenced by measured dispersions, where we find that the nearly free electron behaviour deviates at  $k_{||} \cong 0.25 \text{ \AA}^{-1}$ . We observe that the dispersions level off and eventually change their sign (at  $k_{||} \cong 0.35 \text{ \AA}^{-1}$ ). The photoemission peak lineshape analysis enables us to

## 8. SUMMARY AND CONCLUSIONS

evaluate the hole-electron, the hole-impurity and the hole-phonon contributions to the s-p QW state photohole (quasiparticle) lifetime. Moreover, from the temperature dependence of the photoemission spectra we have reliably measured the hole-phonon coupling constant,  $\lambda$ , for the s-p QW states. The enhanced strength of the hole-phonon coupling is found to show a strong oscillatory dependence on film thickness, with an absolute maximum for 2 ML Ag/V(100) ( $\lambda = 1$ ) and an additional local maximum for 5 ML Ag/V(100) ( $\lambda = 0.52$ ). We have shown that the photohole dominantly couples to the vibrational mode of the surface layer and the variations in the coupling strength are attributed to the changes in the amplitude of the QW state wave function at the surface-vacuum interface. From the measurements of the hole-phonon interaction away from the Brillouin zone center we found indications that the phonon spectrum that is included in the s-p hole-phonon interaction has probably more structure than just the Rayleigh wave that was included in our model calculation.

From the high resolution photoemission investigation of the d-band QW region we have identified a large number of d-QW state peaks. The phase accumulation model accurately reproduced the thickness and energy dependence of the measured QW photoemission peaks. These QW states show as expected high level of localisation. For the leading peak for 2 ML Ag/V(100) it was measured to exhibit free electron-like behaviour with large effective mass of  $5.9 \cdot m_e$ . For 1 and 2 ML Ag/V(100) we have measured the peak splitting which we attribute to the combined effects of spin-orbit and crystal field interactions. The observed splitting was also correctly predicted by a tight binding calculation. From the comparison of the experiment and the calculation we find that for 1 ML the energy of the states is, through the interaction with the vanadium surface, substantially lowered with respect to the states in the unsupported silver monolayer. From the photoemission peak width analysis of the leading d- QW peak we find that the electrons of the d-symmetry in the silver films epitaxially grown on V(100) are fully confined within the film suggesting a perfect reflection at the vanadium-silver interface. This implies that the symmetry gap in the substrate acts as a potential barrier, as efficient as a total energy gap. This makes the ultra thin silver films on V(100) a perfect model system to study properties of two-dimensional d-symmetry electrons.

Finally, the constant current STM measurements performed at room temperature have shown the strong surface wave pattern on the surface of Ag/V(100) system for studied thicknesses (1-5 ML). In the data analysis a FT–STM method was implied. Interestingly, we have found that for all thicknesses the measured surface Fermi contour exhibits two ring-like contributions positioned at almost the same radii for the studied silver thicknesses. Taking photoemission results into account we have attributed the rings to the fingerprints of the substrate  $G_3$  d-band that crosses the Fermi level and which hybridises with the s-p QW states.

## 8. SUMMARY AND CONCLUSIONS

In conclusion, the presented results show that the Ag/V(100) system properties are, mainly, a consequence of the reduced dimensionality of the electronic states within the ultra thin film. Probably, the most striking example in that sense is the measured variation and the enhancement of the hole-phonon interaction for the s-p QW states, where the film-vacuum interface was found to play a crucial role. On the other hand, we found that some of the system's properties are determined by the interaction with the substrate, i.e. the film-substrate interface. In that respect the enhancement of the s-p QW state effective masses were measured. We also found that the substrate influence can be detected with STM for films up to 5 ML thick.



## 9. Sažetak (prema poglavljima)

### 9.1. Uvod

Danas je opće poznato da materijali smanjenih dimenzija mogu imati znatno drugačija svojstva (elektronska, magnetska, transportna, ...) u odnosu na *bulk* materijale. Kada je veličina svedena na nanometarske, odnosno atomske dimenzije, tako zvani *quantum size effect* (QSE) može poprimiti značajnu ulogu u oblikovanju svojstava materijala. Na taj način moguće je proizvesti nove materijale unaprijeđenih karakteristika. Istraživanja svojstava nanometarskih struktura danas su sastavni dio multidisciplinarnih nanoznanosti (*nanoscience*) i nanotehnologije. U ultra tankim slojevima također nalazimo pojavu QS učinka. Naime, svojstva ultra tankih slojeva vezana su uz pojavu diskretnih elektronskih stanja, tako zvanih stanja kvantnih jama (*quantum well states*, QWS). Energija tih stanja i prostorna lokaliziranost u smjeru okomitom na površinu ovise o debljini sloja. Ta se stanja mogu koristiti u ciljanom "krojenju" svojstava sistema. Jedan od već komercijaliziranih primjera temelji se na strukturi naizmjeničnih tankih magnetskih i nemagnetskih metalnih slojeva koji imaju svojstvo gigantskog magnetootpora i koji se koriste kao senzori u čitačima tvrdih magnetskih diskova [1].

Kvantizaciju elektronskih stanja u ultra tankim slojevima moguće je razumjeti u okvirima jednostavnog jednodimenzionalnog modela kvantne čestice u potencijalnoj kutiji. U toj je slici elektronska struktura sloja određena njegovom debljinom i potencijalnim zidovima koji vežu elektrone unutar sloja. Potencijalni zidovi se nalaze na granici sloja i vakuuma, te sloja i podloge. Osobito je zanimljivo da, za povoljnu kombinaciju metala, potencijalni zid na granici sloja i podloge može postojati i uslijed razlika u simetrijama elektronskih stanja u sloju i podlozi. Čini se da su takvi hibridizacijski procjepi vrlo učinkoviti u lokalizaciji elektrona u ultra tankim slojevima. Ipak, stanja kvantnih jama mogu u određenoj mjeri i hibridizirati sa stanjima podloge. Vezano uz opažanja diskretnih elektronskih stanja u ultra tankim slojevima vrlo je bitno kakvo je slaganje sloja na podlogu, odnosno kakav je njegov rast. Atomski gladak rast nužan je za mogućnost studiranja QW stanja s današnjom točnošću.

Ultra tanki slojeve plemenitih metala na prijelaznim metalima istraživani su u velikom opsegu. Diskretizacija elektronskih vrpca kao funkcija debljine sloja utvrđena je za stanja s-p i d-simetrije. Uglavnom su istraživana s-p QW stanja, a puno je manje radova koji istražuju svojstva d-QW stanja. Fotoemisija je korištena u mjerenju vezivnih energija QW stanja, koje su uobičajeno interpretirane upotrebom modela višestrukih refleksija. Druge metode, poput Fabry-Perota, korištene su za precizno određivanje lokaliziranosti pojedinih QW stanja. Kvantizacija stanja u ultra tankim filmovima omogućuje da se na elegantan način odredi disperzija pripadajućih volumnih vrpca. Mjerenja fotoemisijskog udarnog presjeka u ovisnosti o

fotonskoj energiji pokazala su da mehanizam fotoemisije za različite QW sisteme može biti različit: s jedne strane prevladava značaj periodičkog potencijala unutar sloja, a s druge strane potencijalni zidovi na granicama sloja i podloge i sloja i vakuuma. Svi ti rezultati potanko su diskutirani u novijim preglednim radovima [2-4].

U ovoj tezi istražujemo svojstva ultra tankih slojeva srebra na vanadijevoj (100) podlozi. Cilj istraživanja su strukturna i elektronska svojstva (u području valentnih vrpca) ovog interesantnog QW sistema. Konkretno, istražujemo srebrne slojeve u rasponu debljina 1-8 atomskih slojeva (monoslojeva, ML). Naime, prethodna mjerenja su pokazala da su raznoliki aspekti koji znatno utječu na svojstva sistema najizraženiji upravo za najtanje slojeve (< 10 ML) u usporedbi sa debljim slojevima (10-100 ML). U rasvjetljavanju elektronskih svojstava sistema koristimo se kutno razlučivom ultraljubičastom fotoelektronskom spektroskopijom (ARUPS) i skenirajućom-tunelirajućom mikroskopijom (STM). ARUPS metoda se tradicionalno primjenjuje za određivanje volumne i površinske elektronske strukture. Za dvodimenzionalne sisteme, kao što su stanja kvantnih jama ili površinska stanja do izražaja dolazi njezina jedinstvena sposobnost da direktno mjeri spektralnu funkciju fotošupljine [6-8]. Takva mjerenja mogu biti upotrebljena za određivanje kvazičestičnih svojstava, odnosno međudjelovanja u sistemu. S druge strane, novija tehnika STM pokazala se kao vrlo učinkovita metoda za istraživanje ne samo atomske strukture, već i elektronske strukture površina. Diskusija o prednostima i manama pojedine metode može se, primjerice, naći u Ref. 9.

Za s-p QW stanja mjerili smo njihove disperzije i istraživali učinke hibridizacije sa elektronskim stanjima podloge, koji se odražavaju na efektivnim masama ili mimoilaženjima elektronskih vrpca. Također smo ispitivali dinamička svojstva s-p QW stanja. Iz temperaturne ovisnosti u fotoemisijskim spektrima mjerili smo promjene u vezivnoj energiji, efektivnim masama i širinama fotoemisijskih linija. Izolirali smo i odredili konstantu šupljina-fonon međudjelovanja u sistemu. U području d-vrpca pratili smo razvoj kvantiziranih stanja sa debljinom sloja i određivali stupanj lokalizacije d-elektrona unutar srebrnog sloja. Pomoću STM-a mjerili smo elektronsku strukturu Ag/V(100) sistema na površini, odnosno odredili smo površinsku Fermijevu plohu za slojeve različitih debljina.

## 9.2. Eksperimentalne metode

### 9.2.1. Skenirajuća-tunelirajuća mikroskopija

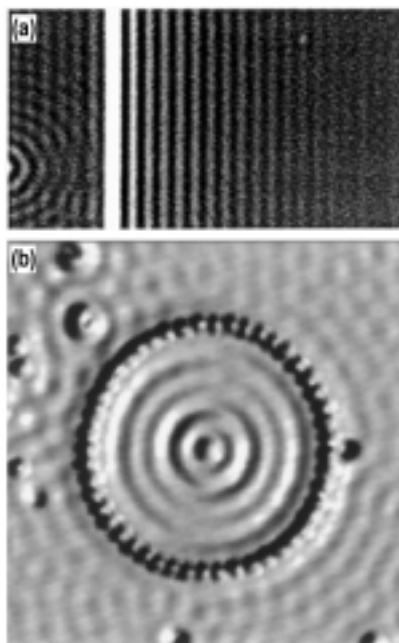
STM je metoda koja daje informaciju o atomskoj strukturi površina. Osim toga, ta je metoda osjetljiva na elektronsku strukturu površine. Osobito se spektroskopski mod (skenirajuća-tunelirajuća spektroskopija, STS) primjenjuje u istraživanju elektronske strukture površine. Izvrsnu vertikalnu osjetljivost STM-a lako je opisati na jednostavnom modelu dviju planparalelnih elektroda, iz kojeg proizlazi da struja tuneliranja eksponencijalno ovisi o udaljenosti između elektroda. S druge strane, za opis trodimenzionalne osjetljivost STM-a potrebno je primijeniti kompleksniji model koji uključuje atomsku i elektronsku strukturu obiju elektroda. U tom smislu koristi se perturbativni pristup koji su razvili Tersoff i Hamann [11]. Oni su pokazali da je struja tuneliranja,  $I$ , konvolucija gustoće stanja igle i površine. Za slučaj vrlo oštne igle (igla je tada modelirana delta funkcijom) to se svodi na:

$$I \propto \sum_v |\psi_v(\vec{r}_0)|^2 \cdot \delta(E_v - E_F) \quad (9.1)$$

U ovakvom obliku, gdje figuriraju samo valne funkcije površine,  $\psi_v$ , struja tuneliranja proporcionalna je lokalnoj gustoći stanja na površini  $\text{LDOS}(\vec{r}, E_F)$ . U modu konstantne struje tuneliranja dobivamo tako informaciju o topografiji površine. Topografija površine može, međutim, biti pogrešan pojam. To je najviše izraženo u prisutnosti lokaliziranih stanja na površini, koja sudjeluju u zasjenjenjima nečistoća (stepenica, adatomska, dislokacija) i uspostavljaju valove gustoće naboja, kako bi minimizirala unutrašnju energiju sistema (slika 9.1). Upravo se takva "topografska" informacija koristi u određivanju površinske Fermijeve plohe iz STM mjerenja.

Oscilacije na površini koje vidimo u STM slikama jednostavno i pouzdano možemo izmjeriti u Fourierovim transformatima STM slika. Razmatranje u dvodimenzionalnom elektronskom plinu sa potencijalnom barijerom (stepenica), vodi na izraz koji povezuje opažene oscilacije i Fermijev valni vektor,  $k_F$ , vezan uz tu pojavu:

$$\text{LDOS}(\vec{r}, E_F) \propto \int_0^\pi \sin^2(\vec{k}_F \cdot \vec{x} \cdot \sin \theta) \cdot d\theta \propto 1 - J_0(2 \cdot \vec{k}_F \cdot \vec{x}) \quad (9.2)$$



Slika 9.1. (a) [19] dI/dV slika u blizini stepenice na Cu(111) površini. Lijevo se vidi i atom nečistoća. LDOS oscilacije nastaju oko stepenice i nečistoće. (b) [20] STM slika kvantnog korala.

### 9.2.2. Fotoelektronska spektroskopija

Kutno razlučiva ultraljubičasta fotoelektronska spektroskopija najpogodnija je metoda za mjerenje valentne elektronske strukture kristala i površina, što je osobito jednostavno uz upotrebu promjenjive fotonske svjetlosti. U mjerenoj fotostruji sadržana je spektralna funkcija sistema,  $A(\vec{k}, E)$ . Ako je sistem u slaboj interakciji tako dobivamo direktnu informaciju o kvazičestičnim svojstvima sistema ( $\phi$  su valne funkcije početnog i konačnog stanja sistema):

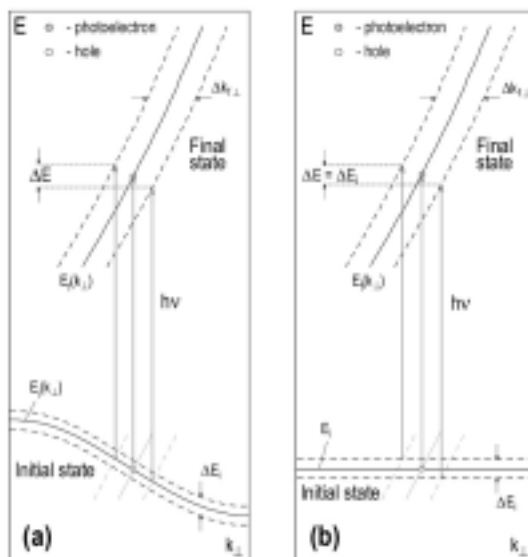
$$I \propto \sum_{f,i,\vec{k}} \left| \langle \phi_{f,E_{kin}} | \vec{r} | \phi_{i,\vec{k}} \rangle \right|^2 A(\vec{k}, E) \quad (9.3)$$

$$A(\vec{k}, E) = \frac{1}{\pi} \cdot \frac{\text{Im}\{\Sigma(\vec{k}, E)\}}{[E - E_{\vec{k}}^0 - \text{Re}\{\Sigma(\vec{k}, E)\}]^2 + [\text{Im}\{\Sigma(\vec{k}, E)\}]^2}$$

U spektralnoj funkciji se pojavljuje vlastita energija,  $\Sigma(\vec{k}, E)$ , koja određuje renormalizaciju stanja kvazičestice (energiju i vrijeme života). U procesu fotoemisije su, u principu, uključena dva kvazičestična stanja: pobuđeni fotoelektron i fotošupljina koja je nastala u procesu izbacivanja elektrona. Zakon očuvanja energije povezuje te dvije kvazičestice. U moru preostalih elektrona fotošupljina se može razmatrati u jednoelektronskoj slici. U načelu, obje kvazičestice imaju konačno vrijeme života i obje doprinose mjerenoj širini fotoemisijske linije:

$$\Gamma_{\text{exp}} = \left( \Gamma_{\text{hole}} + \frac{v_{\text{hole}}}{v_{\text{electron}}} \cdot \Gamma_{\text{electron}} \right) \cdot \left( \left| 1 - \frac{v_{\text{hole}}}{v_{\text{electron}}} \right| \right)^{-1} \quad (9.4)$$

Postoje specijalni slučajevi kada je moguće direktno mjeriti samo doprinos fotošupljine ukoliko je  $k_{\perp}$  disperzija početnog elektronskog stanja 0. To vrijedi za dvodimenzionalne sisteme, ali i za 3-D sisteme, uobičajeno u točkama na rubu Brillouinove zone (sliku 9.2).



Slika 9.2. Doprinosi mjerenoj fotoemisijijskoj širini linije za: (a) 3-D sisteme i (b) 2-D sisteme.

Doprinosi koji se linearno zbrajaju u širini fotoemisijske linije su šupljina-elektron (š-e), šupljina-fonon (š-f) i šupljina-nečistoća (š-n) međudjelovanja:

$$\Gamma = \Gamma_{\text{š-e}} + \Gamma_{\text{š-f}} + \Gamma_{\text{š-n}} \quad (9.5)$$

U konkretnim primjerima se, u tom smislu, fotoemisija počela koristiti tek od 1990-tih kada su konstruirani elektronski analizatori visoke energetske (i kutne) rezolucije. Naime, za dugoživa stanja u blizini Fermijevog nivoa, koja su uobičajeno od interesa, ključna energetska skala je na razini nekoliko meV i za lošije analizatore ta je informacija bila nedostupna, jer je uvijek bila nadmašena instrumentalnim Gaussijanskim širenjem. Osobito je jednostavno, u fotoemisiji, mjeriti konstantu šupljina-fonon vezanja iz temperaturne ovisnosti širine fotoemisijjskih maksimuma [47].

### 9.3. Uređaji

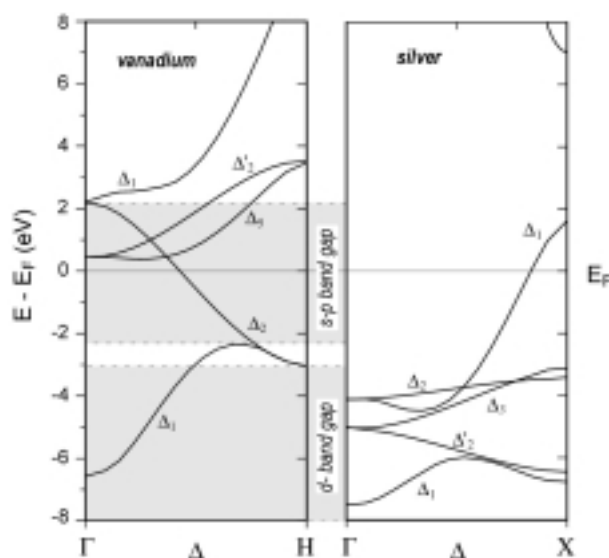
Rezultati prikazanih mjerenja dobiveni su na pet različitih ultra visoko vakuumskih uređaja. U ultra visoko vakuumskoj komori u Zagrebu imali smo na raspolaganju sve eksperimentalne tehnike korištene u ovom radu (STM [49], LEED, AES i ARUPS). STM uređaj u Zagrebu identičan je onom kakvog smo koristili u laboratoriju u Bonnu, gdje smo imali na raspolaganju i AES tehniku. Komora u Ljubljani je VG Microlab 310F sistem, koji omogućuje HRAES mjerenja. Ovaj sistem specifično smo koristili u istraživanju vanadijeve

podloge. U Brookhavenu (National Synchrotron Light Source), korištena je U13UB linija [50], koja daje fotone energija 12-23 eV. Kao analizator koristi se Scienta SES 200 analizator. Energetska rezolucija je unutar područja 8-25 meV, a kutna rezolucija je  $\pm 0.2^\circ$ . Komora je opremljena i He lampom i LEED uređajem. U Trstu (ELETTRA sinhrotron, 3.2 R VUV linija [51]) korišten je znatno širi raspon fotonskih energija (18-100 eV). Energetska rezolucija VSW-50 analizatora je 30 meV, a kutna rezolucija je  $\pm 0.5^\circ$ . U toj komori na raspolaganju je i LEED tehnika.

## 9.4. Stanja kvantnih jama

### 9.4.1. Stanja u ultra tankim slojevima

Najjednostavniji primjer ultra tankih slojeva su slojevi plemenitih plinova na površinama [57-63], jer je međudjelovanje sa podlogom zanemarivo. Međudjelovanje adsorbiranog sloja i podloge značajno određuje lokalizaciju elektronskih stanja unutar sloja. Postojanje lokaliziranih stanja primarno je određeno međusobnim odnosom elektronskih struktura adsorbiranog sloja i podloge. Kao primjer sistema u kojem postoji veliko simetrijsko neslaganje elektronskih struktura sloja i podloge upravo ističemo Ag/V(100), gdje postojanje dva sp-d hibridizacijska procjepa omogućuje postojanje s-p i d-stanja kvantnih jama (vidi sliku 9.3). Postoje i slučajevi u kojima nalazimo znatno uže energetske procjepe. Na rubovima procjepa uobičajeno nastaju, tako zvana, stanja kvantnih rezonanci (QWR) koja za razliku od pravih QW stanja, prodiru u podlogu i hibridiziraju sa elektronskim stanjima podloge [67,68].



Slika 9.3. [65] Izračunate elektronske vrpce bcc vanadija i fcc srebra duž  $\Gamma$ - $\Delta$ -H and  $\Gamma$ - $\Delta$ -X smjerova visoke simetrije u Brillouinovoj zoni. Uočite dva hibridizacijska procjepa.

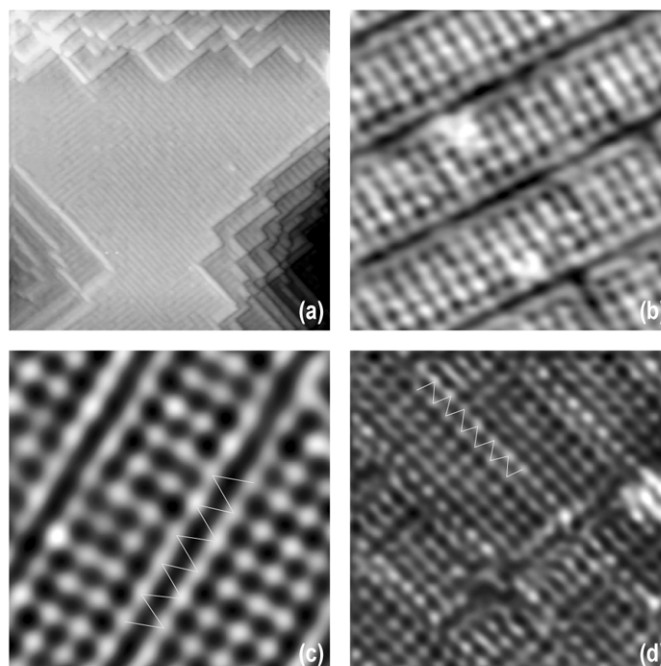
### 9.4.2. Literaturni pregled

Najpogodnija metoda za istraživanje efekata kvantizacije u ultra tankim filmovima je fotoemisija, no ne treba zanemariti i potencijale STM i STS metoda, koje se s obzirom na svoje mogućnosti, za sada, premalo koriste u tim istraživanjima. Jedan od prvih primjera gdje je ostvarena i detektirana kvantizacija d-stanja za jedan ML srebra na Cu(100) površini je fotoemisijsko mjerenje još iz 1983. godine [111]. Od tada je objavljeno puno radova koji izvještavaju o s-p i d-stanjima kvantnih jama u ultra tankim srebrnim slojevima na različitim podlogama. Primjeri fotoemisijskih studija čija tema su s-p stanja kvantnih jama u ultra tankim srebrnim slojevima dani su u Ref. [66-72,112-121], a primjeri istraživanja d-QW stanja u Ref. [111,114,115,122]. U novije vrijeme od osobitog su interesa istraživanja svojstava nisko-dimenzionalnih sistema - smanjenja dimenzionalnost smanjuje fazni prostor za korelacije u sistemu, što može dovesti do pojačanih međudjelovanja. Od interesa su stanja u samoj blizini Fermijevog nivoa, jer upravo ona određuju ključna svojstva sistema, kao što je transport. Kao 2-D sistemi, QW stanja u ultra tankim slojevima, također su meta tih istraživanja. Pretežno je istraživano šupljina-fonon međudjelovanje i to za Na/Cu(111) [123-124], Ag/V(100) [125-126], Ag/Fe(100) [127-128,130] and Ag/Cu(111) [129]. Neka od tih istraživanja, kao ona za Ag/V(100), pokazala su da uslijed smanjenje dimenzionalnosti sistema dolazi do znatnog pojačanja šupljina-fonon međudjelovanja u sistemu. Slično je i u srodnim istraživanjima površinskih stanja [43,45,133-143], kod kojih je isto tako opažena mogućnost znatnog pojačanja korelacija u sistemu. Teoretski rad na tim problemima je u povojima i u vezi problema šupljina-fonon međudjelovanja tek je nedavno došlo do ozbiljnijih napredaka [48,131-132].

## 9.5. Podloga

### 9.5.1. (5×1) rekonstruirana V(100) površina

Priprema čiste i istovremeno dobro uređene vanadijeve površine vrlo je mukotrpan postupak. Vrijeme i strogo kontrolirani uvjeti u ultra visokom vakuumu nužni su zahtjevi koji omogućuju uspješnu pripremu čiste površine. U realnim uvjetima sinhrotronskih mjerenja najčešće je na raspolaganju 10-14 dana i to vrijeme nije dovoljno za dobivanje čiste V(100) površine. Rezultati prethodnih istraživanja međudjelovanja kisika i srebra na V(100) površini ukazuju da nanašanje srebra na (5×1) kisikom rekonstruiranu površinu može rezultirati uklanjanjem kisika iz površinskog sloja, a time i do uklanjanja rekonstrukcije. Prednost V(100)-(5×1) površine je da zadnji koraci pripreme uključuju dugotrajnije zagrijavanje na visoku temperaturu (1200 K), što rezultira stvaranjem širokih i uređenih terasa na površini. Osobito taj razlog čini V(100)-(5×1) površinu pogodnom za rast uređenih srebrnih slojeva.



Slika 9.4. STM slike dobro uređene V(100)-(5×1) površine. (a) 74×74 nm<sup>2</sup>, (b) 4.6×4.6 nm<sup>2</sup>, (c) 3.2×3.2 nm<sup>2</sup>, (d) 4.5×4.5 nm<sup>2</sup>. Na slikama (c) i (d) uočite trokutastu simetriju među vanadijevim atomima duž tamnih linija.

### 9.5.2. Priprema i karakterizacija površine

V(100)-(5×1) površina pripremljena je kako je opisano u Ref. 162, ciklusima Ar<sup>+</sup> ionskog bombardiranja i dugotrajnim zagrijavanjima na temperaturi do 1200 K. Dominantne nečistoće u uzorku su: vodik, fosfor i sumpor, koje je relativno jednostavno ukloniti. Preostale nečistoće su ugljik i kisik, koje se međusobno natječu za ista adsorpcijska mjesta na površini što može rezultirati njihovim različitim međusobnim koncentracijama na površini. Dobro uređena V(100)-(5×1) površina sadrži ≈ 1 ML kisika i do 0.2 ML ugljika. U određivanju kemijskog sastava površine na nanometarskoj razini koristili smo se HRAES mjerenjima. Pokazalo se da kemijski sastav površine (kisik-ugljik omjer) varira kako se pomičemo po površini za samo 10-100 nm. Te varijacije su intrinzično svojstvo dobro uređene V(100)-(5×1) površine.

### 9.5.3. STM karakterizacija

Tipična STM slika V(100)-(5×1) površine na većoj skali (75 nm) prikazana je na slici 9.4a. Tipične atomski razlučive slike prikazane su na slikama 9.4b-d. Glavna značajka vanadijeve rekonstrukcije je razmicanje vanadijevih redova, svakih 5 atomskih redova, pri čemu dolazi do povećanja vanadij-vanadij udaljenosti od 17% u odnosu na nerekonstruiranu vrijednost. Nadalje, na temelju atomski razlučivih STM mjerenja opažamo niz različitih strukturnih detalja, što potvrđuju i mjerenja drugih autora.

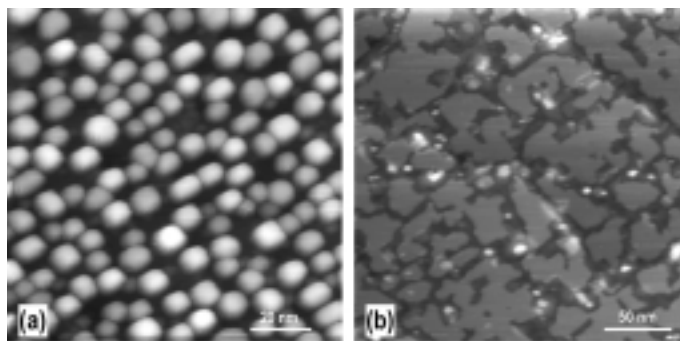
#### 9.5.4. Diskusija

Pojava triangularne simetrije u poziciji vanadijevih atoma na površini upućuje na postojanje kisikovih atoma koji tvore trostruku vezu sa vanadijem. Za opis modela (5×1) rekonstrukcije V(100) površine u dosadašnjim radovima su ključnu ulogu imala AES mjerenja koja su dala informaciju o kemijskom sastavu površine [157]. Naime, interpretacija STM slika otežana je činjenicom da kisikovi i ugljikovi atomi nisu direktno vidljivi na STM slikama. Kako je naše HRAES istraživanje pokazalo, kemijski sastav površine varira na nanometerarskoj skali. Pojavu različitih opaženih strukturnih detalja možemo pripisati upravo tim varijacijama. Zaključujemo da u računanju energetski povoljnih konfiguracija za V(100)-(5×1) rekonstrukciju u obzir treba uzeti i kemijsku varijaciju.

### 9.6. Ag/V(100): rezultati

#### 9.6.1. Strukturna karakterizacija

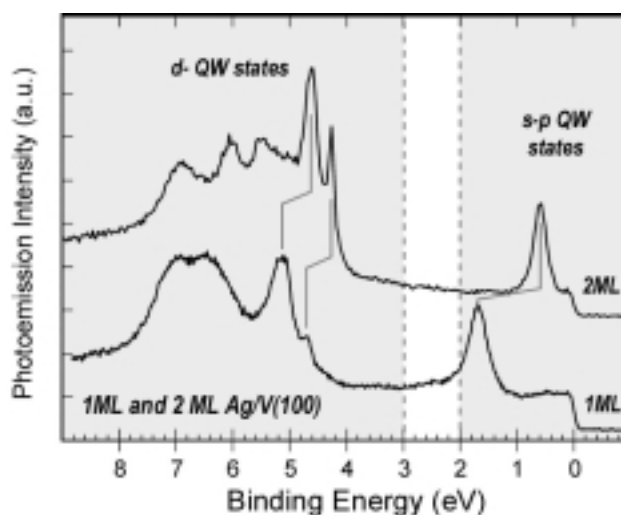
Najprije određujemo postupak pripreme atomski glatkih srebrnih slojeva. Rezultati naparavanja srebra na dobro definiranu V(100)-(5×1) površinu pri sobnoj temperaturi pokazuju da srebro raste trodimenzionalno, odnosno da dolazi do stvaranja srebrnih klastera. To potvrđuju AES mjerenja kod kojih opažamo znatne intenzitete sa V(100)-(5×1) podloge, čak i za naparenu količinu ekvivalentnu 10 ML srebra. Slično pokazuju i STM slike (vidi sliku 9.5a). Utvrđujemo da zagrijavanje na dobro definiranu temperaturu dovodi do uređivanja glatkih srebrnih slojeva (slika 9.5b). Utvrdili smo da je uzorak potrebno zagrijati na 700-800 K, pri čemu dolazi do uređivanja 2 ML Ag/V(100), ili na 900 K što dovodi do uređivanja srebrnog monosloja. Postupak pripreme uređenih srebrnih slojeva većih debljina sastoji se od naparavanja dodatnih količina srebra na 2 ML Ag/V(100). Rezultati pokazuju da stvaranjem uređenog srebrnog sloja dolazi do uklanjanja vanadijeve rekonstrukcije. Cijeli postupak pripreme pratili smo fotemisijским i LEED mjerenjima. Iz LEED mjerenja ocjenjujemo da je dugodosežna bcc(100) periodičnost površinskog sloja očuvana do debljine od najmanje 10 ML, pri čemu kod debljina većih od 5 ML dolazi do pojave znatnijeg nereda u sistemu.



Slika 9.5. (a) STM slika nakon naparavanja 1.5 ML Ag na V(100)-(5×1) pri sobnoj temperaturi. (b) Slika iste površine nakon zagrijavanja na 750 K.

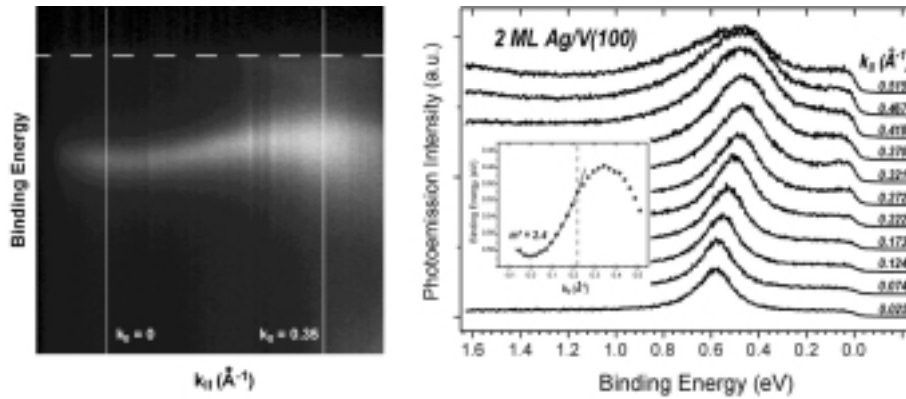
Dobro uređene slojeve detaljno smo istražili STM-om. Utvrdili smo da je skeniranje srebrnog sloja vrlo delikatan postupak s obzirom na činjenicu da skeniranjem ponekad oštećujemo srebrni sloj. Odredili smo da je, u tom smislu, najpovoljnije koristiti male struje tuneliranja (manje od 0.5 nA) i bias napone u rasponu 0.2-0.5 eV. Za pokrivenosti manje od 1 ML izmjerili smo da vanadijeva podloga zadržava V(100)-(5×1) strukturu, odnosno da su nepokriveni dijelovi još uvijek rekonstruirani. Također smo izmjerili i visine srebrnih slojeva STM-om. Rezultati pokazuju da je struktura srebrnog sloja tetragonalna, odnosno da je u smjeru okomito na površinu parametar rešetke 0.18 nm za prvi sloj, te 0.2 nm za ostale srebrne slojeve. Mjerenja u atomskoj rezoluciji pokazuju da je konstanta rešetke u smjeru paralelno s površinom identična konstanti rešetke nerekonstruiranog vanadijia od 3 Å.

### 9.6.2. HRARUPS mjerenja

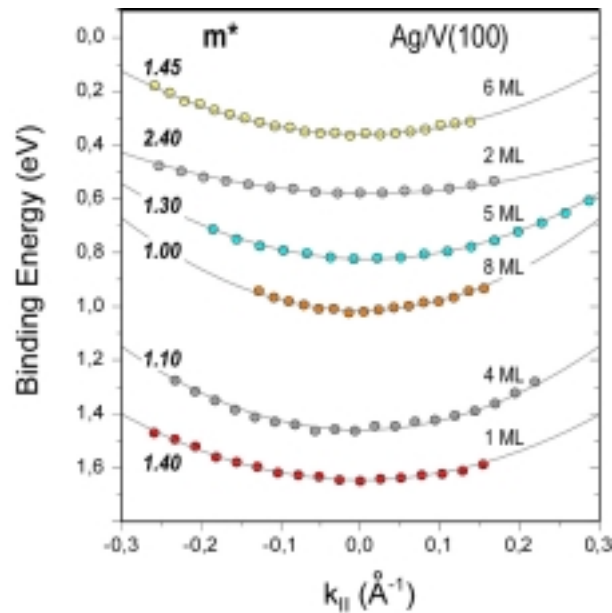


Slika 9.6. n.e. fotoemisijiski spektri za 1 i 2 ML Ag/V(100). Osjenčani dijelovi naznačuju područja u kojima nastaju s-p i d-QW stanja.

Tipičan primjer fotoemisijiskog spektra koji prikazuje i s-p i d- stanja kvantne jame prikazan je na slici 9.6. U HRARPES mjerenjima iz 2-D mapa uočavamo razlike u vezivnim energijama i disperzijama stanja kvantnih jama za razne debljine srebrnih slojeva. Osim oko samog centra Brillouinove zone, mjerili smo disperzije s-p stanja i dalje od centra zone. Jedan rezultat prikazan je na slici 9.7 za 2 ML Ag/V(100). Uočavamo da disperzije mijenjaju ponašanje u odnosu na parabolični izgled oko centra zone. Na otprilike  $0.35 \text{ \AA}^{-1}$  u  $\Gamma M$  smjeru površinske Brillouinove zone mijenja se predznak zbog utjecaja elektronske vrpce koja prelazi Fermijev nivo. Takvo ponašanje koreliramo s pojedinim fotoemisijiskim intenzitetima. Unutar područja gdje je disperzija parabolična odredili smo efektivne mase pojedinih s-p QWS elektrona, pri čemu mase variraju od  $2.4m_e$  (za 2 ML Ag/V(100)) do praktički slobodnoelektronske (za 8 ML Ag/V(100)). Ti su rezultati na slici 9.8.



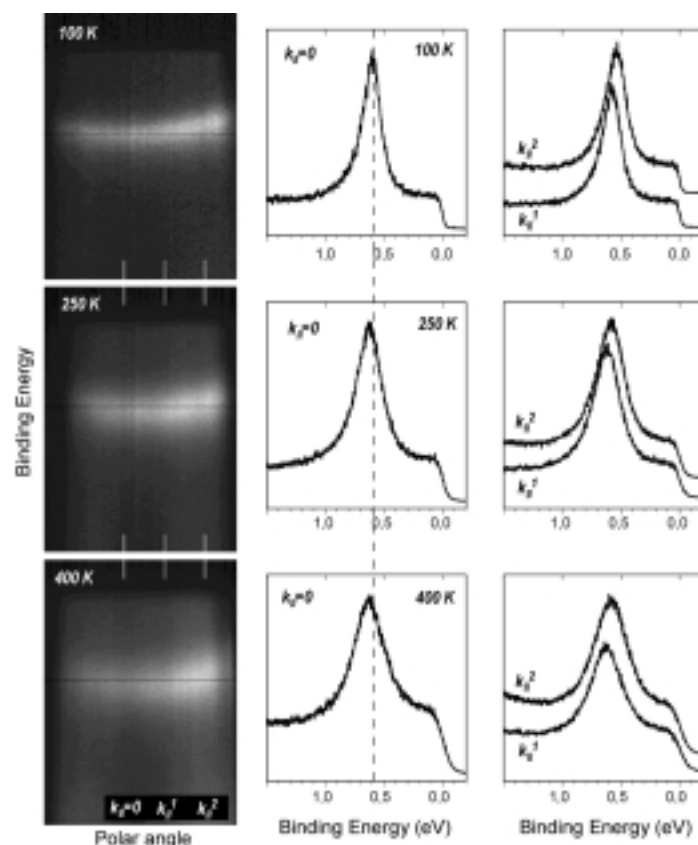
Slika 9.7. 2 ML Ag/V(100): kombinacija dvije mape 2-D fotoemisijских intenziteta koje prate disperziju s-p QW stanja. S desne strane su pripadni EDC spektri dobiveni sa slike lijevo.



Slika 9.8. Disperzije za s-p QW stanja oko centra površinske Brillouinove zone. Pune linije predstavljaju parabole koje se najbolje slažu s izmjerenim vrijednostima.

Da bi precizno odredili parametar šupljina-fonon vezanja mjerili smo temperaturnu ovisnost fotoemisijских spektara (vidi slike 9.9, 9.10 i 9.11). Opaženo ponašanje u centru Brillouinove zone može se sažeti u slijedećem; Porastom temperature dolazi do:

- povećanja širine spektralnih linija
- smanjenja spektralnog intenziteta
- pomaka prema većim vezivnim energijama
- smanjenja efektivne mase elektrona

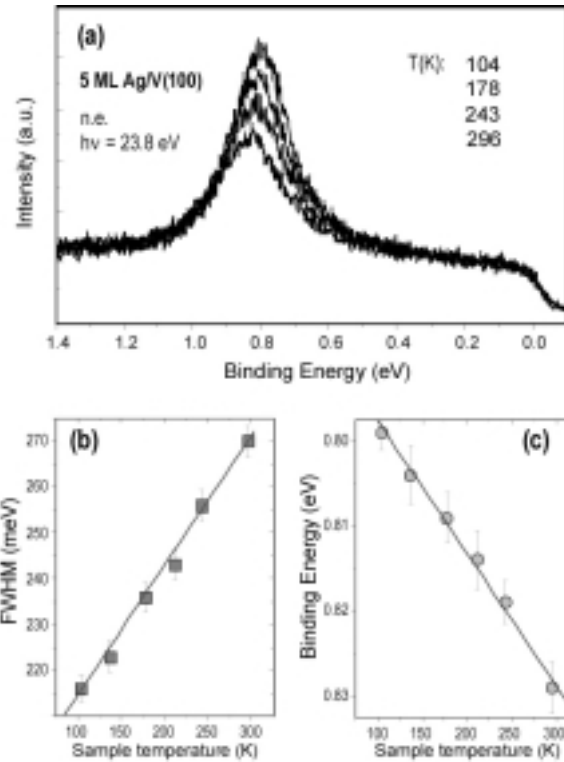


Slika 9.9. U lijevom stupcu su 2-D mape fotoemisijjskih intenziteta za 2 ML Ag/V(100) za naznačene temperature. Srednji stupac odgovra EDC spektrima u centru Brillouinove zone, a u desnom stupcu po dva EDC spektra van centra Brillouinove zone.

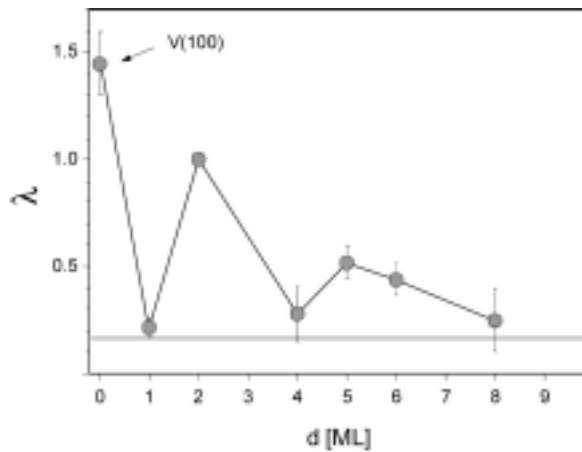
Debljina sloja (ML)	Vezivna energija (eV) na 90 K	Efektivna masa $m^*$ na 90 K	Temperaturni pomak ( $\text{eV} \cdot \text{K}^{-1} \cdot 10^{-4}$ )	Parametar š-f vezanja $\lambda$
0 (p.s.)	$E_F$	—	—	$1.45 \pm 0.15$
1	$1.65 \pm 0.01$	$1.40 \pm 0.05$	1.5	$0.21 \pm 0.05$
2	$0.58 \pm 0.01$	$2.40 \pm 0.05$	1.6	$1.00 \pm 0.03$
3	—	—	—	—
4	$1.43 \pm 0.01$	$1.10 \pm 0.05$	1.0	$0.28 \pm 0.12$
5	$0.82 \pm 0.01$	$1.30 \pm 0.05$	1.6	$0.52 \pm 0.07$
6	$0.36 \pm 0.01$	$1.45 \pm 0.05$	1.8	$0.44 \pm 0.07$
7	$1.44 \pm 0.01$	—	—	—
8	$1.02 \pm 0.01$	$1.02 \pm 0.05$	1.1	$0.25 \pm 0.15$

Tabela 9.1. Podaci dobiveni za s-p QW stanja na temelju HRARUPS mjerenja

Analizom mjerenja temperaturne ovisnosti, kako je ilustrirano na slici 9.10b za 5 ML Ag/V(100) odredili smo parametar š-f vezanja,  $\lambda$ . Izmjereni  $\lambda$  za proučavane debljine srebrnih slojeva prikazan je grafom na slici 9.11. Iz grafa je jasno vidljivo da parametar vezanja varira kako se mijenja debljina sloja, sa izraženim apsolutnim maksimumom za 2 ML Ag/V(100) i dodatnim lokalnim maksimumom za 5 ML Ag/V(100). U tabelu 9.1 uvršteni su glavni rezultati dobiveni iz HRARUPS mjerenja za s-p stanja kvantne jame.

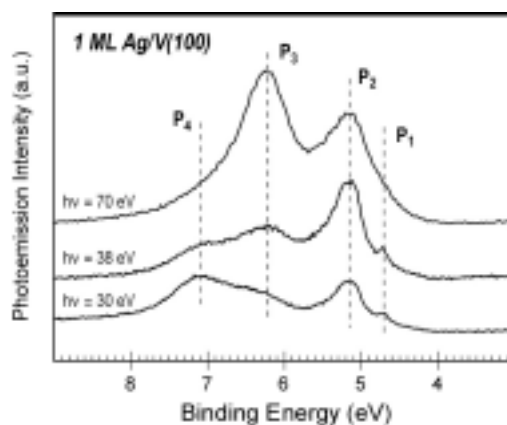


Slika 9.10. (a) n.e. fotoemisijski spektri za 5 ML Ag/V(100) dobiveni na nekoliko različitih temperatura. (b) Ovisnost širine fotoemisijskog maksimuma o temperaturi. (c) Ovisnost vezivne energije s-p QW stanja u ovisnosti o temperaturi.

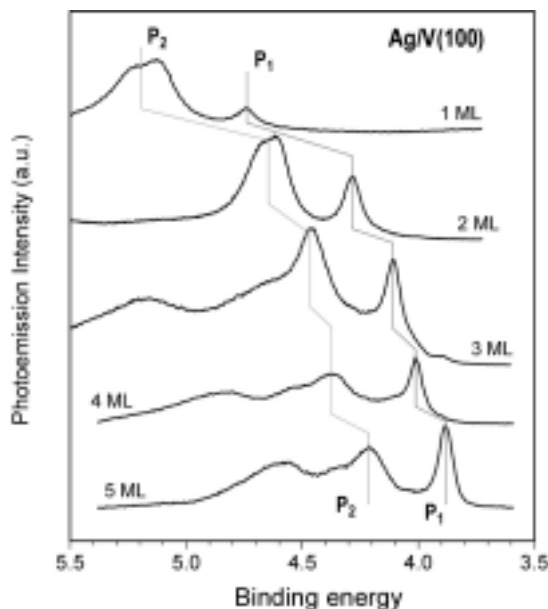


Slika 9.11. Izmjerena konstanta šupljina-fonon vezanja  $\lambda$ , kao funkcija debljine srebrnog sloja. Na grafu je također prikazana izmjerena vrijednost  $\lambda$  za V(100) površinsko stanje i volumna Ag vrijednost (siva horizontalna linija).

Opažanje i karakterizacija d-QW stanja znatno je delikatnije nego što je to slučaj za s-p stanja. Prvo, broj stanja naglo raste sa brojem slojeva  $N$ , kao  $5N$ , što je posljedica broja d-elektrona koje donosi svaki srebrni atom u sloj. Nadalje, zbog velikog broja fotoemisijских maksimuma, teško je točno identificirati sve maksimume, čak i za male debljine. Osim toga, d-QW stanja znatno se manje dispergiraju nego s-p stanja. Upotrebom fotonskih energija u širokom rasponu bili smo u mogućnosti identificirati sve QW maksimume za 1 ML Ag/V(100) (slika 9.12). Promjenom fotonske energije ne dolazi do pomaka u vezivnoj energiji d-QW stanja, što sugerira njihov izraženi 2-D karakter. Uprkos navedenim preprekama uspješno smo identificirali vodeće fotoemisijске maksimume za 1-5 ML Ag (slika 9.13).



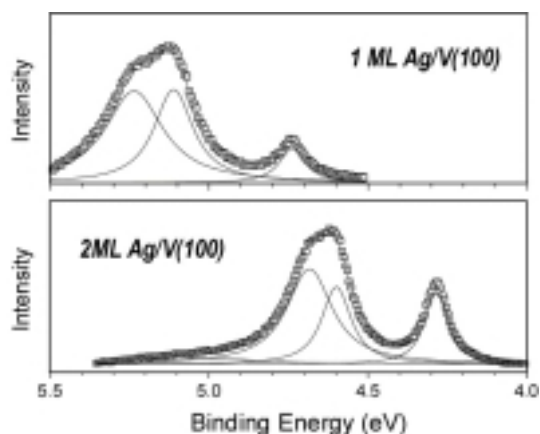
Slika 9.12. n.e. fotoemisijски spektri za 1 ML Ag/V(100) za razne fotonske energije.



Slika 9.13. n.e. fotoemisijски spektri za d-QW stanja i razne debljine srebrnog sloja, snimljeno uz upotrebu fotonske energije od 18 eV.

U HRARUPS mjerenjima jasno smo razlučili da dolazi do cijepanja  $P_2$  fotoemisijskog maksimuma od 120 i 80 meV za 1 i 2 ML Ag/V(100), dok za veće debljine to cijepanje nije opaženo (vidi sliku 9.14). Oblik fotoemisijških maksimuma se vrlo dobro prilagođava

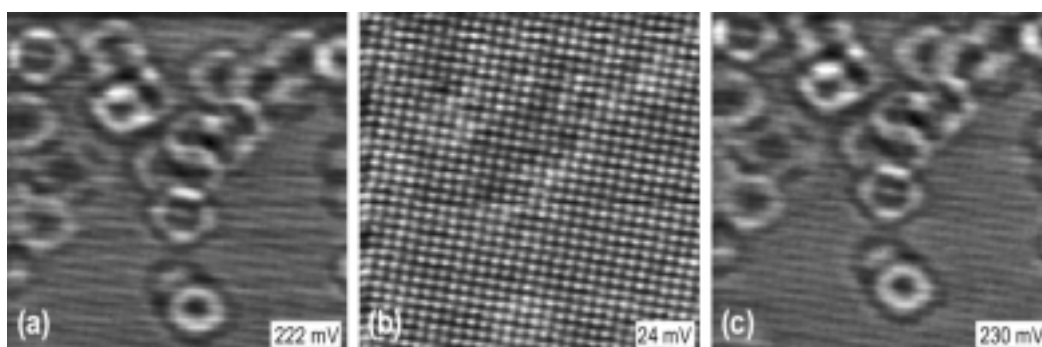
Lorentzovim funkcijama.



Slika 9.14. Dekonvoluirani n.e. fotoemisijski spektri za d-QW stanja za 1 i 2 ML Ag/V(100) koji pokazuje cijepanje  $P_2$  fotoemisijskog maksimuma.

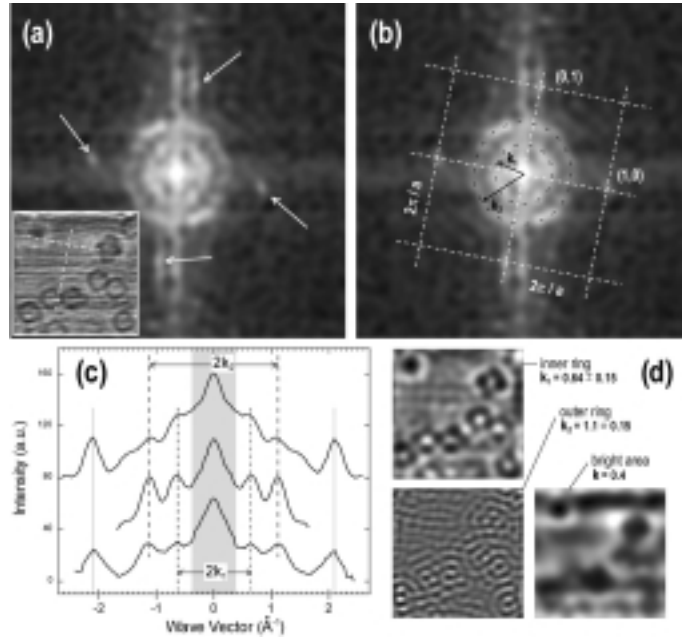
### 9.6.3. STM kao proba elektronske strukture

U STM mjerenjima smo primijetili da je izgled atomski razlučivih slika jako osjetljiv na detaljni odabir parametara tuneliranja. Naime, za veće struje tuneliranja (veće od 5 nA) i napone u rasponu 100-300 mV u apsolutnom iznosu na površini je jako izražena pojava površinskih valova, kako se i jasno vidi na slici 9.15. Površinski valovi se opažaju kao oscilacije oko pojedinih nečistoća na površini, kao što su adatom ili stepenice.



Slika 9.15. 5 ML Ag/V(100). Niz STM mjerenja gdje je mijenjan samo bias napon. Struja tuneliranja je u svakom slučaju bila 19 nA, te (a)  $U_B = 222$  mV, (b)  $U_B = 24$  mV, (c)  $U_B = 230$  mV. Veličina slika je  $7 \times 7$  nm<sup>2</sup>.

Pouzdana analiza površinskih valova moguća je pomoću metode Fourierovog transformiranja STM slika. Naime, prelaskom u inverzni prostor u mogućnosti smo izmjeriti koji valni vektori konstituiraju površinske valove koje opažamo na slici. FTSTM slika proporcionalna je površinskoj Fermijevoj plohi. Cijeli postupak analize rezultata prikazan je na slici 9.16 za 1 ML Ag/V(100). Za sve proučavane debljine srebrnog sloja rezultati su sažeti u tablici 9.2. Ukratko, unutar preciznosti našeg eksperimenta u FTSTM analizi uvijek opažamo gotovo istu površinsku Fermijevu plohu.



Slika 9.16. 1 ML Ag/V(100). (a) Fourierov transformat STM slike pokazane u umetku. Paramteri tuneliranja:  $U_B = 252$  mV,  $I_T = 4.5$  nA. Veličina slike  $7.9 \times 7.9$  nm<sup>2</sup>. (b) Isti Fourierov transformat sa naznačenim tačkama atomske periodičnosti ((0,1), (1,0), ...), te prstenovima  $k_1$  i  $k_2$  koji su odgovaraju površinskim valovima. (c) Profilni presjeci kroz FT sliku. (d) Odvojeno filtrirani doprinosi u direktnom prostoru iz FT slike.

Debljina srebrnog sloja	$k_F$ polumjeri prstenova u Fourierovim transformatima STM slika u Å <sup>-1</sup>				
	Centralni dio	$k_1^F$	$k_2^F$	$k_3^F$	$\Delta k$
1 ML	$\cong 0.2$	<b>0.32</b>	<b>0.55</b>	—	0.1
2 ML	$\cong 0.2$	<b>0.35</b>	<b>0.58</b>	—	0.1
3 ML	$\cong 0.2$	<b>0.30</b>	<b>0.48</b>	—	0.1
5 ML	$\cong 0.2$	<b>0.35</b>	<b>0.55</b>	<b>0.7</b>	0.1
3 ML Aniso.	$\cong 0.2$	<b>0.38</b>	<b>0.55</b>	—	0.1

Tabela 9.2. Mjereni polumjeri "prstenova" u Fourierovim transformatima STM slika.

## 9.7. Ag/V(100): diskusija

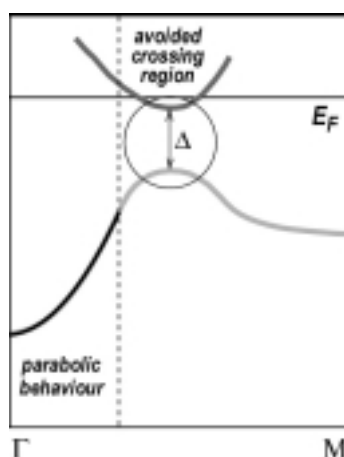
### 9.7.1. Uređeni srebrni sloj

Na temelju karakterizacijskih AES, LEED, STM i ARUPS rezultata zaključujemo da, zagrijavanjem srebrnog sloja na dobro definirane temperature, možemo prirediti dobro uređena 1 i 2 ML debela srebrna sloja. Tijekom procesa uređivanja sloja dolazi do uklanjanja rekonstrukcije vanadijeve površine, što omogućuje nesputani rast srebrnih otoka i konačno

formaciju uniformnih srebrnih slojeva. Atomi srebra slijede parametar rešetke vanadija, odnosno rastu u skladu s površinom. Kako su rezultati pokazali, struktura srebrnog sloja je tetragonalna. Velika stabilnost i uređenost sloja je, prema našem mišljenju posljedica dobrog slaganja parametara rešetki srebra i vanadija i povoljne površinske energije srebrnog sloja, što ukupno rezultira energetski povoljnim uvjetima u sistemu.

### 9.7.2. s-p stanja kvantne jame

Neobičajeno velike izmjerene efektivne mase s-p stanja kvantnih jama u srebrnom sloju pripisujemo efektima hibridizacije sa volumnim d-stanjem podloge. Argumente nalazimo u fotoemisijским rezultatima koji van centra Brillouinove zone ukazuju na mimoilaženje elektronskih vrpca s-p QWS i d-stanja podloge, što u pravilu znači i miješanje njihovih svojstava. Na taj način s-p stanja poprimaju lokaliziraniji karakter i povećava im se efektivna masa (vidi sliku 9.17).



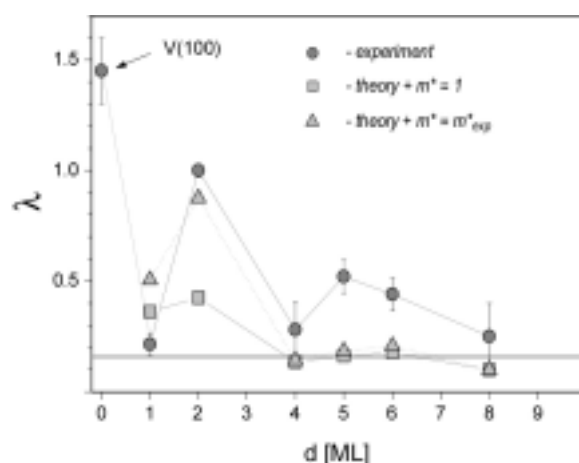
Slika 9.17. Shematski prikaz hibridizacije s-p QW stanja sa d-stanjima podloge.

Opažene rezultate temperaturne ovisnosti objašnjavamo na temelju statičkih i dinamičkih efekata. Naime, statičko temperaturno širenje mijenja širinu kvantne jame i dolazi do promjene energije vezanja s-p QWS. Temperaturni efekt je znatno izraženiji u srebru, nego u vanadiju, što je nužno, jer važnost igra i pozicija Fermijevog nivoa. U našem je slučaju Fermijev nivo dominantno određen vanadijem. Razmatrajući dinamičke efekte perturbativnim pristupom dolazimo do izraza za inverzno vrijeme života fotošupljine, odnosno širinu fotoemisijske linije:

$$\frac{1}{\tau} = \frac{A_c}{M\hbar^2} \left[ \sum_f \{m_{xy}^f |T_{fi}|^2 (2n(\omega_0) + 1) \frac{Y^2(Q_{f,i})}{\omega_0}\} + m_{xy}^i |T_{ii}|^2 (n(\omega_0) + 1) \frac{Y^2(Q_{i,i})}{\omega_0} \right] \quad (9.6)$$

gdje je  $m_{xy}$  efektivna masa elektrona,  $T_{ij}$  matrični element prijelaza,  $Y$  tako zvani geometrijski faktor koji ovisi o fononskom valnom vektoru  $Q$ ,  $n$  je Bose-Einsteinova raspodijela,  $A_c$  površina površinske Wigner-Seitzove ćelije, te  $M$  masa površinskog atoma. U model ugrađujemo osnovnu pretpostavku da su fononske vibracije u sistemu najizraženije na samom površinskom sloju (nedisperzivni Rayleighov površinski mod frekvencije  $\omega_0$ ), što na

tom mjestu izaziva šupljina-fonon prijelaze, pri čemu ključnu ulogu poprima amplituda valne funkcije na sloj-površina granici. Unutar takvih razmatranja kvalitativno i kvantitativno možemo vrlo dobro opisati opaženo ponašanje (vidi sliku 9.18). Eksperimentalni rezultati, osobito oni temperaturne ovisnosti širine fotoemisijских linija van centra Brillouinove zone, ukazuju da je fononska struktura spektra vjerojatno kompliciranija. Kvalitativno je, ipak, ključno da je težina fononskog spektra najveća na granici sloja i vakuuma, barem za naš sistem. Temperaturnu promjenu efektivne mase objašnjavamo kombinacijom argumenata da dolazi do pomaka u vezivnoj energiji stanja sa temperaturom sa činjenicom da s-p stanja hibridiziraju sa d-stanjem podloge.

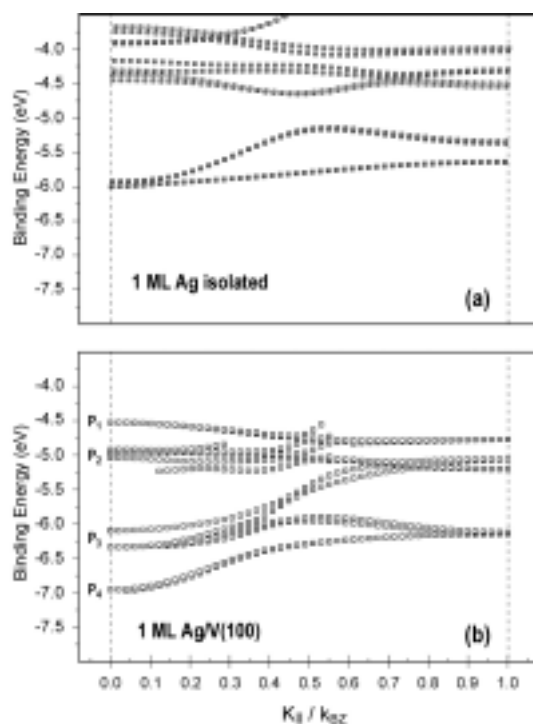


Slika 9.18. Konstanta e-p vezanja ( $\lambda$ ) kao funkcija debljine srebrnog sloja. Kružići su eksperimentalno dobivene vrijednosti, kvadratići teoretski modelirane vrijednosti sa  $m_{xy} = m_e$ , dok najbolje slaganje daju trokutići koji su teorijske vrijednosti sa uključenim mjenjenim efektivnim masama  $m_{xy}$ .

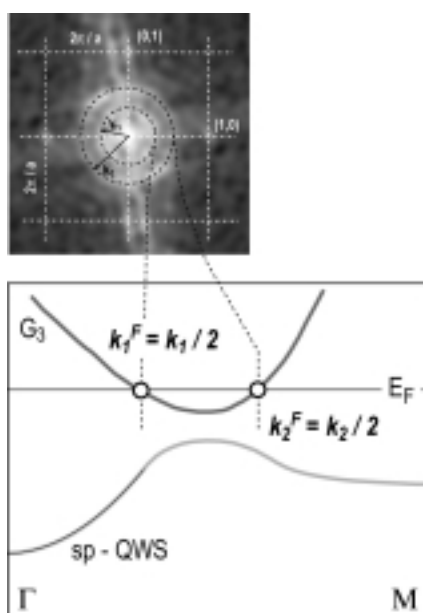
### 9.7.3 d-stanja kvantne jame

d-QW stanja uspješno možemo modelirati unutar modela višestrukih refleksija, za identifikaciju energije vezanja pojedinih d-fotoemisijских maksimuma, pa i za opaženo cijepanje  $P_2$  maksimuma. Vrlo uske mjerene širine fotoemisijских maksimuma d-QW stanja, kao i ovisnost širine o debljini sloja (osobito za najtanje slojeve) upućuje na to da je ultra tanki srebrni sloj na vanadiju idealan primjer dvodimenzionalnog sistema. To zaključujemo i usporedbom sa Ag/Fe(100) i Ag/Mo(110) sistemima.

Kao specijalni slučaj možemo izdvojiti 1 ML Ag/V(100). Provedeni TB računi pokazuju da uslijed međudjelovanja sa podlogom dolazi do znatnog utjecaja i pomaka vezivnih energija. S druge strane, računi pokazuju da je utjecaj podloge za veće debljine zanemariv. Račun pravilno predviđa i opaženo cijepanje fotoemisijских linija d-QW stanja za 1 i 2 ML. Cijepanje pripisujemo efektima spin-orbit međudjelovanja. Računi za izolirani i adsorbirani 1 ML Ag/V(100) prikazani su na slici 9.19.



Slika 9.19. [193] TB račun elektronske strukture Ag/V(100) za: (a) slobodnostojeći srebrni sloj duž [110] smjera, (b) TB račun elektronske strukture 1 ML Ag/V(100) duž [100] smjera.



Slika 9.20. Shematski prikaz veze Ag/V(100) elektronske strukture i površinske Fermijeve plohe koju mjerimo u FT-STM slikama.

#### 9.7.4. STM i elektronska struktura

Za objašnjavanje efekta površinskih valova potrebno je razmotriti vezu elektronske strukture na površini i opažene pojave. Kao potencijalni kandidati koji bi mogli doprinjeti mjerenoj površinskoj Fermijevoj plohi su ponajprije s-p QW stanja. Potencijalno bi s-p QW

stanja rezultirala različitim Fermijevim ploham za različite debljine srebrnog sloja. Međutim, kako su fotoemisijiska mjerenja pokazala, dolazi do hibridizacije s-p QW stanja sa d-stanjem podloge i ona ne prelaze Fermijev nivo, te ne mogu konstituirati površinsku Fermijevu plohu. To navodi na zaključak da je opažena površinska Fermijeve ploha upravo određena elektronskom vrpcom podloge (vanadija) koja hibridizira sa stanjima sloja. Da bi efekti podloge bili vidljivi na površini potrebno je da je efekt hibridizacije jaki, kako smo i opazili u našim mjerenjima. Slika 9.20 shematski ilustrira kako elektronska vrpca podloge određuje površinsku Fermijevu plohu.

## 9.8. Zaključak

U ovom radu temeljito smo ispitali elektronska i strukturna svojstva ultra tankih srebrnih slojeva naparenih na vanadijevu (100) podlogu. Elektronska svojstva su u valentnom području dominantno utjecana postojanjem dva hibridizacijska energetska procjepa, koji su posljedica neslaganja elektronskih struktura vanadija i srebra. Mjerenja su provedena u pet različitih ultra-visoko vakuumskih sistema. Korišten je širok spektar eksperimentalnih tehnika (AES, LEED, STM i HRARUPS). U fotoemisijiskim mjerenjima korišteni su izvori promjenjive fotonske energije (sinhrotroni).

Utvdili smo jednostavnu i ponovljivu proceduru za pripremu (5×1) rekonstruirane vanadijeve površine koja služi kao podloga za rast srebrnih slojeva. Ključni korak pripreme podloge uključuje zagrijavanje na visoku temperaturu (do 1200 K), što rezultira ravnom površinom sa velikim brojem širokih terasa. Također smo pronašli da se kemijski sastav površine mijenja na nanometarskoj skali, što se poklapa sa rezultatima atomski razlučivih STM istraživanja koja su pokazala niz lokalnih atomskih uređenja. Nadalje smo istraživali metodu za rast atomskih glatkih srebrnih slojeva. Pronašli smo da naparavanje srebra na podlogu pri sobnoj temperaturi završava trodimenzionalnim srebrnim klasterima, dok zagrijavanje na dobro definirane temperature dovodi do formiranja atomski uniformnih 1 ili 2 sloja srebra. Tijekom tog temperaturnog tretmana dolazi do difuzije kisikovih i ugljikovih atoma odgovornih za postojanje vanadijeve rekonstrukcije, te do potpunog uklanjanja (5×1) rekonstrukcije vanadijeve površine čime je omogućen nesputani rast (1×1) uniformnih srebrnih slojeva. Prema rezultatima za pročavane debljine (1-8 ML) srebro raste u skladu sa podlogom, odnosno struktura srebrnog sloja je tetragonalna, što potvrđuju i STM i LEED mjerenja. Vjerujemo da je tetragonalna struktura srebra stabilna zbog relativno malog neslaganja parametara rešetke vanadija i srebra i vjerojatno zbog malih razlika u volumnim energijama tetragonalnog i fcc srebra.

Za 1-8 ML debele srebrne slojeve karakterizirali smo s-p stanja kvantnih jama mjereći im disperziju duž  $\Gamma M$  smjera u površinskoj Brillouinovoj zoni. Nalazimo da, otprilike  $\pm 0.25 \text{ \AA}^{-1}$  u okolini centra Brillouinove zone, s-p QW elektroni pokazuju slobodnoelektronsko ponašanje

(parabolične disperzije). Izmjerali smo da efektivne mase u smjeru površine,  $m_{xy}$ , variraju sa debljinom filma od gotovo slobodnoelektronskih (za 8 ML Ag/V(100)) do  $2.4 \cdot m_e$  za 2 ML Ag/V(100). Vjerujemo da su varijacija i relativno velike efektivne mase s-p elektrona kvantnih jama posljedica hibridizacije sa d-stanjem podloge. To nalazimo iz mjerenih disperzijskih krivulja gdje opažamo odstupanja od paraboličnih disperzija nakon  $\cong 0.25 \text{ \AA}^{-1}$ , pri čemu se disperzije savijaju i oko otprilike  $0.35 \text{ \AA}^{-1}$  mijenjaju predznak. Analiza oblika fotoemisijskih maksimuma omogućila nam je da razdvojimo utjecaje šupljina-elektron, šupljina-nečistoća i šupljina-fonon međudjelovanja u ukupnom mjenom kvazičestičnom vremenu života za s-p stanja kvantnih jama. Nadalje, iz temperaturne ovisnosti fotoemisijskih spektara pouzdano smo odredili šupljina-fonon konstantu vezanja  $\lambda$ . Jačina tog vezanja pokazuje jaki oscilatorni karakter u odnosu na debljinu sloja, sa apsolutnim maksimumom za 2 ML Ag/V(100) ( $\lambda = 1$ ) i dodatnim lokalnim maksimumom za 5 ML Ag/V(100) ( $\lambda = 0.52$ ). Pokazali smo da se fotošupljina dominantno veže na vibracijski mod na samoj površini i da je varijacija i pojačanje šupljina-fonon vezanja posljedica promjena amplitude stanja kvantne jame na površini. Iz mjerenja temperaturnih učinaka u fotoemisiji van centra površinske Brillouinove zone nalazimo dokaze da je fononski spektar uključen u šupljina-fonon međudjelovanje kompliciraniji nego što predviđamo jednostavnim računom koji uzima u obzir samo Rayleighov fononski mod.

Na temelju rezultata fotoemisijskih mjerenja stanja kvantnih jama d-simetrije identificirali smo veliki broj stanja. Primjenom modela višestrukih refleksija pravilno smo reproducirali energetske pozicije tih kvantnih stanja. d-QW stanja pokazuju znatno blaže disperzije u odnosu na s-p stanja. Vodeći fotoemisijski maksimum za 2 ML Ag/V(100) pokazuje slobodnoelektronsko ponašanje sa velikom efektivnom masom od  $-5.9 \cdot m_e$ . Za 1 i 2 ML Ag/V(100) izmjerili smo cijepanje fotoemisijskog maksimuma što pripisujemo učincima spin-orbit međudjelovanja. Izmjereno cijepanje pravilno opisuju i TB računi. Iz usporedbe mjerenih i računatih vrijednosti nalazimo da je za 1 ML srebra znatan utjecaj vanadijeve podloge, što se vidi u velikom pomaku energije stanja slobodnostojećeg i adsorbiranog srebrnog sloja. Na temelju analize širina vodećih fotoemisijskih maksimuma u d-području nalazimo da su srebrni slojevi uniformno narašteni na V(100) podlogu idealni primjer dvodimenzionalnog srebra. d-elektroni su u potpunosti locirani unutar srebrnog sloja, što je posljedica savršene refleksije na samoj podlozi. Zaljučujemo da je simetrijski energetski procjep za d-elektrone efikasan poput totalnog energetskog procjepa.

I konačno, STM mjerenja u modu konstantne struje skeniranja pokazuju pojavu izraženih površinskih valova za studirane debljine srebrnih slojeva (1-5 ML). Za obradu tih podataka korištena je metoda Fourier transformiranih STM slika. Interesantno je da, za sve proučavane debljine, opažamo otprilike sličnu površinsku Fermijevu plohu sa dva izražena prstenasta doprinosa. U usporedbi sa fotoemisijskim rezultatima pripisujemo te prstenaste doprinose otiscima prisutnosti  $G_3$  d-vanadijeve volumne vrpce koja prelazi Fermijev nivo i

hibridizira sa s-p stanjima kvantnih jama.

Zaključno, nalazimo da rezultati prikazanih istraživanja odaju mnoga interesantna svojstva srebrnih ultra tankih slojeva na vanadijevoj (100) površini. Fotoemisija i STM pokazale su se kao idealne metode za proučavanje svojstava dvodimenzionalnih sistema. Svojstva Ag/V(100) sistema uglavnom su posljedica smanjene dimenzionalnosti elektronskih stanja koja se formiraju u srebrnom sloju. U tom smislu najfascinantniji je primjer pojačanja i varijacije šupljina-fonon međudjelovanja za s-p QW stanja, gdje smo našli da granica prema vakuumu igra ključnu ulogu. S druge strane, nalazimo da su neka svojstva sistema određena prisustvom podloge, odnosno granice sloja sa podlogom. U tom smislu izmjerili smo pojačanje efektivnih masa s-p elektrona kvantnih jama. Značajan utjecaj podloge opažen je i za d-stanja kvantne jame u slučaju sloja debljine 1 ML. Također, pokazalo se da površinska Fermijeva ploha predstavlja otisak stanja podloge za debljine do 5 ML srebra.

## Životopis

ROĐEN SAM 19. VELJAČE 1973. GODINE U ZAGREBU. PRIRODOSLOVNO MATEMATIČKI FAKULTET (1991-1997), SMJER INŽ FIZIKE, ZAVRŠIO SAM U OŽUJKU 1997. GODINE OBRANOM DIPLOMSKOG RADA: "ELEKTRONSKA I STRUKTURNA SVOJSTVA VANADIJEVIH ULTRA-TANKIH FILMOVA NA  $Cu(100)$  POVRŠINI". OD RUJNA 1997. GODINE RADIM KAO ASISTENT NA INSTITUTU ZA FIZIKU U ZAGREBU, POD MENTORSTVOM DR. PETRA PERVANA. MAGISTARSKI RAD: "TEMPERATURNNA SVOJSTVA STANJA KVANTNIH JAMA U ULTRA-TANKIM SLOJEVIMA SREBRA NA  $V(100)$  POVRŠINI (STM, LEED I UPS STUDIJA)" OBRANIO SAM U TRAVNJU 2001. GODINE.

DO SADA SAM OBJAVIO SLIJEDEĆE ZNANSTVENE RADOVE:

1. *GROWTH, STRUCTURE AND PROPERTIES OF ULTRA-THIN COPPER FILMS ON A  $V(110)$  SURFACE*,  
MARKO KRALJ, PETAR PERVAN AND MILORAD MILUN, SURF. SCI. 423 (1999) 24
2. *STM INVESTIGATIONS OF CONTAMINATED AND CLEAN  $V(100)$  SURFACE*,  
MARKO KRALJ, PETAR PERVAN, MILORAD MILUN, JÖRG SCHNEIDER, BERNHARD SCHAEFER, AXEL ROSENHAHN AND KLAUS WANDEL, FIZIKA A 8(3) (1999) 123
3. *OSCILLATORY ELECTRON-PHONON COUPLING IN ULTRA-THIN SILVER FILMS ON  $V(100)$* ,  
TONICA VALLA, MARKO KRALJ, ANTONIO SIBER, PETER D. JOHNSON, MILORAD MILUN, PETAR PERVAN AND DAVID P. WOODRUFF, J. PHYS.: CONDENS. MATTER 12 (2000) L477
4. *TEMPERATURE DEPENDENCE OF PHOTOEMISSION FROM QUANTUM-WELL STATES IN  $Ag/V(100)$ : MOVING SURFACE-VACUUM BARRIER EFFECTS*,  
MARKO KRALJ, ANTONIO ŠIBER, PETAR PERVAN, MILORAD MILUN, TONICA VALLA, PETER D. JOHNSON AND DAVID P. WOODRUFF, PHYS. REV. B 64 (2001) 085411
5. *GROWTH OF COPPER AND VANADIUM ON A THIN  $Al_2O_3$ -FILM ON  $Ni_3Al(111)$* ,  
ALMUTH WILTNER, AXEL ROSENHAHN, JÖRG SCHNEIDER, CONRAD BECKER, PETAR PERVAN, MILORAD MILUN, MARKO KRALJ AND KLAUS WANDEL, THIN SOLID FILMS 400 (2001) 71
6.  *$Al_2O_3$ -FILMS ON  $Ni_3Al(111)$ : A TEMPLATE FOR NANOSTRUCTURED CLUSTER GROWTH*,  
CONRAD BECKER, AXEL ROSENHAHN, ALMUTH WINTLER, KATHRIN VON BERGMANN, JÖRG SCHNEIDER, PETAR PERVAN, MILORAD MILUN, MARKO KRALJ AND KLAUS WANDEL, NEW JOURNAL OF PHYSICS 4 (2002) 75.1
7. *HRAES, STM AND ARUPS STUDY OF THE  $(5 \times 1)$  RECONSTRUCTED  $V(100)$  SURFACE*,  
MARKO KRALJ, PETAR PERVAN, MILORAD MILUN, KLAUS WANDEL, DJORDJE MANDRINO AND MONIKA JENKO, SURF. SCI. 526 (2003) 166-176

## Curriculum vitae

I WAS BORN ON 19<sup>TH</sup> OF FEBRUARY 1973. IN ZAGREB, CROATIA. IN 1991. I HAVE ENROLLED THE FACULTY OF SCIENCE (PHYSICS) AND REACHED THE B.Sc. DEGREE IN 1997. WITH DIPLOMA THESIS TITLED "ELECTRONIC AND STRUCTURAL PROPERTIES OF VANADIUM ULTRA THIN FILMS ON A Cu(100) SURFACE". SINCE THE AUTUMN OF 1997. I AM EMPLOYED AS A RESEARCH ASSISTANT AT THE INSTITUTE OF PHYSICS IN ZAGREBU. IN 2001. I HAVE REACHED THE M.Sc. DEGREE UNDER THE SUPERVISION OF DR. PETAR PERVAN. THE M.Sc. THESIS IS TITLED "TEMPERATURE PROPERTIES OF QUANTUM WELL STATES IN ULTRA THIN VANADIUM FILMS ON V(100)".

IN ADDITION TO THE PUBLISHED PAPERS I HAVE PARTICIPATED IN ABOUT 12 INTERNATIONAL CONFERENCES WITH 10 ORAL AND 6 POSTER PRESENTATIONS. LIST OF PUBLISHED PAPERS (FEBRUARY 2003.):

1. *GROWTH, STRUCTURE AND PROPERTIES OF ULTRA-THIN COPPER FILMS ON A V(110) SURFACE*,  
MARKO KRALJ, PETAR PERVAN AND MILORAD MILUN, SURF. SCI. **423** (1999) 24
2. *STM INVESTIGATIONS OF CONTAMINATED AND CLEAN V(100) SURFACE*,  
MARKO KRALJ, PETAR PERVAN, MILORAD MILUN, JÖRG SCHNEIDER, BERNHARD SCHAEFER, AXEL ROSENHAHN AND KLAUS WANDEL, FIZIKA A **8**(3) (1999) 123
3. *OSCILLATORY ELECTRON-PHONON COUPLING IN ULTRA-THIN SILVER FILMS ON V(100)*,  
TONICA VALLA, MARKO KRALJ, ANTONIO SIBER, PETER D. JOHNSON, MILORAD MILUN, PETAR PERVAN AND DAVID P. WOODRUFF, J. PHYS.: CONDENS. MATTER **12** (2000) L477
4. *TEMPERATURE DEPENDENCE OF PHOTOEMISSION FROM QUANTUM-WELL STATES IN Ag/V(100): MOVING SURFACE-VACUUM BARRIER EFFECTS*,  
MARKO KRALJ, ANTONIO ŠIBER, PETAR PERVAN, MILORAD MILUN, TONICA VALLA, PETER D. JOHNSON AND DAVID P. WOODRUFF, PHYS. REV. B **64** (2001) 085411
5. *GROWTH OF COPPER AND VANADIUM ON A THIN AL<sub>2</sub>O<sub>3</sub>-FILM ON Ni<sub>3</sub>Al(111)*,  
ALMUTH WILTNER, AXEL ROSENHAHN, JÖRG SCHNEIDER, CONRAD BECKER, PETAR PERVAN, MILORAD MILUN, MARKO KRALJ AND KLAUS WANDEL, THIN SOLID FILMS **400** (2001) 71
6. *AL<sub>2</sub>O<sub>3</sub>-FILMS ON Ni<sub>3</sub>Al(111): A TEMPLATE FOR NANOSTRUCTURED CLUSTER GROWTH*,  
CONRAD BECKER, AXEL ROSENHAHN, ALMUTH WINTLER, KATHRIN VON BERGMANN, JÖRG SCHNEIDER, PETAR PERVAN, MILORAD MILUN, MARKO KRALJ AND KLAUS WANDEL, NEW JOURNAL OF PHYSICS **4** (2002) 75.1
7. *HRAES, STM AND ARUPS STUDY OF THE (5x1) RECONSTRUCTED V(100) SURFACE*,  
MARKO KRALJ, PETAR PERVAN, MILORAD MILUN, KLAUS WANDEL, DJORDJE MANDRINO AND MONIKA JENKO, SURF. SCI. **526** (2003) 166-176

## 10. References

---

- [1] M.N. Baibich, J.M. Broto, A. Fert, F. Nguyen Van Dau, F. Petroff, P. Etienne, G. Creuzet, A. Friederich and J. Chazelas, *Giant magnetoresistance of (001)Fe/(001)Cr magnetic superlattices*, Phys. Rev. Lett. **61** (1988) 2472
- [2] F.J. Himpsel, J.E. Ortega, G.J. Mankey, R.F. Willis, *Magnetic nanostructures*, Adv. Phys. **47** (1998) 511
- [3] T.-C. Chiang, *Photoemission studies of quantum well states in thin films*, Surf. Sci. Rep. **39** (2000) 181
- [4] M. Milun, P. Pervan and D.P. Woodruff, *Quantum well structures in thin metal films: simple model physics in reality*, Rep. Prog. Phys. **65** (2002) 99
- [5] T. Valla, *Electronic and structural properties of ultra-thin metallic films on metal surfaces*, Dissertation, Zagreb, 1996
- [6] N.V. Smith, P. Thiry and Y. Petroff, *Photoemission linewidths and quasiparticle lifetimes*, Phys. Rev. B **47** (1993) 15476
- [7] S. Hüfner, *Photoelectron spectroscopy*, Springer Series in Solid-State Sciences Vol. **82**, Springer, Berlin, 1995
- [8] R. Matzdorf, *Investigation of line shapes and line intensities by high-resolution uv-photoemission spectroscopy – some case studies on noble-metal surfaces*, Surf. Sci. Rep. **30** (1998) 153
- [9] R. Matzdorf, *Quasi-particle lifetimes on noble metal surfaces studied by ARPES and STM*, Chem. Phys. **251** (2000) 151
- [10] D.P. Woodruff and T.A. Delchar, *Modern techniques of surface science*, Cambridge University Press, Cambridge, 1986
- [11] J. Tersoff and D.R. Hamann, *Theory of the scanning tunnelling microscope*, Phys. Rev. B **31** (1985) 805
- [12] N. Klipa, M. Šunjić, *Dynamical effective potentials in electron tunnelling - path-integral study*, Phys. Rev. B **52** (1995) 12408
- [13] D. Šestović and M. Šunjić, *Tunnelling barrier reduction and asymmetry in scanning tunnelling microscope due to the dynamical screening*, Solid State Commun. **98** (1996) 375
- [14] D. Šestović, L. Marušić and M. Šunjić, *Dynamical screening in the scanning tunnelling microscope and metal-insulator-metal junctions*, Phys. Rev. B **55** (1997) 1741
- [15] F. Besenbacher, *Scanning tunnelling microscopy studies of metal surfaces*, Rep. Prog. Phys. **59** (1996) 1737
- [16] G.A.D. Briggs and A.J. Fisher, *STM experiment and atomistic modelling hand in hand: Individual molecules on semiconductor surfaces*, Surf. Sci. Rep. **33** (1999) 1
- [17] D. Drakova, *Theoretical modelling of scanning tunnelling microscopy, scanning tunnelling spectroscopy and atomic force microscopy*, Rep. Prog. Phys. **64** (2001) 205
- [18] L. Bürgi, *Scanning tunnelling microscopy as local probe of electron density, dynamics, and transport at metal surfaces*, Dissertation, Lausanne 1999
- [19] L. Bürgi, H. Brune, O. Jeandupeux and K. Kern, *Quantum coherence and lifetimes of surface-state electrons*, J. Elec. Spec. Rel. Phen. **109** (2000) 33
- [20] M.F. Crommie, C.P. Lutz, D.M. Eigler, *Imaging standing waves in a 2-dimensional electron-gas*, Nature **363** (1993) 524

## 10. REFERENCES

---

- [21] Y. Hasegawa, P. Avouris, *Direct observation of standing wave formation at surface steps using scanning tunnelling spectroscopy*, Phys. Rev. Lett. **71** (1993) 1071
- [22] M.F. Crommie, C.P. Lutz, D.M. Eigler, *Confinement of electrons to quantum corrals on a metal surface*, Science **262** (1993) 218
- [23] P. Avouris, I.-W. Lyo, *Observation of quantum-size effects at room temperature on metal surfaces with STM*, Science **264** (1994) 942
- [24] P. Avouris, I.-W. Lyo, R.E. Walkup, Y. Hasegawa, *Real space imaging of electron scattering phenomena at metal surfaces*, J. Vac. Sci. Technol. B **12** (3) (1994) 1447
- [25] S. Crampin, M.H. Boon, J.E. Inglesfield, *Influence of bulk states on laterally confined surface state electrons*, Phys. Rev. Lett. **73** (1994) 1015
- [26] J. Li, W.D. Schneider, R. Berndt, O.R. Bryant and S. Crampin, *Surface-state lifetime measured by scanning tunnelling spectroscopy*, Phys. Rev. Lett. **81** (1998) 4464
- [27] J. Li, W.-D. Schneider, S. Crampin, R. Berndt, *Tunnelling spectroscopy of surface state scattering and confinement*, Surf. Sci. **422** (1999) 95
- [28] J. Kliewer, R. Berndt, E.V. Chulkov, V.M. Silkin, P.M. Echenique and S. Crampin, *Dimensionality effects in the lifetime of surface states*, Science **288** (2000) 1399
- [29] E. Wahlström, I. Ekvall, H. Olin and L. Walldén, *Long-range interaction between adatoms at the Cu(111) surface imaged by scanning tunnelling microscopy*, Appl. Phys. A **66** (1998) S107
- [30] C. Nagl, O. Haller, E. Platzgummer, M. Schmid, P. Varga, *Submonolayer growth of Pb on Cu(111) – surface alloying and de-alloying*, Surf. Sci. **321** (1994) 237
- [31] S. Crampin, *Surface states as probes of buried impurities*, J. Phys.: Condens. Matt. **6** (1994) L613
- [32] M. Schmid, S. Crampin, P. Varga, *STM and STS of bulk electron scattering by subsurface objects*, J. Elec. Spec. Rel. Phen. **109** (2000) 71
- [33] P.T. Sprunger, L. Petersen, E.W. Plummer, E. Laegsgaard and F. Besenbacher, *Giant Friedel oscillations on the beryllium(0001) surface*, Science **275** (1997) 1764
- [34] L. Petersen, P.T. Sprunger, Ph. Hofmann, E. Laegsgaard, B.G. Briner, M. Doering, H.-P. Rust, A.M. Bradshaw, F. Besenbacher and E.W. Plummer, *Direct imaging of the two-dimensional Fermi contour – Fourier-transform STM*, Phys. Rev. B **57** (1998) R6858
- [35] L. Petersen, Ph. Hofmann, E.W. Plummer and F. Besenbacher, *Fourier transform – STM: determining the surface Fermi contour*, J. Elec. Spec. Rel. Phen. **109** (2000) 97
- [36] L. Petersen, B. Schaefer, E. Lægsgaard, I. Stensgaard, F. Besenbacher, *Imaging the surface Fermi contour on Cu(110) with scanning tunnelling microscopy*, Surf. Sci. **457** (2000) 319
- [37] J. Friedel, *Metallic alloys*, Nuovo Cimento Suppl. **7** (1958) 287
- [38] N.W. Ashcroft and N.D. Mermin, *Solid state physics*, Saunders College, Philadelphia, 1976
- [39] S.D. Kevan, Ed., *Angle-resolved Photoemission*, Vol. 74 of Studies in Surface Science and Catalysis, Elsevier, Amsterdam, 1992
- [40] L. Hedin, S. Lundquist, *Solid state physics 23*, Academic, New York, 1969
- [41] D. Pines and P. Nozières, *The theory of quantum liquids*, Benjamin, New York, 1969

## 10. REFERENCES

- 
- [42] T.Valla, P.D. Johnson, Z. Yusof, B. Wells, Q. Li, S.M. Lourelro, R.J. Cava, M. Mikami, Y. Mori, M. Yoshimura and T. Sasaki, *Coherence-incoherence and dimensional crossover in layered strongly correlated metals*, Nature **417** (2002) 627
- [43] F. Reinert, G. Nicolay, S. Schmidt, D. Ehm and S. Hüfner, *Direct measurements of the L-gap surface states on the (111) face of the noble metals by photoelectron spectroscopy*, Phys. Rev. B **63** (2001) 115415
- [44] For details see <http://www.scienta.se/scientae.html>
- [45] T. Valla, A.V. Fedorov, P.D. Johnson and S.L. Hulbert, *Many-body effects in angle-resolved photoemission: quasiparticle energy and lifetime of a Mo(110) surface state*, Phys. Rev. Lett. **83** (1999) 2085
- [46] N.V. Smith, Comments Condens. Matter Phys. **15** (1992) 263
- [47] G. Grimvall, *The electron-phonon interaction in metals*, North-Holland, New York, 1981
- [48] A. Eiguren, B. Helsing, F. Reinert, G. Nicolay, E.V. Chulkov, V.M. Silkin, S. Hüfner, and P.M. Echenique, *Role of bulk and surface phonons in the decay of metal surface state*, Phys. Rev. Lett. **88** (2002) 066805
- [49] The STM is designed and built in the group of Prof. Klaus Wandelt from Bonn. The details are described in the paper: M. Wilms, M. Schmidt, G. Bermes and K. Wandelt, *New and versatile ultrahigh vacuum scanning tunnelling microscope for film growth experiments*, Rev. Sci. Instrum. **69** (1998) 2696
- [50] For details of the beamline see <http://nslsweb.nsls.bnl.gov/nsls/beamlines/home/U13UB.asp>
- [51] For details of the beamline see <http://www.elettra.trieste.it/experiments/beamlines/vuv/index.html>
- [52] P. Pervan, T. Valla, M. Milun, AB. Hayden, DP. Woodruff, *Photoemission and inverse photoemission spectroscopy of V(100)*, J. Phys. Condens. Matter **8** (1996)
- [53] W. Shockley, *On the surface states associated with a periodic potential*, Phys. Rev. **56** (1939) 317
- [54] E.G. McRae, *Electronic surface resonances of crystals*, Rev. Mod. Phys. **51** (1979) 541
- [55] N.V. Smith, D.P. Woodruff, *Inverse photoemission from metal surfaces*, Prog. Surf. Sci. **21** (1986) 295
- [56] I. Tamm, Über eine mögliche Art der Elektronenbindung an Kristalloberflächen, Z. Phys. **76** (1932) 849
- [57] G. Perluzzo, G. Bader, L.G. Caron, L. Sanche, *Direct determination of electron band energies by transmission interference in thin films*, Phys. Rev. Lett. **55** (1985) 545
- [58] T. Schmitz-Hübsch, K. Oster, J. Radnik and K. Wandelt, *Photoemission from quantum-well states in ultrathin Xe crystals*, Phys. Rev. Lett. **64** (1995) 2595
- [59] R. Paniago, R. Matzdorf, G. Meister, A. Goldmann, *Quantization of electron states in ultrathin xenon layers*, Surf. Sci. **325** (1995) 336
- [60] J.D. McNeill, R.L. Lingle Jr., R.E. Jordan, D.F. Padowitz and C.B. Harris, *Interfacial quantum well states of Xe and Kr adsorbed on Ag(111)*, J. Chem. Phys. **105** (1996) 3883
- [61] M. Grüne, T. Pelzer, K. Wandelt and I.T. Steinberger, *Quantum-size effects in thin solid xenon films*, J. Elec. Spec. Rel. Phen. **98-99** (1999) 121
- [62] B. Grimm, H. Hovel, M. Pollman and B. Reihl, *Physisorbed rare-gas monolayers: evidence for domain wall tilting*, Phys. Rev. Lett. **83** (1999) 991
- [63] E. Bertel, *The interaction of rare gases with transition metal surfaces*, Surf. Sci. **367** (1996) L61
- [64] M.C. Desjonqueres and D. Spanjaard, *Concepts in Surface Physics*, Springer, Berlin, 1996
- [65] D.A. Papaconstantopoulos, *Electronic structures database*, downloadable at <http://manybody.nrl.navy.mil/esdata/database.html>

- 
- [66] T. Miller, A. Ssamsavar, G.E. Franklin, T.-C. Chiang, *Quantum-well states in a metallic system: Ag on Au(111)*, Phys. Rev. Lett. **61** (1988) 1404
- [67] W.E. McMahon, T. Miller and T.-C. Chiang, *Electronic properties of the leaky quantum-well system Ag(111)/Au/Ag*, Phys. Rev. B **54** (1996) 10800
- [68] Z.Q. Qiu, J. Person and S.D. Bader, *Oscillatory interlayer magnetic coupling of wedged Co/Cu/Co sandwiches grown on Cu(100) by molecular beam epitaxy*, Phys. Rev. B **46** (1992) 8659
- [69] T. Miller, A. Ssamsavar and T.-C. Chiang, *Ag-Au superlattice band structure*, Phys. Rev. B **50** (1994) 17686
- [70] M.A. Mueller, T. Miller and T.-C. Chiang, *Determination of the bulk band structure of Ag in Ag/Cu(111) quantum-well systems*, Phys. Rev. B **41** (1990) 5214
- [71] K. Takahashi, A. Tanaka, M. Hatano, H. Sasaki, S. Suzuki and S. Sato, *Angle-resolved photoemission study of quantized electronic structures on Ag nanofilms*, J. Electr. Spectr. Rel. Phen. **88** (1998) 347
- [72] J.J. Paggel, T. Miller, T.-C. Chiang, *Quantum-well states as Fabry-Perot modes in a thin-film interferometer*, Science **283** (1999) 1709
- [73] J.B. Pendry and S.B. Gurman, *Theory of surface states: general criteria for their existence*, Surf. Sci. **49** (1975) 87
- [74] P.M. Echenique, J.B. Pendry, *The existence and detection of Rydberg states at surfaces*, J. Phys. C **11** (1978) 2065
- [75] N.V. Smith, C.T. Chen, *Spectroscopic constraints on the potential barrier at metal surfaces*, Surf. Sci. **247** (1991) 133
- [76] N.V. Smith, *Inverse photoemission*, Rep. Prog. Phys. **51** (1988) 1227
- [77] N.V. Smith, N.B. Brooks, Y. Chang, P.D. Johnson, *Quantum-well and tight-binding analyses of spin-polarized photoemission from Ag/Fe(001) overlayers*, Phys. Rev. B **49** (1994) 332
- [78] S.-Å. Lindgren and L. Walldén, *Band mapping by photoemission: analysis of overlayer states in Ag films on Au (111)*, J.Phys. Codens Matter **1** (1989) 2151
- [79] D.A. Cleason, S.-Å. Lindgren and L. Walldén, *Valence-electron dispersion of close-packed Li determined by photoemission from thin films on Cu(111)*, Phys. Rev. B **60** (1999) 5217
- [80] J.J. Paggel, T. Miller and T.-C. Chiang, *Occupied and unoccupied band structure of Ag(100) determined by photoemission from Ag quantum wells and bulk samples*, Phys. Rev. B **61** (2000) 1804
- [81] C. Kittel, *Introduction to Solid State Physics*, John Wiley and Sons, New York, 1976
- [82] R.E. Thomas, *Interference effects in the reflection of low-energy electrons from thin films of Au on Ir*, J. Appl. Phys. **41** (1970) 5330
- [83] R.C. Jaklevic, J. Lambe, M. Mikkor and W.C. Vassell, *Observation of electron standing waves in a crystalline box*, Phys. Rev. Lett. **26** (1971) 2688
- [84] R.C. Jaklevic and J. Lambe, *Experimental study of quantum size effects in thin metal films by electron tunnelling*, Phys. Rev. B **12** (1975) 4146
- [85] M. Jalochowski, *Electron tunnelling in Pb/Ag ultrathin layered structures*, Phys. Status Solidi A **82** (1984) 497
- [86] B.T. Jonker, N.C. Bartelt and R.L. Park, *Quantum size effect in electron transmission through Cu and Ag films on W (110)*, J. Vac. Sci. Technol. A **1** (1983) 1062

## 10. REFERENCES

- 
- [87] R.L. Park, B.T. Jonker, H. Iwasaki and Q.-G. Zhu, *Quantum size effects in the reflection of slow electrons from thin films*, Applications Surf. Sci. **22** (1985) 1
- [88] Q.-G. Zhu, Y. Yang, E.D. Williams and R.L. Park, *Observation of resonant electron transmission through a Ni/Cu/Ni(100) sandwich structure*, Phys. Rev. Lett. **59** (1987) 835
- [89] R. Zdyb, M. Stozak and M. Jalochoowski, *Transmission of low-energy electrons through Pb quantum well*, Electron. Technol. **31** (1998) 315
- [90] J.P. Chauvineau and C. Pariset, *Evidence of a quantum size effect during the growth by successive atomic layers of ultra-thin films of indium and tin on films of gold*, J. Physique I **37** (1976) 1325
- [91] H. Hoffmann and G. Fischer, *Electrical conductivity in thin and very thin platinum films*, Thin Solid Films **36** (1976) 25
- [92] G. Fischer and H. Hoffmann, *Size quantization of electronic states in very thin platinum films*, Z. Phys. B **39** (1980) 287
- [93] P. Chaudhari, H.-U. Habermeier and S. Maekawa, *Localization and size effects in single-crystal Au films*, Phys. Rev. Lett. **55** (1985) 430
- [94] M. Jalochoowski, M. Hoffmann and E. Bauer, *Pb layer-by-layer growth at very low temperatures*, Phys. Rev. B **51** (1995) 7231
- [95] J. Braun and J.P. Toennies, *Observation of a quantum size effect in the surface electron density of thin lead films*, Surf. Sci. **384** (1997) L858
- [96] M. Jalochoowski, M. Hoffmann and E. Bauer, *Quantized Hall effect in ultrathin metallic films*, Phys. Rev. Lett. **76** (1996) 4227
- [97] C. Marliere, *Observation of a quantum size effect with unusual long period by experiments of absorption of low energy electrons and by RHEED – a simple physical model*, Surf. Sci. **269-270** (1992) 777
- [98] M. Wuttig, Y. Gauthier, and S. Blügel, *Magnetically Driven Buckling and Stability of Ordered Surface Alloys: Cu(100) c(2x2) Mn*, Phys. Rev. Lett. **70** (1993) 3619
- [99] F.J. Himpsel, *Fe on Au(100): quantum-well states down to a monolayer*, Phys. Rev. B **44** (1991) 5966
- [100] S.C. Wu, K. Garrison, A.M. Begley, F. Jona and P.D. Johnson, *Electronic structure and magnetism of the Rh(001) surface*, Phys. Rev. B **49** (1994) 14081
- [101] H. Hopster, *Spin-polarized electron energy loss spectroscopy*, Surf. Rev. Lett. **1** (1994) 89
- [102] see, for example, P. Segovia, E.G. Michel and J.E. Ortega, *Quantum well states and short period oscillations of the density of states at the Fermi level in Cu films grown on fcc Co(100)*, Phys. Rev. Lett. **77** (1996) 3455
- [103] R. Otero, A.L.V. de Parga, R. Miranda, *Can electron confinement barriers be determined by STM?*, Surf. Sci. **447** (2000) 143
- [104] J. Kliewer and R. Berndt, *Low temperature scanning tunnelling microscopy of Na/Cu(111)*, Surf. Sci. **477** (2001) 250
- [105] M. Breitholtz, T. Kihlgren, S.-Å. Lindgren, H. Olin, E. Wahlstrom and L. Walldén, *Metal quantum wells with all electrons confined: Na films and islands on graphite*, Phys. Rev. B **64** (2001) 073301
- [106] C. Becker, A. Rosenhahn, A. Wiltner, K. von Bergmann, J. Schneider, P. Pervan, M. Milun, M. Kralj and K. Wandelt, *Al<sub>2</sub>O<sub>3</sub>-films on Ni<sub>3</sub>Al(111): a template for nanostructured cluster growth*, New Journal of Physics **4** (2002) 75.1

## 10. REFERENCES

- 
- [107] M.-H. Schaffner, F. Patthey and W.D. Schneider, *Size-selected  $Ag_n$  and  $Cu_n$  clusters supported on  $MgO(100)$  films*, Eur. Phys. J. D **9** (1999) 609
- [108] H. Hovel, B. Grimm, M. Bodecker, K. Fieger and B. Reihl, *Tunnelling spectroscopy of silver clusters at  $T=5$  K: size dependence and spatial energy shifts*, Surf. Sci. **463** (2000) L603
- [109] B. Grimm, *Tunnelspektroskopie und Photoemission bei tiefen Temperaturen an Edelgas-Modellsystemen und Nanostrukturen*, PhD thesis, 2000;  
.pdf file downloadable at <http://eldorado.uni-dortmund.de:8080/FB2/Is1/forschung/2000/Grimm>
- [110] P.D. Loly and J.B. Pendry, *Removing the limits to accurate band-structure determination by photoemission*, J. Phys. C **16** (1983) 423
- [111] J.G. Tobin, S.W. Robey, L.E. Klebanoff and D.A. Shirley,  *$Ag/Cu(001)$ : observation of the development of the electronic structure in metal overlayers from two to three dimensionality*, Phys. Rev. B **28** (1983) 6169
- [112] T. Valla, P. Pervan, M. Milun, A.B. Hayden and D.P. Woodruff, *Electronic structure of silver and copper ultrathin films on  $V(100)$ : Quantum-well states*, Phys. Rev. B **54** (1996) 11786
- [113] J.E. Ortega, F.J. Himpsel, G.J. Mankey and R.F. Willis, *Inverse photoemission from  $V$ ,  $Cr$ ,  $Mn$ ,  $Fe$  and  $Co$  monolayers on  $Ag(100)$* , Phys. Rev. B **47** (1993) 1540
- [114] J. Feydt, A. Elbe, H. Engelhard, G. Meister and A. Goldmann, *Photoemission studies of the  $W(110)/Ag$  interface*, Surf. Sci. **452** (2000) 33
- [115] A.M. Shikin, D.V. Vyalikh, G.V. Prudnikova, V.K. Adamchuk, *Phase accumulation model analysis of quantum well resonances formed in ultra thin  $Ag$ ,  $Au$  films on  $W(110)$* , Surf. Sci. **487** (2001) 135
- [116] M. Pivetta, F. Patthey and W.D. Schneider, *Stability of ultrathin  $Ag$  films on  $Ta(110)$* , Surf. Sci., in press 2003
- [117] J.J. Paggel, T. Miller, D.-A. Luh and T.-C. Chiang, *Quantum well photoemission from atomically uniform  $Ag$  films: determination of electronic band structure and quasi-particle lifetime in  $Ag(100)$* , App. Surf. Sci. **162** (2000) 78
- [118] D.-A. Luh, T. Miller, J.J. Paggel, M.Y. Chou and T.-C. Chiang, *Quantum electronic stability of atomically uniform films*, Science **292** (2001) 1131
- [119] M. Milun, P. Pervan, B. Gumhalter and D.P. Woodruff, *Photoemission intensity oscillations from quantum-well states in the  $Ag/V(100)$  overlayer system*, Phys. Rev. B **59** (1999) 5170
- [120] P. Pervan, M. Milun and D.P. Woodruff, *Interatomic resonant photoemission from quantum-well states in ultrathin silver films of  $Ag$  on  $V(100)$* , Phys. Rev. Lett. **81** (1998) 4995
- [121] D.P. Woodruff, M. Milun and P. Pervan, *Photoemission intensity variations from the quantum well state in the  $Ag/V(100)$  single-monolayer overlayer structure*, J. Phys.:Condens. Matter **11** (1999) L105
- [122] D.-A. Luh, J.J. Paggel, T. Miller and T.-C. Chiang, *d-band quantum well states*, Phys. Rev. Lett. **84** (2000) 3410
- [123] A. Carlsson, B. Hellsing, S.-Å. Lindgren and L. Walldén, *High-resolution photoemission from a tunable quantum well:  $Cu(111)/Na$* , Phys. Rev. B **56** (1997) 1593
- [124] B. Hellsing, J. Carlsson, L. Walldén and S.-Å. Lindgren, *Phonon-induced decay of a quantum-well hole: One monolayer  $Na$  on  $Cu(111)$* , Phys. Rev. B **61** (2000) 2343
- [125] T. Valla, M. Kralj, A. Šiber, P.D. Johnson, M. Milun, P. Pervan and D.P. Woodruff, *Oscillatory electron-phonon coupling in ultra-thin silver films on  $V(100)$* , J. Phys.: Condens. Matter **12** (2000) L477

## 10. REFERENCES

- 
- [126] M. Kralj, A. Šiber, P. Pervan, M. Milun, T. Valla, P.D. Johnson and D.P. Woodruff, *Temperature dependence of the photoemission from quantum-well states in Ag/V(100): moving surface-vacuum effects*, Phys. Rev. B **64** (2001) 085411
- [127] J.J. Paggel, T. Miller, T.-C. Chiang, *Quasiparticle lifetime in macroscopically uniform Ag/Fe(100) quantum wells*, Phys. Rev. Lett. **81** (1998) 5632
- [128] J.J. Paggel, T. Miller and T.-C. Chiang, *Temperature dependent complex band structure and electron-phonon coupling in Ag*, Phys. Rev. Lett. **83** (1999) 1415
- [129] K. Takahashi, A. Tanaka, H. Sasaki, W. Gondo, S. Suzuki and S. Sato, *Temperature-dependent angle-resolved photoemission study for quantum-well states in Ag nanofilm*, Phys. Rev. B **60** (1999) 8748
- [130] D.A. Luh, T. Miller, J.J. Paggel, T.-C. Chiang, *Large electron-phonon coupling at an interface*, Phys. Rev. Lett. **88** (2002) 256802
- [131] B. Hellsing, A. Eiguren and E.V. Chulkov, *Electron-phonon coupling at metal surfaces*, J. Phys.: Condens. Matter **14** (2002) 5959
- [132] A. Šiber and M.T. Cvitaš, in preparation
- [133] B.A. McDougall, T. Balasubramanian and E. Jensen, *Phonon contribution to quasiparticle lifetimes in Cu measured by angle-resolved photoemission*, Phys. Rev. B **51** (1995) 13891
- [134] R. Paniago, R. Matzdorf, G. Meister and A. Goldmann, *High-resolution photoemission study of the surface states near Gamma on Cu(111) and Ag(111)*, Surf. Sci. **331-333** (1995) 1233
- [135] R. Paniago, R. Matzdorf, G. Meister and A. Goldmann, *Temperature dependence of Shockley-type surface energy bands on Cu(111), Ag(111) and Au(111)*, Surf. Sci. **336** (1995) 113
- [136] R. Matzdorf and A. Goldmann, *High-resolution photoemission study of the M-surface states on Cu(111)*, Surf. Sci. **359** (1996) 77
- [137] F. Theilmann, R. Matzdorf, G. Meister, A. Goldmann, *Influence of surface structural disorder on linewidths in angle-resolved photoemission spectra*, Phys. Rev. B **56** (1997) 3632
- [138] R. Matzdorf, G. Meister and A. Goldmann, *Phonon contributions to photohole linewidths observed for surface states on copper*, Phys. Rev. B **54** (1996) 14807
- [139] T. Balasubramanian, E. Jensen, X.L. Wu and S.L. Hulbert, *Large value of the electron-phonon coupling parameter ( $\lambda=1.15$ ) and the possibility of surface superconductivity at the Be(0001) surface*, Phys. Rev. B **57** (1998) R6866
- [140] S. LaShell, E. Jensen and T. Balasubramanian, *Nonquasiparticle structure in the photoemission spectra for the Be(0001) surface*, Phys. Rev. B **61** (2000) 2371
- [141] M. Henksberger, D. Purdie, P. Segovia, M. Garnier and Y. Baer, *Photoemission study of a strongly coupled electron-phonon system*, Phys. Rev. Lett. **83** (1999) 592
- [142] P. Hofmann, Y.Q. Cai, C. Grütter and J.H. Bilgram, *Electron-lattice interaction on  $\alpha$  - Gd(010) surface*, Phys. Rev. Lett. **81** (1998) 1670
- [143] E. Rotenberg, J. Schaefer and S.D. Kevan, *Coupling between adsorbate vibrations and an electronic surface state*, Phys. Rev. Lett. **84** (2000) 2925
- [144] M. Milun, P. Pervan and D.P. Woodruff, *Synchrotron radiation study of V(100)*, Fizika **8** (1999) 35; See the list of relevant references for vanadium magnetism, electronic and structural properties.

## 10. REFERENCES

---

- [145] H. Beckmann, F. Ye and G. Bergmann, *Weak antiferromagnetism of monolayers and multilayers of V on Au films*, Phys. Rev. Lett. **73** (1994) 1715
- [146] P. Pervan, T. Valla and M. Milun, *Vanadium CVV Auger transition*, Solid State Commun. **99** (1996) 393
- [147] P.W. Davies and R.M. Lambert, *A LEED investigation of the structure and properties of the reconstructed vanadium (100)-(5×1) surface*, Surf. Sci. **107** (1981) 391
- [148] V. Jensen, J.N. Andersen, H.B. Nielsen and D.L. Adams, *Comments on "A LEED investigation of the structure and properties of the reconstructed vanadium (100)-(5×1) surface" by P.W. Davies and R.M. Lambert*, Surf. Sci. **112** (1981) L785
- [149] K. Nakayama, T. Sato, S. Usami and M. Iwatsuki, *Low-energy electron diffraction and scanning tunnelling microscopy study on the reconstruction of the vanadium (111) surface*, Jap. J. Appl. Phys.: (1-Short Notes and Review Papers) **34** (1995) 589
- [150] B.J. Hopkins, M. Leggett and G.D. Watts, *A RHEED study of the adsorption of oxygen, hydrogen, nitrogen and water vapour on the (100) face of tantalum*, Surf. Sci. **28** (1971) 581
- [151] V. Jensen, J.N. Andersen, H.B. Nielsen and D.L. Adams, *The surface structure of V(100)*, Surf. Sci. **116** (1982) 66
- [152] J.S. Foord, A.P.C. Reed and R.M. Lambert, *The (100) surfaces of chromium and vanadium: reconsiderations of their structure and reactivity*, Surf. Sci. **129** (1983) 79
- [153] T. Valla, P. Pervan and M. Milun, *Photoelectron spectroscopy characterisation of the V(100) surface*, Surf. Sci. **309** (1994) 843
- [154] M. Kralj, P. Pervan, M. Milun, J. Schneider, B. Schaefer, A. Rosenhahn and K. Wandelt, *STM investigations of contaminated and clean V(100) surface*, Fizika A **8** (1999) 123
- [155] T. Valla, P. Pervan and M. Milun, *Interaction of oxygen and silver on the V(100) surface*, Appl. Surf. Sci. **89** (1995) 375
- [156] C. Krenn, C. Eibl, W. Mauritch, ELD. Hebenstreit, P. Varga and A. Winkler, *Adsorption kinetics and energetics of atomic hydrogen (deuterium) on oxygen and carbon covered V(100)*, Surf. Sci. **445** (2000) 343
- [157] R. Koller, W. Bergermayer, G. Kresse, E.L.D. Hebenstreit, C. Konvicka, M. Schmid, R. Podloucky and P. Varga, *The structure of the oxygen induced (5× 1) reconstruction of V(100)*, Surf. Sci. **480** (2001) 11
- [158] C. Konvicka, A. Hammerschmid, M. Schmid and P. Varga, *Stabilizing single metal adatoms at room temperature: Pd on C- and O-covered V(100)*, Surf. Sci. **496** (2002) 209
- [159] F. Dulot, P. Turban, B. Kierren, J. Eugene, M. Alnot and S. Andrieu, *(001) V surface structures analysed by RHEED and STM*, Surf. Sci. **473** (2001) 172
- [160] P. Turban, F. Dulot, B. Kierren and S. Andrieu, *Influence of oxygen on surface reconstruction and growth of (001) vanadium*, Appl. Surf. Sci. **177** (2001) 282
- [161] M.M.J. Bischoff, C. Konvicka, A.J. Quinn, M. Schmid, J. Redinger, R. Podloucky, P. Varga and H. van Kempen, *Scanning tunnelling spectroscopy on clean and contaminated V(001)*, Surf. Sci. **513** (2002) 9
- [162] M. Kralj, P. Pervan, M. Milun, K. Wandelt, Đ. Mandrino and M. Jenko, *HRAES, STM and ARUPS study of 5×1 reconstructed surface*, Surf. Sci. **526** (2003) 166
- [163] F.J. Szalkowski and G.A. Somorjai, *The characterisation of some vanadium (100) surface structures using LEED and AES*, J. Chem. Phys. **64** (1976) 2985

## 10. REFERENCES

- 
- [164] M. Todorova, W.X. Li, M.V. Ganduglia-Pirovano, C. Stampfl, K. Reuter, and M. Scheffler, *Role of subsurface oxygen in oxide formation at transition metal surfaces*, Phys. Rev. Lett. **89** (2002) 096103
- [165] T. Valla, M. Milun, *Properties of ultra thin silver films on a V(100) surface in a wide temperature range*, Surf. Sci. **315** (1994) 81
- [166] T. Valla, P. Pervan and M. Milun, *Characterisation of the 1 and 2 ML silver films on the V(100) surface*, Vacuum **46** (1995) 1223
- [167] The possible confusion with respect to the experimentally observed QW peak shifts and the shifts predicted by phase accumulation formula has been discussed in R.K. Kawakami et al., *Quantum-well states in copper thin films*, Nature **398** (1999) 132
- [168] K. Kalki, M. Schick, G. Ceballos and K. Wandelt, *Thin film growth on an O-precovered Ru(0001) surface*, Thin Solid Films **228** (1993) 36
- [169] H. Wolter, K. Meinel, C. Ammer, K. Wandelt and H. Neddermeyer, *O-induced modification of thin Cu films on Ru(0001)*, Phys. Rev. B **56** (1997) 15459
- [170] M. Kralj, T. Valla, P. Pervan and M. Milun, unpublished
- [171] H. Wormeester, M.E. Keine, E. Hüger and E. Bauer, *Growth of hcp Cu on W(100)*, Surf. Sci. **377** (1997) 988
- [172] H. Wormeester, E. Hüger and E. Bauer, *hcp and bcc Cu and Pd films*, Phys. Rev. Lett. **77** (1996) 1540
- [173] M. Kralj, M. Milun, P. Pervan, P. Lazić, R. Brako, Ž. Crljen, J. Schenider, A. Rosenhahn and K. Wandelt, in preparation
- [174] P. Pervan, M. Milun, unpublished
- [175] P.D. Johnson, K. Garrison, Q. Dong, N.V. Smith, Dongqi Li, J. Mattson, J. Pearson and S.D. Bader, *Hybridization and the effective mass of quantum-well states in magnetic multilayers*, Phys. Rev. B **50**, 8954 (1994)
- [176] A. Ernst, J. Henk, M. Lüders, Z. Stozek and W.M. Temmerman, *Quantum-size effects in ultrathin Ag films on V(001): Electronic structure and photoelectron spectroscopy*, Phys. Rev. B **66** (2002) 165435
- [177] L.D. Landau and E.M. Lifschitz, *Quantum mechanics (non-relativistic theory)*, 3<sup>rd</sup> ed., Pergamon Press, Oxford, England, 1973
- [178] *CRC Handbook of Physics and Chemistry*, 59<sup>th</sup> Edition, CRC Press, Boca Raton, FL, 1978
- [179] D.P. Jackson, *Approximate calculation of surface Debye temperatures*, Surf. Sci. **43** (1974) 431
- [180] D.P. Woodruff and M.P. Seah, *The temperature dependence of the magnitudes and positions of the peaks in LEED intensity-energy plots*, Phys. Stat. Solidi **1A** (1970) 429
- [181] P.H. Citrin, G.K. Wertheim and Y. Baer, *Many body processes in X-ray photoemission line shapes from Li, Na, Mg and Al metals*, Phys. Rev. B **15** (1977) 4256
- [182] J.A. Knapp, F.J. Himpsel, A.R. Williams and D.E. Eastman, *Temperature dependence of bulk and surface energy bands in copper using angle-resolved photoemission*, Phys. Rev. B **19** (1979) 2844
- [183] N.E. Christensen, *Photoemission from Au (111) and (110). Temperature effects*, Phys. Rev. B **20** (1979) 3205
- [184] T. Yokoya, A. Chainani and T. Takahashi, *High-resolution temperature-dependent valence-band photoemission spectroscopy of gold: nature of electron-phonon coupling*, Phys. Rev. B **55** (1997) 5574
- [185] R. Paniago, R. Matzdorf, A. Goldmann and R. Courths, *Temperature dependence of d-like surface states on Cu(100) and Cu<sub>3</sub>Au(100) – an angle-resolved photoemission study*, J. Phys.: Condens. Matter **7** (1995) 2095

## 10. REFERENCES

---

- [186] U. Harten, J.P. Toennies and Ch. Wöll, *Helium time-of-flight spectroscopy of surface-phonon dispersion curves of the noble metals*, Farad. Disc. Chem. Soc. **80** (1985) 137
- [187] Y. Chen, S.Y. Tong, M. Rocca, P. Morreto, U. Valbusa, K.P. Bohnen and K.M. Ho, *High-resolution electron energy-loss spectroscopy analysis of Ag(001): discovery of a new surface longitudinal mode using first-principles phonon calculations*, Surf. Sci. **250** (1991) L389
- [188] A. Šiber, *Comment on "Temperature dependent complex band structure and electron-phonon coupling in Ag"*, (downloadable at <http://www.ifs.hr/~asiber/download.htm>) unpublished, 2000
- [189] A. Šiber, private communication
- 190 A.M. Shikin, O. Rader, G.V. Prudnikova, V.K. Adamchuk and W. Gudat, *Quantum well states of sp- and d-character in thin Au overlayers on W(110)*, Phys. Rev. B **65** (2002) 075403
- [191] S. Crampin, S. de Rossi, F. Ciccacci, *Integrity of quantum-well resonances in metallic overlayers*, Phys. Rev. B **53** (1996) 13817
- [192] T.Valla, P.D.Johnson, unpublished
- [193] P.D. Johnson, private communication
- [194] V.Yu. Aristov, M. Bertolo, K. Jackobi, F. Maca and M. Scheffler, *Experimental and theoretical investigation of the electronic structure of silver deposited onto InSb(110) at 10 K*, Phys. Rev. B **48** (1993) 5555
- [195] M. Bode, R. Pascal and R. Wiesendanger, *Distance-dependent STM study of the W(110)/C-R(15×3) surface*, Z. Phys. B **101** (1996) 103
- [196] K.-H. Hansen, J. Gottschalck, L. Petersen, B. Hammer, E. Laegsgaard, F. Besenbacher and I. Stensgaard, *Surface waves on NiAl(110)*, Phys. Rev. B **63** (2001) 115421
- [197] Z. Song, J.I. Pascual, H. Conrad, K. Horn and H.-P. Rust, *Surface states of d character imaged by scanning tunneling microscopy*, Surf. Sci. **491** (2001) 39